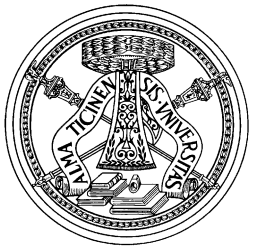

Università degli Studi di Pavia

Dipartimento di Scienze della Terra e dell'Ambiente

SCUOLA DI ALTA FORMAZIONE DOTTORALE

MACRO-AREA SCIENZE E TECNOLOGIE

DOTTORATO DI RICERCA IN SCIENZE DELLA TERRA E DELL'AMBIENTE

Mattia Luca Mazzucchelli

Development of computational mechanics methods for geobarometry of non-ideal host-inclusion systems

Anno Accademico 2017-2018
Ciclo XXXI

Coordinatore
Prof. Roberto Sacchi

Tutor
Prof. M.Chiara Domeneghetti

Co-tutor
Dr. Ross J. Angel

Contents

Abstract

Minerals that are trapped as inclusions within other host minerals, after exhumation to the Earth's surface, will exhibit stress and strain fields that are different to those in the host because of the contrast in their thermoelastic properties. The residual strain in the inclusion can be measured with X-ray diffraction or Raman spectroscopy, and, if interpreted correctly through elastic geobarometry, it allows the determination of the entrapment conditions, giving us invaluable information on the pressures and temperature of metamorphism during geodynamical processes such as subduction. However, current models for elastic geobarometry make several assumptions: the geometry of the system is ideal, with a spherical inclusion isolated at the center of an effectively infinite host, and both the minerals are elastically isotropic. None of these conditions apply in natural systems: no mineral is perfectly elastically isotropic and inclusions might be non-spherical and close to grain boundaries or other inclusions. The effect of these assumptions on the residual strain and stress can be evaluated through numerical calculations, such as Finite Element Modeling (FEM), a well-suited technique to solve mechanical problems over complex geometries.

Keeping the assumption of isotropic elasticity, I define a geometrical factor (Γ) to correct the residual pressure in the inclusion (P_{inc}) for non-ideal geometry. With this analysis it is possible to estimate which geometries of host-inclusion systems lead to deviations in the final P_{inc} smaller than the typical experimental uncertainties in the determination of inclusion pressures, and can therefore be safely used for geobarometry without any correction. The Γ factor can also be applied to correct the residual pressure measured experimentally accounting for the geometric effects. The P_{inc} corrected for the geometry can then be used to calculate the entrapment pressures using ideal-geobarometry models. For more accurate results, I developed a procedure to determine the geometrical factor directly on the 3D model obtained from the micro-tomography of the sample, preserving the shape and mutual orientation of the minerals.

Raman spectroscopy measurements on a zircon inclusion in garnet from the ultrahigh-pressure Dora Maira Massif, revealed that the strain in the inclusion is gradually released as the inclusion approaches the external surface of the host during a step-by-step

polishing of the petrological thick section. The experimental results confirm the outcome of FE models, showing that the rate of strain release depends on the contrast in elastic properties between the host and the inclusion, their elastic anisotropy and the mutual crystallographic orientation. This allows us to give new methodological guidelines for determining the residual strain in inclusions contained in rock sections.

I present also a new method for elastic geobarometry for spherical elastically anisotropic inclusions in quasi-isotropic hosts, based on a combination of equations of state and FEM. The final strain in the inclusion is first calculated as imposed only by the deformation of the cavity (i.e. the host) during the exhumation, without considering any mechanical coupling between the host and the inclusion. The discontinuity in traction at the interface between the two minerals is then relaxed through the anisotropic elastic relaxation of the system, until the mechanical equilibrium is restored. The solution for the change in strain upon relaxation is related to Eshelby's equivalent inclusion problem and can be found analytically for a few cases with specific crystallographic symmetries, but not for host minerals typical of high-pressure metamorphic rocks (e.g. garnets, zircon). It can be computed numerically with FE analyses, without any restriction given by the elastic anisotropic properties of the host and of the inclusion and their mutual orientation. However, this approach is extremely time consuming since a new analysis is needed for each specific initial state. I propose a semi-analytical solution based on the application of FEM, under the assumption of linear elasticity, introducing a linear mapping represented by a fourth order non-symmetric tensor (the relaxation tensor $\mathbf{R}$) to transform the unrelaxed strain into the relaxed strain. This approach can be used to predict the residual strain/stress state in an inclusion if the entrapment conditions are known, or to estimate the entrapment conditions from the residual strain measured in real inclusions. Examples are shown of applications to inclusions in garnets, which are common hosts in ultra-high pressure metamorphic rocks.

Introduction

Application of conventional thermobarometry to High-Pressure (HP) and Ultra-High-Pressure (UHP) metamorphic rocks is extremely challenging due to alteration processes, chemical re-equilibration and diffusion, and kinetic limitations. Elastic geothermobarometry on host-inclusion systems is a complementary method independent of chemical equilibrium. This method allows the determination of the pressure (P) and temperature (T) of entrapment of mineral inclusions in their mineral hosts, essentially on the basis of the elasticity of the two minerals. It therefore can provide new constraints on the P-T conditions attained during metamorphism (Angel et al., 2015b). For example, because it does not rely on chemical equilibrium between minerals, it has the potential to provide information on over-stepping of reaction boundaries (Spear et al., 2014). Several studies reported successful examples of application of elastic geobarometry to natural (e.g. Enami et al., 2007) and synthetic (e.g. Thomas and Spear, 2018) samples. However, some discrepancies still exist that pose limitations to the applicability of the current methodologies (e.g. Ashley et al., 2016) and that required the introduction of arbitrary corrections, such as empirical calibrations for interpreting the Raman spectra collected from inclusions.

A fundamental assumption of elastic geobarometry is that at the moment when the inclusion is trapped by its host crystal, both the host and inclusion experience the same temperature and the same hydrostatic pressure, and that the inclusion crystal fits exactly inside the cavity within the host crystal without any void space. While these P-T conditions are maintained, and there is no change in the external stress field, there is no development of stress gradients across the host and inclusion, and both phases continue to experience the external pressure. If the host and the inclusion have a contrast in elastic properties, when P and T change the inclusion may exhibit stress and strain fields that are different to those in host because the inclusion is constrained to undergo the same volume change as its host mineral. For example, if the inclusion is softer than the host, during decompression from entrapment P_{trap} -T_{trap} conditions to room conditions the volume of the hole in the host expands less than would a free crystal of the inclusion mineral. As a consequence, the inclusion is compressed by the surrounding host to a smaller volume than expected for the final external P and T and

exhibits a pressure significantly greater than the external ambient pressure at room conditions (Angel et al., 2014). All the changes in the system following entrapment are assumed to be elastic. If plastic deformation occurs, it will release some or all of the inclusion stress. Brittle failure of the host by cracking may also release inclusion stress, and is more difficult to evaluate because it can change the inclusion stress in a variety of different ways (Tajčmanová et al., 2014). Phase changes in the inclusions, such as the inversion of trapped coesite to quartz or the crystallization of melt inclusions, may result in the inclusion pressure being buffered (Gillet et al., 1984; Korsakov et al., 2009; Anzolini et al., 2016), and requires more elaborate analysis. Inclusion minerals formed by phase changes can often be identified by the characteristic textures formed, for example the palisade textures seen in quartz inverted from coesite, and cracked inclusions are readily identified by optical microscopy. Therefore, application of elastic geobarometry is usually restricted to un-cracked systems containing a single mineral inclusion which does not undergo reactions or phase transformations. In this case the overpressure in the inclusion can be simply calculated by computing the volume change of the host mineral from entrapment to room conditions, from its PVT Equation of State (EoS), and constraining the inclusion to that volume change. However, current models for elastic geobarometry (e.g. Van der Molen and Van Roermund, 1986; Zhang, 1998; Guiraud and Powell, 2006; Angel et al., 2017b) make further assumptions such as the simplified geometry of the system (the inclusion is spherical and isolated at the center of an effectively infinite host) and the use of isotropic elastic properties for both the host and the inclusion. These conditions mean that during the exhumation the stress in the inclusion is homogeneous and hydrostatic which allows for a simple analytical solution of the problem (Goodier, 1933; Eshelby, 1957; Zhang, 1998). None of these conditions apply in natural systems: no mineral is perfectly elastically isotropic and inclusions are often close to grain boundaries or other inclusions, and they might be non-spherical. This thesis will investigate how the assumptions of ideal geometry and isotropic elastic properties affect the application of elastic geobarometry and the calculation of the entrapment conditions (P_{trap} , T_{trap}), providing examples of application to UHP metamorphic rocks and diamond geobarometry.

Part I: geobarometry for geometrically non-ideal host inclusion systems

Application of ideal elastic geobarometry requires the volume strain or the residual pressure (P_{inc}) to be measured on natural inclusions that can be contained either in a thick or thin section cut from the metamorphic rock specimen or in their diamond host. In both cases, the size of the inclusion, its proximity to the external surfaces and its shape can strongly affect the stress/strain retained by the inclusion and thus the calculation of the entrapment conditions if they are not accounted for. Several

studies pointed out the effects of the inclusion size and of its partial exposure with respect to the mineral host surface on the residual pressure determination (e.g. Rosenfeld and Chase, 1961; Zhang, 1998; Enami et al., 2007). Nevertheless, open questions still remain, including: how much can the contrast in properties between the host and the inclusion and their geometry influence the residual strain? What is the effect of the inclusion anisotropy in the residual strain release? These effects can be evaluated through numerical calculations. In the paper "Elastic geothermobarometry: Corrections for the geometry of the host-inclusion system" (published in *Geology* and reported in chapter 1 of this thesis) I applied the Finite Element Method (FEM) on models of elastically isotropic host-inclusion systems with non-ideal geometries to determine how the geometry affects the residual pressure P_{inc} during the exhumation of the rock from entrapment conditions to the Earth's surface. Through 3D FEM models I explored the effects of several deviations from the ideal geometry, including the size of the inclusion relative to the host and its proximity to external surfaces. To evaluate the effects of non-spherical shapes I modeled ellipsoidal, cylindrical and prismatic inclusions. The residual pressure obtained from each of these models was then compared to the pressures calculated for the same exhumation from the model for ideal-geobarometry (Angel et al., 2017b) for a spherical inclusion contained in an infinite host. This comparison allowed me to introduce a *geometrical factor* (Γ) defined as the normalized deviation of the actual inclusion pressure from that expected for an ideal isolated spherical inclusion, for the same decompression. As a consequence, I could provide guidelines as to which geometries of host-inclusion systems lead to deviations in the final P_{inc} smaller than the typical experimental uncertainties in inclusion pressures obtained from conventional experimental measurements, and can therefore be safely used for geobarometry without any correction. In all the other cases, the Γ factor can be used to correct the residual pressure measured experimentally accounting for the geometric effects. Once the residual inclusion pressure is corrected for the geometry of the system it can then be used to calculate the entrapment pressures using ideal-geobarometry models.

When the shape of the inclusion is not ellipsoidal, or it is not isolated within an infinite host but is close to the external surface of the host or to other inclusions, the stress and the strain fields in the inclusion are not homogeneous. Also, the residual "pressure" (defined as the negative of the mean normal stress $P = -(\sigma_{11} + \sigma_{22} + \sigma_{33})/3$) is not constant within the inclusion, and as a consequence the geometrical factor may change in value from point to point within the inclusion. The state of strain of an inclusion (from which the residual pressure is obtained) can be measured experimentally with mainly two techniques: X-ray diffraction and Raman spectroscopy. The first approach gives the average state of strain of the inclusion since the information on its deformation is averaged over all the unit-cells in the crystal. On the other hand, Raman spectroscopy gives a point measurement, and, if the crystal is sufficiently large com-

pared to the section of the laser beam, it can be used to effectively track the variation of the strain field within an inclusion. The application of Raman spectroscopy as a probe for the strain state of a quartz inclusion in garnet is shown in the paper "Raman elastic geobarometry for anisotropic mineral inclusions" (published in *American Mineralogist* and reported in appendix A) which I coauthored as a side project during my PhD. This paper shows that the strain (and the mean normal stress, i.e. the pressure) is actually not homogeneous in a quartz inclusion with non-ellipsoidal shape. Therefore, the correction factor Γ must be calculated keeping in mind the experimental measurement that needs to be corrected. Γ can be either calculated as a local factor, to correct the measurement obtained from Raman spectroscopy on a specific point in the inclusion (usually its central point that is the least affected by stress concentration given by edges and corners), or as a bulk factor averaged over the entire volume of the sample to correct measurements from X-ray diffraction. The method implemented by this thesis based on FE provides the capability to perform both calculations. The derivation of Γ as a local factor is presented in chapter 1, while in chapter 2 it is defined as an average bulk factor. Chapter 2 presents a manuscript in preparation with the title "Depth of diamond formation obtained from single periclase inclusions" in which I was responsible for the 3D reconstruction, the correction for the geometry and the application of elastic geobarometry. Here is shown that the geometrical factor should be evaluated on a case-by-case basis with FEM analysis carried out on realistic digital models of the inclusions. X-ray micro-tomography was performed on two ferropericlase inclusions in a diamond host. I segmented the tomography to obtain a CAD model of the two inclusions that was meshed and incorporated in the FE model, which therefore preserves the shape of the inclusions and their reciprocal position and orientation. From the FE analysis I obtained two average geometrical factors, one for each inclusion, that allowed me to correct for the geometry the residual pressures obtained from X-ray diffraction. The corrected P_{inc} were then used for the back-calculation of the entrapment conditions of the ferropericlase inclusions in their diamond host.

The effect of the proximity of the inclusion to the external surface of the host is particularly crucial for high-pressure metamorphic rocks that are investigated on thick (thickness 100 μm) or thin (thickness 30 μm) sections cut from the rock specimen. Inclusions may be randomly contained at different depths within the section and the position with respect to the surface can modify the residual strain recorded by the inclusion, possibly leading to large errors in the back-calculation of the entrapment conditions. To verify that the correlation between position and residual strain calculated by FEM models does reproduce the real behavior, in the manuscript "How geometry and anisotropy affect residual strain in host-inclusion system: coupling experimental and numerical approaches" (published in *American Mineralogist* and reported in chapter 3) numerical calculations were combined with experimental measurements on a zircon inclusion in pyrope from the ultrahigh-pressure (UHP) Alpine Dora Maira Massif. The zircon in-

clusion was initially entrapped at the center of the thick section and the Raman spectra were collected performing several steps of polishing of the rock thick section to bring the inclusion closer to the external surface of the host. The residual pressures obtained from the Raman spectra as a function of the position of the inclusion were compared with the results of a set of FEM models that closely reproduce the shape of the inclusion and its proximity to the external surface, and that also account for the elastic anisotropy of the inclusion and its crystallographic orientation within the section. This comparison provided new methodological guidelines and examples of correction curves to adjust measurements carried out on anisotropic inclusions close to the surface of the thin or thick section. A key result is that elastic anisotropy of minerals is relevant and affects the final strain and stress state in the inclusion, especially when the geometry of the system is not ideal. But, as noted above, ideal elastic geobarometry assumes that minerals are elastically isotropic, and the incorporation of elastic anisotropy in models for geobarometry requires an extensive reformulation of the problem.

Part II: geobarometry for elastically anisotropic spherical inclusions

The extension of elastic geobarometry to include elastic anisotropy is best illustrated with the forward-calculation: the entrapment conditions (P_{trap}, T_{trap}) are assumed to be known, and the aim is to calculate the final residual strain and stress developed in the inclusion after the exhumation to the Earth's surface. Section 4.1 in chapter 4 shows that, as for the case of ideal geobarometry, this calculation is split into two steps: thermodynamic calculation and relaxation. The thermodynamic step considers the final strain in the inclusion as imposed only by the deformation of the cavity (i.e. the host) during the exhumation, without considering any mechanical coupling between the host and the inclusion. The calculation is based on non-linear elasticity and requires the knowledge of the volume and axial Equations of State (EoS) of both the host and of inclusion to describe how their crystallographic axes change in length with changing pressure and temperature. If the host and the inclusion are different minerals, when the host is at room condition (i.e. under an hydrostatic stress state with $\sigma_{11} = \sigma_{22} = \sigma_{33} = P \approx 0$ GPa) the inclusion is subject to a different stress field that depends on its elastic properties and on the strain imposed to it by the host. As a consequence, the host and the inclusion are not in mechanical equilibrium, and the discontinuity in traction at the interface between the host and the inclusion forces the elastic relaxation of the system until the mechanical equilibrium is restored. The calculation of the change in strain upon anisotropic relaxation requires the knowledge of the unrelaxed strain state, the full elastic properties of the host and the inclusion, including their variation with direction, and the relative orientation of their crystallographic axes. This problem is related to Eshelby's equivalent inclusion

problem and can be solved analytically for a few cases with specific crystallographic symmetries (e.g. transversely isotropic symmetry), but not for host minerals typical of high-pressure metamorphic rocks (e.g. garnets, zircon). Section 4.2.1 shows that the strain and stress in the inclusion after the relaxation can be found numerically with FE analyses, without any restriction given by the elastic anisotropic properties of the host and of the inclusion and their reciprocal orientation. However, this approach is extremely time consuming and would greatly restrict the routine applicability of elastic geobarometry since a new analysis is needed for any specific initial unrelaxed strain state, requiring hours of computational time. This can be avoided assuming that the elastic properties of both the host and the inclusion stay constant during the relaxation. Under this assumption, in section 4.2.2 I will demonstrate that a linear mapping represented by a fourth order non-symmetric tensor (the relaxation tensor $\mathbf{R}$) exists that transforms the unrelaxed strain into the relaxed strain. The 36 independent components of $\mathbf{R}$ can be found with a set of only six FE analyses. Once the relaxation tensor is calculated for a specific reciprocal orientation of the host and the inclusion it can be applied to relax any unrelaxed strain state for that system, without the need of new FE analyses. With this approach the final residual strain and stress in the inclusion can be predicted after exhumation from any entrapment condition. This allowed me to investigate efficiently the response of specific host-inclusion systems given by their anisotropic elasticity for a wide range of entrapment conditions. To this aim I developed an algorithm in Matlab® to produce contour plots that show synthetically all the relevant results (chapter 6). The code generates a grid of equally-spaced points of entrapment within a P_{trap}, T_{trap} range chosen by the user, and the exhumation of the host-inclusion system from each of these points to room conditions is simulated combining the thermodynamic and the relaxation calculations. The results provide the relaxed strain in the inclusion, from which the relaxed stress and all the other related quantities (e.g. volume strain, residual pressure ecc.) are obtained. I applied this procedure to evaluate the strain and the stress developed during exhumation in several inclusions (diamond, quartz, zircon) contained in garnets, all common mineral phases in Ultra-High Pressure (UHP) metamorphic rocks. Garnets have cubic crystallographic symmetry and are almost elastically isotropic, while the inclusions have been selected over a wide range of crystallographic symmetries (cubic, trigonal and tetragonal) and degree of elastic anisotropy. This choice allowed me to provide examples of exhumation of geologically relevant host inclusion systems, testing at the same time how the symmetry, the anisotropic elasticity and the crystallographic orientation of the inclusion affect the strain and the stress fields developed during exhumation (chapters 7 and 8).

Notes

Chapters 1 and 3 and the appendix A presents pre-print manuscripts of articles that have been published in international peer-review journals. Chapter 2 reports a manuscript

recently submitted for publication. They are self-standing units, complete with their own supplementary materials and references. Part II of this thesis shows the derivation and examples of application of anisotropic geobarometry. The conventions adopted, the elastic properties and the references relative to Part II are reported at the end of the thesis.

Part I

Geobarometry for geometrically non-ideal host inclusion systems

Chapter 1

Elastic geothermobarometry: Corrections for the geometry of the host-inclusion system

This chapter was published as an article in *Geology* with the title:

Elastic geothermobarometry: Corrections for the geometry of the host-inclusion system

Authors: M.L. Mazzucchelli[1*], P. Burnley[2], R.J. Angel[3], S. Morganti[4], M.C. Domeneghetti[1], F. Nestola[3], and M. Alvaro[1]

The final published version of the article can be downloaded at https://doi.org/10.1130/G39807.1.

1.1 Abstract

Elastic geothermobarometry on inclusions is a method to determine P-T conditions of mineral growth independent of chemical equilibrium. Because of the difference in their elastic properties, an inclusion completely entrapped inside a host mineral will develop

[1]Deparment of Earth and Environmental Sciences, University of Pavia, 27100 Pavia, Italy; [2]Department of Geosciences and High Pressure Science and Engineering Center, University of Nevada, Las Vegas, Nevada 89154, USA; [3]Department of Geosciences, University of Padua, 35131 Padua, Italy; [4]Department of Electrical, Computer, and Biomedical Engineering, University of Pavia, 27100 Pavia, Italy.

a residual stress upon exhumation, from which one can back-calculate the entrapment pressure. Current elastic geobarometric models assume that both host and inclusion are elastically isotropic and have an ideal geometry (the inclusion is spherical and isolated at the center of an infinite host). These conditions do not commonly occur in natural rocks, and the consequences for inclusion pressures can only be quantified with numerical approaches. In this paper, we report the results of numerical simulations of inclusions with finite element methods on elastically isotropic systems. We define and determine a geometry factor (Γ) that allows measured residual pressures to be corrected for the effects of non-ideal geometry. We provide simple guidelines as to which geometries can safely be used for elastic geobarometry without correcting for the geometry. We also show that the discrepancies between elastic and conventional geobarometry reported in literature are not due to geometrical effects, and therefore result from other factors not yet included in current models.

1.2 Introduction

Application of conventional geothermobarometry is extremely challenging in many rock types due to alteration processes, chemical re-equilibration and diffusion, and kinetic limitations. Elastic geothermobarometry on host-inclusion systems is a complementary method independent of chemical equilibrium. An inclusion completely entrapped inside a host mineral will develop a residual stress upon exhumation because of the contrast in elastic properties (Rosenfeld and Chase, 1961). If the host does not undergo plastic deformation or brittle failure after trapping the inclusion the entrapment pressure (P_{trap}) can be calculated from the measured residual pressure on the inclusion (or remnant pressure, P_{inc}), provided that the elastic properties (equations of state, EoS) for the host and inclusion are known (e.g., Zhang, 1998; Angel et al., 2014). Elastic geothermobarometry is increasingly applied to metamorphic rocks, where measurements of Raman shifts on quartz inclusions trapped in garnet (QuiG) give information on the residual stresses that can be used to infer growth conditions (e.g., Kouketsu et al., 2016) and the degree of over-stepping of garnet isograds (e.g., Spear et al., 2014). The validity of elastic geobarometric methods has been recently discussed by Ashley et al. (2016) who reported that the P_{trap} inferred from measured P_{inc} of quartz inclusions in garnets do not match those obtained by conventional geobarometry on the same rocks. However, the calculation of P_{trap} currently assumes that the minerals are elastically isotropic with ideal geometry where the inclusion is spherical and isolated at the center of the host (Goodier, 1933; Eshelby, 1957; Van der Molen and Van Roermund, 1986). None of these conditions apply in natural systems; neither quartz nor garnet are elastically isotropic, inclusions are often close to grain boundaries or other inclusions, and they are often not spherical. The resulting changes in P_{inc} can only be quantified using numerical approaches. In this paper we use finite element (FE) models of elastically

isotropic host-inclusion systems with non-ideal geometries to determine the magnitude of the geometric effects on P_{inc}, and in turn on the calculated P_{trap}. We show that the discrepancies reported by Ashley et al. (2016) are only partly due to the geometry of their samples. Finally, we provide guidelines as to which geometries of host-inclusion systems lead to deviations smaller than the typical experimental uncertainties in inclusion pressures obtained from conventional μ-Raman measurements, and can therefore be safely used for geobarometry without any correction.

1.3 Methods

The final stress state of an inclusion is path-independent, and it is convenient to split the $P-T$ change from the entrapment conditions (P_{trap}, T_{trap} see Fig. 1.1) to the final pressure and temperature (P_{end}, T_{end}) into two parts (see Angel et al. 2014). Fig. 1.1 illustrates the stepwise procedure used to calculate the residual pressure from known entrapment conditions. During step 1 the temperature is reduced from T_{trap} to T_{end} along the isomeke (Rosenfeld and Chase, 1961; Adams et al., 1975) thus preserving the reciprocal mechanical equilibrium between the host and the inclusion. The change in external T and P required to maintain the pressure in the inclusion equal to the external P can be calculated directly from the thermodynamic properties of the minerals without any influence of the geometry of the system. In step 2 the isothermal decompression from P_{foot}, T_{end} to the final P_{end}, T_{end} (as in Angel et al., 2014) causes a mechanical disequilibrium between the host and the inclusion. Consequently, the stresses are readjusted through the relaxation process. Since the relaxation depends on force balance at the interface between host and inclusion, in this step the geometry becomes important. The exact amount of relaxation in step 2 can only be calculated if the geometry of the system is ideal, for all other cases a numerical approach is required. In our study we have used two commercially-available engineering packages (MARC Mentat By MSC Software and Abaqus by Dassault Systèmes) to create and solve 2D axisymmetric and 3D models using FE numerical simulations. Always using isotropic elastic properties, we explored the effects of several deviations from ideal geometry, including the size of the inclusion relative to the host and its proximity to external surfaces. To evaluate the effects of non-spherical shapes we modeled ellipsoids of revolution with aspect ratios 1:1:1, 2:1:1, 1:2:2, 5:1:1, and 1:5:5. The effects of edges and corners were then determined by comparing the results against cylindrical and prismatic models (with quadrilateral cross-sections) with the same aspect ratios. To simulate the effects of external pressure, edge loads (for 2D models) or face loads (for 3D models) were applied to the external boundaries of the models. Stationary boundary conditions were placed on the relevant edges and faces to prevent rigid body rotations and translations. An example of a model mesh and the elastic properties used in the models are given in the supplementary materials (section 1.6), more details are also

given in Burnley and Davis (2004), Burnley and Schmidt (2006) and Abaqus (2016). For each model, we performed calculations using different elastic isotropic properties for the host and the inclusion to probe possible scaling laws For each geometry we calculated the actual inclusion pressure $P_{inc}^{non-ideal}$ by performing FE simulations upon isothermal decompression from P_{foot} to P_{end}. We define a geometrical factor (hereafter Γ) as the normalized deviation of the actual inclusion pressure from that expected for an ideal isolated spherical inclusion, P_{inc}^{ideal}, for the same decompression:

$$\Gamma = \frac{P_{inc}^{non-ideal}}{P_{inc}^{ideal}} - 1 \tag{1.1}$$

The value of Γ is obtained using the linear elastic approximation, so it is independent of the magnitude of $P_{foot} - P_{end}$. Because pressures in natural inclusions are typically less than 1 GPa (e.g., Ashley et al., 2016), this linear approximation is not significant for most inclusions, and the Γ parameter can be used to correct experimentally-determined inclusion pressures ($P_{inc}^{exp} = P_{inc}^{non-ideal}$) for geometric effects:

$$P_{inc}^{corrected} = \frac{P_{inc}^{exp}}{1 + \Gamma} \tag{1.2}$$

This corrected residual inclusion pressure can then be used to calculate the entrapment pressures using isotropic elastic geobarometry models (e.g Angel et al., 2014, 2017b).

1.4 Results and discussion

1.4.1 Insights from FEM

Our FE models have been validated against the analytical 'exact' solution by modeling an ideal infinite spherical system. In practice, the host can be considered infinite when the simulation results do not change upon further increase in the size of the host (Fig. 1.2A). Our FE models then reproduce the analytical solution for the pressure inside a spherical inclusion well within the expected numerical precision (i.e., 0.2 %). The stress in the region of the host close to the inclusion is always deviatoric (e.g., Zhang, 1998). Therefore, when a large inclusion is surrounded by a thin layer of host crystal, the deviatoric stress extends throughout the volume of the thin host layer causing the outer boundary of the host to deform. The host is thus no longer able to shield the inclusion from the external P. Consequently, the P_{inc} will be partially released. For a spherical inclusion at the center of the host, the pressure release is a function of the size and the properties of the inclusion with respect to the host (Fig. 1.2A). Hosts much stiffer than the inclusion (e.g., quartz in garnet) can preserve a larger P_{inc} . Our results

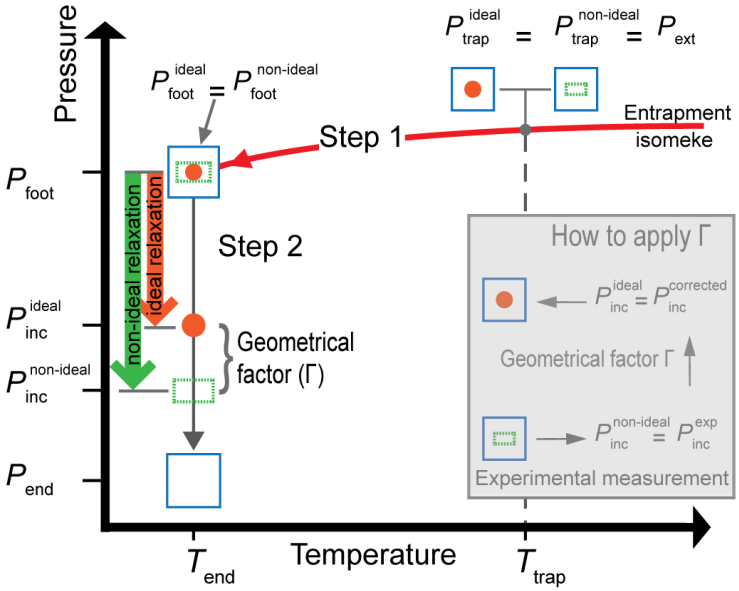

Figure 1.1: Calculation procedure for two host inclusion pairs; one with ideal geometry (red dot inclusion) and one with non-ideal geometry (green dashed rectangle), that are trapped at the same P_{trap}, T_{trap} conditions. Step 1: along the isomeke the host and inclusion are in reciprocal mechanical equilibrium. Therefore, the Pfoot at the final Tend will be the same for any geometry of the system. Step 2: The host is decompressed to the final pressure P_{end}. The relaxation of the inclusion is geometry-dependent and therefore the final P_{inc} will be different for the two systems ($P_{inc}^{non-ideal} \neq P_{inc}^{ideal}$). The geometrical factor Γ is a measure of this discrepancy. The Inset illustrates how to apply Γ to correct the experimental P_{inc}^{exp} measured on natural rocks with non-ideal geometry. The corrected $P_{inc}^{corrected}$ can then be used to back-calculate the P_{trap} using currently available elastic geobarometry models. From Mazzucchelli et al. (2018).

indicate that, if the radius of the host is at least four times that of the inclusion, both the $P_{inc}^{non-ideal}$) and the $P_{trap}^{non-ideal}$ are within 1 % of the value expected for an infinite host. For the same reason, the capacity of the host to act as a pressure vessel for the inclusion is also reduced when a small inclusion is close to the external surface of the host (Fig. 1.2B). Stiffer hosts again preserve more residual pressure than softer hosts. Regardless of the contrast in elastic properties, if the inclusion is at least 3 radii from the external surface of the host the effect on P_{inc} is smaller than 1 %. If a spherical and isotropic inclusion is close to the external surface of the host, the normal stresses in the inclusion are not homogeneous, and the domains of the inclusion closer to the external surface record stresses lower than those toward the center of the host. For a quartz inclusion in pyrope the variation of the pressure across the inclusion can reach up to 8 % when the distance to the surface is half the radius of the inclusion (Fig. 1.2C). Note that these conclusions do not depend on the absolute size of the inclusion but upon the relative sizes of the inclusion and host. For fluid inclusions the aspect ratio and the presence of corners and edges are two major influences on the pressures of isolated inclusions (e.g., Burnley and Davis, 2004; Burnley and Schmidt, 2006). In our models of solid inclusions we find that the aspect ratio of the inclusion gives rise to deviations in P_{inc} greater than 7 % for soft platy inclusions (aspect ratio 1:5:5) in stiff hosts (e.g., quartz in pyrope, see Fig. 1.3). The presence of edges and corners further enhances the deviations ($\approx 9\%$). For non-spherical shapes with edges and corners, the stress in the inclusion is neither homogeneous nor hydrostatic. The pressure varies from the center of the inclusion toward its external surface, by different amounts in different directions. For a quartz inclusion with aspect ratio 1:5:5 in pyrope the pressure variation along the longer axes of the inclusion is 5 %, while it is less than 1 % along the shortest axis (see Fig. 1.5 and Fig. 1.6). For a residual pressure at the center of the inclusion of 0.3 GPa, the differential stress ($\sigma_{max} - \sigma_{min}$) within the inclusion reaches 0.28 GPa. For a stiff inclusion in a soft host with the same shape (e.g., Diamond in Pyrope) the pressure variation within the inclusion is much larger (22 %) and of the opposite sign (see Fig. 1.5). The exact effect of inclusion shape on $P_{inc}^{non-ideal}$ is a complex interplay between the bulk and shear moduli for both host and inclusion (see Fig. 1.3). In general, the influence of non-ideal shapes becomes greater when the bulk modulus of the host and the inclusion are similar, provided there is a significant contrast in shear moduli. For a soft inclusion in a stiffer host (quartz in garnet, or pyrope in diamond) with aspect ratios less than 1:2:2 the deviations induced by the shape are typically smaller than 5 % (Fig. 1.3).

1.4.2 Calculation of Entrapment Pressures

Ashley et al. (2016) used Raman spectroscopy to determine the remnant pressure in quartz inclusions in garnets, while they were heated up to 500 ° C. As the T increases the P_{inc}^{exp} increases because of thermal pressure effects, but the P_{trap} for a single inclusion

should always be a unique value independent of the temperature (T_end) at which the P_{inc}^{exp} is measured. However, Ashley et al. (2016) reported large variations on P_{trap} for the same inclusion calculated from the various P_{inc}^{exp} measured at different T_{end} and none of the calculated P_{trap} agreed with the results from conventional geobarometry. They ascribed this unphysical behavior to the use of unrealistic EoS for quartz close to the α - β structural phase transition. We chose this example to assess if the shape of the inclusion could explain these discrepancies. We consider the case of sample MT 09–09 where several quartz inclusions are entrapped in an almandine-rich garnet (Ashley et al., 2015, 2016). The entrapment pressures P_{trap} at 540 °C were recalculated from the experimental P_{inc}^{exp} of 0.300 GPa and 0.491 GPa at the minimum and maximum T_{end} (31 °C and 500 °C) using a more reliable EoS for quartz (Angel et al., 2017a) that explicitly includes the α - β transition. Assuming ideal geometry for the quartz inclusion the discrepancy between the two P_{trap} values is 0.186 GPa (Table 1.1), similar to that reported by Ashley et al. (2016) confirming that the differences cannot be ascribed to errors in the EoS. To eliminate the discrepancies in P_{trap} values the volume thermal expansion of almandine must be increased by more than 30 % to $\alpha_{298K} \approx 2.76{\cdot}10^{-5}K^{-1}$ which is unrealistic given that this value is much greater than those of any silicate garnet end-member. As the shapes of the inclusions measured by Ashley et al. (2016) are not reported, we then over-estimated the shape effects by modeling the inclusion as a platy prism (aspect ratio 1:5:5). At room temperature the correction factor is $\Gamma = -0.094$, similar to that for quartz in pyrope (Fig. 1.3), but decreases to $\Gamma = -0.078$ at 500 °C (Table 1.1) due to the elastic softening of quartz as it approaches the phase transition (Lakshtanov et al., 2007). The inclusion pressures corrected for shape, $P_{inc}^{corrected}$ are then 0.331 GPa (at 31 °C) and 0.532 GPa (at 500 °C), and result in a small but insignificant reduction of 0.02 GPa in the differences in P_{trap} calculated from the two measurements. Further, even with the geometrical correction the P_{trap} (1.091 and 0.929 GPa) are not in agreement with those from the conventional methods (0.82 GPa, Ashley et al., 2015). Thus neither the EoS nor the shape of the inclusion can explain the discrepancies found by Ashley et al. (2016), and other factors not yet included in the current models must be responsible for the discrepancies in the P_{trap} . One factor is that quartz inclusions in a garnet host will be subject to isotropic strain (leaving aside further perturbations arising from the elastic relaxation and the geometry) because garnet is cubic. As quartz is elastically anisotropic, the isotropic strain will result in a non-hydrostatic stress in the inclusion. The effect of this deviatoric stress on the Raman spectrum of quartz is not known in detail, but both theory (Key, 1967) and experiments (Briggs and Ramdas 1977) show that Raman peak shifts will be different from those predicted from hydrostatic calibrations used by Ashley et al., (2016) to convert measured Raman shifts into pressures. Therefore, the mismatch in the P_{trap} is probably due the combination of an inappropriate Raman-stress calibration and the assumption of elastic isotropy in the geobarometric models.

Table 1.1: Calculation of entrapment pressure (P_{trap}) for sample MT 09-09 before and after the correction for the shape of the inclusion.

	Uncorrected for shape		Correction for shape		
T_{end} °C	P_{inc}^{exp} (GPa)	P_{trap} at 540 °C from P_{inc}^{exp} (GPa)	Geometrical factor (Γ)	$P_{inc}^{corrected}$ (GPa)	P_{trap} at 540 °C from $P_{inc}^{corrected}$ (GPa)
31	0.300	1.041	-0.094	0.331	1.091
500	0.491	0.855	-0.078	0.532	0.929
		$\Delta P_{trap} = 0.186$			$\Delta P_{trap} = 0.162$

Note: ΔP_{trap} is calculated as the difference between P_{trap} from the P_{inc} at T_{end}=31 °C and that from the P_{inc} at 500 °C. The EoS used for quartz and almandine are reported in Table 1.3.

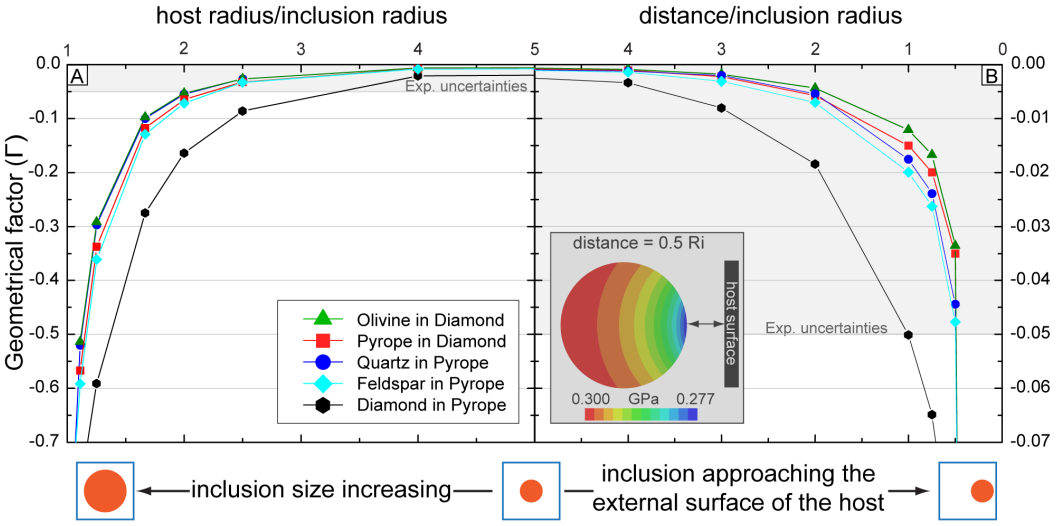

Figure 1.2: Effects of inclusion size and proximity to the external surface. A: Geometrical factor Γ for a spherical inclusion with increasing size (toward the left) with respect to that of the host. B: Γ for a spherical inclusion approaching the external surface of the host (toward the right). Γ is always negative when the distance of the inclusion from the external surface is reduced or when the size of the inclusion increases. This can be interpreted as the P_{inc} in the inclusion being reduced from the ideal P_{inc}. Inset: Stress map of a model of a quartz inclusion in pyrope, where the distance between the inclusion and the external surface of the host was one-half of the inclusion radius, showing the inhomogeneity of the stress. From Mazzucchelli et al. (2018).

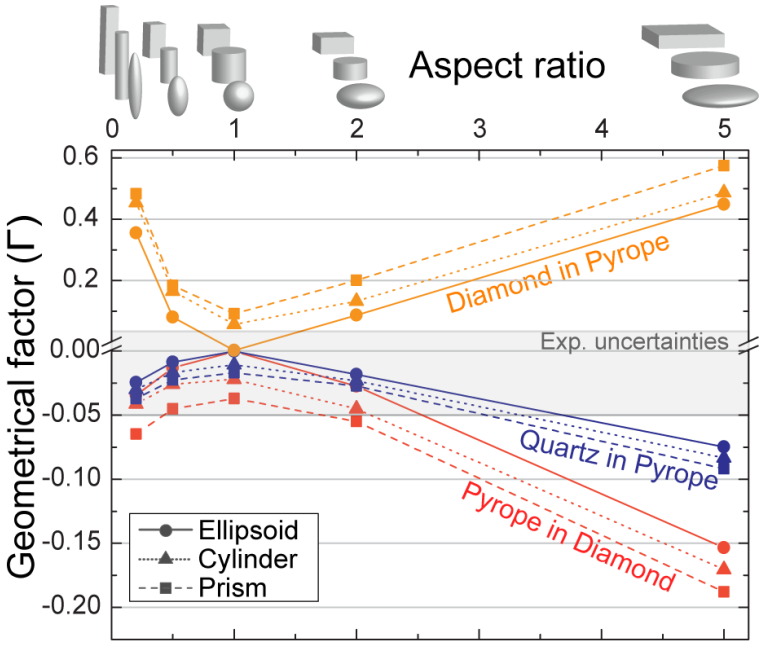

Figure 1.3: Geometrical factor Γ *for several shapes plotted versus the normalized aspect ratio. The latter is calculated with the unique axis as the denominator (e.g., aspect ratio 2:1:1 becomes 1/2 = 0.5). For a soft inclusion in a stiffer host (e.g., quartz in garnet),* $\Gamma < 0$ *and therefore* $P_{inc}^{non-ideal} < P_{inc}^{ideal}$ *(as in Fig. 1.1). The opposite occurs for a stiff inclusion in a softer host (e.g., diamond in pyrope). Note that* Γ *values greater than zero are plotted with a compressed vertical scale. From Mazzucchelli et al. (2018).*

1.5 Conclusions

Current elastic geobarometric models assume isotropic elastic properties for the host and the inclusion, and that the inclusions are isolated and spherical. These conditions do not commonly occur in natural rocks. Regardless of the relative stiffness of host and inclusion, for a big inclusion in a small host and for an inclusion close to the external surface of the host, the P_{inc}^{exp} is reduced relative to the ideal case, but a simple correction factor cannot be defined and Γ should be evaluated on a case-by-case basis with FEM analysis carried out on realistic digital models of the inclusions. For isotropic elasticity, our FEM results show that 'isolated' means that the inclusion must be at least 3 radii from external surfaces or other inclusions, for the geometric effects on P_{inc}^{exp} to be below 1 % (Fig. 1.2B). Under these conditions the shape effects then dominate the geometric corrections to the measured P_{inc}^{exp} (Fig. 1.3). For soft inclusions in a stiff host (e.g., quartz in garnet) non-spherical inclusions ($\Gamma < 0$), will exhibit a lower pressure than spherical inclusions. Correction of the measured P_{inc}^{exp} for the shape effects will therefore result in $P_{inc}^{corrected} > P_{inc}^{exp}$ and thus an increase in the calculated P_{trap}. By contrast, for stiff inclusions in soft hosts ($\Gamma > 0$), the correction will lead to $P_{inc}^{corrected} < P_{inc}^{exp}$ and therefore a reduction in P_{trap}. Experimental uncertainties on P_{inc}^{exp} are typically smaller than 5 % when measured by Raman spectroscopy (e.g., Ashley et al., 2016, Kouketsu et al., 2016). For P_{inc} below 1 GPa, the uncertainties propagated into the P_{trap} are smaller than those on the P_{inc} . Therefore, pressures from inclusions for which the geometrical effects on P_{inc}^{exp} are less than 5 % will provide reliable estimates of P_{inc}, and hence P_{trap} without the need for correction. For soft inclusions in stiff hosts, such as quartz in garnet, this means:

- the radius of the inclusion must be smaller than $\frac{1}{2}$ of that of the host
- the distance from the external surface is larger than $\frac{1}{2}$ the radius of the inclusion
- the inclusion aspect ratio is lower than 1:3:3 with few sharp edges and corners

These guidelines do not apply to inclusions stiffer than the host (e.g., diamond in garnet) which require much larger corrections of opposite sign (Fig. 1.3).

1.6 Supplementary materials

1.6.1 Computational details

We have used a commercially available engineering package, MSC MARC/ Mentat, to create and analyze 2D axisymmetric and 3D finite-element models. Another engineering software, Abaqus Standard v.2016 (Dassault Systèmes, Simulia, Providence),

has been used to replicate the 3D models adopting the same simulation strategy, and cross-check for consistency in the stress calculation for those shapes that have edges and corners. For those models that have at least one rotational axis (sphere, ellipsoids of revolution and cylinders), 2D axisymmetric models were constructed with MARC/Mentat using six-node triangular elements (element 126 in the MARC library) that have a node at each vertex and at the midpoint of each side that allows a parabolic interpolation function to be used along each edge. These models were calculated assuming an axisymmetric geometry utilizing full integration. For the other shapes, 3D models have been reproduced with both MARC/Mentat and Abaqus to check for consistency in the obtained solutions for the stress. All 3D models have at least three orthogonal mirror planes, therefore only 1/8 of the selected shape was created. The resulting model consisted of about 400000 four-node linear isoparametric tetrahedral elements (element 134 and C3D10 in the MARC and Abaqus library respectively). The finished 1/8 model was then reflected through three orthogonal mirror planes and joined along the resulting inner surfaces. Material properties and boundary conditions were assigned, and then a mesh convergence analysis was performed. The models were calculated as 3D solids assuming constant dilation using full integration. The element is integrated numerically at a single point at the centroid of the element and linear interpolation functions are used. An iterative process was used to discretize the model with different mesh sizes. Smaller elements were used to discretize the region around and inside the inclusion while larger elements were used for the remaining part of the model (Fig. 1.4). The mesh was refined in the areas with higher stress gradients until the calculated stress distribution appeared smooth. To simulate the external pressure, edge loads were applied to the external boundaries of the 2D models and face loads were applied to the 3D elements on the external boundaries of the host. MARC uses numerical integration to calculate equivalent nodal loads given the dimensions of the area over which the distributed load is applied. Face loads are integrated using a single integration point at the centroid of the element face to which they are applied. Face and edge loads are assumed by MARC to have the same units as the elastic moduli (i.e. GPa). Boundary conditions were placed on the appropriate edges and faces of the models to avoid rigid body rotation and translation in the x, y and z directions.

1.6.2 Elastic properties

As discussed in the main text, the calculation of the remnant pressure on the inclusion were performed using linear elasticity (i.e. neglecting the temperature and pressure derivatives of the moduli, dK/dT, dK/dP, dG/dT, dG/dP). The properties used are reported in Table 1.2. The correction for the geometry for the specific case reported by Ashley et al. (2016) requires the calculation of geometrical factor Γ at two different values of Tend (31 and 500 °C). Therefore, the elastic properties to be used in the FE calculations must be evaluated at these two temperatures. The bulk modulus of

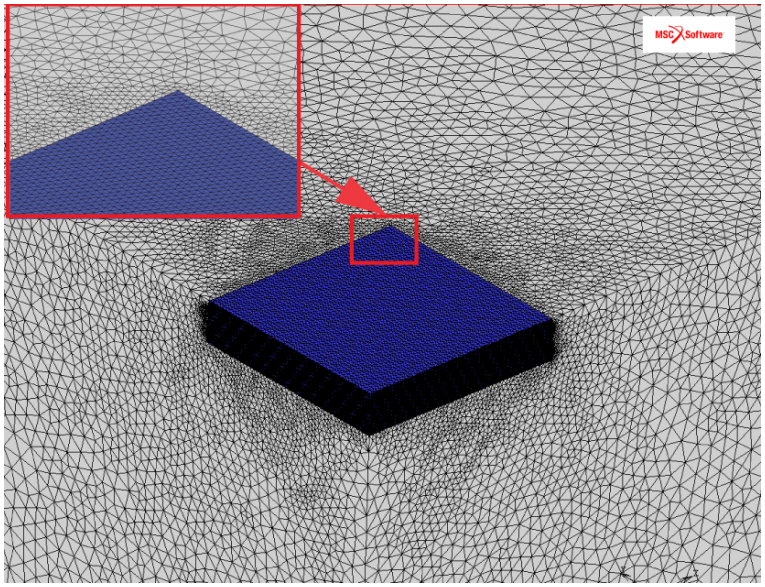

Figure 1.4: 3D Finite element meshes of a prismatic inclusion with aspect ratio 1:5:5 (blue region) and of the surrounding host. Only an eighth of each model is shown. The full model is obtained by reflection through three orthogonal mirror planes, as described in the text. From Mazzucchelli et al. (2018).

almandine has been calculated with a PVT-EoS that combines data from Milani et al. (2015) and Scandolo (2016). Its shear modulus is allowed to change with temperature and pressure according to the P and T derivatives from Arimoto et al. (2015). The variation of the quartz bulk modulus has been evaluated with the new EoS proposed by Angel et al. (2017a), that includes an improved description of the α - β structural transition. The shear modulus of quartz has a small variation over T (Lakshtanov et al., 2007) which does not affect significantly the results of the calculations, and is therefore assumed to be constant. The resultant elastic parameter used for the simulations at each T_{end} are reported in Table 1.3.

1.6.3 Stress within and around the inclusion

For a spherical inclusion included in an infinite host, the analytical models (Zhang, 1998; Angel et al., 2015a) predict that: (i) in the portions of the host far away from the inclusion the stress is hydrostatic, homogeneous, and equal to the external pressure; (ii) in the host close to the inclusion the stress is deviatoric even if the pressure (defined as the negative of the average of the three normal stresses) remains equal to the external pressure; (iii) in the inclusion the stress is homogeneous and hydrostatic. With FEM the complete stress distribution within and around an inclusion for any geometry is obtained, solving for each component of the stress tensor at any given position within

Table 1.2: Isotropic elastic properties used for the simulations reported in Fig. 1.2 and 1.3.

Mineral	Bulk Modulus K_{0T} (GPa)	Ref.	Shear Modulus, G_{0T} (GPa)	Ref.	Young's Modulus, E (GPa)	Poisson's ratio ν,
Quartz	37.0	Scheidl et al. (2016)	44	Wang et al. (2015)	94.53	0.0742
Pyrope	163.7	Milani et al. (2015)	94	Sinogeikin and Bass (2002)	236.7	0.2590
Diamond	444	Angel et al. (2015b)	535	Grimsditch and Ramdas (1975)	1145.1	0.0702
Olivine	126.3	Angel et al. (2017c)	78	Abramson et al. (1997)	194.1	0.2440
Feldspar	55	Average value for alkali feldspars e.g. Waeselmann et al. (2016)	35	Brown et al. (2006)	86.63	0.2375

Table 1.3: Elastic properties for almandine and quartz used for the calculations of the geometrical factor reported in Table 1.1.

T_{end}	P_{end}	P_{inc}	Almandine (host)		Quartz (inclusion)		Geometrical factor (Γ)
			K_{0T} (GPa)	G_{0T} (GPa)	K_{0T} (GPa)	G_{0T} (GPa)	
31	0	0.3	172.54	94.86	39.03	44.4	-0.094
500	0	0.491	161.86	88.68	32.17	44.4	-0.078

the model. As an example, here we show the stress distribution calculated for a quartz (soft) and a diamond (stiff) inclusion with prismatic shape and aspect ratio 1:5:5 included in a pyrope host. In Fig. 1.5 is reported the stress distribution along two different sections that cut the model from the center of the system (i.e. the center of both the host and the inclusion) along the shortest (x-axis) and longest (y-axis) directions of the inclusion. As could be expected, in the portion of the host that are not perturbed by the presence of the inclusion the stress is still homogeneous and hydrostatic. Closer to the inclusion the stress in the host becomes deviatoric, and the amount of differential stress developed in the host is different along the two geometrically non-equivalent directions (x- and y-axes). It should be noted that here the pressure is not constant and deviates from the external pressure.

Our results also show that, even when the elastic properties are isotropic, non-spherical inclusions always develop deviatoric stresses. For a quartz inclusion in garnet with a residual pressure (negative of the mean normal stress) of 0.3 GPa and with an aspect ratio of 1:5:5, the differential stress ($\sigma_{max} - \sigma_{min}$) within the inclusion can reach up to 0.22 GPa for an ellipsoid, and 0.28 GPa for a prism (see Fig. 1.5).

The pressure, defined as the negative of the mean normal stress, is homogeneous in ellipsoids but in prisms a gradient is developed, with the "pressure" changing by 5 % percent from the center of the inclusion to its surface on the longest axis (Fig. 1.5 and Fig. 1.6). Fig. 1.5 shows that for the same shape of the inclusion under the same P_{inc} (0.3 GPa), a stiff inclusion in a softer host, such as diamond included in pyrope, develops a much larger differential stress (0.37 GPa) and pressure change (22 %).

1.7 Acknowledgments

This project has received funding from the European Research Council (ERC) under the European Union's Horizon 2020 research and innovation program (grant agreements 714936 to MA and 307322 to FN). MA has also been supported by the MIUR-SIR grant "MILE DEEp" (RBSI140351) to M. Alvaro. Support for P. Burnley and computational resources were provided by the United States National Nuclear Security Administration under the Stewardship Science Academic Alliances program through DOE Cooperative Agreement DE-NA0001982. We thank Matthew Steele-MacInnis and two anonymous reviewers for very constructive comments on the manuscript.

1.8 References

Abaqus, 2016, Abaqus Documentation: Providence, Rhode Island, USA, Dassault Systèmes.

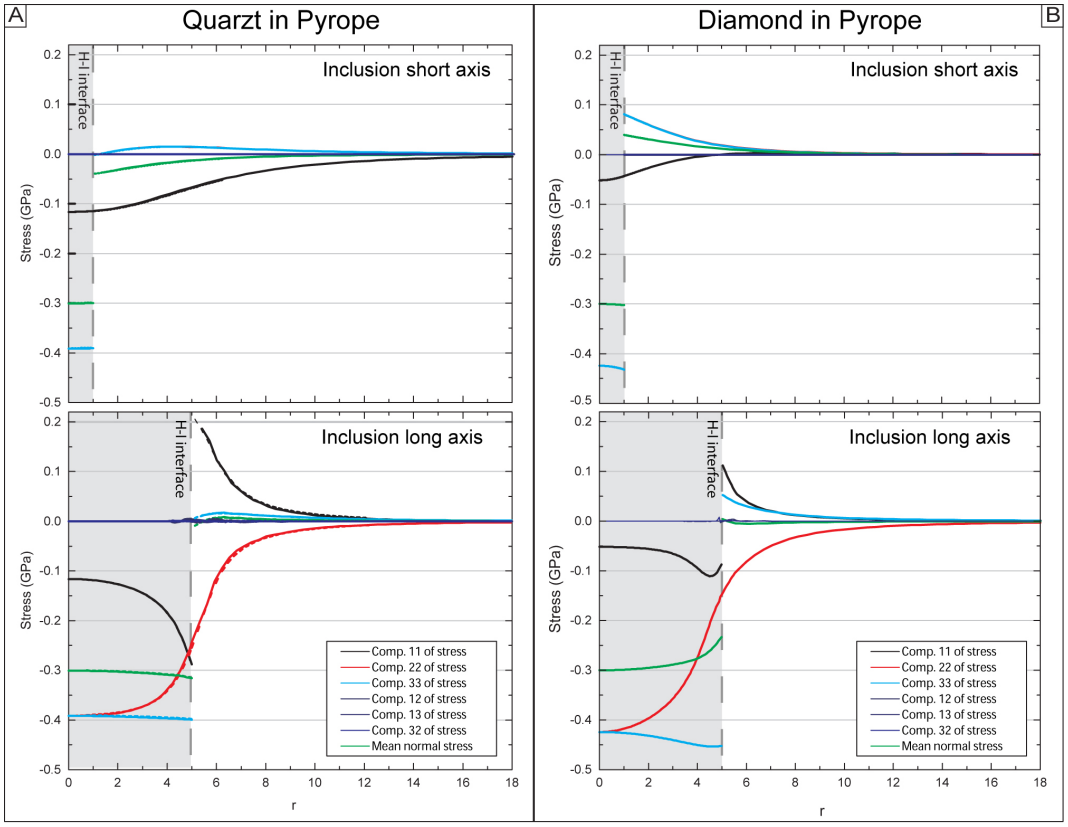

Figure 1.5: Stress distribution inside and around a prismatic inclusion with aspect ratio 1:5:5. The shaded area represents the inclusion. Two cases are reported: A) quartz included in pyrope (soft inclusion in stiffer host); B) diamond included in pyrope (stiff inclusion in softer host). For both, a section along the shorter inclusion axis (x-axis of the model) and along one of the two geometrically equivalent longer inclusion axis (y-axis of the model) are shown. The stresses calculated with MARC/Mentat (solid lines) and Abaqus (dashed lines) always agree within 0.3 %. From Mazzucchelli et al. (2018).

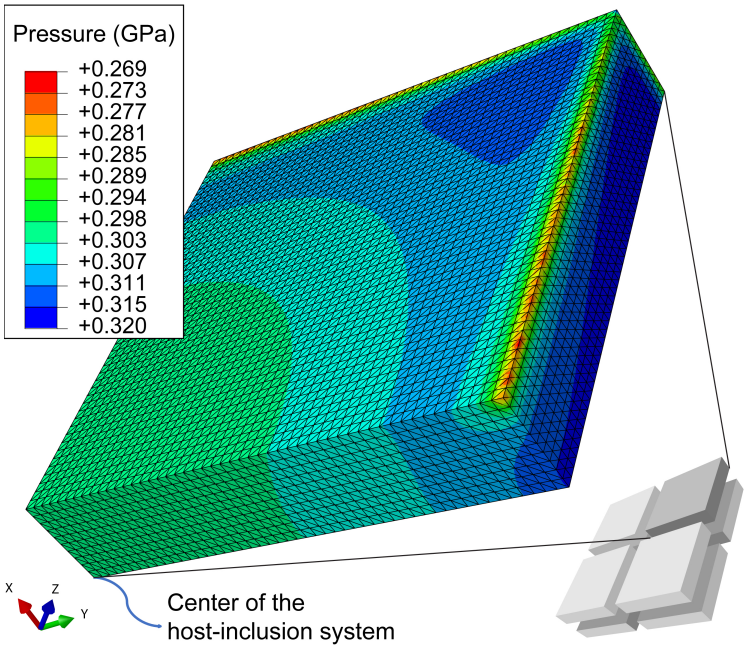

Figure 1.6: Pressure distribution calculated in 1/8 of a quartz inclusion (aspect ratio of 1:5:5) in pyrope. From Mazzucchelli et al. (2018).

Abramson, E.H., Brown, M., Slutsky, L.J., and Zaug, J., 1997, The elastic constants of San Carlos olivine up to 17 GPa: J. Geophys. Res., v. 102, p. 12252–12263.

Adams, H.G., Cohen, L.H., and Rosenfeld, J.L., 1975, Solid inclusion piezothermometry I: Comparison dilatometry: The American Mineralogist, v. 60, p. 574–583.

Angel, R.J., Mazzucchelli, M.L., Alvaro, M., Nimis, P., and Nestola, F., 2014, Geobarometry from host-inclusion systems: The role of elastic relaxation: The American Mineralogist, v. 99, p. 2146–2149.

Angel, R.J., Nimis, P., Mazzucchelli, M.L., Alvaro, M., and Nestola, F., 2015a, How large are departures from lithostatic pressure? Constraints from host–inclusion elasticity: Journal of Metamorphic Geology, v. 33, p. 801–813.

Angel, R.J., Alvaro, M., Nestola, F., and Mazzucchelli, M.L., 2015b, Diamond thermoelastic properties and implications for determining the pressure of formation of diamond–inclusion systems: Russ Geol Geophys, v. 56, p. 225–234.

Angel, R.J., Alvaro, M., Miletich, R., and Nestola, F., 2017a, A simple and generalised P–T–V EoS for continuous phase transitions, implemented in EosFit

and applied to quartz: Contributions to Mineralogy and Petrology, v. 172, p. 29.

Angel, R.J., Mazzucchelli, M.L., Alvaro, M., and Nestola, F., 2017b, EosFit-Pinc: A simple GUI for host-inclusion elastic thermobarometry: The American Mineralogist, v. 102, p. 1957–1960.

Angel, R.J., Alvaro, M., and Nestola, F., 2018, 40 years of mineral elasticity: a critical review and a new parameterisation of equations of state for mantle olivines and diamond inclusions: Physics and Chemistry of Minerals, v. 45, p. 95–113.

Arimoto, T., Gréaux, S., Irifune, T., Zhou, C., and Higo, Y., 2015, Sound velocities of Fe3Al2Si3O12 almandine up to 19 GPa and 1700 K: Physics of the Earth and Planetary Interiors, v. 246, p. 1–8.

Ashley, K.T., Thigpen, J.R., and Law, R.D., 2015, Prograde evolution of the Scottish Caledonides and tectonic implications: Lithos, v. 224–225, p. 160–178.

Ashley, K.T., Steele-MacInnis, M., Bodnar, R.J., and Darling, R.S., 2016, Quartz-in-garnet inclusion barometry under fire: Reducing uncertainty from model estimates: Geology, v. 44, p. 699–702.

Briggs, R.J., and Ramdas, A.K., 1977, Piezospectroscopy of the Raman spectrum of α - quartz: Physical Review B: Condensed Matter and Materials Physics, v. 16, p. 3815.

Brown, J.M., Abramson, E.H., and Angel, R.J., 2006, Triclinic elastic constants for low albite: Physics and Chemistry of Minerals, v. 33, no. 4, p. 256–265.

Burnley, P.C., and Davis, M.K., 2004, Volume changes in fluid inclusions produced by heating and pressurization: An assessment by finite element modeling: Canadian Mineralogist, v. 42, p. 1369–1382.

Burnley, P.C., and Schmidt, C., 2006, Finite element modeling of elastic volume changes in fluid inclusions: Comparison with experiment: The American Mineralogist, v. 91, p. 1807–1814.

Eshelby, J.D., 1957, The determination of the elastic field of an ellipsoidal inclusion, and related problems: Proceedings of the Royal Society of London A: Mathematical, Physical and Engineering Sciences, v. 241, p. 376–396.

Goodier, J.N., 1933, Concentration of stress around spherical and cylindrical inclusions and flaws: Journal of Applied Mechanics, v. 55, p. 39–44.

Grimsditch, M.H., and Ramdas, A.K., 1975, Brillouin scattering in diamond: Physical Review B, v. 11, no. 8, p. 3139–3148.

Key, S.W., 1967, Grüneisen tensor for anisotropic materials: Journal of Applied Physics, v. 38, p. 2923–2928.

Kouketsu, Y., Hattori, K., Guillot, S., and Rayner, N., 2016, Eocene to Oligocene retrogression and recrystallization of the Stak eclogite in northwest Himalaya: Lithos, v. 240–243, p. 155–166.

Lakshtanov, D.L., Sinogeikin, S.V., and Bass, J.D., 2007, High-temperature phase transitions and elasticity of silica polymorphs: Physics and Chemistry of Minerals, v. 34, p. 11–22

Mazzucchelli, M.L., Burnley, P., Angel, R.J., Morganti, S., Domeneghetti, M.C., Nestola, F., and Alvaro, M., 2018, Elastic geothermobarometry: Corrections for the geometry of the host-inclusion system: Geology, 46(3), 231-234.

Milani, S., Nestola, F., Alvaro, M., Pasqual, D., Mazzucchelli, M.L., Domeneghetti, M.C., and Geiger, C.A., 2015, Diamond–garnet geobarometry: The role of garnet compressibility and expansivity: Lithos, v. 227, no. 0, p. 140–147.

Rosenfeld, J.L., and Chase, A.B., 1961, Pressure and temperature of crystallization from elastic effects around solid inclusions in minerals?: American Journal of Science, v. 259, p. 519–541.

Scandolo L., 2016, Thermal expansion of mantle minerals inclusions in diamonds [Ph.D. thesis]: University of Pavia.

Scheidl, K.S., Kurnosov, A., Trots, D.M., Boffa Ballaran, T., Angel, R.J., and Miletich, R., 2016, Extending the single-crystal quartz pressure gauge up to hydrostatic pressure of 19 GPa: Journal of Applied Crystallography, v. 49, no. 6, p. 2129–2137.

Sinogeikin, S. V, and Bass, J.D., 2002, Elasticity of pyrope and majorite-pyrope solid solutions to high temperatures: Earth and Planetary Science Letters, v. 203, no. 1, p. 549–555.

Spear, F.S., Thomas, J.B., and Hallet, B.W., 2014, Overstepping the garnet isograd: A comparison of QuiG barometry and thermodynamic modeling: Contributions to Mineralogy and Petrology, v. 168, p. 1059.

Van der Molen, I., and Van Roermund, H.L.M., 1986, The pressure path of solid inclusions in minerals: The retention of coesite inclusions during uplift: Lithos, v. 19, p. 317–324.

Waeselmann N., Brown J.M., Angel R.J., Ross N.L., Zhao J., Kaminski W. (2016) The elastic tensor of monoclinic alkali feldspars: American Mineralogist ,101:1228-1231.

Wang, J., Mao, Z., Jiang, F., and Duffy, T.S., 2015, Elasticity of single-crystal quartz to 10 GPa: Physics and Chemistry of Minerals, v. 42, no. 3, p. 203–212.

Zhang, Y., 1998, Mechanical and phase equilibria in inclusion–host systems: Earth and Planetary Science Letters, v. 157, p. 209–222.

Chapter 2

Depth of diamond formation obtained from single periclase inclusions

This chapter has been adapted from a manuscript, recently submitted for publication to *Geology*, with the title *Depth of diamond formation obtained from single periclase inclusions*, authored by C. Anzolini[1], F. Nestola[1], M.L. Mazzucchelli[2], M. Alvaro[2], P. Nimis[1], A. Gianese[1], S .Morganti[3], F. Marone[4], M. Campione[5], and J. W. Harris[6]. Modifications made to the submitted manuscript are intended to highlight my contributions, focusing on the application of elastic geobarometry and on the computational aspects.

2.1 Introduction

Diamonds, and the mineral inclusions they trap during their growth, are pristine samples from the Earth's mantle and provide information on processes operating in inaccessible regions of our planet. This information is particularly valuable if it can be combined with depth estimates. Based on the mineral inclusions, it is estimated that the majority of diamonds (99%) originate within the lithosphere (e.g. Stachel and Harris, 2008). The other 1% are believed to be sub-lithospheric and formed at depths between 300 and 800 km (Harte, 2010; Walter et al., 2011; Smith et al., 2016; Nestola et al., 2018), and hence are called super-deep diamonds (hereafter SDDs). Early in-

[1]Department of Geosciences, University of Padova, I-35131 Padova, Italy; [2]Department of Earth and Environmental Sciences, University of Pavia, I-27100 Pavia, Italy; [3]Department of Electrical, Computer, and Biomedical Engineering, University of Pavia, I-27100 Pavia, Italy; [4]Swiss Light Source, Paul Scherrer Institut, 5232 Villigen, Switzerland; [5]Department of Earth and Environmental Sciences, University of Milano Bicocca, Milan, Italy; [6]School of Geographical and Earth Sciences, University of Glasgow, G12 8QQ Glasgow, United Kingdom.

clusion work (Harte et al., 1999; Stachel et al., 2000; McCammon, 2001) concluded that Fe-rich periclase was a lower mantle mineral, especially when found in the same diamond as low-Ni enstatite, which was interpreted as the inversion product of silicate perovskite. But the fact that the Fe^{2+} content in some periclase inclusions is too high compared to the expected ferrous iron partitioning in the lower mantle (e.g. Muir and Brodholt, 2016) and the findings of Fe-rich periclase in association with olivine and jeffbenite in some SDDs (Hutchison et al., 2001) cast doubt on that conclusion. In addition, synthesis of Fe-rich periclase and diamond by carbonate melt-peridotite reactions (Thomson et al., 2016) suggested an upper-mantle to transition-zone formation for some Fe-rich periclases. The presence of nanometric exsolutions of magnesioferrite in some Fe-rich periclase inclusions (Harte et al., 1999; Wirth et al., 2014; Kaminsky et al., 2015) led Palot et al. (2016) to propose an origin in the uppermost part of the lower mantle, but Uenver-Thiele et al. (2017a,b) showed that magnesioferrite cannot exsolve directly from Fe-rich periclase in the lower mantle. Hence, it is evident that the depth of formation of Fe-rich periclase inclusions in diamond has a large uncertainty. Elastic geobarometry may give hints to constrain this problem providing at least a minimum estimate of the pressure conditions at which the periclase inclusions are entrapped in their diamond host. We estimated the entrapment pressure (P_{trap}) of two Fe-rich periclase inclusions in a diamond from the São Luiz area, Juina, Brazil (sample AZ1, Fig. 2.1) applying isotropic elastic geobarometry (Angel et al., 2015; 2017), including the correction for the full geometry of the inclusions applied to a realistic 3D reconstruction of the sample. We also compared the results of the purely elastic calculation with those obtained by a simple elasto-plastic model (Campione, 2018) that accounts for the plasticity of the diamond host at high temperature.

2.2 Methods

2.2.1 Sample

The diamond investigated in this study (Fig. 2.1) was recovered in the mid to late 1980s from alluvial deposits of the São Luiz river in the Juina area of south-western Brazil (Harte et al., 1999; Kaminsky et al., 2001; Hayman et al., 2005). The sample contains two main black inclusions, identified as Fe-rich periclase by Single-Crystal X-ray Diffraction (SCXRD). The smaller one, whose longest dimension is $\sim$ 160 µm, is named AZ1_1; the bigger one, whose longest dimension is $\sim$ 280 µm, is named AZ1_2.

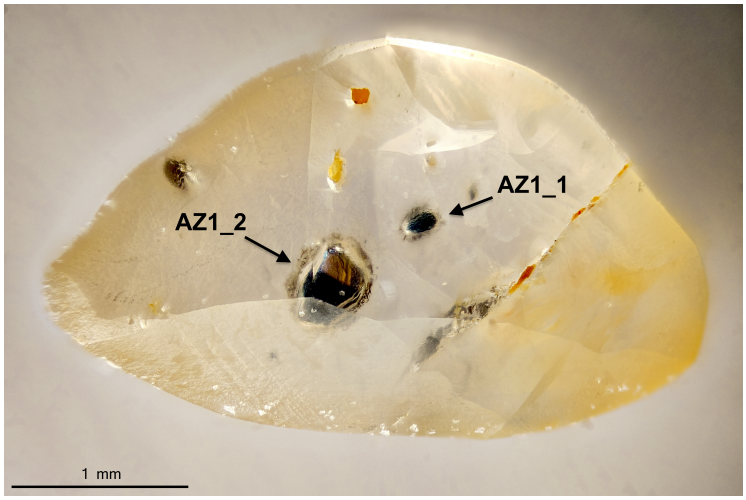

Figure 2.1: The inclusion-bearing diamond studied in this work. The sample was recovered from the São Luiz river alluvials (Juina, Brazil) and contains two main black inclusions identified as Fe-rich periclase by single-crystal X-ray diffraction.

2.2.2 Synchrotron X-ray Tomographic Microscopy

This non-destructive, high-resolution technique allows the acquisition of 3D maps of the variations of the X-ray attenuation coefficient within a sample. X-ray micro-tomography experiments were carried out at the Swiss Light Source (SLS) at TOMCAT, a beamline for TOmographic Microscopy and Coherent rAdiology experimenTs (Stampanoni et al., 2006). Measurements were performed at 13.5 keV in order to maximize contrast. A total of 1501 X-ray radiographs were acquired from different angular positions around a vertical rotation axis for each sample. The imaging setup consisted of a 20 μm thick LuAG:Ce scintillator screen, a 20x objective and a sCMOS (PCO.edge) camera. The tomographic reconstruction was performed using optimized routines based on the Fourier Transform Method (Marone and Stampanoni, 2012). The resulting volume consisted of 2160 axial slices of 2560 x 2560 pixels, with a pixel size of 0.33 μm.

2.2.3 Single-Crystal X-ray Diffraction (SCXRD)

SCXRD measurements were performed on the Fe-rich periclase inclusions both before and after release from their diamond host at the Department of Geosciences (University of Padova). X-ray data were collected using a Rigaku Oxford Diffraction SuperNova single-crystal diffractometer, equipped with a Dectris Pilatus 200 K area detector and with a Mova X-ray microsource. A monochromatized MoKa radiation (λ = 0.71073

Å), working at 50 kV and 0.8 mA, was used. The sample-to-detector distance was 68 mm. Data reduction was performed using the CrysAlisPro software (Rigaku Oxford Diffraction).

2.2.4 Field Emission Gun – Scanning Electron Microscopy (FEG-SEM)

The two Fe-rich periclase inclusions were first extracted by mechanical crushing of the host, then polished in a three-step process after which they were carbon coated. FEG-SEM measurements were carried out at the Department of Physics and Astronomy (University of Padova), using a Zeiss SIGMA HD FEG-SEM microscope operating at 20 kV, with a spot size of $\sim$ 1 nm. Imaging was performed using an InLens secondary electron detector. Compositional analysis was performed using an energy dispersive X-ray spectrometer (EDX by Oxford Instruments). The spatial resolution in micro-analysis was of $\sim$ 1 μm.

2.2.5 Finite Element (FE) analysis

The FE analysis was performed on the real 3D model built from the segmentation of the X-ray microtomographic data (Fig. 2.2). The surface of the model was simplified and smoothed to improve the quality of the final FE mesh, having care to not obliterate the surface topography of the inclusions. The final 3D model was then assembled in Simulia Abaqus, a commercial engineering package for FE analysis, placing the two inclusions in the diamond host. An elastically isotropic FE analysis was run (for more details on the procedure see Mazzucchelli et al., 2018 and section 1.6.1). The elastic properties for the Fe-rich periclase inclusions were obtained from the re-fitting of the original *P-V-T* data of Mao et al. (2011) up to 2000 K and 50 GPa using a 3^{rd}-order Birch-Murnaghan equation of state (EoS) combined with a Berman-type thermal expansion, that gives an isothermal bulk modulus K_{0TR} = 162(14) GPa (full EoS reported at http://www.rossangel.com). The Reuss shear modulus G_{0R} = 87(2) GPa was obtained from the elastic constants reported by Jacobsen et al. (2002) for a Fe-rich periclase with composition $(Mg_{0.63}Fe_{0.37})O$ that is close to the composition of our inclusions, $(Mg_{0.60}Fe_{0.40})O$. For diamond we used the K_{0TR} = 444(2) GPa and G_{0TR}= 535 GPa from Angel et al (2015).

2.2.6 Elasto-plastic model

The calculation is split into two steps, dividing the calculation into an isothermal, quasi-static decompression from P_{trap}, T_{trap} to P_{room}, T_{trap}, followed by an isobaric cooling to room temperature. This is assumed to be a realistic approximation of the

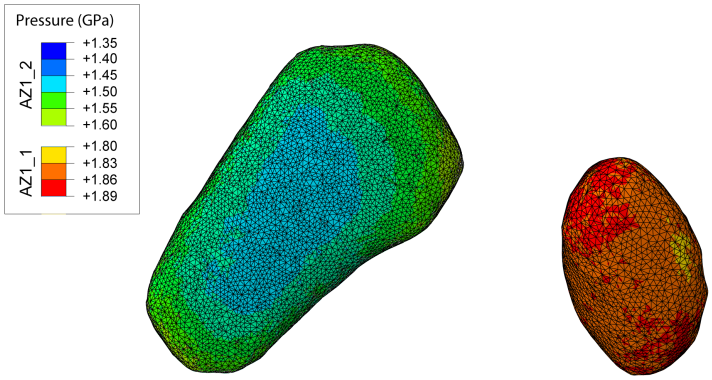

Figure 2.2: Real 3D model of the periclase inclusions built from the segmentation of the X-ray microtomographic dataset. The reconstruction, which preserves the morphology of the two inclusions and their mutual distances and orientations, reveals the absence of fractures both around the inclusions and at the diamond-inclusion interface. The inclusions' residual pressure (P_{inc}) as calculated by FE analysis on the basis of their shape predicts a higher P_{inc} for AZ1_1 (red) compared to AZ1_2 (blue).

P-T path experienced by diamonds exhumed to the Earth's surface through Kimberlite pipes. The model is solved by inversion. The host-inclusion system is initially at P_{room}, T_{room} with the inclusion at the experimentally measured P_{inc}^{exp}. First, an entrapment temperature (T_{trap}) is chosen and the over-pressure $P_{inc}^{P_{room},T_{trap}}$ developed in the inclusion during isobaric heating to P_{room} ,T_{trap} is calculated adjusting the elastic properties of the host and the inclusion according to their EoS. A P_{trap} is guessed at the chosen T_{trap} , and the elasto-plastic deformation of the host and inclusion pressure are calculated during the quasi-static decompression of the host from P_{trap}, T_{trap} to P_{room} ,T_{trap} according to Campione (2018). The guessed P_{trap} is adjusted until the pressure calculated in the inclusion at P_{room} ,T_{trap} matches the previously found $P_{inc}^{P_{room},T_{trap}}$. The elastic properties for diamond are from Angel et al. (2015) and from Zouboulis et al. (1998). The variation of σ_Y with T (between 1273 and 1823 K) was obtained from Weidner et al. (1994). The EoS of the inclusion was obtained from the re-fitting of the original P-V-T data of Mao et al. (2011) as discussed above.

2.3 Results

2.3.1 Sample analysis

The diamond was a flattened colourless dodecahedron from the São Luiz alluvial area, Juina, Brazil in which two Fe-rich periclase inclusions occurred in the central area of

the stone (sample AZ1, Fig. 2.1). The final 3D reconstruction (Fig. 2.2) of the inclusions revealed the absence of fractures around them, suggesting that the host did not experience brittle deformation during exhumation. SCXRD measurements on the two Fe-rich periclase inclusions revealed the presence of another phase, which was identified as magnesioferrite. Diffraction images (Fig. 2.3) only show the second (1.49 Å) and the third (2.44 Å) most intense peaks of Fe-rich periclase, as the main peak (2.10 Å) cannot be detected due to an overlap with the most intense diamond peak, located at the same d spacing (2.07 Å). In addition, the first (2.53 Å) and the third (2.97 Å) most intense peaks of magnesioferrite are visible. Again, the second peak of magnesioferrite in order of intensity (1.48 Å) cannot be unambiguously detected due to overlapping with the peak of Fe-rich periclase (1.49 Å). As indicated by the diffraction data, Fe-rich periclase and the exsolutions of magnesioferrite show an almost identical crystallographic orientation. In order to produce pseudo-single-crystal X-ray diffraction spots like those shown in Fig. 2.3, there must be a high density of nanometer-sized magnesioferrite grains in topotaxial relation to the Fe-rich periclase. Both inclusions after release and polishing exhibited pervasively and homogeneously distributed exsolutions of magnesioferrite of about 200 nm size, which often coalesced into chains of 2–3 μm length and constituted about 6% of the total surface area (calculated using the ImageJ software, Abràmoff et al., 2004). EDX analyses of both Fe-rich periclases gave a similar average and approximate composition of $(Mg_{0.60}Fe_{0.40})O$.

2.3.2 Inclusion residual pressure

X-ray analyses provided the lattice parameters and the relative unit-cell volumes reported in Table 2.1. By comparing the unit-cell volumes before (V) and after (V_0) release from the diamond host and using the P-V-T EoS for Fe-rich periclase discussed above (and reported at http://www.rossangel.com), we obtained a residual pressure, P_{inc} of 1.84(65) GPa for inclusion AZ1_1 and of 1.48(67) GPa for inclusion AZ1_2. The high uncertainties in P_{inc} are due to the high uncertainty in the bulk modulus value of Fe-rich periclase (Mao et al., 2011).

2.3.3 Depth of formation of the Fe-rich periclase – diamond pair by elasto-plastic geobarometry

Given the absence of fracture systems around the inclusions, the calculated P_{inc} can be linked to the depth of formation by elastic geobarometry. Standard elastic methods rely on simplified models which assume that the inclusion is spherical and sitting isolated in an infinitely large host (e.g. Zhang, 1998). However, numerical simulations based on elasticity theory and including geometrical effects predict that platy inclusions should exhibit a lower P_{inc} compared to more rounded inclusions of the same

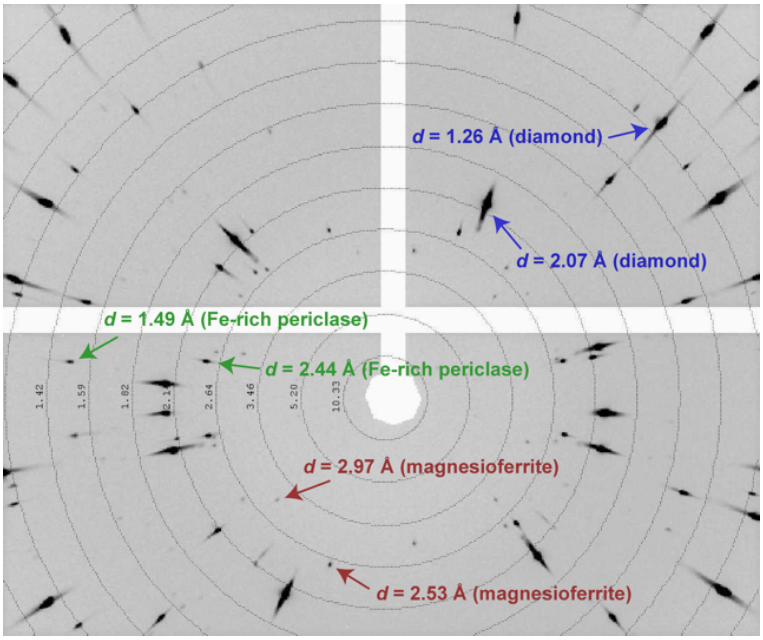

Figure 2.3: Single-crystal X-ray diffraction images of inclusion AZ1_2 showing the second and the third diffraction peaks of Fe-rich periclase together with the first and the third most intense peaks of magnesioferrite. Peaks at 2.07 Å and 1.26 Å belong to diamond.

mineral entrapped at the same pressure (Mazzucchelli et al., 2018). This is consistent with our measurements, which show a lower P_{inc} for the platy AZ1_2 than for the more rounded AZ1_1. We applied the Finite Element (FE) analysis described by Mazzucchelli et al. (2018), reported in chapter 1 of this thesis, to determine appropriate geometrical correction factors (Γ) for AZ1_2 and AZ1_1. To obtain realistic corrections, we performed the FE analysis on the real 3D model built from the segmentation of the X-ray microtomographic data, thereby modelling the correct morphology of the two inclusions and their mutual orientation (Fig. 2.2). When the morphology of the inclusion is not perfectly ellipsoidal, the residual strain, stress and pressure in the inclusion are not homogeneous (Eshelby, 1957; Campomenosi et al., 2018) and vary from point to point depending on the presence of edges, corners and in general on the specific morphology. SCXRD measurements give a mean volume strain that is averaged over the entire volume of the inclusion; as a consequence, the experimental P_{inc} is not associated to any specific point in the inclusion and should be regarded as an average over the inclusion volume. Accordingly, Γ, calculated as a local factor, can also vary from point to point in the inclusion depending on the local stress concentration due to the specific morphology. Therefore, for applications to XRD measurements, Γ was calculated as an average factor integrated over the inclusion volume. The Γ factors obtained in this way are –0.016(5) and –0.080(10) for inclusions AZ1_1 and

AZ1_2, respectively. Applying the correction factor to our experimental determined residual pressures we obtained the corrected P_{inc} of 1.87(66) GPa and 1.61(73) GPa for the inclusions, respectively. We then calculated the entrapment isomeke for the two Fe-rich periclase-diamond pairs using the corrected values for P_{inc} and the software EosFit-Pinc (Angel et al., 2017). Since both the host and the inclusion have cubic crystallographic symmetry, the effect of anisotropic elasticity is limited (see chapter 7 of this thesis), allowing the use of current isotropic elastic geobarometry models. To maintain consistency among each step of the calculation, we used the same elastic properties reported above for the determination of the residual pressure and for the calculation of the geometrical factors. The intersection of the isomeke with the mantle geotherm, accounting for the isomeke uncertainty, gave an entrapment pressure for AZ1_1 of P_{trap} = 13.4(1.4) GPa and for AZ1_2 of P_{trap} = 12.8(1.6) GPa at a temperature T_{trap} = 1790(30) K (see Table 2.2 and Fig. 2.4). This estimate does not take into account plastic deformation in the diamond, which may accommodate part of the inclusion expansion during uplift to surface (Anzolini et al., 2016). Plastic deformation is well documented in diamond and, particularly, in SDDs (e.g., Cayzer et al., 2008), consistent with its low yield strength (σ_Y) at high temperatures (Weidner et al., 1994). Therefore, the P_{trap} calculated from a purely elastic model is likely to be underestimated. To account for plastic deformation, the elasto-plastic (EP) model for barometry proposed by Campione (2018) (see Methods) was applied to these data. The back-calculation of $P_{trap,EP}$ as a function of T was solved by adjusting the (σ_Y) of diamond according to the experimental measurements of Weidner et al. (1994) and the elastic parameters for diamond and Fe-rich periclase, previously noted. Since the EP model assumes that the inclusion is spherical, we applied this method only to the most rounded of the two inclusions, i.e. AZ1_1. The best agreement between the calculated $P_{trap,EP}(T)$ and the geotherm is at 15.7(2.5) GPa and 1823(30) K [$\sim$ 450(70) km depth]. Considering the uncertainties, this result is compatible with an origin in the lowermost upper mantle or in the upper transition zone (Fig. 2.4). Unfortunately, the depth obtained is only an estimate restricted by a lack of experimental values of (σ_Y) for temperatures higher than $\sim$ 1850 K (Weidner et al. (1994) and the fact that the EP model only considers the deformation caused by over-pressurization of the inclusion with respect to the external lithostatic pressure (Campione, 2018). If external tectonic stresses act on diamonds during uplift through the sub-lithospheric mantle, they may promote additional plastic deformation, which may contribute to release of part of the P_{inc} being built on the inclusion. Therefore, the $P_{trap,EP}$ value of 15.7(2.5) GPa for AZ1_1, which corresponds to a depth of about 450(70) km, should be regarded as a minimum estimate. In addition, models used in this work do not take into account the effect that the magnesioferrite exsolution may have on P_{inc} and, in turn, the calculated P_{trap}. However, given the small contrast in elastic properties between Fe-rich periclase and magnesioferrite (Reichmann and Jacobsen, 2014) and the small amount

Table 2.1: Lattice parameter and unit-cell volume of the two Fe-rich periclase inclusions. The residual pressure is calculated by comparing the volume before (V) and after (V_0) release from the diamond host.

Inclusion	a (Å)	a_0 (Å)	V (Å^3)	V_0 (Å^3)	P_{inc} (GPa)
AZ1_1	4.253(4)	4.2685(2)	76.91(12)	77.770(5)	1.84(65)
AZ1_2	4.256(8)	4.2689(3)	77.1(2)	77.795(9)	1.48(67)

Table 2.2: Isomeke calculations for the two diamond-Fe-rich periclase host-inclusion systems studied in this work. Pressures in GPa.

	P_{trap} inclusion AZ1_1			P_{trap} inclusion AZ1_2		
T (K)	P_{inc} - esd	P_{inc} = 1.87	P_{inc} + esd	P_{inc} - esd	P_{inc} = 1.61	P_{inc} + esd
1448	10.26	11.74	13.25	9.54	11.15	12.81
1498	10.52	11.99	13.51	9.80	11.41	13.07
1548	10.77	12.25	13.76	10.05	11.66	13.32
1598	11.02	12.49	14.01	10.29	11.90	13.57
1648	11.26	12.73	14.25	10.53	12.14	13.81
1698	11.49	12.97	14.48	10.77	12.38	14.04
1748	11.72	13.20	14.71	11.00	12.61	14.27
1798	11.95	13.42	14.94	11.22	12.83	14.50
1848	12.16	13.64	15.16	11.44	13.05	14.72
1898	12.38	13.85	15.37	11.66	13.27	14.93
1948	12.59	14.06	15.58	11.87	13.48	15.14
1998	12.79	14.27	15.78	12.07	13.68	15.34

of magnesioferrite ($\sim$ 6% by volume), the effect is probably limited and well within the uncertainties already accounted for in the calculations.

2.4 Conclusions

The application of non-ideal elastic geobarometry, that incorporates the correction for geometrical effects based on a real 3D model of the sample, may give hints to constrain the origin of Fe-rich periclase inclusions found in diamonds. Results from purely elastic models give an entrapment at the lower part of the upper mantle (P_{trap} = 13.4(1.4) GPa at T_{trap} = 1790(30) K). At those entrapment conditions, however, the plasticity of the diamond host may be high enough to accommodate part of the expansion of the inclusion, resulting in the underestimation of the entrapment pressure by purely elastic methods. Simple elasto-plastic model that assume a quasi-static isothermal

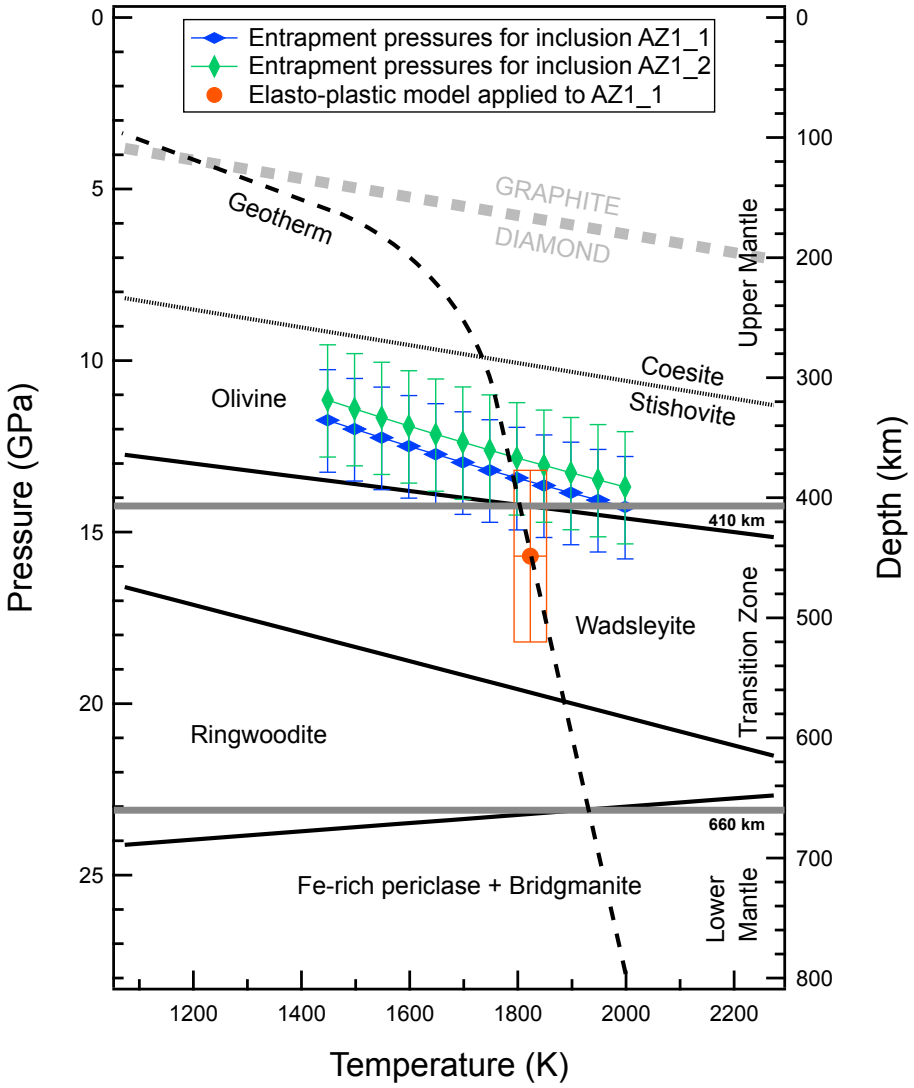

Figure 2.4: Entrapment pressures of the periclase inclusions determined by elastic and elasto-plastic models. The main phase boundaries (solid lines) are after Akaogi et al. (1989), Katsura and Ito (1989), Fei et al. (2004). The coesite-stishovite phase boundary (black broken line) is after Zhang et al. (1996). The graphite-diamond phase boundary (thick grey dashed line) is after Day (2012). The geotherm (black dashed line) is calculated for a typical cratonic surface heat flow of 40 mW/m2 (Hasterok and Chapman, 2011) and a mantle adiabat (Turcotte and Schubert, 2014). The 410 and 660 km discontinuities enclosing the mantle transition zone are indicated by bold lines. Entrapment pressures (P_{trap}) calculated for inclusions AZ1_1 and AZ1_2 at various T with the purely elastic model are represented by blue and green diamonds, respectively. The $P_{trap,EP}$ calculated with the elasto-plastic model for inclusion AZ1_1 at T consistent with the geotherm is represented by the red box. This $P_{trap,EP}$ provides a minimum estimate for the pressure of formation of the diamond.

uplift of the diamond, accounting for the variation of its yield strength (σ_Y) with T, give an entrapment at $P_{trap} = 15.7(2.5)$ GPa and $T_{trap} = 1823(30)$ K, that corresponds to the upper mantle-transition zone boundary (depth of 450(70) km). However, this calculation only considers the plastic deformation of the diamond due to the over-pressurization of the cavity. Non-lithostatic tectonic stresses acting on the diamond during uplift may result in further plastic deformation that is not accounted by our models, resulting in deeper entrapment conditions.

2.5 Acknowledgments

The synchrotron work was carried out at the TOMCAT beamline of the Swiss Light Source at the Paul Scherrer Institut, Switzerland. M. Stampanoni, S. Milani and G. Rustioni are thanked for help with this work. L. Tauro and N. Michieli are acknowledged for their help in the SEM-EDX sample preparation and analysis, respectively. S. Castelli is thanked for providing the macrophotography of the diamond. The DeBeers Group of Companies is thanked for the donation of the diamond to Jeff W. Harris.

2.6 References

Abaqus, 2016, Abaqus Documentation: Providence, Rhode Island, Dassault Systèmes, http://50.16.225.63/v2016/.

Abràmoff, M.D., Magalhães, P.J. and Ram, S.J. (2004) Image processing with ImageJ. Biophotonics International, 11, 36-42.

Angel, R.J., Mazzucchelli, M.L., Alvaro, M. and Nestola, F. (2017) EosFit-Pinc: A simple GUI for host-inclusion elastic thermobarometry. American Mineralogist, 102, 1957–1960.

Angel, R.J., Alvaro, M., Nestola, F. and Mazzucchelli, M.L. (2015) Diamond thermoelastic properties and implications for determining the pressure of formation of diamond-inclusion systems. Russian Geology and Geophysics, 56, 211-220.

Anzolini, C., Angel, R.J., Merlini, M., Derzsi, M., Tokar, K., Milani, S., Krebs, M.Y., Brenker, F.E., Nestola, F. and Harris, J.W. (2016) Depth of formation of $CaSiO_3$-walstromite included in super-deep diamonds. Lithos, 265, 138–147.

Anzolini, C., Prencipe, M., Alvaro, M., Romano, C., Vona, A., Lorenzon, S., Smith, E.M., Brenker, F.E. and Nestola, F. (2018) Depth of formation of super-deep diamonds: Raman barometry of CaSiO3-walstromite inclusions. American Mineralogist, 103, 69-74.

Brenker, F.E., Vollmer, C., Vincze, L., Vekemans, B., Szymanski, A., Janssens, K., Szaloki, I., Nasdala, L., Joswig, W. and Kaminsky, F. (2007) Carbonates from the lower part of transition zone or even the lower mantle. Earth and Planetary Science Letters, 260, 1-9.

Campione, M. (2018) Threshold Effects for the Decrepitation and Stretching of Fluid Inclusions. Journal of Geophysical Research: Solid Earth, 123, 3539-3548.

Cayzer, N.J., Odake, S., Harte, B. and Kagi, H. (2008) Plastic deformation of lower mantle diamonds by inclusion phase transformations. European Journal of Mineralogy, 20, 333-339.

Day, H.W. (2012) A revised diamond-graphite transition curve. American Mineralogist, 97, 52-62.

Eshelby, J.D. (1957) The determination of the elastic field of an ellipsoidal inclusion, and related problems, in Proceedings of the Royal Society of London A: Mathematical, Physical and Engineering Sciences, The Royal Society, 241, 376-396.

Harte, B. (2010) Diamond formation in the deep mantle: the record of mineral inclusions and their distribution in relation to mantle dehydration zones. Mineralogical Magazine, 2, 189-215.

Harte, B., Harris, J.W., Hutchison, M.T., Watt, G.R. and Wilding, M.C. (1999) Lower mantle mineral associations in diamonds from Sao Luiz, Brazil. Mantle petrology: Field observations and high-pressure experimentation: A tribute to Francis R. (Joe) Boyd, 125-153.

Hasterok, D. and Chapman, D.S. (2011) Heat production and geotherms for the continental lithosphere. Earth and Planetary Science Letters, 307, 59-70.

Hayman, P.C., Kopylova, M.G. and Kaminsky, F.V. (2005) Lower mantle diamonds from Rio Soriso (Juina area, Mato Grosso, Brazil). Contributions to Mineralogy and Petrology, 149, 430-445.

Hofmeister, A.M. (1999) Mantle values of thermal conductivity and the geotherm from phonon lifetimes. Science, 283, 1699-1706.

Hutchison, M.T., Hursthouse, M.B. and Light, M.E. (2001) Mineral inclusions in diamonds: associations and chemical distinctions around the 670-km discontinuity. Contributions to Mineralogy and Petrology, 142, 119-126.

Jacobsen, S.D., Reichmann, H.J., Spetzler, H.A., Mackwell, S.J., Smyth, J.R., Angel, R.J. and McCammon, C.A. (2002) Structure and elasticity of single-crystal

(Mg,Fe)O and a new method of generating shear waves for gigahertz ultrasonic interferometry. Journal of Geophysical Research: Solid Earth, 107(B2).

Kaminsky, F., Zakharchenko, O., Davies, R., Griffin, W., Khachatryan-Blinova, G. and Shiryaev, A. (2001) Superdeep diamonds from the Juina area, Mato Grosso State, Brazil. Contributions to Mineralogy and Petrology, 140, 734-753.

Kaminsky, F. (2012) Mineralogy of the lower mantle: A review of 'super-deep' mineral inclusions in diamond. Earth-Science Reviews, 110, 127-147.

Kaminsky, F.V., Ryabchikov, I.D., McCammon, C.A., Longo, M., Abakumov, A.M., Turner, S. and Heidari, H. (2015) Oxidation potential in the Earth's lower mantle as recorded by Fe-rich periclase inclusions in diamond. Earth and Planetary Science Letters, 417, 49-56.

Katsura, T. and Ito, E. (1989) The system $Mg_2SiO_4 - Fe_2SiO_4$ at high pressures and temperatures: Precise determination of stabilities of olivine, modified spinel, and spinel. Journal of Geophysical Research: Solid Earth, B11, 15663-15670.

Katsura, T., Yamada, H., Nishikawa, O., Song, M., Kubo, A., Shinmei, T., Yokoshi, S., Aizawa, Y., Yoshino, T. and Walter, M.J. (2004) Olivine-wadsleyite transition in the system $(Mg, Fe)_2SiO_4$. Journal of Geophysical Research: Solid Earth, B2.

Mao, Z., Lin, J., Liu, J. and Prakapenka, V.B. (2011) Thermal equation of state of lower-mantle Fe-rich periclase across the spin crossover. Geophysical Research Letters, 38, L23308.

Marone, F. and Stampanoni, M. (2012) Regridding reconstruction algorithm for real-time tomographic imaging. Journal of synchrotron radiation, 19, 1029-1037.

Mazzucchelli, M.L., Burnley, P., Angel, R.J., Morganti, S., Domeneghetti, M.C., Nestola, F. and Alvaro, M. (2018) Elastic geothermobarometry: Corrections for the geometry of the host-inclusion system. Geology, 46, 231-234.

McCammon, C. (2001) Geophysics. Deep diamond mysteries. Science, 293, 813-814.

Muir, J.M.R. and Brodholt, J.P. (2016) Ferrous iron partitioning in the lower mantle. Physics of the Earth and Planetary Interiors, v. 257, p. 12–17

Nestola, F., Korolev, N., Kopylova, M., Rotiroti, N., Pearson, D.G., Pamato, M.G., Alvaro, M., Peruzzo, L., Gurney, J.J., Moore, A.E., Davidson, J. (2018) $CaSiO_3$-perovskite in diamond indicates the recycling of oceanic crust into the lower mantle. Nature, 555, 237-241.

Palot, M., Jacobsen, S.D., Townsend, J.P., Nestola, F., Marquardt, K., Miyajima, N., Harris, J.W., Stachel, T., McCammon, C.A. and Pearson, D.G. (2016) Evidence for H_2O-bearing fluids in the lower mantle from diamond inclusion. Lithos, 265, 237-243.

Pearson, D., Brenker, F., Nestola, F., McNeill, J., Nasdala, L., Hutchison, M., Matveev, S., Mather, K., Silversmit, G., and Schmitz, S. (2014) Hydrous mantle transition zone indicated by ringwoodite included within diamond. Nature, 507, 221–224.

Reichmann, H.J. and Jacobsen, S.D. (2004) High-pressure elasticity of a natural magnesioferrite crystal. American Mineralogist, 89, 1061-1066.

Smith, E.M., Shirey, S.B., Nestola, F., Bullock, E.S., Wang, J.H., Richardson, S.H. and Wang, W.Y. (2016) Large gem diamonds from metallic liquid in Earth's deep mantle. Science, 354, 1403-1405.

Stachel, T. and Harris, J.W. (2008) The origin of cratonic diamonds—constraints from mineral inclusions. Ore Geology Reviews, 34, 5-32.

Stachel, T., Harris, J.W., Brey, G.P. and Joswig, W. (2000) Kankan diamonds (Guinea) II: lower mantle inclusion parageneses. Contributions to Mineralogy and Petrology, 140, 16-27.

Stampanoni, M., Groso, A., Isenegger, A., Mikuljan, G., Chen, Q., Bertrand, A., Henein, S., Betemps, R., Frommherz, U., Bohler, P., Meister, D., Lange, M. and Abela, R.: Trends in synchrotron-based tomographic imaging: the SLS experience, in Bonse, U. (Ed.): Developments in X-Ray Tomography V (Spie-Int Soc Optical Engineering, 2006), pp. 63180M.

Thomson, A.R., Walter, M.J., Kohn, S.C. and Brooker, R.A. (2016) Slab melting as a barrier to deep carbon subduction. Nature, 529, 76-79.

Turcotte, D. and Schubert, G. (2014) Geodynamics, ed. 3rd Cambridge University Press.

Uenver-Thiele, L., Woodland, A.B., Boffa Ballaran, T., Miyajima, N. and Frost, D.J. (2017a) Phase relations of $MgFe_2O_4$ at conditions of the deep upper mantle and transition zone. American Mineralogist, 102, 632-642.

Walter, M.J., Kohn, S.C., Araujo, D., Bulanova, G.P., Smith, C.B., Gaillou, E., Wang, J., Steele, A. and Shirey, S.B. (2011) Deep mantle cycling of oceanic crust: evidence from diamonds and their mineral inclusions. Science, 334, 54-57.

Weidner, D.J., Wang, Y. and Vaughan, M.T. (1994) Strength of diamond. Science, 266, 419-422.

Wirth, R., Dobrzhinetskaya, L., Harte, B., Schreiber, A. and Green, H.W. (2014) High-Fe (Mg,Fe)O inclusion in diamond apparently from the lowermost mantle. Earth and Planetary Science Letters, 404, 365-375.

Zhang, Y. (1998) Mechanical and phase equilibria in inclusion–host systems. Earth and Planetary Science Letters, 157, 209-222.

Zhang, J., Li, B., Utsumi, W. and Liebermann, R.C. (1996) In situ X-ray observations of the coesite-stishovite transition: reversed phase boundary and kinetics. Physics and Chemistry of Minerals, 23, 1-10.

Zouboulis, E.S., Grimsditch, M., Ramdas, A.K. and Rodriguez, S. (1998) Temperature dependence of the elastic moduli of diamond: A Brillouin-scattering study. Physical Review B, 57, 2889-2896.

Chapter 3

How geometry and anisotropy affect residual strain in host-inclusion systems: coupling experimental and numerical approaches

This chapter was published as an article in *American Mineralogist* with the title:

How geometry and anisotropy affect residual strain in host-inclusion systems: Coupling experimental and numerical approaches

Authors: N. Campomenosi[1], M.L. Mazzucchelli[2], B.D. Mihailova[3], M. Scambelluri[1], R.J. Angel[2], F. Nestola[4], A. Reali[5], and M. Alvaro[2]

The final published version of the article can be downloaded at https://doi.org/10.2138/am-2018-6700CCBY.

[1]Department of Earth Science, Environment & Life, University of Genoa, Corso Europa 26, 16132 Genoa, Italy; [2]Department of Earth and Environmental Sciences, University of Pavia, Via A. Ferrata, 1 I-27100 Pavia, Italy; [3]Department of Earth Sciences, University of Hamburg, Grindelallee 48, D-20146 Hamburg, Germany; [4]Department of Geosciences, University of Padua, 35131 Padua, Italy; [5]Department of Civil Engineering and Architecture, University of Pavia, Via A. Ferrata 3, I-27100 Pavia, Italy.

3.1 Abstract

Raman spectroscopy provides information on the residual strain state of host-inclusion systems that, coupled with the elastic geobarometry theory, can be used to retrieve the P-T conditions of inclusion entrapment. In-situ Raman measurements of zircon and coesite inclusions in garnet from the Ultrahigh-pressure Dora Maira Massif show that rounded inclusions exhibit constant Raman shifts throughout their entire volume. In contrast, we demonstrate that Raman shifts can vary from the center to the edges and corners of faceted inclusions. Step-by-step polishing of the garnet host show that the strain in both rounded and prismatic inclusions is gradually released as the inclusion approaches the free surface of the host. More importantly our experimental results coupled with selected numerical simulations demonstrate that the magnitude and the rate of the strain release depends also on the contrast in elastic properties between the host and the inclusion and on the inclusion crystallographic orientation with respect to the external surface (anisotropy). These results allowed us to give new methodological guidelines for determining the residual strain in host inclusion systems.

3.2 Introduction

Elastic geobarometry for host-inclusion systems is based on measurements of the residual strains produced during exhumation as a consequence of the contrast in elastic properties between the host and the inclusion. The residual strain in the inclusions can be measured by micro-Raman spectroscopy or X-ray diffraction and can be used to calculate pressure and temperature (P-T) estimates for metamorphic rocks that are not dependent on chemical equilibrium (e.g., Rosenfeld and Chase, 1961; Enami et al., 2007; Angel et al., 2015; Anzolini et al., 2018; Murri et al., 2018). Models for elastic geobarometry only apply to the simple case of elastically isotropic host-inclusion pairs with a simple ideal geometry where a small spherical inclusion is trapped in an infinite host (Angel et al., 2015). Recent numerical models showed that any deviations from the idealized geometry significantly affects the estimation of "residual pressure" (Mazzucchelli et al., 2018). Indeed, gradients in non-spherical inclusions have been already reported (e.g. Zhukov and Korsakov, 2015; Murri et al., 2018). Moreover, several studies pointed out the effects on the residual "pressure" determination of the inclusion size and its partial exposure with respect to the mineral host surface (e.g. Rosenfeld and Chase, 1961; Enami et al., 2007; Zhang, 1998; Mazzucchelli et al. 2018). Nevertheless, open questions still remain, including: what is the effect of the inclusion anisotropy in the residual strain release? How much can the contrast in properties between the host and the inclusion and their geometry influence the residual strain? Therefore, we propose an alternative way to test the effect of the geometry of the host-inclusion system on the Raman signal and on the calculated residual pressure upon polishing: to

collect spectra from selected inclusions with different shape, size and crystallographic orientation, while performing several steps of polishing of the rock thick section to bring the inclusion closer to the external surface of the host. In this manuscript we report the Raman spectra of rounded and elongated zircon inclusions and a rounded coesite inclusion in pyrope from the ultrahigh-pressure (UHP) Alpine Dora Maira Massif measured before and after several subsequent steps of polishing. The measured "residual pressures" are compared with the results of a set of Finite Element models following the approach of Mazzucchelli et al. (2018). This allows us to provide new methodological guidelines and examples of correction curves to adjust measurements carried out on faceted and anisotropic inclusions and/or close to the host surface.

3.3 Sample description

We analyzed zircon and coesite inclusions within pyrope megablasts and porphyroblasts respectively, from the whiteschist of the Brossasco-Isasca UHP unit in the Gilba locality, whose petrography and petrology were reported by several authors (e.g. Chopin, 1984; Hermann, 2003). Whiteschists occur as lenses inside ortho-gneiss and para-gneiss of the Monometamorphic Complex (supplementary materials, section 3.7) and mainly consist of quartz, phengite, kyanite and porphyroblastic to megablastic pyrope-rich garnet. The Dora Maira whiteschist shows a phengite, garnet and kyanite-bearing foliation that wraps around the garnet megablasts (up to 15 cm across). The latter contain numerous inclusions (from few microns to 1 mm in size) mainly of kyanite, rutile and zircon. Garnet porphyroblasts (up to 2 mm in size) within the foliated rock matrix contain rutile, zircon and coesite inclusions. Coesite grains are frequently surrounded by quartz rims and palisade quartz structures (Chopin, 1984), but we only measured the rare monocrystalline unaltered coesite inclusions. For the application of elastic geobarometry we selected garnet-core and rim domains unaltered and free of fractures. In these domains the coesite and zircon inclusions are surrounded by birefringent haloes (Fig. 3.1), indicating that the structure of the garnet host around the inclusions is anisotropically strained.

3.4 Methods

As pointed out previously (Zhang, 1998; Mazzucchelli et al., 2018), only small isolated inclusions far from any free surface of the garnet thick sections (e.g. distance $>$ 3 radii of the inclusion) do not suffer potential strain release. Therefore, for this study we prepared polished sections of 250-260 μm thickness. We performed Raman spectroscopic measurements only on inclusions at the center of the section with a mean linear size smaller than 50 μm, (i.e. considerably less than the distance to the

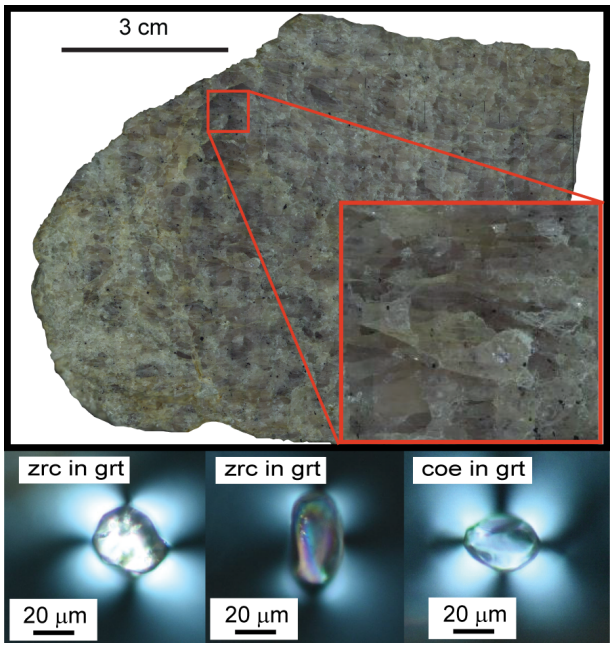

Figure 3.1: A polished pyrope megablast section with partial talc + chlorite alteration along fractures and rims. The red square shows an example of a mm-sized fracture-free garnet area selected for this study, in which zircon and coesite crystalline inclusions exhibiting strain-induced birefringent haloes in the surrounding host have been found. From Campomenosi et al. (2018).

host surface). Micro-Raman scattering measurements were conducted in backscattering geometry with a Horiba Jobin-Yvon T64000 triple-monochromator spectrometer with a spectral resolution of $\approx 2\,\mathrm{cm}^{-1}$ and instrumental accuracy in peak positions of $\approx 0.35\,\mathrm{cm}^{-1}$. For each inclusion a series of spot measurements were carried out along the equatorial plane of the inclusion as shown in Fig. 3.2. Details of the measurements and data processing are given in the supplementary materials (section 3.7). We collected Raman spectra before and after polishing of the garnet hosts by known amounts. The inclusion distance from the surface (i.e. the distance between the equatorial plane of the inclusion and the host external surface) was estimated by means of optical focus coupled with the controlled z-position motorized microscope stage. We repeated the procedure until the inclusion was half-exposed. This allowed us to observe the "real time" evolution of the strains inside the inclusions in terms of changes in the Raman frequencies. Here we show examples of single crystals of zircon: one rounded ($\approx 20\,\mu$m in radius) and one prismatic ($\approx 80\,\mu$m along the long axis), labelled S2 and S3, respectively) and one rounded single crystal of coesite ($\approx 15\,\mu$m in radius, sample S24) in the garnet megablasts and porphyroblasts, respectively. No prismatic or idiomorphic coesite inclusions have been found. Since our inclusions are elastically anisotropic, their orientation with respect to the polishing surface is critical for the interpretation of the results by means of numerical simulations. The idiomorphic zircon grain S3 has the c axis inclined with respect to the polishing surface by approximately 20° (estimated optically). Analysis of the peak intensities in the polarized Raman spectra suggests that the rounded zircon grain S2 has its c axis almost perpendicular to the surface. The coesite crystal S24 was rounded and the absence of pronounced changes in the Raman intensities measured in different scattering geometries makes it impossible to determine its orientation and therefore it was not possible to perform numerical simulations for this inclusion. Finite element simulations have been carried out to support the interpretation of our measurements of zircon inclusions S2 and S3 and to evaluate the effect of the proximity of the inclusion to the external surface of the thick section on the residual strain of the inclusion (procedures as in Mazzucchelli et al., 2018, further details are reported in supplementary materials). Elastic anisotropy has been incorporated in the model for the zircon inclusions. The pyrope host was treated as isotropic because its universal anisotropic index (Ranganathan and Ostoja-Starzewski, 2008) is negligible (i.e. $9 \cdot 10^{-4}$), based on the elastic moduli reported by Sinogeikin and Bass (2002). The use of isotropic elastic properties for the host allows us to neglect the mutual crystallographic orientation of the host and the inclusion. For our purposes the only relevant orientation is that of the inclusion with respect to the surface of the petrographic section.

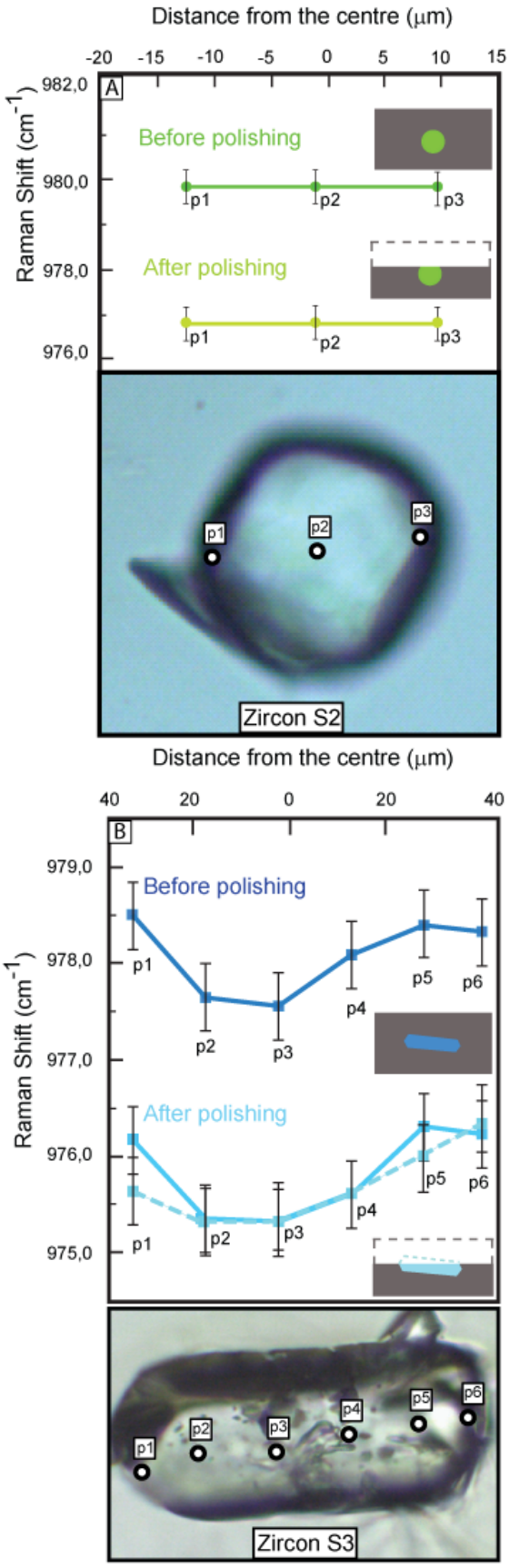

Figure 3.2: Position of the Raman peak $A_{1g} \approx 975\,cm^{-1}$ *in a rounded (A) and an idiomorphic (B) zircon crystal before and after the final step of polishing. The solid lines in the plots are guides for the eye; the dashed line in (B) traces the data points measured after two days of final exposure of the grain. From Campomenosi et al. (2018).*

3.5 Results and discussion

Both rounded and idiomorphic inclusions close to the center of the section display Raman peak positions shifted toward higher wavelengths compared to free reference crystals. Within the instrumental precision ($\pm 0.35\,\mathrm{cm}^{-1}$) the rounded zircon inclusion S2 and the rounded coesite inclusion S24 showed no spatial variation of the Raman peak positions within the inclusions. On the other hand, for idiomorphic crystals (zircon inclusion S3 with well-developed corners and edges) there is a steady increase in the peak positions of about $1\,\mathrm{cm}^{-1}$ from the center towards the edges of the inclusions (Fig. 3.2B). This is a direct consequence of strain heterogeneity in the inclusion, which can be caused by chemical zonation, zoned radiation-induced damage and/or an imposed strain gradient. The substitution of elements such as Th, U, or Hf for Zr, may cause expansion (U, Th) or contraction (Hf) of the zircon unit cell (Nasdala et al., 1998), leading to a change in the phonon wavenumbers. However, compositional analysis of the exposed grain performed after the final step of polishing did not reveal any chemical zonation (see supplementary material). Radioactive decay of elements such as U and Th can induce structural damage, leading to Raman peak broadening and a shift towards lower wavenumbers (Binvignat et al., 2018). However, the full-width-at-half-maximum (FWHM) of our zircon inclusions is equal to that of full crystalline zircon ($\approx 4-5\,\mathrm{cm}^{-1}$), thus indicating a high degree of crystallinity throughout the entire grain bulk. Since the zircon inclusion S3 is chemically homogeneous (see Appendix A.1) and well-crystalline, the variable Raman shift in it is due to its faceted shape (Eshelby, 1957) because the edges and corners act as stress concentrators (Zhang, 1998; Mazzucchelli et al., 2018). Then, after polishing, the Raman spectra of S3 become homogeneous within the fully exposed part of the sample (Fig. 3.2B), confirming that the variation in the peak position in a single crystal for all bands was caused by the shape of the crystal. A decrease in the Raman band wavenumbers was measured at the center of the inclusions upon polishing for all the investigated samples of zircon and coesite. As an example, Fig. 3.3A shows the B1g mode near 1008 cm^{-1} measured on zircon sample S3 at three different steps of polishing. Strictly speaking, the phonon wavenumbers are directly related to the strain, rather than to the applied pressure. Moreover, for elastically anisotropic materials the same relative volume change can be obtained by different strains, for example as induced by hydrostatic or deviatoric stress. Therefore, the commonly used direct proportionality between the Raman peak positions and residual pressure is a strongly oversimplified assumption (Murri et al., 2018). Nonetheless, if we assume that the change in Raman wavenumber ω is linear with mean stress P (i.e. $\partial\omega/\partial P$ is constant), we can introduce the normalized change in the peak position $\Delta\omega_{norm}$ as a parameter to express the relative release in "pressure" as the inclusion becomes closer to the external surface of the host during polishing:

$$\Delta\omega_{norm} = \frac{(\omega_{I,d} - \omega_{I,0})\frac{\partial P}{\partial \omega} - (\omega_{I,\infty} - \omega_{I,0})\frac{\partial P}{\partial \omega}}{(\omega_{I,\infty} - \omega_{I,0})\frac{\partial P}{\partial \omega}} = \\ = \frac{(\omega_{I,d} - \omega_{I,\infty})}{\omega_{I,\infty} - \omega_{I,0}} \approx \frac{P_{i,d} - P_{i,\infty}}{P_{i,\infty}} = \Gamma \tag{3.1}$$

Where $\omega_{I,0}$ is the wavenumber for a free crystal measured at ambient conditions, $\omega_{I,\infty}$ and $P_{I,\infty}$ are the wavenumber and the corresponding pressure for an inclusion in an infinitely large host (i.e. before the polishing, when the inclusion was far away from the surface of the host), while $\omega_{I,d}$ and $P_{I,d}$ are the wavenumber measured on the inclusion and its pressure after each polishing step and associated to a specific normalized distance d (i.e. the distance from the inclusion center to the host external surface divided by the corresponding inclusion radius). Under these assumptions equation (3.1) shows that $\Delta\omega_{norm}$ becomes equivalent to the geometrical factor Γ defined by Mazzucchelli et al, (2018). As can be seen in Fig. 3.3B and C, the normalized change in the peak position $\Delta\omega_{norm}$ decreases progressively towards -1 (i.e. the Raman shift becomes equal to that of the free inclusion), when the inclusion approaches the host surface. The trends of "pressure" release estimated from the Raman spectra measured on our zircon samples show the same pattern with those calculated from numerical simulations performed on similar geometries and crystallographic orientations (e.g. see the dotted lines in Fig. 3.3B). However, the experimental data suggest a greater amount of stress release compared to the numerical simulations. For example, at a normalized distance of 1 (inclusion just in contact with the external surface), the calculated stress release is approximately 50%, whereas that obtained from experimental data is about 70% (Fig. 3.3B). There are at least two contributions to this discrepancy: (i) for non-cubic inclusions direct conversion of Raman shifts into pressures using a hydrostatic calibration is incorrect; (ii) when the inclusion is close to the surface, strain gradients may be relaxed through plasticity or micro-fractures that are not considered in our purely elastic numerical models. Interestingly, our experiments show that even after partial exposure of the inclusion (i.e. for normalized distances ≤ 1) the Raman shift does not record full strain release (i.e. the inclusion is not at ambient conditions). In Fig. 3.3C , for example, the polished coesite inclusion still shows 40% of its residual strain. Finally, the difference in the strain release between zircon and coesite inclusions is probably due to the different contrast in properties with respect the host garnet. Indeed, since coesite is softer than zircon, the host garnet can still retain a greater amount of its residual strain even if half of the inclusion is exposed. This implies the possibility to have thinner hosts for softer inclusions such as coesite or quartz in garnet but, however, the possibility of fracturing during polishing is high (Enami et al., 2007).

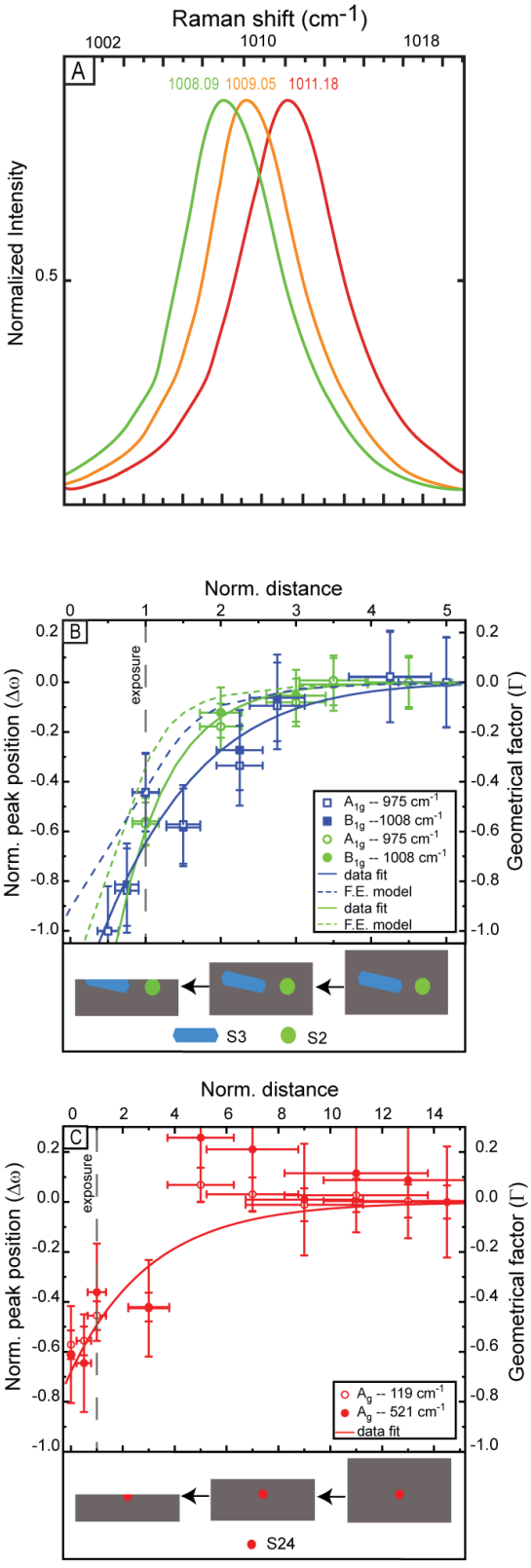

Figure 3.3: (A) Raman scattering arising from the antisymmetric SiO4 stretching (the B1g crystal phonon mode $\approx 1008\,\mathrm{cm}^{-1}$*) measured when the grain was fully entrapped (red line), at an intermediate stage of polishing (yellow), and when the inclusion was exposed at the final stage of polishing (green line). The numbers are the measured Raman shifts. (B) Measured normalized wavenumber shifts* $\Delta\omega_{norm}$ *for zircon S2 (green circles) and zircon S3 (blue squares) versus the normalized distance d to the host surface along with the fit to the corresponding data* $\mathrm{A_{1g}} \approx 975$ *and* $\mathrm{B_{1g}} \approx 1008\,\mathrm{cm}^{-1}$ *data sets (solid lines) as well as the calculated geometrical factor* Γ *(dashed lines) from the FE model;* $\Delta\omega_{norm}$ *(d) and* Γ *(d) show the same trend within uncertainties. (C) Measured* $\Delta\omega_{norm}$ *(d) (circles) for the modes* $\mathrm{A_{1g}} \approx 119$ *and* $\approx 521\,\mathrm{cm}^{-1}$ *(solid line) for S24 coesite inclusion. Red line: fit trough the experimental points. From Campomenosi et al. (2018).*

3.6 Implications

Our measurements show that Raman shift is homogeneous only in rounded inclusions while it is non-homogeneous in faceted ones (Fig. 3.2 A and B), in a full agreement with numerical calculations (Mazzucchelli et al. 2018) and theory (Eshelby, 1957). Therefore, multiple Raman spectra collected on faceted inclusions should not be averaged if their differences are larger than the instrumental peak precision. Instead, to avoid the effects of grain shape on Raman peak positions, only Raman spectra measured at the center of the inclusions should be used because there we can apply the geometrical correction (see Mazzucchelli et al., 2018). Our polishing experiments confirm that the Raman shift on the inclusion decreases as the inclusion gets closer to the external surface (Rosenfeld and Chase, 1961; Zhang, 1998; Mazzucchelli et al., 2018). Therefore, only inclusions whose centers are distant more than 4 radii (Fig. 3.3 B) from the section surface and internal surfaces of the host should be used. If the Raman peak positions vary from one inclusion to another, even when the inclusions are properly selected, this indicates that some other factor is responsible, such as chemical variation in the host or inclusions, or growth of the host and thus inclusion entrapment under different conditions, such as along a prograde subduction path. More importantly, our results, coupled with our FE numerical simulations, show how anisotropy (i.e. crystallographic orientation of the inclusion with respect to the external surface) and the contrast between the inclusion and host physical properties influences the strain release during polishing. Furthermore, even when an inclusion is exposed at the surface of the host grain, it can still exhibit a variation in the peak position with respect to a free crystal, and thus residual strains and stresses (Fig. 3.3 C). Therefore, partially entrapped grains to be used as a strain free standard against which to measure the Raman shifts of unexposed inclusions should be avoided or chosen extremely carefully. Finally, as an example, if we calculate from our experimental data on Raman shift values the strain and then the mean stress in the inclusion after subsequent polishing steps, following the approach given by Murri et al. (2018), we have for the zircon S3 an initial residual pressure (Pinc) of 0.5 GPa. After 55 microns of polishing (1.5 of normalized distance in Fig. 3.3 B), when the inclusion is still buried in its garnet host the Pinc is dropped at 0.2 GPa. A value of 0.06 GPa is recorded when the inclusion is half exposed. For zircon S2 the initial Pinc was of about 0.9 GPa and of about 0.3 GPa when the inclusion was just touching the external surface of the host. In the supplementary material a table showing the evolution of the Pinc as function of the polishing for the two zircon inclusions is reported (Table 3.8) For coesite no reliable data are presents to give the strain state of the inclusion by means of the Raman peak positions.

3.7 Supplementary materials

3.7.1 Sample provenance and geological background: the Dora Maira massif

Our study focusses on solid inclusions in pyrope megablasts (up to 15 cm across) and porphyroblasts (up to 2 cm across) from the Dora Maira Massif (DMM; Italian Western Alps; Fig. 3.4), a slice of continental crust involved in Alpine subduction and exhumation. Since the discovery of coesite inclusions in garnet from phengite whiteschists (Chopin, 1984), the DMM became a world-known setting for ultrahigh-pressure (UHP) metamorphism and attracted interest of numerous scientists who defined its structure, tectonic and metamorphic histories (e.g. Chopin, 1984; Hermann, 2003). The DMM consists of Variscan orto- and para-gneiss involved in Alpine subduction and exhumation (for a review see also Carswell and Compagnoni, 2005). The UHP, coesite-bearing Brossasco-Isasca Unit of the DMM is tectonically sandwiched between two lower pressure units (Rocca du Soleil and Pinerolo Units, Fig. 3.4). It consists of two main litostratigraphic sub-units, the Monometamorphic and the Polymetamorphic Complexes, made of orthogneiss and of amphibolite-facies basement rocks, respectively. We investigated pyrope megablasts and porphyroblasts from whiteschist lenses hosted in the Monometamorphic Complex (Gilba locality, Fig. 3.4). The whiteschist is interpreted to either derive from evaporite (Chopin, 1984), or from metasomatism of former orthogneiss by Mg-rich fluids infiltrating during UHP metamorphism (e.g. Ferrando et al., 2009);. The $P-T-t$ path of the DMM has been defined in a number of papers: here we refer to Rubatto and Hermann, (2001), who combined $P-T$ estimates with in-situ U-Pb titanite dating. These authors defined a peak metamorphic stage at 3.5 GPa - 750 °C at 35.1 ± 0.9 Ma, and three decompression steps at 32.9 ± 0.9 Ma, 31.8 ± 06 Ma and 29.9 ± 1.4 Ma, respectively. Rubatto & Hermann (2001) proposed different exhumation velocities of the DMM, from 3.4 cm/yr during the first stage of exhumation from peak conditions, to 1.6 cm/yr and 0.5 cm/yr during the last two exhumation steps. More recently, further experimental and petrological studies carried out on whiteschists by Hermann (2003) indicated that the peak metamorphic pressure was in the diamond facies stability field at 43 kbar and 730 °.

3.7.2 Mineral chemistry of garnet and zircon

The mineral chemistry of garnets was determined by means of a TESCAN Vega-3 electron microprobe at the University of Genova (DISTAV department), using an energy-dispersive technique with an acceleration voltage of 15 keV, a beam current of 14 nA. The standard used were: K pyrope USNM 143968, MAC N° 10642 forsterite. Empirical formula recalculation was computed based on 12 oxygens and the ferric iron was estimated by filling octahedral sites to the theoretical value of 2.0 per formula unit

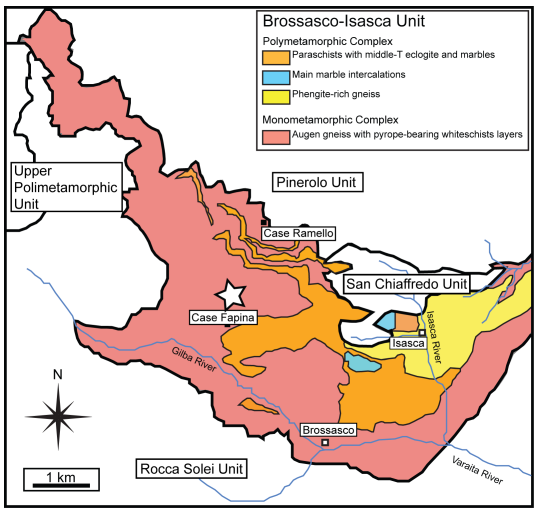

Figure 3.4: Tectono-metamorphic sketch map of the southern part of Dora Maira Massif (modified from Castelli et al. 2007). The white star indicates the locality from which garnet bearing white schists come from (Gilba locality near Case Fapina). From Campomenosi et al. (2018).

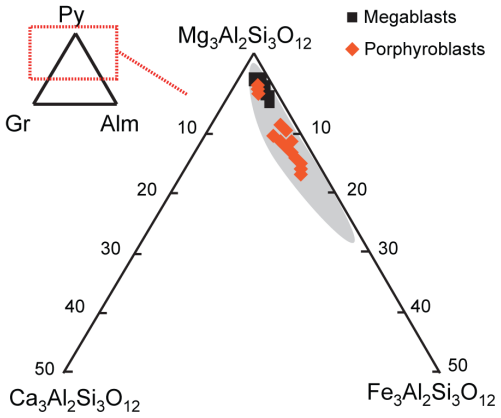

Figure 3.5: Chemical composition of garnet porphyroblasts and megablasts in the ternary diagrams Py-Alm-Gr. In grey is reported the composition of garnets from literature data (Ferrando et al. 2009). From Campomenosi et al. (2018).

(see Table 3.1). The electron microprobe analysis and chemical element mapping of the idiomorphic polished zircon was performed using a Cameca SX-100 SEM system electron microprobe available at University of Hamburg (Earth Science department), using a wavelength-dispersive technique with an acceleration voltage of 15 keV, a beam current of 40 nA. The standard used were: Al_2O_3 for Al, $ZrSiO_4$ for Si and Zr, apatite for P, wollastonite for Ca, $MnTiO_3$ for Mn, andradite for Fe, REE1 for Y, REE2 for Ce, REE4 for Nd, Hf for Hf, Pb-Glass for Pb, Th-Glass for Th, UO_2 for U. Where REE1 = Si : 23.27%, Al : 6.23%, Ca : 13.43%, Y : 3.97%, Pr : 3.93%, Dy : 4.02%, Er : 3.97%, O : 40.46%, REE2 = Si : 23.53%, Al : 6.3%, Ca : 13.49%, Ce : 3.93%, Eu : 3.99%, Ho : 3.92%, Tm : 4.01%, O : 40.47% and REE4 = Si : 24.76%, Al : 6.66%, Ca : 14.42%, Nd : 3.89%, Tb : 4%, Lu : 3.97%, O : 41.8%. Empirical formula recalculation was computed on the basis of 16 oxygens per formula unit. Garnets, with colours ranging from pale to dark pink, occur either as megablasts (up to 15 cm across) and porphyroblasts (up to 1 cm across) in coesite-bearing whiteschists from the Brossasco-Isasca UHP unit. The garnet megablast (sample DMG.2), in which the selected polished zircon inclusions have been studied, displays a pyrope-rich composition (up to 94 mol%) with minor amounts of almandine (up to 5 mol%) and grossular ($<$ 2 mol%) from the core to the rim. Garnet porphyroblasts display a zonation characterized by almandine-rich (up to 20 mol%) cores and almost pure pyrope rims (up to 95 mol%) (see Figure 3.5). The variation of Mg and Fe components in garnet is antipathetic whereas the grossular component seldom reaches 3 mol%. The most outer garnet rims often show an increase in the almandine component that was already interpreted by previous authors as the result of retrogression in the later metamorphic stages. Table 3.1 reports some representative chemical analysis of both the garnet megablasts and porphyroblasts. We performed chemical analysis on the idiomorphic elongated crystal of zircon in order to understand if the heterogeneity in Raman peak position was caused by the presence of heterogeneity in the chemical composition (i.e. zonation). It is important to stress that Raman peak positions are commonly influenced by chemical variation greater than 1 wt % and therefore WDS microprobe analysis are sufficient for our purposes. Chemical analyses performed on the same points in which Raman spectra were collected show no significant chemical heterogeneities for this zircon crystal. Zircon chemical analyses results are reported in Table 3.1.

3.7.3 selection rules for phonon modes in zircon and coesite, and data acquisition and evaluation

Zircon has tetragonal symmetry with space group $I41/amd$. According to group theory analysis, the optic phonons at the Brillouin-zone center of zircon are (Kroumova et al., 2003):

$$\Gamma_{opt} = 2A_{1g} + A_{1u} + A_{2g} + 3A_{2u} + 4B_{1g} + B_{1u} + B_{2g} + 2B_{2u} + 5E_g + 4E_u$$

The A_{1g}, B_{1g}, B_{2g} and E_g modes are Raman-active and therefore a total of 12 Raman peaks can be observed in the spectrum of a randomly oriented zircon. According to previous experimental results (Knittle and Williams, 1993; Mihailova et al. unpublished data) the B_{1g} mode near 1008 cm^{-1}, the A_{1g} mode near 975 cm^{-1} and the E_g mode near 357 cm^{-1} are the most pressure-sensitive peaks. For this reason, our discussion is mainly focused on these vibrational modes. Note that the B_{1g} modes are symmetry allowed in $\bar{y}(xx)y$ scattering geometry (Porto's notation), A_{1g} in $\bar{y}(xx)y$, $\bar{y}(zz)y$, and $\bar{z}(xx)z$, whereas E_g in $\bar{y}(xz)y$, with x, y, z along the a, b and c crystallographic axes, respectively. Coesite is a monoclinic crystal with space group C2/c (unique axis b). The irreducible representation of the optical vibrations are (Kroumova et al., 2003):

$$\Gamma_{opt} = 16A_g + 18A_u + 17B_g + 18B_u$$

The A_g and B_g modes are Raman-active and therefore a total of 33 Raman peaks can be theoretically observed in the spectrum of a randomly oriented coesite crystal. Experimental results by Hemley (1987) suggest that the Ag mode near 119 cm^{-1}, near 183 cm^{-1} and near 521 cm^{-1} are the most pressure-sensitive Raman peaks and they were used as our "sensors" for the polishing effect in coesite. However not all of the peaks predicted by group theory were observed in our spectra because of their weak intensities or because of partial overlap with the main garnet peaks. Micro-Raman scattering measurements were conducted in backscattering geometry with a Horiba Jobin-Yvon T64000 triple-monochromator spectrometer (holographic gratings of 1800 grooves/mm) equipped with an Olympus BX41 confocal microscope (Olympus LM Plan FLN 50X objective with a numerical aperture of 0.5) and a Symphony liquid-N2-cooled charge-coupled device detector. Raman spectra were excited either by the 488.0 or 514.532 nm line of a Coherent 90C Fred Ar^+ laser, in order to achieve a minimum level of continuum photoluminescence background. For both laser lines the laser power on the sample surface was approximately 14 mW, to avoid sample overheating during the experiment. The spectrometer was calibrated to the silicon Raman peak at 520.5 cm^{-1}. The spectral resolution was 2 cm^{-1} and the instrumental accuracy in determining the peak positions was 0.35 cm^{-1}. Parallel and cross polarized Raman spectra were collected for all samples in the spectral range 15–1215 cm^{-1}. In the case of zircon S3, the grains were oriented with the c axis perpendicular to the polarization of the incident light, which ensured maximum Raman intensity of the major peak near 1008 cm^{-1}. Spectra were collected for 7 s averaging over 3 accumulations. For each inclusion a series of spot measurements were carried out along the equatorial plane of the inclusion as shown in Fig. 3.3. OriginLab-Pro 2018 software package was used

for data fitting and evaluation. The collected spectra were baseline corrected for the continuum luminescence background when necessary, temperature-reduced to account for the Bose-Einstein occupation factor (Kuzmany, 2009) and normalized to the acquisition time. Peak positions, full-widths at half maximum (FWHMs), and integrated intensities were determined from fits with pseudo-Voigt functions [PV = (1 – q)·Lorentz + q·Gauss, q is the weight coefficient]. The criterion for the maximum number of fitted peaks was $\Delta I < I/2$, where I and ΔI are the calculated magnitude and uncertainty of each peak intensity, respectively

3.7.4 Finite element (FE): computational details

We have used a commercially available engineering package, Abaqus Standard v.2016 (Dassault Systèmes, Simulia, Providence), to create and analyze 3D finite-element models following the same procedures outlined in Mazzucchelli et al., 2018. The models reproduce the geometry and the crystallographic orientations of our zircon inclusions in pyrope (samples S2 and S3), at several steps of distance of the inclusion from the external surface of the host. All our 3D models have at least one mirror plane, therefore only half of the selected shape was created and the full model was obtained by reflection through that mirror plane. Since the mirror plane of the model corresponds to the [1 0 0] crystallographic plane, it does not restrict the deformation of zircon that is tetragonal. The resulting model consisted of more than 400000 10-node quadratic tetrahedral elements (element C3D10 in the Abaqus library). Material properties and boundary conditions were assigned, and then a mesh convergence analysis was performed. The mesh was refined in the areas with higher stress gradients until the calculated stress distribution appeared smooth. An example of one model and the mesh used is reported in Fig. 3.6. To simulate the external pressure, face loads were applied to the 3D elements on the external boundaries of the host. Boundary conditions were placed on the appropriate edges and faces of the models to avoid rigid body rotation and translation in the x, y and z directions.

The constitutive equation used by Abaqus for anisotropic linear elasticity is:

$$\sigma_{ij} = C_{ijkl}\varepsilon_{kl}$$

where σ_{ij} and ε_{kl} are the stress and the strain tensor respectively, and C_{ijkl} are the elastic stiffness moduli. For the zircon inclusion the elastic stiffness moduli at room conditions reported by Ozkan et al. (1974) were used in FE analysis (Table 3.7). The pyrope host was treated as isotropic because its universal anisotropic index (Ranganathan and Ostoja-Starzewski, 2008) is only $9 \cdot 10^{-4}$, essentially zero, based on the elastic moduli reported by Sinogeikin and Bass (2002). The isothermal bulk modulus

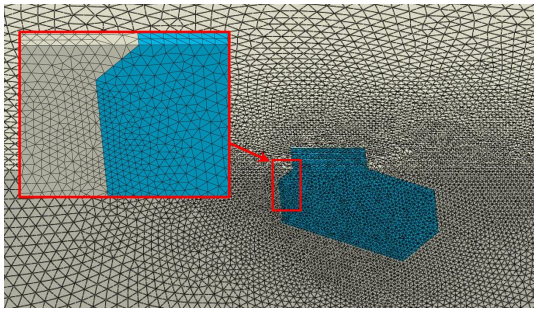

Figure 3.6: 3D Finite element meshes of a faceted inclusion partially exposed to the surface of the host. Only half of the model is shown. The full model is obtained by reflection through the mirror plane, as described in the text. From Campomenosi et al. (2018).

at room conditions was derived from Milani et al. (2015) while the shear modulus was obtained from the elastic moduli reported by Sinogeikin and Bass (2002).

3.7.5 Residual pressure estimation

Residual "pressure" estimation from Raman shift frequencies made using the approach given by Murri et al., (2018) is reported in Table 3.8. The phonon frequencies taken as reference for the B1g and the A1g modes refer to the zircon crystal S3 once completely exposed to the external surface of the host (1008.68 cm^{-1} and 974.85 cm^{-1}). Note that these reference values are in agreement with free zircon crystals having similar composition (Binvignat et al., 2018).

Table 3.1: Representative chemical analysis of zircon sample S3 and garnet megablasts and porphyroblasts from whiteschists.

Mineral	Zircon						mineral	garnet megablast		garnet porphyroblasts	
p. analysis	p1	p2	p3	p4	p5	p6	p. analysis	core	rim	core	rim
oxide	(wt%)	(wt%)	(wt%)	(wt%)	(wt%)	(wt%)	oxide	(wt%)	(wt%)	(wt%)	(wt%)
Al_2O_3	0.01	0.00	0.00	0.00	0.00	0.01	SiO_2	42.50	42.85	42.14	42.83
SiO_2	32.85	32.42	32.74	32.50	32.40	31.60	TiO_2	b.d.l.	b.d.l.	0.16	0.00
P_2O_5	0.23	0.40	0.27	0.27	0.35	0.09	Al_2O_3	25.11	25.00	24.64	25.23
CaO	0.02	0.02	0.01	0.02	0.02	0.02	Cr_2O_3	b.d.l.	b.d.l.	b.d.l.	b.d.l.
MnO	0.01	0.02	0.01	b.d.l.	0.01	b.d.l.	Na_2O	b.d.l.	b.d.l.	b.d.l.	b.d.l.
Fe_2O_3	0.10	0.17	0.12	0.14	0.11	0.20	FeO	2.80	3.36	8.98	2.82
Y_2O_3	b.d.l.	0.00	b.d.l.	b.d.l.	b.d.l.	b.d.l.	MgO	28.16	28.13	23.04	28.30
ZrO_2	66.11	64.04	65.44	64.55	65.17	66.51	MnO	b.d.l.	b.d.l.	b.d.l.	0.09
Ce_2O_3	b.d.l.	b.d.l.	0.01	b.d.l.	b.d.l.	b.d.l.	CaO	0.86	0.73	1.31	0.93
HfO_2	1.49	1.64	1.45	1.43	1.52	1.69	H_2O+	b.d.l.	b.d.l.	b.d.l.	b.d.l.
PbO	b.d.l.	b.d.l.	b.d.l.	0.03	0.01	b.d.l.	H_2O-	b.d.l.	b.d.l.	b.d.l.	b.d.l.
ThO_2	0.02	b.d.l.	b.d.l.	0.03	b.d.l.	b.d.l.	Sum	99.43	100.07	100.27	100.20
UO_2	0.07	0.14	0.03	0.09	0.07	0.04					
Nd_2O_3	b.d.l.	0.02	0.03	b.d.l.	0.01	0.03					
Sum	100.91	98.87	100.10	99.07	99.68	100.19					
Occupancy	moles	moles	moles	moles	moles	moles	occupancy	moles	moles	moles	moles
Zr	3.92	3.86	3.90	3.89	3.91	4.01	Si	2.92	2.93	2.95	2.92
Hf	0.05	0.06	0.05	0.05	0.05	0.06	Al	0.08	0.07	0.05	0.08
U	-	0.01	-	-	-	-	Sum site IV	3.00	3.00	3.00	3.00
Th	-	-	-	-	-	-	Al	1.95	1.95	1.99	1.95
Y	-	-	-	-	-	-	Fe^{3+}	0.05	0.05	0.01	0.05
Al	-	-	-	-	-	-	Cr^{3+}	-	-	-	-
Ca	-	-	-	-	-	-	Sum site VI	2.00	2.00	2.00	2.00
Mn	-	-	-	-	-	-	Fe^{2+}	0.11	0.14	0.51	0.11
Fe^{3+}	0.01	0.02	0.01	0.01	0.01	0.02	Mg	2.88	2.87	2.41	2.88
Sum VIII site	3.98	3.94	3.97	3.96	3.98	4.09	Mn^{2+}	-	-	-	0.01
P	0.02	0.04	0.03	0.03	0.04	0.01	Ca	0.06	0.05	0.10	0.07
Si	3.99	4.01	4.00	4.01	3.98	3.90	Na2O	-	-	-	-
Sum IV site	4.01	4.05	4.03	4.04	4.02	3.91	Sum site VIII	3.06	3.06	3.01	3.06

Table 3.2: Raman shift heterogeneity inside one single crystal.

p. analysis*	B_{1g} (cm^{-1})	FWHM (cm^{-1})	A_{1g} (cm^{-1})	FWHM (cm^{-1})	E_g (cm^{-1})	FWHM (cm^{-1})
p6	1011.90(1)	5.30(2)	978.51(8)	4.84(12)	360.07(1)	7.44(8)
p5	1012.09(2)	5.61(3)	977.66(9)	5.35(16)	358.90(2)	8.07(9)
p4	1011.60(2)	6.02(3)	977.56(9)	5.34(16)	358.77(2)	7.82(9)
p3	1011.18(2)	6.18(3)	978.10(7)	5.28(12)	359.65(2)	7.30(7)
p2	1011.26(2)	6.31(5)	978.41(7)	5.15(12)	359.98(2)	7.51(6)
p1	1012.18(2)	5.72(4)	978.34(7)	4.79(11)	360.08(2)	6.94(6)
p. analysis†	B_{1g} (cm^{-1})	FWHM (cm^{-1})	A_{1g} (cm^{-1})	FWHM (cm^{-1})	E_g (cm^{-1})	FWHM (cm^{-1})
p6	1010.03(1)	5.71(3)	976.23(5)	4.86(8)	358.37(1)	7.50(2)
p5	1010.05(2)	6.38(3)	976.30(5)	5.50(8)	358.25(1)	7.77(3)
p4	1009.37(2)	5.86(3)	975.60(5)	4.97(9)	357.51(1)	7.36(2)
p3	1009.05(2)	6.63(4)	975.32(8)	5.39(16)	357.13(1)	8.08(3)
p2	1008.99(2)	6.23(4)	975.37(8)	5.23(15)	357.17(1)	7.68(4)
p1	1009.92(2)	5.92(4)	976.18(9)	4.77(14)	357.96(1)	6.78(4)
p. analysis§	B_{1g} (cm^{-1})	FWHM (cm^{-1})	A_{1g} (cm^{-1})	FWHM (cm^{-1})	E_g (cm^{-1})	FWHM (cm^{-1})
p6	1009.58(2)	6.07(5)	976.40(5)	5.39(9)	358.23(2)	7.97(8)
p5	1009.53(1)	6.50(1)	975.86(3)	5.54(5)	357.18(1)	7.75(2)
p4	1009.01(1)	6.49(2)	975.61(4)	5.87(7)	357.31(1)	8.26(3)
p3	1008.94(1)	7.34(2)	975.39(4)	6.40(7)	357.09(1)	8.86(4)
p2	1008.85(1)	7.47(3)	975.33(5)	6.32(10)	356.60(9)	8.51(3)
p1	1009.18(1)	7.25(2)	975.65(4)	6.07(7)	357.06(1)	8.14(4)

Note: the errors in bracket are referred to the fit
*Value measured before polishing
† Value mesured just after polishing
§ Value measured two days after polishing end

Table 3.3: Polishing effect on zircon sample S3.

p. analysis	Shift (cm-1)	Normalized shift	Uncertainty norm. shift	Shift (cm-1)	Normalized shift	Uncertainty norm. shift	Distance (μm)	Normalized Distance	Uncertaint norm. distance
p0	1011.28	0.00	0.18	977.56	0.00	0.18	100	5.00	0.52
p7	1011.34	0.02	0.18	977.63	0.02	0.18	85	4.25	0.44
p13	1011.11	-0.06	0.17	977.31	-0.09	0.17	55	2.75	0.30
p16_bis	1010.53	-0.27	0.16	976.65	-0.34	0.16	45	2.25	0.26
p19	1009.68	-0.58	0.16	976.01	-0.57	0.16	30	1.50	0.20
p36	1010.06	-0.44	0.16	976.36	-0.44	0.16	20	1.00	0.16
p53	1009.04	-0.81	0.17	975.29	-0.84	0.17	15	0.75	0.15
reference	*1008.53*	*-1.00*	*0.18*	*974.85*	*-1.00*	*0.18*			

Table 3.4: Polishing effect on zircon sample S2.

p. analysis	Shift (cm-1)	Normalized shift	Uncertainty norm. shift	Shift (cm-1)	Normalized shift	Uncertainty norm. shift	Distance (□m)	Normalized distance	Uncertainty nom. distance
2	1013.16	0.00	0.11	979.80	0.00	0.10	90	4.50	0.47
6	1013.13	-0.01	0.11	979.84	0.01	0.10	70	3.50	0.37
8	1012.91	-0.05	0.10	979.40	-0.08	0.10	60	3.00	0.33
9	1012.60	-0.12	0.10	978.92	-0.18	0.09	40	2.00	0.24
27	1010.57	-0.56	0.09	976.98	-0.57	0.09	20	1.00	0.16
reference	1008.53	-1.00	0.18	974.85	-1.00	0.18			

Table 3.5: Polishing effect on coesite sample S24.

p. analysis	Shift (cm-1)	Norm. shift	uncertainty norm. shift	Shift (cm-1)	Norm. shift	uncertainty norm. shift	Shift (cm-1)	Norm. shift	uncertainty norm. shift	Distance (µm)	Norm. Distance	uncertainty norm. distance
p0	127.21	0.00	0.07	183.84	0.00	0.091	524.18	0.00	0.22	145	14.5	2.9
p1	127.01	-0.03	0.07	183.41	-0.08	0.088	524.03	-0.07	0.22	140	14	2.8
p2	127.20	0.00	0.07	184.09	0.04	0.094	524.30	0.06	0.23	135	13.5	2.7
p3	127.24	0.00	0.07	183.88	0.01	0.092	524.37	0.09	0.23	130	13	2.6
p4	127.41	0.03	0.07	184.10	0.05	0.094	524.43	0.11	0.24	110	11	2.2
p5	127.13	-0.01	0.07	183.71	-0.02	0.090	524.20	0.01	0.22	90	9	1.8
p6	127.44	0.03	0.07	184.25	0.07	0.095	524.64	0.21	0.25	70	7	1.4
p7	127.72	0.07	0.07	184.15	0.06	0.094	524.75	0.26	0.26	50	5	1
p8	124.07	-0.42	0.06	181.35	-0.46	0.079	523.23	-0.43	0.19	30	3	0.6
p9	123.82	-0.46	0.06	181.00	-0.52	0.079	523.37	-0.36	0.20	10	1	0.2
p10	123.06	-0.56	0.06	180.50	-0.62	0.080	522.74	-0.65	0.20	5	0.5	0.1
p11	122.95	-0.57	0.06	180.63	-0.59	0.080	522.82	-0.61	0.19	0	0	0
reference	119.75	-1.00		178.42	-1.00		521.95	-1.00				

Table 3.6: Polishing effect vs hydrostatic pressure calibration.

P. analysis	Shift (cm-1)	Delta shift (cm-1)	dw/dP (cm-1/GPa)	Pressure (GPa)	Schift (cm-1)	Delta shift (cm-1)	dw/dP (cm-1/GPa)	Pressure (GPa)	Schift (cm-1)	Delta shift (cm-1)	dw/dP (cm-1/GPa)	Pressure (GPa)
p0	127.21	7.46	7.40	1.01	183.84	5.42	5.26	1.03	524.18	2.23	2.90	0.77
p0	127.01	7.26	7.40	0.98	183.41	4.99	5.26	0.95	524.03	2.08	2.90	0.72
p1	127.20	7.45	7.40	1.01	184.09	5.67	5.26	1.08	524.30	2.35	2.90	0.81
p2	127.24	7.49	7.40	1.01	183.88	5.46	5.26	1.04	524.37	2.42	2.90	0.83
p3	127.41	7.66	7.40	1.04	184.10	5.68	5.26	1.08	524.43	2.48	2.90	0.86
p4	127.13	7.38	7.40	1.00	183.71	5.29	5.26	1.01	524.20	2.25	2.90	0.77
p5	127.44	7.69	7.40	1.04	184.25	5.83	5.26	1.11	524.64	2.69	2.90	0.93
p6	127.72	7.97	7.40	1.08	184.15	5.73	5.26	1.09	524.75	2.80	2.90	0.96
p7	124.07	4.32	7.40	0.58	181.35	2.93	5.26	0.56	523.23	1.28	2.90	0.44
p8	123.82	4.07	7.40	0.55	181.00	2.58	5.26	0.49	523.37	1.42	2.90	0.49
p9	123.06	3.31	7.40	0.45	180.50	2.08	5.26	0.39	522.74	0.79	2.90	0.27
p11	122.95	3.20	7.40	0.43	180.63	2.21	5.26	0.42	522.82	0.87	2.90	0.30
reference	119.75				178.42				521.95			

Table 3.7: Elastic parameters at room conditions for zircon and pyrope used for finite element calculations.

Zircon (anisotropic elastic properties)	C11	C33	C44	C66	C12	C13
	(GPa)					
	423.7	490	113.6	48.5	70.3	149.5
Pyrope (isotropic elastic properties)	K_{0T} (GPa)			G_{0T} (GPa)		
	163.7			94.0		

Table 3.8: Residual pressures for the zircon S2.

N. Distance	$\Delta\omega$ 975 (cm^{-1})	$\Delta\omega$ 1008 (cm^{-1})	e_1-e_2	e_3	P_{inc} (GPa)
4.5	4.96000	4.63000	-1.162525	-0.44395	0.923
3.5	5.00000	4.60000	-1.1895	-0.40035	0.92645
3.0	4.56000	4.38000	-1.027	-0.4618	0.8386
2.0	4.08000	4.07000	-0.8892	-0.5382	0.7722
1.0	2.13000	2.04000	-0.4888	-0.21595	0.39785

Table 3.9: Residual pressures for the zircon S3.

N. Distance	$\Delta\omega$ 975 (cm^{-1})	$\Delta\omega$ 1008 (cm^{-1})	e_1-e_2	e_3	P_{inc} (GPa)
5.0	2.78000	2.94017	-0.56355	-0.46095	0.52935
4.2	2.78000	2.81077	-0.5928	-0.3588	0.5148
2.7	2.46000	2.58099	-0.4992	-0.38205	0.46015
2.2	1.81000	2.00278	-0.3562	-0.3754	0.3626
1.5	1.16000	1.14690	-0.2717	-0.16445	0.23595
1.0	1.52000	1.52951	-0.3211	-0.19435	0.27885
0.7	0.44000	0.51245	-0.06435	-0.0789	0.0692

3.8 Acknowledgments

This project received funding from the European Research Council (ERC) under the European Union's Horizon 2020 research and innovation program grant agreements 714936 to Alvaro and ERC Starting Grant n. 307322 to Nestola. Alvaro has also been supported by the MIUR-SIR (Ministry of Education, University and Research–Scientific Independence of Young Researchers, Italy) grant MILE DEEp (Mineral Inclusion Elasticity for a New Deep Subduction Geobarometer; RBSI140351). Campomenosi acknowledges the University of Genova for funding. The authors are grateful to Peter Stutz, Hamburg, for thin-section polishing and to Alessandra Gavoglio and Paolo Campanella, Genova, for the thin-section preparation, Stefanie Heidrich, Hamburg, and Laura Negretti, Genova, for help with electron microprobe analysis.

3.9 References

Angel, R.J., Nimis, P., Mazzucchelli, M.L., Alvaro, M., and Nestola, F., 2015, How large are departures from lithostatic pressure? Constraints from host-inclusion elasticity: Journal of Metamorphic Geology, 33, 801–813.

Anzolini, C., Prencipe, M., Alvaro, M., Romano, C., Vona, A., Lorenzon, S., Smith, E. M., Brenker, F. E., Nestola, F., 2018, Depth of formation of super-deep diamonds: Raman barometry of CaSiO3-walstromite inclusions: American Mineralogist, 103(1): 69-74.

Campomenosi, N., Mazzucchelli, M.L., Mihailova, B., Scambelluri, M., Angel, R.J., Nestola, F., Reali, A., and Alvaro, M., 2018, How geometry and anisotropy affect residual strain in host-inclusion systems: Coupling experimental and numerical approaches: American Mineralogist, 103, 2032–2035.

Chopin, C., 1984, Coesite and pure pyrope in high-grade blueschists of the Western Alps: a first record and some consequences: Contributions to Mineralogy and Petrology, 86, 107–118.

Binvignat F. A. P., Malcherek T., Angel R. J., Paulmann C., Schlüter J. Mihailova B. D., 2018, Radiation-damaged zircon under high pressures: Physics and Chemistry of Minerals.

Carswell, D.A., and Compagnoni, R., 2005, Ultrahigh Pressure Metamorphism: EMU notes in mineralogy, Volume 5.

Chopin, C., 1984, Coesite and pure pyrope in high-grade blueschists of the Western Alps: a first record and some consequences: Contributions to Mineralogy and Petrology, v. 86, p. 107–118

Enami, M., Nishiyama, T., and Mouri, T., 2007, Laser Raman microspectrometry of metamorphic quartz: A simple method for comparison of metamorphic pressures: American Mineralogist, 92, 1303–1315.

Eshelby, J. d., 1957, The determination of the elastic field of an ellipsoidal inclution and related problems: Proceedings of the Physical Society of London, Series A, 241, 376-396.

Ferrando, S., Frezzotti, M.L., Petrelli, M., and Compagnoni, R., 2009, Metasomatism of continental crust during subduction: The UHP whiteschists from the Southern Dora-Maira Massif (Italian Western Alps): Journal of Metamorphic Geology, v. 27, p. 739–756.

Hemley, R. J., 1987, Pressure dependence of Raman spectra of SiO_2 polymorphs: α-quartz, coesite and stishovite: High Pressure Research in Mineral Physics, p. 347–359.

Hermann, J., 2003, Experimental evidence for diamond-facies metamorphism in the Dora-Maira massif: Lithos, 70, 163-182.

Knittle, E., and Williams, Q., 1993, High-pressure Raman spectroscopy of ZrSiO4: observation of the zircon to scheelite transition at 300 K. American Mineralogist, v. 78, p. 245 – 252.

Kroumova, E., Aroyo, M.I., Perez-Mato, J.M., Kirov, A., Capillas, C., Ivantchev S. & Wondratschek, H., (2010) Bilbao Crystallographic Server : Useful Databases and Tools for Phase-Transition Studies. Phase Transitions, 76:1-2, 155-170.

Kuzmany, H. (2009) Solid-state spectroscopy — An introduction, 554 p. Springer, Berlin.

Mazzucchelli, M.L., Burnley, P., Angel, R.J., Morganti, S., Domeneghetti, M.C., Nestola, F., and Alvaro, M., 2018, Elastic geothermobarometry: Corrections for the geometry of the host-inclusion system: Geology, 46(3), 231-234.

Milani, S., Nestola, F., Alvaro, M., Pasqual, D., Mazzucchelli, M.L., Domeneghetti, M.C., and Geiger, C.A., 2015, Diamond–garnet geobarometry. The role of garnet compressibility and expansivity: Lithos, v. 227, p. 140–147.

Murri M., Mazzucchelli M. L., Campomenosi, N., Korsakov, A. V., Prencipe, M., Mihailova, B. D., Scambelluri, M., Angel, R. J., and Alvaro, M., 2018 Raman elastic geobarometry for anisotropic mineral inclusions: American Mineralogist, in press

Nasdala, L., Pidgeon, R.T., Wolf, D., and Irmer, G., 1998, Metamictization and U-PB isotopic discordance in single zircons: a combined Raman microprobe and

SHRIMP ion probe study: Mineralogy and Petrology, 62, 1–27.

Özkan, H., Cartz, L., and Jamieson, J.C., 1974, Elastic constants of nonmetamict zirconium silicate: Journal of Applied Physics, v. 45, p. 556–562.

Ranganathan, S.I., and Ostoja-Starzewski, M., 2008, Universal elastic anisotropy index: Physical Review Letters, v. 101, p. 3–6.

Rosenfeld, J.L. & Chase, A.B., 1961. Pressure and temperature of crystallization from elastic effects around solid inclusion minerals? American Journal of Science, 259, 519-541.

Rubatto, D., and Hermann, J., 2001, Exhumation as fast as subduction? Geology, v. 29, p. 3–6

Sinogeikin, S. V., and Bass, J.D., 2002, Elasticity of pyrope and majorite-pyrope solid solutions to high temperatures: Earth and Planetary Science Letters, 203, 549-555.

Zhang, Y., 1998. Mechanical and phase equilibria in inclusion–host systems: Earth and Planetary Science Letters, 157, 209-222.

Zhukov, V. P., & Korsakov, A. V. (2015). Evolution of host-inclusion systems: a visco-elastic model: Journal of Metamorphic Geology, 33(8), 815-828.

Part II

Geobarometry for elastically anisotropic spherical inclusions

Chapter 4

Elastically anisotropic geobarometry: theory

4.1 Unrelaxed strain in the inclusion: thermodynamic calculation

We are interested in calculating the final strain and stress state in the inclusion after exhumation from entrapment conditions (P_{trap}, T_{trap}) to the Earth's surface (P_{room}, T_{room}). A first approximation would be to consider the final strain in the inclusion as imposed only by the deformation of the cavity (i.e. the host) during the exhumation, without considering any mechanical coupling between the host and the inclusion. This is easily illustrated for the case of a cubic host for which the deformation of the three equivalent crystallographic axes of length l_i during exhumation from entrapment to room conditions is given by:

$$\left[\frac{V_h^0}{V_h^{Ttrap}}\right]^{1/3} = \frac{l_{i,h}^0}{l_{i,h}^{trap}} \tag{4.1}$$

where V_h^0 and V_h^{Ttrap} are the volume of the host at room conditions (P_{room}, T_{room}) and at entrapment (P_{trap}, T_{trap}), respectively, and $l_{i,h}^0$ and $l_{i,h}^{trap}$ are the lengths of the crystallographic axes at room conditions and at entrapment respectively.

The deformation of the cavity induces an equal deformation on the inclusion given by:

$$\left[\frac{V_h^0}{V_h^{Ttrap}}\right]^{1/3} = \frac{l_{i,inc}^{thermo}}{l_{i,inc}^{trap}} \tag{4.2}$$

where $l_{i,inc}^{trap}$ are the lengths of the crystallographic axes of the inclusion at entrapment (P_{trap}, T_{trap}). $l_{i,inc}^{thermo}$ are the lengths of the crystallographic axes of the inclusion after the deformation of the cavity and in general they are not equal to those of a free inclusion crystal at room conditions. This can be proved calculating the strain of $l_{i,inc}^{thermo}$ with respect to the length $l_{i,inc}^{0}$ of the axes of a free inclusion at room conditions. Equation (4.1) can be written as:

$$\left[\frac{V_h^0}{V_h^{Ttrap}}\right]^{1/3} = \frac{l_{i,inc}^{thermo}}{l_{i,inc}^{trap}} = \frac{l_{i,inc}^{thermo}}{l_{i,inc}^{0}} \frac{l_{i,inc}^{0}}{l_{i,inc}^{trap}} \tag{4.3}$$

from which the unrelaxed strain in the inclusion is found as:

$$\begin{aligned} \varepsilon_{ij}^{unrel} &= \frac{l_{i,inc}^{thermo}}{l_{i,inc}^{0}} - 1 = \left[\frac{V_h^0}{V_h^{Ttrap}}\right]^{1/3} \frac{l_{i,inc}^{trap}}{l_{i,inc}^{0}} - 1 \qquad for \quad i = j \\ \varepsilon_{ij}^{unrel} &= 0 \qquad for \quad i \neq j \end{aligned} \tag{4.4}$$

It follows from equation (4.4) that the normal components of the strain ε_{ii}^{unrel} are zero only when the inclusion and the host are the same mineral, or when $P_{trap} = P_{room}$ and $T_{trap} = T_{room}$. The shear components of the strain ε_{ij}^{unrel} are always zero. The same principle expressed in equation (4.3) can be applied to any host-inclusion pair with any crystallographic symmetry, by replacing the left-hand side of the equation with the lattice spacing of the direction in the host parallel to $l_{i,inc}$. When the host is at room condition its stress state is hydrostatic with $\sigma_{11} = \sigma_{22} = \sigma_{33} = P \approx 0$ GPa. On the other hand, it follows from equation (4.4) that the inclusion is under the unrelaxed strain ε^{unrel} which corresponds to a stress $\sigma^{unrel} = C_{inc}\varepsilon^{unrel}$. In this unrelaxed state (i.e. before the relaxation) the host and the inclusion are not in mechanical equilibrium, and the discontinuity in the traction at the interface between the host and the inclusion forces the elastic relaxation of the system until the mechanical equilibrium is restored, i.e. until the traction in the host and inclusion across the interface are equal. After the elastic relaxation, the system is at the final condition.

Therefore, the calculation of the residual strain and stress state in the inclusion can be divided into two steps: (i) the thermodynamic calculation of the deformation of the inclusion, forced to be equal to that of the cavity (i.e. the host), during the exhumation of the host from entrapment to room conditions; (ii) the calculation of the elastic relaxation to restore the mechanical equilibrium. The first step of the calculation is based on non-linear elasticity that takes into account explicitly the variation of the unit-cell parameters of the host and of the inclusion with both P and T. For cubic minerals this reduces to knowing the volume equation of state (the V-EoS, see equation 4.1). For

minerals with lower symmetry, but higher than monoclinic, the EoS that describe the behaviour of the unit-cell parameters must be known explicitly through their axial EoS. For the case, discussed in the following chapters, of quartz and zircon that are trigonal and tetragonal, respectively, this problem reduces to knowing the a-EoS of the a unit-cell parameter. The EoS of the b parameter is equal to that of a by symmetry, while the change in length of the c-axis at each P and T can be found as the value such that, combined with the a-EoS, gives the V (from the V-EoS) at that conditions. On the other hand, the calculation of the relaxation requires the knowledge of the unrelaxed strain state, the full elastic properties of the host and the inclusion, including their variation with direction, and the relative orientation of their crystallographic axes. As shown in the following sections, the problem of calculating the change in strain upon anisotropic relaxation can be solved analytically, but only in a few cases with specific crystallographic symmetries, or numerically.

4.2 Relaxation tensor: numerical derivation

4.2.1 Finite element analysis with a prestress in the inclusion

The change in the strain state of the inclusion due to the anisotropic relaxation can be calculated numerically with the Finite Element Method (FEM), without any restriction given by the elastic anisotropic properties of the host and of the inclusion, their reciprocal crystallographic orientation and the geometry of the system. All the proposed 3D FEM models were created and solved with Dassault Systèmes Abaqus®, a commercial software suite for finite element analysis. In our models the inclusion is spherical, sitting at the center of its host (assumed to be cubic) and with a radius at least 50 times smaller than the distance between the center of the inclusion and the external surface of the host in any direction. This ensures that the host is practically infinite with respect to the inclusion. Three concentric spherical shells surround the inclusion to allow a gradual reduction of the elements size in the portions of the model where stress gradients are higher. An iterative process was used to discretize the model with different mesh sizes (Fig. 4.1b-c). Smaller elements were used to discretize the region around and inside the inclusion while larger elements were used for the remaining part of the model. The mesh was refined in the areas with higher stress gradients until the calculated stress distribution appeared smooth. Boundary conditions were placed on the appropriate edges and faces of the models to avoid rigid body motions (Fig. 4.1d). The resulting model consisted of about 500,000 ten-node second-order tetrahedral elements (element C3D10 in the Abaqus® library).

The anisotropic elastic properties of both the host (C_{ijkl}^{host}) and the inclusion (C_{ijkl}^{inc}) are defined. Two different local reference systems, one for the host and one for the inclusion, are specified and they are oriented according to the desired relative crystallographic

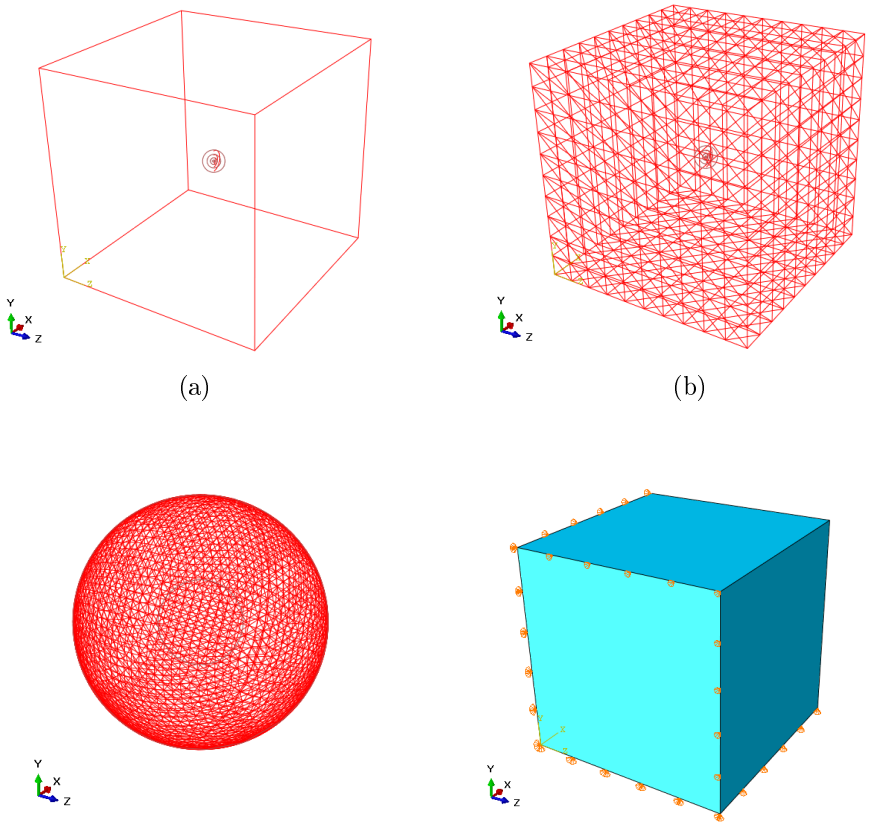

(a) (b)

(c) (d)

Figure 4.1: (a) 3D model with a spherical inclusion at the center of a host with cubic shape. The radius of the inclusion and the length of the side of the host are in the ratio 1/100. Three spherical shells surround the inclusion to allow a progressively reduction in the mesh size in the portions of the model where stress gradients are higher. (b) A coarse mesh is applied to the host. (c) Progressively finer meshes are refined in the shells around the inclusion and in the inclusion. (d) Boundary conditions of fixed displacements are applied to three of the six faces of the host.

orientation (see section 4.2.5 for further details). Since the host is at room conditions ($P \approx 0$ GPa), no face load is applied to the external surface of the host.

The aim of the FE analysis is to relax the unrelaxed strain ε_{kl}^{unrel} obtained from the thermodynamic calculation (see equation 4.4). The corresponding unrelaxed stress in the inclusion is:

$$\sigma_{ij}^{unrel} = C_{ijkl}^{inc} \varepsilon_{kl}^{unrel} \tag{4.5}$$

where C_{ijkl}^{inc} is the stiffness tensor of the inclusion.

The inclusion is pre-stressed with the stress σ_{ij}^{unrel}. In the FE model the inclusion is unstrained since no deformation has been applied to the inclusion at this stage. The analysis in Abaqus® starts with the inclusion under the specified pre-stress, but with no stress in the host. As discussed in section 4.1, this is a mechanical disequilibrium because the forces at the host/inclusion interface are not balanced. The interface will therefore move until the mechanical equilibrium is reached again forcing the elastic relaxation of the inclusion.

The static FE analysis is run with a single step. At the end of the simulation Abaqus® gives as result the components of the stress (σ^{FE}) and of the strain (ε^{FE}) in the inclusion. It is fundamental to note that in the output the strain does not correspond to the stress:

$$\sigma_{ij}^{FE} \neq C_{ijkl}^{inc} \varepsilon_{kl}^{FE} \tag{4.6}$$

The stress obtained from the FE analysis is the relaxed stress in the inclusion ($\sigma_{ij}^{FE} = \sigma_{ij}^{rel}$) and is related to the pre-stress as:

$$\sigma_{ij}^{rel} = C_{ijkl}^{inc} \varepsilon_{kl}^{FE} + \sigma_{ij}^{unrel} \tag{4.7}$$

It follows from equation (4.7) that the strain obtained from the FE analysis is the strain due to the relaxation:

$$C_{ijkl} \varepsilon_{kl}^{FE} = C_{ijkl} \varepsilon_{kl}^{rel} - C_{ijkl} \varepsilon_{kl}^{unrel} = C_{ijkl} \varepsilon_{kl}^{relaxation} \tag{4.8}$$

Therefore, since the unrelaxed strain in the inclusion (from which the pre-stress σ_{ij}^{unrel} was obtained) is known, the relaxed strain can be found as:

$$\varepsilon_{ij}^{rel} = \varepsilon_{ij}^{unrel} + \varepsilon_{ij}^{FE} \tag{4.9}$$

The strain $\varepsilon_{ij}^{relaxed}$ is the final relaxed strain in the inclusion referred to a free inclusion at room condition.

The components of all the tensors that describe the unrelaxed and relaxed strain and stress in the inclusion are specified in the local reference system of the inclusion (see section 4.2.5).

4.2.2 The relaxation matrix R_{ij}

As shown above, the relaxed strain and stress in the inclusion after the relaxation can be found numerically with a FE analysis, without any restriction given by the elastic anisotropic properties of the host and of the inclusion and their reciprocal crystallographic orientation. However, this approach is extremely time consuming and would greatly restrict the routine applicability of elastic geobarometry since a new analysis is needed for each specific initial unrelaxed or relaxed strain state, requiring hours of computational time. This can be avoided by assuming that the elastic properties of both the host and the inclusion stay constant during the relaxation. Expressing the strain states before and after relaxation as vectors in Voigt notation (see equation C.2 in Appendix C), we look for a linear mapping $f : \mathbb{R}^6 \mapsto \mathbb{R}^6$ such that:

$$f(\varepsilon^{unrel}) = \varepsilon^{rel} \tag{4.10}$$

This linear mapping can be defined through a matrix $\mathbf{R} \in \mathbb{R}^{6\times6}$. Suppose that $\{\boldsymbol{v}_1, ..., \boldsymbol{v}_6\}$ is the canonical basis of $\mathbb{R}^6$, then any element $\boldsymbol{v}$ of $\mathbb{R}^6$ can be written in a unique way as $a_1\boldsymbol{v}_1 + ... + a_6\boldsymbol{v}_6$ and

$$\begin{aligned} f(v) &= f(a_1\boldsymbol{v}_1 + ... + a_6\boldsymbol{v}_6) \\ &= a_1 f(\boldsymbol{v}_1) + ... + a_6 f(\boldsymbol{v}_6) \end{aligned} \tag{4.11}$$

Therefore the linear mapping $f : \mathbb{R}^6 \mapsto \mathbb{R}^6$ is completely determined by the vectors $f(\boldsymbol{v}_1), ..., f(\boldsymbol{v}_6)$.

The $\{f(\boldsymbol{v}_1), ..., f(\boldsymbol{v}_6)\}$ are calculated numerically with six FE analyses, performed following the procedure outlined in section 4.2.1. For each of the six analyses, a vector $\boldsymbol{v}_i$ of the basis is selected as unrelaxed strain state and the corresponding pre-stress is obtained from equation (4.5). Each analysis is run with a pre-stress and gives as a result the strain $\boldsymbol{w}_i^{FE}$ in the inclusion. The corresponding $f(\boldsymbol{v}_i)$ (i.e. the relaxed strain corresponding to the unrelaxed $\boldsymbol{v}_i$) is found as (compare with equation 4.9):

$$f(\boldsymbol{v}_i) = \boldsymbol{v}_i + \boldsymbol{w}_i^{FE} \tag{4.12}$$

The matrix $\mathbf{R} \in \mathbb{R}^{6\times6}$ with respect to the basis $\{\boldsymbol{v}_1, ..., \boldsymbol{v}_6\}$ is the matrix whose j-th column gives the coefficients of $f(\boldsymbol{v}_j)$ in terms of $\boldsymbol{v}_1, ..., \boldsymbol{v}_6$. if $\mathbf{R} = R_{ij}$

$$f(\boldsymbol{v}_j) = \sum_{i=1}^{6} R_{ij}\boldsymbol{v}_i =$$
$$= R_{1j}\begin{pmatrix}1\\0\\0\\0\\0\\0\end{pmatrix} + R_{2j}\begin{pmatrix}0\\1\\0\\0\\0\\0\end{pmatrix} + R_{3j}\begin{pmatrix}0\\0\\1\\0\\0\\0\end{pmatrix} + R_{4j}\begin{pmatrix}0\\0\\0\\1\\0\\0\end{pmatrix} + R_{5j}\begin{pmatrix}0\\0\\0\\0\\1\\0\end{pmatrix} + R_{6j}\begin{pmatrix}0\\0\\0\\0\\0\\1\end{pmatrix} \tag{4.13}$$

Since the $\{\boldsymbol{v}_1, ..., \boldsymbol{v}_6\}$ are the vectors of the canonical basis, the components of the relaxation matrix $\mathbf{R}$ can be found as:

$$\mathbf{R} = \{f(\boldsymbol{v}_1), ..., f(\boldsymbol{v}_6)\} \tag{4.14}$$

Therefore each of the six vectors $\{f(\boldsymbol{v}_1), ..., f(\boldsymbol{v}_6)\}$ obtained from the six FE analyses gives the corresponding column of the relaxation matrix $\mathbf{R}$. This matrix in general is not symmetric ($R_{ij} \neq R_{ji}$)

All the results are obtained in the local reference system of the inclusion that does not necessarily correspond to that of the host (see section 4.2.5 for further details). Therefore, also the R_{ij} components are always calculated with respect to the reference system of the inclusion. With this choice, the R_{ij} can be applied without any further transformation to "relax" the strains obtained from the thermodynamic calculation (see chapter 4.1) or to "unrelax" the strains measured experimentally by X-ray diffraction or Raman spectroscopy, before applying the thermodynamic calculation to find the entrapment conditions.

Given any unrelaxed strain vector (in Voigt notation) ε_j^{unrel} the corresponding relaxed strain is found as:

$$\varepsilon_i^{rel} = R_{ij}\varepsilon_j^{unrel} \tag{4.15}$$

On the other hand, if the relaxed strain vector (in Voigt notation) ε_j^{rel} is measured from experiments the corresponding unrelaxed strain is found applying the inverse of $\mathbf{R}$ as:

$$\varepsilon_i^{unrel} = R_{ij}^{-1}\varepsilon_j^{rel} \tag{4.16}$$

The relaxation tensor found with this procedure can only be used to convert between the unrelaxed and the relaxed strain components, but it cannot be applied directly to the conversion of stresses. The stress state can be found applying the stiffness tensor of the inclusion (C_{ijkl}) to the corresponding strain state.

4.2.3 Conversion from matrix to tensor

The relaxation matrix R_{ij} is the representation in Voigt notation of a fourth order non-symmetric tensor (R_{ijkl}) that relates the two 2^{nd}-order tensors of the strain before and after the relaxation. Here we show how the components of the matrix in Voigt notation are related to those of the fourth order tensor.

From equation (4.15), the component ε_1^{rel} (in Voigt notation) can be found as:

$$\varepsilon_1^{rel} = R_{11}\varepsilon_1^{unrel} + R_{12}\varepsilon_2^{unrel} + R_{13}\varepsilon_3^{unrel} + R_{14}\varepsilon_4^{unrel} + R_{15}\varepsilon_5^{unrel} + R_{16}\varepsilon_6^{unrel} \tag{4.17}$$

The same equation in tensor notation reads:

$$\begin{aligned}\varepsilon_{11}^{rel} =& R_{1111}\varepsilon_{11}^{unrel} + R_{1112}\varepsilon_{12}^{unrel} + R_{1113}\varepsilon_{13}^{unrel} + \\ & R_{1121}\varepsilon_{21}^{unrel} + R_{1122}\varepsilon_{22}^{unrel} + R_{1123}\varepsilon_{23}^{unrel} + \\ & R_{1131}\varepsilon_{31}^{unrel} + R_{1132}\varepsilon_{32}^{unrel} + R_{1133}\varepsilon_{33}^{unrel}\end{aligned} \tag{4.18}$$

Substituting the strain in Voigt notation in equation (4.18) we obtain:

$$\begin{aligned}\varepsilon_1^{rel} = \varepsilon_{11}^{rel} =& R_{1111}\varepsilon_1^{unrel} + R_{1112}\frac{\varepsilon_6^{unrel}}{2} + R_{1113}\frac{\varepsilon_5^{unrel}}{2} + \\ & R_{1121}\frac{\varepsilon_6^{unrel}}{2} + R_{1122}\varepsilon_2^{unrel} + R_{1123}\frac{\varepsilon_4^{unrel}}{2} + \\ & R_{1131}\frac{\varepsilon_5^{unrel}}{2} + R_{1132}\frac{\varepsilon_4^{unrel}}{2} + R_{1133}\varepsilon_3^{unrel}\end{aligned} \tag{4.19}$$

Since $\mathbf{R}$ relates two second order symmetric tensors of the strain it possesses the minor symmetries ($R_{ijkl} = R_{jikl} = R_{ijlk} = R_{jilk}$), but in general it does not possess the major symmetries ($R_{ijkl} \neq R_{klij}$). From the comparison of equations (4.17) and (4.19) it follows that:

$$\begin{aligned} R_{1111} &= R_{11} & \frac{R_{1132} + R_{1123}}{2} &= R_{1132} = R_{14} \\ R_{1122} &= R_{12} & \frac{R_{1131} + R_{1113}}{2} &= R_{1131} = R_{15} \\ R_{1133} &= R_{13} & \frac{R_{1121} + R_{1112}}{2} &= R_{1121} = R_{16} \end{aligned} \tag{4.20}$$

The same approach can be applied to calculate the component $\varepsilon_{12}^{unrel} = \varepsilon_6^{unrel}$ of the unrelaxed strain. In Voigt notation we have:

$$\varepsilon_6^{rel} = R_{61}\varepsilon_1^{unrel} + R_{62}\varepsilon_2^{unrel} + R_{63}\varepsilon_3^{unrel} + R_{64}\varepsilon_4^{unrel} + R_{65}\varepsilon_5^{unrel} + R_{66}\varepsilon_6^{unrel} \tag{4.21}$$

The same equation in tensor notation becomes:

$$\begin{aligned} \varepsilon_{12}^{rel} =& R_{1211}\varepsilon_{11}^{unrel} + R_{1212}\varepsilon_{12}^{unrel} + R_{1213}\varepsilon_{13}^{unrel} + \\ & R_{1221}\varepsilon_{21}^{unrel} + R_{1222}\varepsilon_{22}^{unrel} + R_{1223}\varepsilon_{23}^{unrel} + \\ & R_{1231}\varepsilon_{31}^{unrel} + R_{1232}\varepsilon_{32}^{unrel} + R_{1233}\varepsilon_{33}^{unrel} \end{aligned} \tag{4.22}$$

Substituting the strain in Voigt notation in equation (4.22) we obtain:

$$\begin{aligned} \varepsilon_6^{rel} = 2\varepsilon_{12}^{rel} =& 2R_{1211}\varepsilon_1^{unrel} + 2R_{1212}\frac{\varepsilon_6^{unrel}}{2} + 2R_{1213}\frac{\varepsilon_5^{unrel}}{2} + \\ & 2R_{1221}\frac{\varepsilon_6^{unrel}}{2} + 2R_{1222}\varepsilon_2^{unrel} + 2R_{1223}\frac{\varepsilon_4^{unrel}}{2} + \\ & 2R_{1231}\frac{\varepsilon_5^{unrel}}{2} + 2R_{1232}\frac{\varepsilon_4^{unrel}}{2} + 2R_{1233}\varepsilon_3^{unrel} = \\ & 2R_{1211}\varepsilon_1^{unrel} + R_{1212}\varepsilon_6^{unrel} + R_{1213}\varepsilon_5^{unrel} + \\ & R_{1221}\varepsilon_6^{unrel} + 2R_{1222}\varepsilon_2^{unrel} + R_{1223}\varepsilon_4^{unrel} + \\ & R_{1231}\varepsilon_5^{unrel} + R_{1232}\varepsilon_4^{unrel} + 2R_{1233}\varepsilon_3^{unrel} \end{aligned} \tag{4.23}$$

From the comparison of equations (4.21) and (4.23), and knowing that $\mathbf{R}$ possesses the minor symmetries, it follows that:

$$
\begin{aligned}
2R_{1211} &= R_{61} & \qquad R_{1232} + R_{1223} &= 2R_{1232} = R_{64} \\
2R_{1222} &= R_{62} & \qquad R_{1231} + R_{1213} &= 2R_{1231} = R_{65} \\
2R_{1233} &= R_{63} & \qquad R_{1221} + R_{1212} &= 2R_{1221} = R_{66}
\end{aligned}
\tag{4.24}
$$

The same procedure can be extended to all the other components of the unrelaxed strain. The relations between all the components of the relaxation tensor $\mathbf{R}$ in tensor and Voigt notation are reported in Table 4.1.

Table 4.1: Relations to convert the components of the relaxation tensor $\mathbf{R}$ *from tensor to Voigt notation.*

	R_{i1}	R_{i2}	R_{i3}	R_{i4}	R_{i5}	R_{i6}
R_{1j}	R_{1111}	R_{1122}	R_{1133}	R_{1132}	R_{1131}	R_{1121}
R_{2j}	R_{2211}	R_{2222}	R_{2233}	R_{2232}	R_{2231}	R_{2221}
R_{3j}	R_{3311}	R_{3322}	R_{3333}	R_{3332}	R_{3331}	R_{3321}
R_{4j}	$2R_{2311}$	$2R_{2322}$	$2R_{2333}$	$2R_{2332}$	$2R_{2331}$	$2R_{2321}$
R_{5j}	$2R_{1311}$	$2R_{1322}$	$2R_{1333}$	$2R_{1332}$	$2R_{1331}$	$2R_{1321}$
R_{6j}	$2R_{1211}$	$2R_{1222}$	$2R_{1233}$	$2R_{1232}$	$2R_{1231}$	$2R_{1221}$

4.2.4 Proof that R_{ijkl} is a tensor

A tensor represents a physical quantity independently of the particular choice of reference axes $\boldsymbol{X}_i$. However, the components of a tensor express that physical quantity with respect to a specific set of axes $\boldsymbol{X}_i$ and therefore they must change with another choice of the reference axes, even if the physical quantity does not change. The components of tensors of the second and of the fourth order transform according to (Nye, 1985)

$$\varepsilon'_{ij} = a_{ik} a_{jl} \varepsilon_{kl} \tag{4.25}$$

$$R'_{ijkl} = a_{im} a_{jn} a_{kp} a_{lq} R_{mnpq} \tag{4.26}$$

where $\mathbf{a}$ is the transformation matrix, $\mathbf{R}$ is the initial tensor and $\mathbf{R}'$ is the tensor after the transformation. Equations (4.25) and (4.26) can be used as a definition of tensor (Nye, 1985). For the case of the relaxation tensor, if the 81 coefficients of R_{ijkl} transform according to equation (4.26) and for any choice of reference axes they relate the components of two second order tensors in linear relationships, the R_{ijkl} form a fourth order tensor.

To show that equation (4.26) holds for the relaxation tensor we take the example of a quartz inclusion in a pyrope host that share the same orientation ($\boldsymbol{a}_{qtz} || \boldsymbol{a}_{pyr} || \boldsymbol{X}_1$,

$\boldsymbol{c}_{qtz}||\boldsymbol{c}_{pyr}||\boldsymbol{X}_3$). The components of the relaxation tensor expressed in Voigt notation are:

$$R_{ij} = \begin{pmatrix} 0.7324 & 0.0348 & 0.0242 & -0.0933 & 1.8275 & 1.6470 \\ 0.2588 & 0.5085 & 0.0242 & 1.4515 & 0.3566 & 1.3924 \\ 0.2245 & -0.1965 & 0.6985 & 1.2767 & 1.6714 & 0.0293 \\ -0.0268 & 0.0268 & 0 & 0.8376 & -0.2337 & -0.1368 \\ -0.0111 & 0.0111 & 0 & -0.0674 & 0.7059 & -0.1569 \\ -0.0113 & 0.0113 & 0 & -0.0686 & -0.2250 & 0.7714 \end{pmatrix}$$

Given any unrelaxed strain, the final relaxed strain can be found as $\varepsilon_i^{rel} = R_{ij}\varepsilon_j^{unrel}$. For example:

$$\varepsilon_j^{unrel} = \begin{pmatrix} -0.1 \\ -0.2 \\ -0.3 \\ -0.4 \\ -0.5 \\ -0.6 \end{pmatrix} \qquad \varepsilon_i^{rel} = R_{ij}\varepsilon_j^{unrel} = \begin{pmatrix} -1.95211 \\ -1.72916 \\ -1.55663 \\ -0.13883 \\ -0.23295 \\ -0.32400 \end{pmatrix}$$

The reference system is transformed according to the following transformation matrix:

$$a_{ij} = \begin{pmatrix} 0.5567 & -0.3144 & 0.7689 \\ 0.6634 & 0.7254 & -0.1837 \\ -0.5000 & 0.6124 & 0.6124 \end{pmatrix}$$

Note that the transformation must be applied to the components in tensor notation and not in Voigt notation (see equation 4.26). Therefore the $\mathbf{R}$ matrix and the $\boldsymbol{\varepsilon^{rel}}$ and $\boldsymbol{\varepsilon^{unrel}}$ strain vectors must be converted back to the original tensor notation before applying the transformation.

The components R'_{ijkl} of the relaxation tensor with respect to the new orientation of the reference system can be found from equation 4.26. In Voigt notation they become:

$$R'_{ij} = \begin{pmatrix} 1.5785 & -0.0256 & -0.7998 & 1.0247 & 0.4437 & 1.4051 \\ -0.0007 & 1.7655 & -0.9756 & 0.6942 & 0.9058 & 1.2150 \\ 0.2272 & 0.3144 & 0.2255 & 0.8760 & 0.6910 & 1.4376 \\ -1.6514 & 0.0536 & 1.6124 & 0.2737 & 0.3552 & 0.1935 \\ 0.3642 & -1.6411 & 1.2158 & 0.2149 & 0.1659 & 0.3139 \\ 0.7737 & 0.5941 & -1.3495 & 0.0797 & -0.0793 & 0.2453 \end{pmatrix}$$

The same transformation is applied to the strain. The components $\varepsilon_{ij}^{unrel'}$ and $\varepsilon_{ij}^{rel'}$ of the strain tensors with respect to the new orientation of the reference system are found through equation (4.25). In Voigt notation they are:

$$\varepsilon_j^{unrel'} = \begin{pmatrix} -0.24044 \\ -0.33387 \\ -0.02570 \\ -0.45172 \\ -0.53825 \\ -0.46515 \end{pmatrix} \qquad \varepsilon_i^{rel'} \begin{pmatrix} -1.70568 \\ -1.93049 \\ -1.60173 \\ -0.06711 \\ 0.09671 \\ -0.45711 \end{pmatrix}$$

If $\mathbf{R}$ is a tensor and transforms according to equation (4.26), the components of the relaxed strain in the new reference system can be also found as $\varepsilon_i^{rel''} = R'_{ij}\varepsilon_j^{unrel'}$ and $\varepsilon_i^{rel''}$ must be equal to $\varepsilon_i^{rel'}$ found above as transformation of the initial unrelaxed strain. This can be proved numerically in our example:

$$\varepsilon_i^{rel'} = \varepsilon_i^{rel''} = R'_{ij}\varepsilon_j^{unrel'} = \begin{pmatrix} -1.70568 \\ -1.93049 \\ -1.60173 \\ -0.06711 \\ 0.09671 \\ -0.45711 \end{pmatrix}$$

4.2.5 Reciprocal crystallographic orientation of the host and the inclusion

In the general case, when there are no simplifications given by the crystallographic symmetry of the host and of the inclusion (i.e. both the host and the inclusion are elastically anisotropic), one $\mathbf{R}$ tensor is only valid for a specific reciprocal orientation between the host and the inclusion. The components of $\mathbf{R}$ must be recalculated for another orientation. To handle the reciprocal orientations of the host and of the inclusion, five sets of reference system axis must be considered during the calculation: two sets of crystallographic axes (for the host and the inclusion), two sets of orthonormal axes in which the components of the elastic tensors are written (for the host and the inclusion), and one set of orthonormal axes to express the global reference system of the FE model. The crystallographic axes of the host and of the inclusion are defined by their directions ***a*, *b*, *c***. The components of the tensors that represent the physical properties of crystals are defined with respect to a set of Cartesian axes (in our notation $\boldsymbol{Ox}^h$, $\boldsymbol{Oy}^h$, $\boldsymbol{Oz}^h$ for the host and $\boldsymbol{Ox}^i$, $\boldsymbol{Oy}^i$, $\boldsymbol{Oz}^i$ for the inclusion). The orientation

of the $\boldsymbol{Ox}$, $\boldsymbol{Oy}$, $\boldsymbol{Oz}$ in relation to the $\boldsymbol{a}$, $\boldsymbol{b}$, $\boldsymbol{c}$ of the crystal is a convention. For each mineral we follow the convention that was assumed at the moment of the experimental determination of its stiffness tensor C_{ijkl}, and we maintain it for all of our calculations. This convention is usually reported together with the experimental results, because the components C_{ijkl} are expressed in terms of the chosen orientation of the reference system $\boldsymbol{Ox}$, $\boldsymbol{Oy}$, $\boldsymbol{Oz}$. The FE model is designed with respect to a Cartesian reference system $\boldsymbol{X}$, $\boldsymbol{Y}$, $\boldsymbol{Z}$ that is assumed to be the global reference system since the geometry and the property tensors of the minerals defined in the analysis are referred to it. The reciprocal orientation between the host and the inclusion is also expressed in the global reference system $\boldsymbol{X}, \boldsymbol{Y}, \boldsymbol{Z}$. Since the absolute orientation of the two minerals in the system is not relevant, a convenient way to proceed is to assume that the $\boldsymbol{Ox}^h$, $\boldsymbol{Oy}^h$, $\boldsymbol{Oz}^h$ are parallel to the global $\boldsymbol{X}$, $\boldsymbol{Y}$, $\boldsymbol{Z}$, while the local reference system of the inclusion ($\boldsymbol{Ox}^i$, $\boldsymbol{Oy}^i$, $\boldsymbol{Oz}^i$) is free to have any orientation imposed by the user. The orientation of the $\boldsymbol{Ox}^i$, $\boldsymbol{Oy}^i$, $\boldsymbol{Oz}^i$ with respect to the $\boldsymbol{X}$, $\boldsymbol{Y}$, $\boldsymbol{Z}$ (and therefore with respect to the $\boldsymbol{Ox}^h$, $\boldsymbol{Oy}^h$, $\boldsymbol{Oz}^h$ of the host) is defined by a rotation matrix.
Before the FE analysis the components of the stiffness tensor of the inclusion C_{ijkl}^{inc} and those of the pre-stress to be applied to the inclusion are first transformed to the global reference system $\boldsymbol{X}$, $\boldsymbol{Y}$, $\boldsymbol{Z}$ (for the choice we made above, the C_{ijkl}^{host} of the host are already expressed in the global reference system). After the FE analysis, the output tensors (strain and stress) must be converted back to the initial local reference system of the inclusion (i.e. the $\boldsymbol{Ox}^i$, $\boldsymbol{Oy}^i$, $\boldsymbol{Oz}^i$). This procedure can be performed automatically in FE softwares such as Abaqus®, or externally during the pre- and the post-processing (for example with Matlab®). The $\mathbf{R}$ tensor is calculated from the components of the relaxed strain (see section 4.2.1) expressed in the local reference system of the inclusion. With this choice the $\mathbf{R}$ tensor (and its inverse) can be directly applied to "relax" or "unrelax" the components of the strain in the inclusion that are also expressed in the system $\boldsymbol{Ox}^i$, $\boldsymbol{Oy}^i$, $\boldsymbol{Oz}^i$.

4.3 The Eshelby's approach

John D. Eshelby in 1957 (Eshelby, 1957) proposed a thought experiment to determine the possible stress, strain, and displacement fields in a linear elastic body containing an inclusion. In particular, he considered the situation in which the inclusion has undergone a transformation (such as twinning or localized thermal expansion) but its change in shape and size are restricted because of the surrounding material. In that situation, the inclusion and the surrounding material remains in a stressed state and the strain states in the body and the inclusion are potentially inhomogeneous and complicated. Eshelby found that the resulting elastic field can be found using a "sequence of imaginary cutting, straining and welding operations" (Eshelby, 1957), and he proposed analytical solutions for the case of an ellipsoidal inclusion. This situation

is analogous to the calculation of the elastic relaxation. In our approach for elastic geobarometry (outlined in section 4.1) we first imagine that during the exhumation the host constrains the change in shape and size of the inclusion, and when the host is at room conditions the inclusion is deformed and stressed (unrelaxed state). The aim is to calculate the final ("relaxed") elastic strain state in the inclusion. We will outline the approach proposed by Eshelby (1957) following the derivation reported by Weinberger et al. (2005). We will also show the analogies with our method based on FE (section 4.2).

4.3.1 The inclusion problem: Eshelby tensor

In this approach a region of an infinite homogeneous isotropic elastic medium (the inclusion) undergoes a deformation that leads to a state of internal stress. The inclusion is defined by its volume V^{inc} and its surface area S^{inc} and is surrounded by a matrix. Both the inclusion and the matrix have the same elastic properties. The aim is to find the final elastic state (stress and strain field) of the inclusion and of the matrix. The problem is solved in a series of imaginary steps where the inclusion is removed form the matrix, deformed and put back into the matrix, applying the superposition principle of linear elasticity.

Step 1. The inclusion is removed from the matrix. The inclusion will assume a uniform strain ε^*_{ij} (referred to the initial constrained state) but will experience no stress. The uniform strain state ε^*_{ij} is called the *eigenstrain*. In this step the matrix is under no strain and stress.

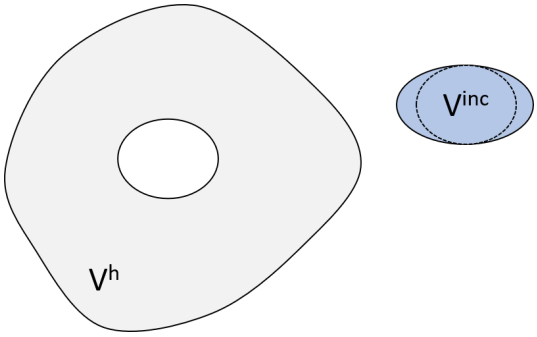

Figure 4.2: Step 1

Step 2. A surface traction is applied to the surface S^{inc} to deform the inclusion to its original shape. The elastic strain applied on the inclusion is $\varepsilon^{el}_{ij} = -\varepsilon^*_{ij}$ and exactly cancels the eigenstrain. Therefore, at this stage the strain field in the inclusion is:

$$\varepsilon_{ij} = \varepsilon^{el}_{ij} + \varepsilon^*_{ij} = 0 \tag{4.27}$$

The inclusion is in a state of internal stress:

$$\sigma_{ij}^{el} = C_{ijkl}\varepsilon_{kl}^{el} = -\sigma_{ij}^{*} = -C_{ijkl}\varepsilon_{kl}^{*} \tag{4.28}$$

where $C_{ijkl} = C_{ijkl}^{host} = C_{ijkl}^{inc}$ is the stiffness tensor of the host and of the inclusion since they are the same material. The traction force applied to S^{inc} is $T_j = -\sigma_{ij}^{*} n_i$, where n_i is the normal to the surface.

This situation corresponds to that expressed in equation (4.5), under the assumption that the host and the inclusion are the same material. Therefore:

$$\sigma_{ij}^{el} = C_{ijkl}\varepsilon_{kl}^{el} = \sigma_{ij}^{unrel}$$

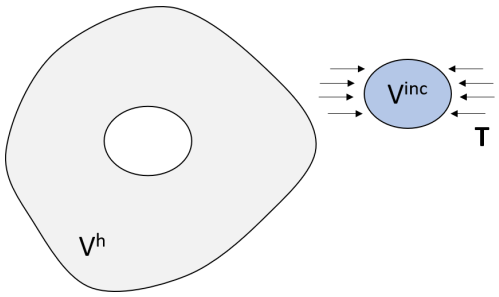

Figure 4.3: Step 2

Step 3. The inclusion is put back into the matrix. No change in the strain and stress fields with respect to step 2

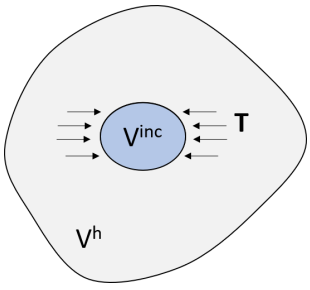

Figure 4.4: Step 3

Step 4. The traction T is removed, and we go back to the initial problem. This is equivalent to applying a cancelling body force $\boldsymbol{F} = -\boldsymbol{T}$ to the internal surface S^{inc}

of the inclusion. In this step the strain field in the inclusion is $\varepsilon_{ij}^{c} \neq \varepsilon_{ij}^{el}$. Note that ε_{ij}^{c} is the final relaxed strain in the inclusion taking the initial constrained state of the inclusion as the undeformed state.

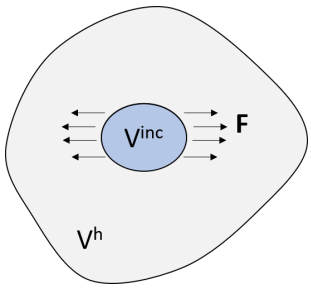

Figure 4.5: Step 4

The final strain state in the inclusion referred to a free crystal is:

$$\varepsilon_{ij} = \varepsilon_{ij}^{c} - \varepsilon_{ij}^{*} = \varepsilon_{ij}^{c} + \varepsilon_{ij}^{el} \tag{4.29}$$

and the corresponding stress field is:

$$\sigma_{ij} = C_{ijkl}(\varepsilon_{kl}^{c} + \varepsilon_{kl}^{el}) \tag{4.30}$$

where $C_{ijkl} = C_{ijkl}^{host} = C_{ijkl}^{inc}$ is the stiffness tensor of the host and of the inclusion. This situation corresponds to that described by equation (4.7) when the host and the inclusion are the same material: the stress found with equation (4.30) is the relaxed stress in the inclusion (σ_{ij}^{rel}), while ε_{kl}^{c} corresponds to the strain obtained from the FE analysis (ε_{kl}^{FE}).

Eshelby (1957) demonstrated that a fourth order tensor (the Eshelby tensor) can be introduced to relate the constrained strain in the inclusion to the eigenstrain:

$$\varepsilon_{ij}^{c} = S_{ijkl}\varepsilon_{kl}^{*} \tag{4.31}$$

The Eshelby tensor is a fourth order tensor with minor symmetries because it relates two symmetric second order tensors

$$S_{ijkl} = S_{jikl} = S_{ijlk} = S_{jilk}$$

but it does not possess the major symmetries

$$S_{ijkl} \neq S_{klij}$$

It should be noted that for an ellipsoidal inclusion in an homogeneous infinite matrix the Eshelby tensor is a constant tensor and therefore the stress and strain fields in the inclusion are uniform.

4.3.2 The inhomogeneity problem

In the applications of elastic geobarometry we are interested in the situation where the inclusion has different elastic properties with respect to the host. In the original work of Eshelby (1957) the inclusion with different properties with respect to the host is called an inhomogeneity. The inhomogeneity problem can be defined when the inhomogeneity has a general shape but it can be solved using the Eshelby's equivalent inclusion method only when the inhomogeneity is an ellipsoid (Eshelby, 1957).

The idea is to replace the inhomogeneity with an inclusion (the equivalent inclusion) whose eigenstrain is chosen such that the stress and the strain fields in the inclusion are equal to those in the inhomogeneity. In the following discussion all the properties referred to the inhomogeneity will be identified with '.

The final stress inside the inhomogeneity is (see equation 4.30):

$$\sigma_{ij}^{'} = C'_{ijkl}(\varepsilon_{kl}^{c'} - \varepsilon_{kl}^{*'}) = \sigma_{ij}^{c'} - \sigma_{ij}^{*'} \tag{4.32}$$

where C'_{ijkl} is the stiffness tensor of the inhomogeneity, that might be different from that of the matrix. This situation corresponds to that described by equation (4.7) under the assumption that the host and the inclusion are different materials, with:

$$\begin{aligned} \sigma_{ij}^{'} &= \sigma_{ij}^{rel} \\ \varepsilon_{kl}^{c'} &= \varepsilon_{kl}^{FE} \\ -\varepsilon_{kl}^{*'} &= \varepsilon_{kl}^{unrel} \end{aligned}$$

The stress in the equivalent inclusion is:

$$\sigma_{ij} = C_{ijkl}(\varepsilon_{kl}^{c} - \varepsilon_{kl}^{*}) = \sigma_{ij}^{c} - \sigma_{ij}^{*} \tag{4.33}$$

where C_{ijkl} is the stiffness tensor of the equivalent inclusion that is equal to that of the matrix.

The stress in the inhomogeneity and in the inclusion must be equal, therefore:

$$C'_{ijkl}(\varepsilon^{c'}_{kl} - \varepsilon^{*'}_{kl}) = C_{ijkl}(\varepsilon^{c}_{kl} - \varepsilon^{*}_{kl}) \tag{4.34}$$

Applying the Eshelby tensor we have that $\varepsilon^{c}_{ij} = S_{ijkl}\varepsilon^{*}_{kl}$ and therefore:

$$[(C^{'}_{ijkl} - C_{ijkl})S_{klmn} + C_{ijmn}]\varepsilon^{*}_{mn} = C^{'}_{ijkl}\varepsilon^{*'}_{kl} \tag{4.35}$$

from which the equivalent strain in the inclusion ε^{*}_{mn} can be found in terms of the eigenstrain of the inhomogeneity ($\varepsilon^{*'}_{kl}$). Rearranging equation (4.35) we can find another fourth order tensor (D_{ijkl}) that relates the equivalent strain in the inclusion ε^{*}_{ij} to the eigenstrain of the inhomogeneity ($\varepsilon^{*'}_{kl}$) :

$$\varepsilon^{*}_{ij} = [(C^{'}_{ijmn} - C_{ijmn})S_{mnpq} + C_{ijpq}]^{-1}C^{'}_{pqkl}\varepsilon^{*'}_{kl} = D_{ijkl}\varepsilon^{*'}_{kl} \tag{4.36}$$

The strain in the inhomogeneity is equal to that in the equivalent inclusion:

$$\varepsilon^{c'}_{ij} = \varepsilon^{c}_{ij} = S_{ijkl}\varepsilon^{*}_{kl} = S_{ijkl}D_{klmn}\varepsilon^{*'}_{mn} \tag{4.37}$$

Note that $\varepsilon^{c'}$ is the strain in the inhomogeneity referred to the initial constrained state. The final relaxed strain state in the inhomogeneity referred to the undeformed state at room condition is (compare with equation 4.9):

$$\varepsilon^{rel}_{ij} = \varepsilon^{c'}_{ij} - \varepsilon^{*'}_{ij} \tag{4.38}$$

Therefore, equations (4.37 - 4.38) can be rearranged into an equation that relates the eigenstrain in the homogeneity ($\varepsilon^{*'}_{ij} = -\varepsilon^{unrel}_{ij}$) to the corresponding final relaxed strain state referred to the undeformed state at room condition.

$$\varepsilon^{rel}_{ij} = S_{ijkl}D_{klmn}\varepsilon^{*'}_{mn} - \varepsilon^{*'}_{mn} = (I_{ijmn} - S_{ijkl}D_{klmn})\varepsilon^{unrel}_{mn} \tag{4.39}$$

Where I_{ijmn} is the fourth order identity tensor. Therefore the relaxation tensor can be found analytically as:

$$R^{an}_{ijmn} = (I_{ijmn} - S_{ijkl}D_{klmn}) \tag{4.40}$$

The relation expressed by equation (4.39) corresponds to equation (4.9), where ε^{FE}_{ij} was found numerically with FE. The possibility of using practically equations (4.39)

and (4.40) and solve analytically for the components of $\mathbf{R}^{an}$ however is limited by the computation of the Eshelby tensor $\mathbf{S}$, since its components can be found analytically only for ellipsoidal inclusions and only for specific crystallographic symmetry of the host, such as transversely isotropic materials (Parnell, 2016) that belong to the hexagonal crystal system. With these restrictions, even assuming a spherical shape of the inclusion, the relaxation tensor cannot be calculated for host minerals typical in high-pressure metamorphic rocks (e.g. garnets, zircon...). Therefore, the numerical solution base on FE must be applied. To check the reliability of $\mathbf{R}^{FE}$ as obtained from FE, in Chapter 5 the analytical and the numerical solutions will be compared for several cases for which the analytical $\mathbf{R}^{an}$ can be calculated (e.g. for an ideal isotropic host).

Chapter 5

Test of the anisotropic relaxation tensor R

As shown in section 4.2 the relaxation tensor can be calculated numerically with a set of six FE analysis. The calculated $\mathbf{R}^{FE}$ therefore is strongly dependent on the accuracy of the FE model (i.e. the geometry, the choice of the boundary conditions with respect to the symmetry elements of the host and of the inclusion...). To test the reliability of our FE models that generated the $\mathbf{R}^{FE}$ tensor, in this chapter we compare the analytical and the numerical solutions for several cases for which the analytical $\mathbf{R}^{an}$ can be calculated. To this aim we compare the relaxation calculated applying three different approaches, starting from the same unrelaxed strain state. The first approach consists in performing a FE analysis with a pre-stress in the inclusion corresponding to the unrelaxed strain state (see section 4.2.1 and equation 4.5). In the other two approaches the relaxed strain states are calculated applying respectively the R_{ij}^{an} and the R_{ij}^{FE} to the unrelaxed strain.

5.1 Elastically isotropic host

For a spherical inclusion in a isotropic materials the Eshelby's tensor is expressed as (Weinberger et al., 2005):

$$S_{ijkl} = \frac{5\nu - 1}{15(1-\nu)}\delta_{ij}\delta_{kl} + \frac{4 - 5\nu}{15(1-\nu)}\left(\delta_{ik}\delta_{jl} + \delta_{il}\delta_{jk}\right) \tag{5.1}$$

where ν is the Poisson's ratio of the host

The components in Voigt notation of the Eshelby tensor for isotropic pyrope (properties in Table B.6) are:

$$\mathbf{S} = \begin{pmatrix} 0.51327 & 0.02655 & 0.02655 & 0.00000 & 0.00000 & 0.00000 \\ 0.02655 & 0.51327 & 0.02655 & 0.00000 & 0.00000 & 0.00000 \\ 0.02655 & 0.02655 & 0.51327 & 0.00000 & 0.00000 & 0.00000 \\ 0.00000 & 0.00000 & 0.00000 & 0.48673 & 0.00000 & 0.00000 \\ 0.00000 & 0.00000 & 0.00000 & 0.00000 & 0.48673 & 0.00000 \\ 0.00000 & 0.00000 & 0.00000 & 0.00000 & 0.00000 & 0.48673 \end{pmatrix} \tag{5.2}$$

5.1.1 Elastically isotropic inclusion

The components of the analytical $\mathbf{R}^{an}$ tensor for an ideally isotropic quartz inclusion in isotropic pyrope can be calculated from equation 4.40, knowing the Eshelby tensor reported in equation (5.2) and the isotropic elastic constants of quartz reported in Table B.9:

$$\mathbf{R}^{an} = \begin{pmatrix} 0.71884 & 0.02626 & 0.02626 & 0.00000 & 0.00000 & 0.00000 \\ 0.02626 & 0.71884 & 0.02626 & 0.00000 & 0.00000 & 0.00000 \\ 0.02626 & 0.02626 & 0.71884 & 0.00000 & 0.00000 & 0.00000 \\ 0.00000 & 0.00000 & 0.00000 & 0.69258 & 0.00000 & 0.00000 \\ 0.00000 & 0.00000 & 0.00000 & 0.00000 & 0.69258 & 0.00000 \\ 0.00000 & 0.00000 & 0.00000 & 0.00000 & 0.00000 & 0.69258 \end{pmatrix}$$

Using the same elastic properties, the numerical $\mathbf{R}$ can be obtained from FE:

$$\mathbf{R}^{FE} = \begin{pmatrix} 0.71886 & 0.02625 & 0.02625 & 0.00000 & 0.00000 & 0.00000 \\ 0.02625 & 0.71886 & 0.02625 & 0.00000 & 0.00000 & 0.00000 \\ 0.02625 & 0.02625 & 0.71886 & 0.00000 & 0.00000 & 0.00000 \\ 0.00000 & 0.00000 & 0.00000 & 0.69261 & 0.00000 & 0.00000 \\ 0.00000 & 0.00000 & 0.00000 & 0.00000 & 0.69261 & 0.00000 \\ 0.00000 & 0.00000 & 0.00000 & 0.00000 & 0.00000 & 0.69261 \end{pmatrix}$$

The discrepancy between the components of R_{ij}^{an} and R_{ij}^{FE} is less than 0.05%.

Test on strain

The relaxed strain was calculated for several initial unrelaxed strain states applying the three approaches outlined above. Results are compared in Table 5.1. All the three approaches lead to the same results with discrepancies on the strain components lower than 10^{-6}, both when the unrelaxed strain is isotropic (Test 1) or deviatoric with shear components different from zero (Test 2).

Table 5.1: Relaxed strain for isotropic quartz in isotropic pyrope.

	Unrelaxed strain	Relaxed strain (FE calculation)	Relaxed strain (R^{an})	Relaxed strain (R^{FE})
Test 1	$\varepsilon_i = \begin{pmatrix} -0.010000 \\ -0.010000 \\ -0.010000 \\ 0.000000 \\ 0.000000 \\ 0.000000 \end{pmatrix}$	$\varepsilon_i = \begin{pmatrix} -0.007714 \\ -0.007714 \\ -0.007714 \\ 0.000000 \\ 0.000000 \\ 0.000000 \end{pmatrix}$	$\varepsilon_i = \begin{pmatrix} -0.007714 \\ -0.007714 \\ -0.007714 \\ 0.000000 \\ 0.000000 \\ 0.000000 \end{pmatrix}$	$\varepsilon_i = \begin{pmatrix} -0.007714 \\ -0.007714 \\ -0.007714 \\ 0.000000 \\ 0.000000 \\ 0.000000 \end{pmatrix}$
Test 2	$\varepsilon_i = \begin{pmatrix} -0.000658 \\ -0.001795 \\ -0.002931 \\ -0.013636 \\ -0.011364 \\ -0.009091 \end{pmatrix}$	$\varepsilon_i = \begin{pmatrix} -0.000597 \\ -0.001384 \\ -0.002171 \\ -0.009445 \\ -0.007871 \\ -0.006296 \end{pmatrix}$	$\varepsilon_i = \begin{pmatrix} -0.000597 \\ -0.001384 \\ -0.002171 \\ -0.009444 \\ -0.007870 \\ -0.006296 \end{pmatrix}$	$\varepsilon_i = \begin{pmatrix} -0.000597 \\ -0.001384 \\ -0.002171 \\ -0.009445 \\ -0.007871 \\ -0.006296 \end{pmatrix}$

5.1.2 Elastically anisotropic inclusion

The components of the analytical $\mathbf{R}^{an}$ tensor for an elastically anisotropic quartz inclusion in isotropic pyrope can be calculated from equation 4.40, knowing the Eshelby tensor reported in equation (5.2) and the anisotropic elastic constants of quartz reported in Table B.7:

$$\mathbf{R}^{an} = \begin{pmatrix} 0.74247 & 0.02459 & 0.02435 & -0.03048 & 0.00000 & 0.00000 \\ 0.02459 & 0.74247 & 0.02435 & 0.03048 & 0.00000 & 0.00000 \\ 0.01411 & 0.01411 & 0.69817 & 0.00000 & 0.00000 & 0.00000 \\ -0.06096 & 0.06096 & 0.00000 & 0.63008 & 0.00000 & 0.00000 \\ 0.00000 & 0.00000 & 0.00000 & 0.00000 & 0.63008 & -0.06096 \\ 0.00000 & 0.00000 & 0.00000 & 0.00000 & -0.06096 & 0.71788 \end{pmatrix}$$

Using the same elastic properties, the numerical **R** can be obtained from FE:

$$\mathbf{R}^{FE} = \begin{pmatrix} 0.74249 & 0.02458 & 0.02434 & -0.03048 & 0.00000 & 0.00000 \\ 0.02458 & 0.74249 & 0.02434 & 0.03048 & 0.00000 & 0.00000 \\ 0.01410 & 0.01410 & 0.69819 & 0.00000 & 0.00000 & 0.00000 \\ -0.06096 & 0.06096 & 0.00000 & 0.63012 & 0.00000 & 0.00000 \\ 0.00000 & 0.00000 & 0.00000 & 0.00000 & 0.63012 & -0.06096 \\ 0.00000 & 0.00000 & 0.00000 & 0.00000 & -0.06096 & 0.71791 \end{pmatrix}$$

The discrepancy between the components of R_{ij}^{an} and R_{ij}^{FE} is less than 0.05%.

Test on strain

The relaxed strain was calculated for several initial unrelaxed strain states applying the three approaches outlined above. Results are compared in Table 5.2. All the three approaches always lead to the same results with discrepancies on the strain components lower than 10^{-6}.

Table 5.2: Relaxed strain for anisotropic quartz in isotropic pyrope.

	Unrelaxed strain	Relaxed strain (FE calculation)	Relaxed strain (R^{an})	Relaxed strain (R^{FE})
Test 1	$\varepsilon_i = \begin{pmatrix} -0.010000 \\ -0.010000 \\ -0.010000 \\ 0.000000 \\ 0.000000 \\ 0.000000 \end{pmatrix}$	$\varepsilon_i = \begin{pmatrix} -0.007914 \\ -0.007914 \\ -0.007264 \\ 0.000000 \\ 0.000000 \\ 0.000000 \end{pmatrix}$	$\varepsilon_i = \begin{pmatrix} -0.007914 \\ -0.007914 \\ -0.007264 \\ 0.000000 \\ 0.000000 \\ 0.000000 \end{pmatrix}$	$\varepsilon_i = \begin{pmatrix} -0.007914 \\ -0.007914 \\ -0.007264 \\ 0.000000 \\ 0.000000 \\ 0.000000 \end{pmatrix}$
Test 2	$\varepsilon_i = \begin{pmatrix} -0.002100 \\ -0.002100 \\ -0.002900 \\ 0.000000 \\ 0.000000 \\ 0.000000 \end{pmatrix}$	$\varepsilon_i = \begin{pmatrix} -0.001681 \\ -0.001681 \\ -0.002084 \\ 0.000000 \\ 0.000000 \\ 0.000000 \end{pmatrix}$	$\varepsilon_i = \begin{pmatrix} -0.001681 \\ -0.001681 \\ -0.002084 \\ 0.000000 \\ 0.000000 \\ 0.000000 \end{pmatrix}$	$\varepsilon_i = \begin{pmatrix} -0.001681 \\ -0.001681 \\ -0.002084 \\ 0.000000 \\ 0.000000 \\ 0.000000 \end{pmatrix}$
Test 3	$\varepsilon_i = \begin{pmatrix} -0.001000 \\ -0.003000 \\ -0.005000 \\ -0.012000 \\ -0.004000 \\ -0.008000 \end{pmatrix}$	$\varepsilon_i = \begin{pmatrix} -0.000572 \\ -0.002739 \\ -0.003547 \\ -0.007683 \\ -0.002033 \\ -0.005499 \end{pmatrix}$	$\varepsilon_i = \begin{pmatrix} -0.000572 \\ -0.002739 \\ -0.003547 \\ -0.007683 \\ -0.002033 \\ -0.005499 \end{pmatrix}$	$\varepsilon_i = \begin{pmatrix} -0.000572 \\ -0.002739 \\ -0.003547 \\ -0.007683 \\ -0.002033 \\ -0.005499 \end{pmatrix}$

Chapter 6

Relaxed strain and stress in the inclusion as a function of the entrapment conditions

6.1 Contour plots

Once the relaxation tensor **R** is calculated for a specific reciprocal orientation of the host and the inclusion it can be applied to relax any unrelaxed strain state for that system, without the need of new FE analyses. This is particularly useful, since the final relaxed strain and stress state developed in the inclusion after exhumation to room conditions strongly depends on the initial P_{trap} and T_{trap} of entrapment. Therefore, the response of a specific host-inclusion system given by their anisotropic elasticity can only be understood investigating a wide range of entrapment conditions. To this aim I developed an algorithm in Matlab® that combines the thermodynamic calculation based on non-linear elasticity and the elastic relaxation (outlined in chapter 4).
With this code the user can set the range of P_{trap}, T_{trap} to be investigated and the resolution of the contour plot (i.e. the steps in P_{trap} and T_{trap}). The algorithm first discretizes the P-T range of entrapment conditions generating a grid of equally-spaced points of entrapment according to the requested resolution. For each of the entrapment points the thermodynamic calculation, based on a new implementation of the EosFit-7c code (Angel et al., 2017b), is performed to find the unrelaxed strain and stress. The relaxation tensor is then applied to find the relaxed strain in the inclusion, from which the relaxed stress and all the other related quantities (e.g. volume strain, residual pressure...) are obtained. The average residual pressure and the volume strain in the inclusion are obtained from the anisotropic calculation as:

$$P_{inc}^{aniso} = -\frac{\sigma_{11}^{rel} + \sigma_{22}^{rel} + \sigma_{33}^{rel}}{3}$$

$$\left(\frac{\Delta V}{V}\right)_{inc}^{aniso} = \varepsilon_{11}^{rel} + \varepsilon_{22}^{rel} + \varepsilon_{33}^{rel}$$

These results are compared to the P_{inc}^{iso} and $(\Delta V/\ V)_{inc}^{iso}$ predicted for the same exhumation by currently available isotropic models for geobarometry (Angel et al., 2017b) where the relaxation is calculated with linear (i.e. the elastic properties are constant during the relaxation, model 2 in Eosfit-7c) and non-linear (i.e. the elastic properties are allowed to change with P, model 5 in Eosfit-7c) elasticity. Throughout the following discussion, all the results from isotropic geobarometry will be referred to as *linear* or *non-linear* referring to the assumption used in the calculation of the relaxation. The thermodynamic part of the calculation is always performed with non-linear elasticity (i.e assuming finite strains and allowing the elastic properties of the minerals to change with P and T). The full procedure is summarized in Fig. 6.1.

All the calculations can be replicated over a wide range of entrapment conditions and several contour plots are generated to show synthetically all the relevant results (the relaxed strain and stress state in the inclusion and the discrepancy between the volume strain and the residual pressure predicted by the isotropic and the anisotropic models) as a function of the entrapment P_{trap}, T_{trap}. In the next chapter these contour plots, each based on more than ten thousand calculations, will be used to summarize the effect of the anisotropic elasticity for several geologically relevant host-inclusion pairs.

6.2 Uncertainties on the calculations

The uncertainties on the components of the relaxed strain and stress are given by:

$$\delta(\varepsilon_i^{rel}) = \sum_{j=1}^{6} \left(\left(\left(\frac{\delta(R_{ij})}{R_{ij}} \right)^2 + \left(\frac{\delta(\varepsilon_j^{unrel})}{\varepsilon_j^{unrel}} \right)^2 \right)^{1/2} |R_{ij}\varepsilon_j^{unrel}| \right) \tag{6.1}$$

$$\delta(\sigma_i^{rel}) = \sum_{j=1}^{6} \left(\left(\left(\frac{\delta(C_{ij})}{C_{ij}} \right)^2 + \left(\frac{\delta(\varepsilon_j^{rel})}{\varepsilon_j^{rel}} \right)^2 \right)^{1/2} |C_{ij}\varepsilon_j^{rel}| \right) \tag{6.2}$$

where R_{ij} is the relaxation tensor and C_{ij} is the stiffness of the inclusion.

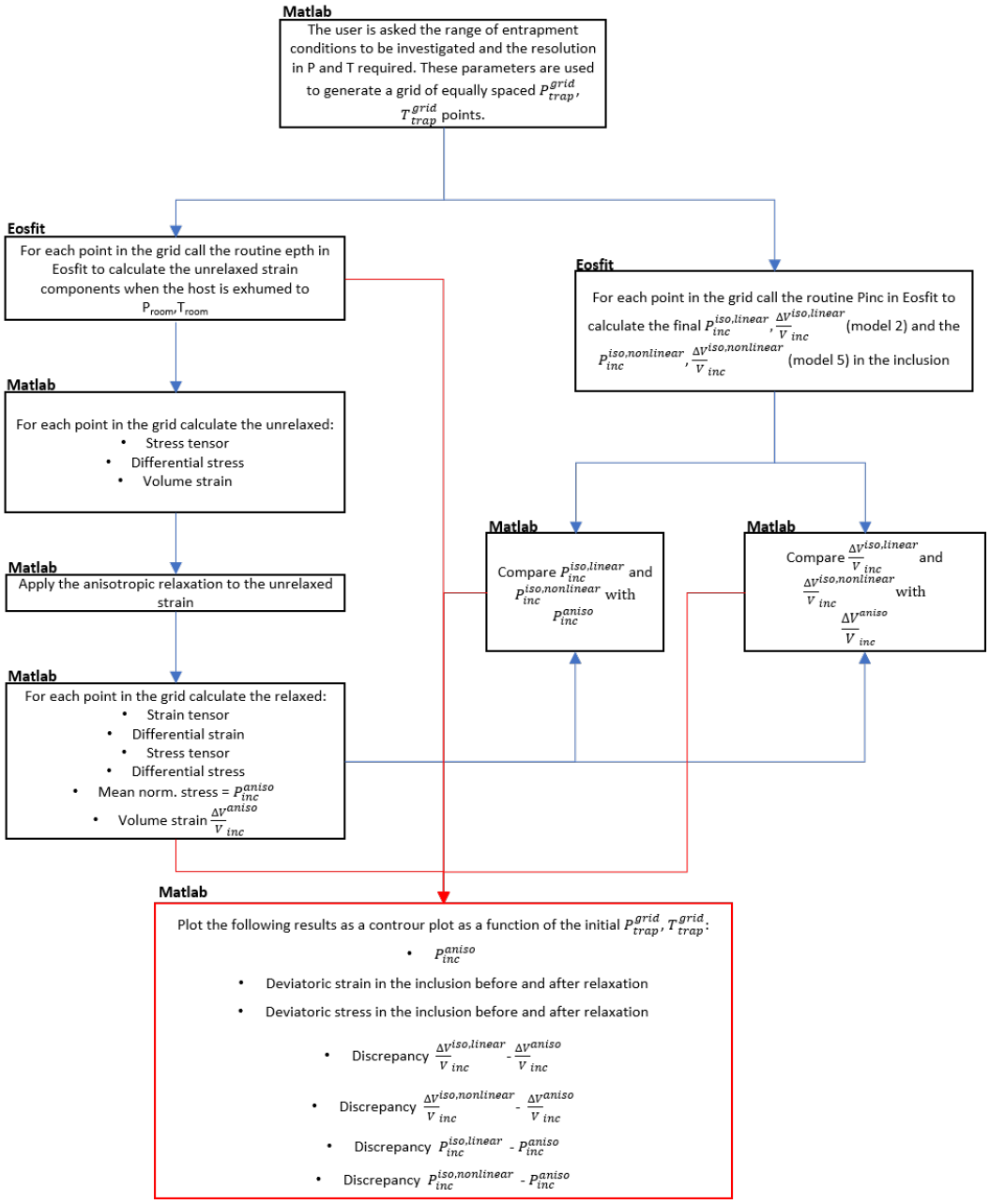

Figure 6.1: Flowchart summarizing the procedure to calculate the residual strain and stress in the inclusion (and all the other related quantities) and to produce synthetic contour plots that summarize the results.

The uncertainties on the components of the stress and on those of the strain might be not independent, but in general their variance-covariance matrix $((VcV)_{ij})$ is not known. Assuming the worst possible case, with a correlation coefficient $r = \frac{\delta_{ij}}{\delta_i \delta_j} = 1$, the upper limit on the uncertainties propagated on the pressure and on the volume strain can be found as a simple sum with equations (6.3) and (6.4), respectively:

$$\delta(P_{inc}) = \frac{\left(\delta(\sigma_1^{rel}) + \delta(\sigma_2^{rel}) + \delta(\sigma_3^{rel})\right)}{3} \tag{6.3}$$

$$\delta\left(\frac{\Delta V}{V}\right) = \left(\delta(\varepsilon_1^{rel}) + \delta(\varepsilon_2^{rel}) + \delta(\varepsilon_3^{rel})\right) \tag{6.4}$$

The numerical precision on the components of the unrelaxed strain obtained from the thermodynamic calculation is $\delta(\varepsilon_i^{unrel}) \approx 1 \cdot 10^{-6}$. The relative uncertainties on the components of the tensors C_{ij} are assumed to be 1% (typical experimental uncertainty), and, since the uncertainties on the calculation of the relaxation are dominated by those on the elastic constants, the same uncertainty is assumed for the R_{ij}. Equations (6.1 - 6.4) give the numerical precision of our calculations.

Chapter 7

Examples of anisotropic geobarometry: spherical inclusions in garnet

In this chapter we evaluate the strain and the stress developed during exhumation for geologically relevant systems with garnets as hosts. Garnets are minerals with cubic crystallographic symmetry that are common hosts in Ultra-High Pressure (UHP) metamorphic rocks. The strain and the stress developed in the inclusion during the exhumation of the host inclusion pair from entrapment to room conditions were calculated combining the thermodynamic calculation and the elastic relaxation (chapter 4). These calculations were repeated over a wide range of entrapment conditions (P_{trap}, T_{trap}) to generate contour plots that summarize the relevant results, following the procedure outlined in chapter 6.1. Results are reported for a range that spans to temperatures up to 1600 °C, much higher than what expected for P-T path of UHP metamorphic rocks. Such a large P-T window allows us to test the internal reliability of the calculation, even when extrapolated to high P and T. However, the significance of the residual strains and stresses calculated with anisotropic elastic geobarometry for entrapment at high pressure and temperature conditions depends on the rheology of the minerals involved. The resistance to plastic deformation of garnets is larger than most other minerals in UHP metamorphic rocks (Karato et al., 1995), and experiments and natural observations suggest that silicate garnets start to deform plastically at $T > 900$ °C (Martelat et al., 2012; Voegelé et al., 1998), depending on the strain rate. Entrapment at temperature conditions higher than this limit would therefore likely result in the plastic resetting of the strain in the inclusion, that cannot be predicted with the elastic model presented so far (e.g. Zhong et al., 2018). Therefore, geological implications can only be derived from the contour plots presented in this chapter for entrapment

conditions at which no plastic deformation of the minerals occurs.

7.1 Cubic inclusion in cubic host

7.1.1 Diamond in pyrope

Pyrope ($Mg_3Al_2Si_3O_{12}$) is one of the pure end-members of garnet and is a main component of garnets in UHP metamoprhic rocks. It crystallizes in the cubic system and is elastically isotropic with an universal anisotropic index (Ranganathan and Ostoja-Starzewski, 2008) A^U=0.0009. The anisotropic relaxation tensor was calculated for a spherical diamond inclusion in pyrope garnet with the elastic properties reported in Tables B.1 and B.5 and with relative orientation $\boldsymbol{a}_{diam}||\boldsymbol{a}_{pyr}$, $\boldsymbol{b}_{diam}||\boldsymbol{b}_{pyr}$, $\boldsymbol{c}_{diam}||\boldsymbol{c}_{pyr}$:

$$R_{ij} = \begin{pmatrix} 0.18856 & 0.01580 & 0.01580 & 0.00000 & 0.00000 & 0.00000 \\ 0.01580 & 0.18856 & 0.01580 & 0.00000 & 0.00000 & 0.00000 \\ 0.01580 & 0.01580 & 0.18857 & 0.00000 & 0.00000 & 0.00000 \\ 0.00000 & 0.00000 & 0.00000 & 0.14674 & 0.00000 & 0.00000 \\ 0.00000 & 0.00000 & 0.00000 & 0.00000 & 0.14674 & 0.00000 \\ 0.00000 & 0.00000 & 0.00000 & 0.00000 & 0.00000 & 0.14674 \end{pmatrix}$$

To investigate how the symmetry of the host and of the inclusion affect the change in strain during the relaxation, we test several cases with different initial strain and stress states that range from isotropic to deviatoric. The results are reported in Table 7.1. When the unrelaxed strain and stress are isotropic (cases 1 and 2) the relaxation of the diamond inclusion is equal along the three crystallographic axis. This follows from the fact that, for both diamond and pyrope, the a, b and c crystallographic directions are equally stiff, and with the current orientation each crystallographic axis of the inclusion points toward the correspondent axis of the host. Cases 1 and 2 also show that, as a consequence of the assumption of constant elastic properties in the derivation of the R_{ij}, the amount of relaxation starting from an initial compressive unrelaxed strain is equal to that calculated from an initial tensional strain. Cases 3, 4 and 5 show that the relaxation, even if in principle should be equal along the three principal directions, is actually larger along the directions that are initially more strained and stressed. This leads to the consequence that the deviatoric strain and stress in the inclusion decrease upon relaxation. Moreover, even if one of the normal components of the stress is extensional in the unrelaxed state, it can become compressive after relaxation as a consequence of the complete stress field acting on the inclusion (case 5).

Table 7.1: Relaxation calculated from a known unrelaxed strain state for diamond in pyrope with relative orientation $a_{diam}||a_{pyr}$, $b_{diam}||b_{pyr}$, $c_{diam}||c_{pyr}$. Stresses in GPa.

	Case 1			Case 2			Case 3			Case 4			Case 5		
	Unrelaxed state	Relaxed state	Change upon relax	Unrelaxed state	Relaxed state	Change upon relax	Unrelaxed state	Relaxed state	Change upon relax	Unrelaxed state	Relaxed state	Change upon relax	Unrelaxed state	Relaxed state	Change upon relax
ε_{11}	-0.00080	-0.00018	0.00062	0.00080	0.00018	-0.00062	-0.00060	-0.00014	0.00046	-0.00010	-0.00010	0.00000	0.00000	-0.00004	-0.00004
ε_{22}	-0.00080	-0.00018	0.00062	0.00080	0.00018	-0.00062	-0.00080	-0.00018	0.00062	-0.00600	-0.00112	0.00488	0.00000	-0.00004	-0.00004
ε_{33}	-0.00080	-0.00018	0.00062	0.00080	0.00018	-0.00062	-0.00100	-0.00021	0.00079	0.00100	0.00009	-0.00091	-0.00240	-0.00045	0.00195
$2\varepsilon_{23}$	0	0	0	0	0	0	0	0	0	0	0	0	0	0	0
$2\varepsilon_{13}$	0	0	0	0	0	0	0	0	0	0	0	0	0	0	0
$2\varepsilon_{12}$	0	0	0	0	0	0	0	0	0	0	0	0	0	0	0
Differential strain ($\varepsilon_{max} - \varepsilon_{min}$)	0.00000	0.00000	—	0.00000	0.00000	—	0.00040	0.00007	—	0.00700	0.00121	—	0.00240	0.00041	—
σ_{11}	-1.066	-0.235	0.831	1.066	0.235	-0.831	-0.875	-0.202	0.674	-0.742	-0.236	0.506	-0.304	-0.103	0.201
σ_{22}	-1.066	-0.235	0.831	1.066	0.235	-0.831	-1.066	-0.235	0.831	-6.356	-1.205	5.151	-0.304	-0.103	0.201
σ_{33}	-1.066	-0.235	0.831	1.066	0.235	-0.831	-1.256	-0.267	0.988	0.305	-0.055	-0.360	-2.588	-0.498	2.090
σ_{23}	0	0	0	0	0	0	0	0	0	0	0	0	0	0	0
σ_{13}	0	0	0	0	0	0	0	0	0	0	0	0	0	0	0
σ_{12}	0	0	0	0	0	0	0	0	0	0	0	0	2	0	0
Differential stress ($\sigma_{max} - \sigma_{min}$)	0.000	0.000	—	0.000	0.000	—	0.381	0.066	—	6.661	1.151	—	2.284	0.395	—

Relaxed strain, stress and pressure in the inclusion as a function of the entrapment conditions

The strain and the stress developed in the inclusion during the exhumation were investigated as a function of a wide range of entrapment conditions (P_{trap}, T_{trap}) following the procedure outlined in chapter 6.1. The EoS for diamond and pyrope used for the thermodynamic part of the anisotropic calculation and for the isotropic calculation are from Angel et al. (2015a) and Milani et al. (2015), respectively. Diamond and pyrope have both cubic crystallographic symmetry and, as a consequence, the unrelaxed strain in the diamond inclusion is isotropic for any choice of the initial P_{trap}, T_{trap} (see equation 4.4). This together with the fact that the top left block of the $\mathbf{R}$ tensor is symmetric with $R_{11} = R_{22} = R_{33}$ and $R_{12} = R_{13} = R_{23}$ guarantees that also the final relaxed strain in the diamond inclusion is isotropic for any entrapment P and T. Since the strain is isotropic and the inclusion is cubic the final relaxed stress is always hydrostatic.

The numerical precision on the calculation (see section 6.2 and equations 6.1 - 6.4) is $\delta(\varepsilon_i^{rel}) \approx 2 \cdot 10^{-7}$ on the components of the relaxed strain, $\delta(\sigma_i^{rel}) \approx 3 \cdot 10^{-4}$ GPa on the components of the relaxed stress, $\delta(P_{inc}) \approx 3 \cdot 10^{-4}$ GPa on the residual pressure, $\delta\left(\frac{\Delta V}{V}\right) \approx 7 \cdot 10^{-7}$ on the relaxed volume strain.

Residual pressure ($\mathbf{P_{inc}}$)

Fig. 7.1 shows the residual pressure in the inclusion obtained from the relaxed stress ($P_{inc}^{aniso} = -(\sigma_{11}+\sigma_{22}+\sigma_{33})/3$) as a function of the entrapment conditions (P_{trap}, T_{trap}). The isomeke passing through room conditions is also reported. For an entrapment at P_{trap} and T_{trap} conditions lying on this isomeke the isotropic model would predict zero residual pressure in the inclusion after exhumation to room conditions (Angel et al., 2014). Since the inclusion (diamond) is stiffer than the host (pyrope) the P_{inc} is positive below this isomeke and negative above. As shown in Fig. 7.1, the line of $P_{inc} = 0$ GPa obtained from the anisotropic calculation overlaps perfectly with the zero-P_{inc} isomeke, that is based on isotropic elasticity, indicating a close agreement between the isotropic and the anisotropic calculations.

Discrepancy between the isotropic and the anisotropic volume strain

Fig. 7.2a shows the discrepancy between the volume strain in the inclusion calculated assuming linear isotropic elasticity ($(\Delta V/\ V)_{inc}^{iso,linear}$) and linear anisotropic elasticity ($(\Delta V/\ V)_{inc}^{aniso}$) for the relaxation. At P_{trap}, T_{trap} conditions below the isomeke the volume strains are negative (i.e. compressive) and the discrepancy $(\Delta V/\ V)_{inc}^{iso,linear} - (\Delta V/\ V)_{inc}^{aniso}$ is negative meaning that the isotropic inclusion is more compressed than the anisotropic case. This implies that the anisotropic inclusion tends to relax more than the isotropic inclusion when both the calculations assume linear elasticity for the

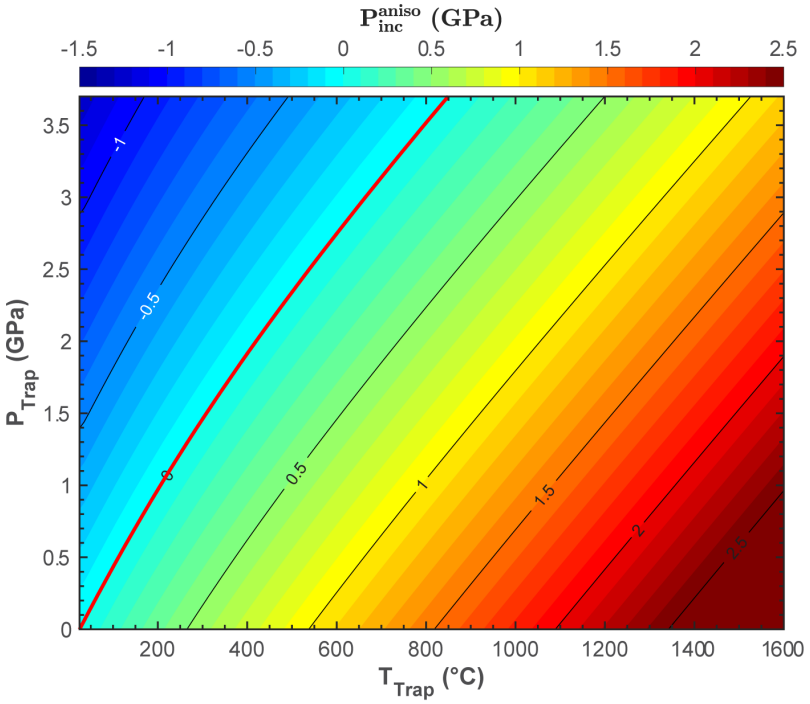

Figure 7.1: Diamond in pyrope: residual pressure in the inclusion obtained from the relaxed stress ($P_{inc} = -(\sigma_{11} + \sigma_{22} + \sigma_{33})/3$) as a function of the entrapment conditions (P_{trap}, T_{trap}). Solid line: zero-P_{inc} isomeke.

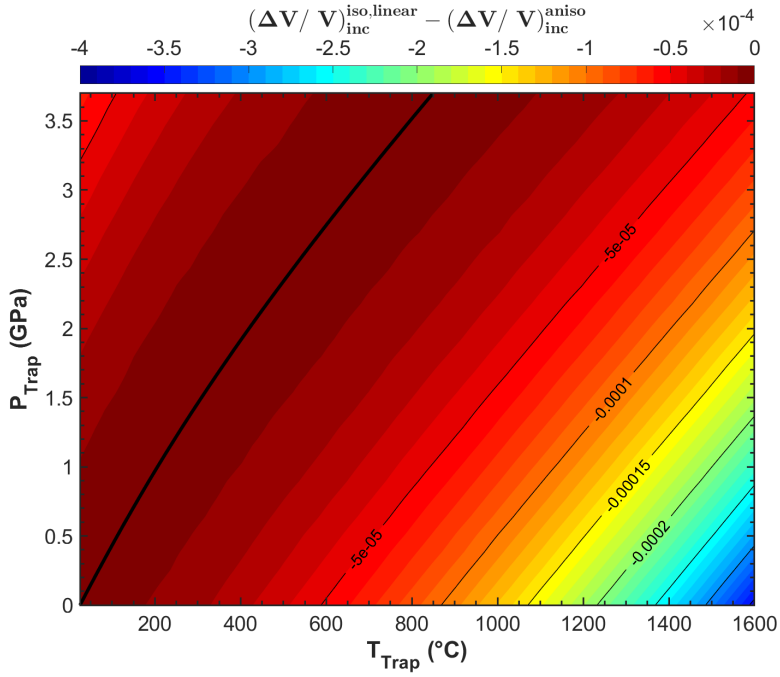

(a)

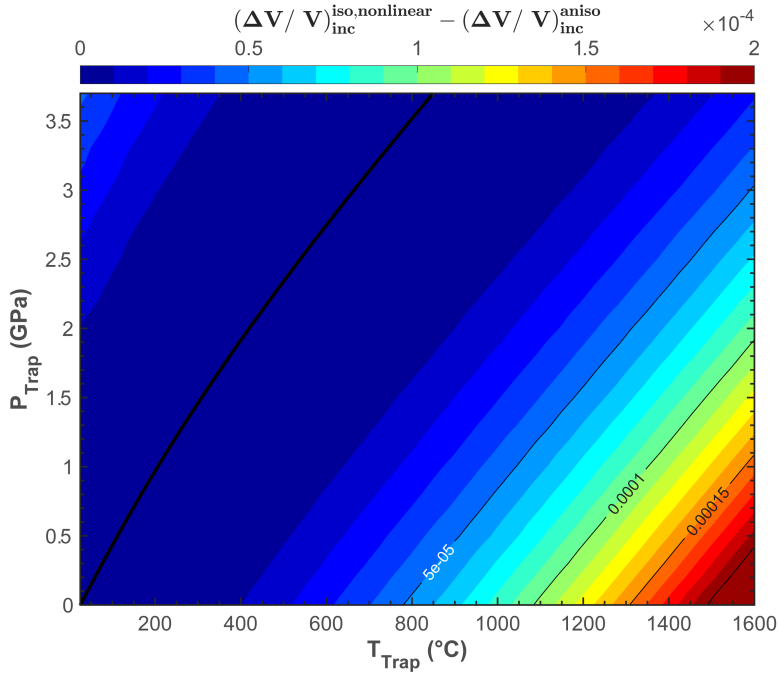

(b)

Figure 7.2: Diamond in pyrope: discrepancy between the relaxed volume strain of the inclusion calculated with isotropic and anisotropic elasticity as a function of the entrapment conditions (P_{trap}, T_{trap}). In the isotropic model the relaxation is calculated with: (a) linear elasticity (i.e. the elastic properties are constant); (b) non-linear elasticity (i.e. the elastic properties are allowed to change). Solid line: zero-P_{inc} isomeke.

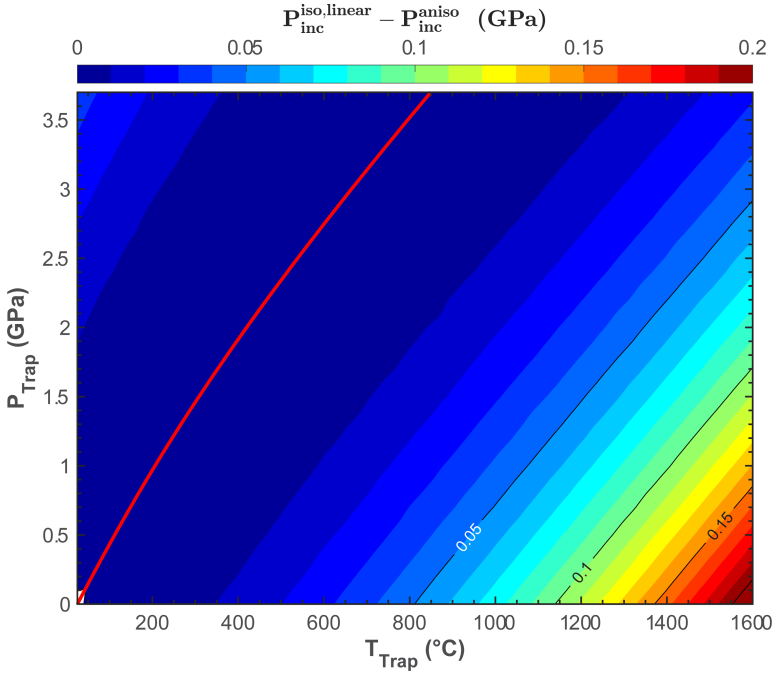

(a)

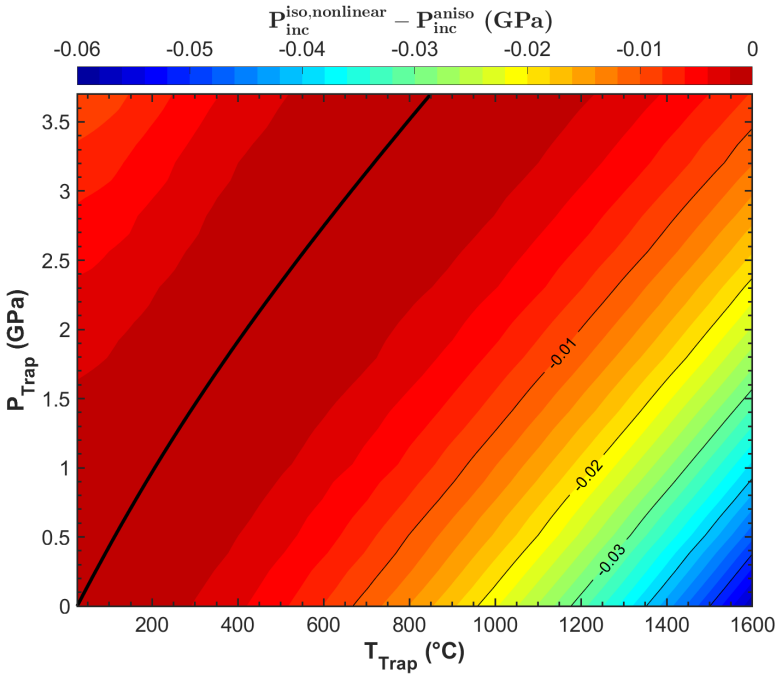

(b)

Figure 7.3: Diamond in pyrope: discrepancy between the residual pressure in the inclusion calculated with isotropic (P_{inc}^{iso}) and anisotropic (P_{inc}^{aniso}) elasticity as a function of the entrapment conditions (P_{trap}, T_{trap}). In the isotropic model the relaxation is calculated with: (a) linear elasticity (i.e. the elastic properties are constant); (b) non-linear elasticity (i.e. the elastic properties are allowed to change). Solid line: zero-P_{inc} isomeke.

relaxation.
The opposite behavior is found in Fig. 7.2b where the isotropic strain is calculated applying non-linear elasticity for the relaxation. At P_{trap}, T_{trap} conditions above the isomeke the volume strain are still negative (i.e. compressive) but the discrepancy $(\Delta V/\ V)_{inc}^{iso,nonlinear} - (\Delta V/\ V)_{inc}^{aniso}$ is positive meaning that the isotropic inclusion is less compressed than the anisotropic case.
The discrepancies between the isotropic and the anisotropic calculations are smaller than the typical experimental uncertainties on the determination of the volume strain in natural inclusions ($\delta\left(\frac{\Delta V}{V}\right) \approx 3 \cdot 10^{-4}$) for all the entrapment conditions investigated. This suggests that for a diamond inclusion in pyrope the use of an elastically isotropic model for geobarometry should still lead to a reliable estimation of the entrapment pressure. This is particularly relevant when the experimental measurement is performed with Raman spectroscopy, that for cubic minerals only gives the volume strain and therefore only allows the application of isotropic geobarometry (Angel et al., 2018).

Discrepancy between the isotropic and the anisotropic P_{inc}
Fig. 7.3a shows the discrepancy between the relaxed pressure calculated assuming linear isotropic elasticity ($P_{inc}^{iso,linear}$) and linear anisotropic elasticity ($P_{inc}^{aniso} = -(\sigma_{11} + \sigma_{22} + \sigma_{33})/3$) for the relaxation. At P_{trap}, T_{trap} conditions below the isomeke the P_{inc} is positive and the discrepancy $P_{inc}^{iso,linear} - P_{inc}^{aniso}$ is positive meaning that the residual pressure of the isotropic calculation is higher than the pressure obtained form the anisotropic calculation. As an example, for a P_{inc} less than 1 GPa the discrepancy is smaller than 0.03 GPa.
The opposite behaviour is observed in Fig. 7.3b where the residual pressure calculated with non-linear isotropic elasticity is lower than the anisotropic calculation at metamorphic conditions, in agreement with what observed in Fig. 7.2b where the non-linear isotropic calculation gives a less compressed inclusion compared to the anisotropic calculation. For a P_{inc} less than 1 GPa the discrepancy is smaller in magnitude than 0.008 GPa.

7.1.2 Diamond in grossular

Grossular ($Ca_3Al_2Si_3O_{12}$) is one of the end-members of garnet and is a main component of garnets in UHP metamoprhic rocks. It crystallizes in the cubic system and is elastically more anisotropic than pyrope (universal anisotropic index A^U=0.01124 compared to A^U=0.0009 of pyrope). The use of grossular as host allows as to test the behaviour of a cubic inclusion when it is included in a cubic host that is not elastically isotropic. The anisotropic relaxation tensor was calculated for a spherical diamond inclusion in grossular garnet with the elastic properties reported in Tables B.1 and B.3

and with relative orientation $\boldsymbol{a}_{diam}||\boldsymbol{a}_{grs}$, $\boldsymbol{b}_{diam}||\boldsymbol{b}_{grs}$, $\boldsymbol{c}_{diam}||\boldsymbol{c}_{grs}$:

$$R_{ij} = \begin{pmatrix} 0.20639 & 0.01772 & 0.01772 & 0.00000 & 0.00000 & 0.00000 \\ 0.01772 & 0.20639 & 0.01772 & 0.00000 & 0.00000 & 0.00000 \\ 0.01772 & 0.01772 & 0.20639 & 0.00000 & 0.00000 & 0.00000 \\ 0.00000 & 0.00000 & 0.00000 & 0.15939 & 0.00000 & 0.00000 \\ 0.00000 & 0.00000 & 0.00000 & 0.00000 & 0.15939 & 0.00000 \\ 0.00000 & 0.00000 & 0.00000 & 0.00000 & 0.00000 & 0.15939 \end{pmatrix}$$

Relaxed strain, stress and pressure in the inclusion as a function of the entrapment conditions

The EoS for diamond and grossular used for the thermodynamic part of the anisotropic calculation and for the isotropic calculation are from Angel et al., 2015a and Milani et al., 2017, respectively. As for diamond in pyrope, also in this case the strain and the stress in the inclusion are isotropic for any choice of the initial P_{trap}, T_{trap}. The numerical precision on the calculation (see section 6.2 and equations 6.1 - 6.4) is $\delta(\varepsilon_i^{rel}) \approx 3 \cdot 10^{-7}$ on the components of the relaxed strain, $\delta(\sigma_i^{rel}) \approx 3 \cdot 10^{-4}$ GPa on the components of the relaxed stress, $\delta(P_{inc}) \approx 3 \cdot 10^{-4}$ GPa on the residual pressure, $\delta\left(\frac{\Delta V}{V}\right) \approx 7 \cdot 10^{-7}$ on the relaxed volume strain.

Residual pressure ($\mathbf{P_{inc}}$)

Fig. 7.4 shows the residual pressure ($P_{inc} = -(\sigma_{11} + \sigma_{22} + \sigma_{33})/3$) in the inclusion obtained from the relaxed stress as a function of the entrapment conditions (P_{trap}, T_{trap}). The isomeke passing through room conditions is also reported. For an entrapment at P and T conditions lying on this isomeke the isotropic model would predict zero residual pressure in the inclusion after exhumation to room conditions (Angel et al., 2014). As for diamond in pyrope, the line of $P_{inc} = 0$ GPa obtained from the anisotropic calculation overlaps perfectly with the zero-P_{inc} isomeke, that is based on isotropic elasticity, indicating a close agreement between the isotropic and the anisotropic calculations.

Discrepancy between the isotropic and the anisotropic calculations

The comparison of Fig. 7.2 and 7.5 shows that the discrepancy between the isotropic (linear and non-linear) and the anisotropic volume strain in the inclusion ($(\Delta V/\ V)_{inc}^{iso} - (\Delta V/\ V)_{inc}^{aniso}$) is slightly smaller in magnitude compared to the case of a pyrope host. The same is observed for the discrepancy in the residual pressure ($P_{inc}^{iso} - P_{inc}^{aniso}$). This is a consequence of grossular being slightly stiffer than pyrope (cf. Tables B.6 and B.4).

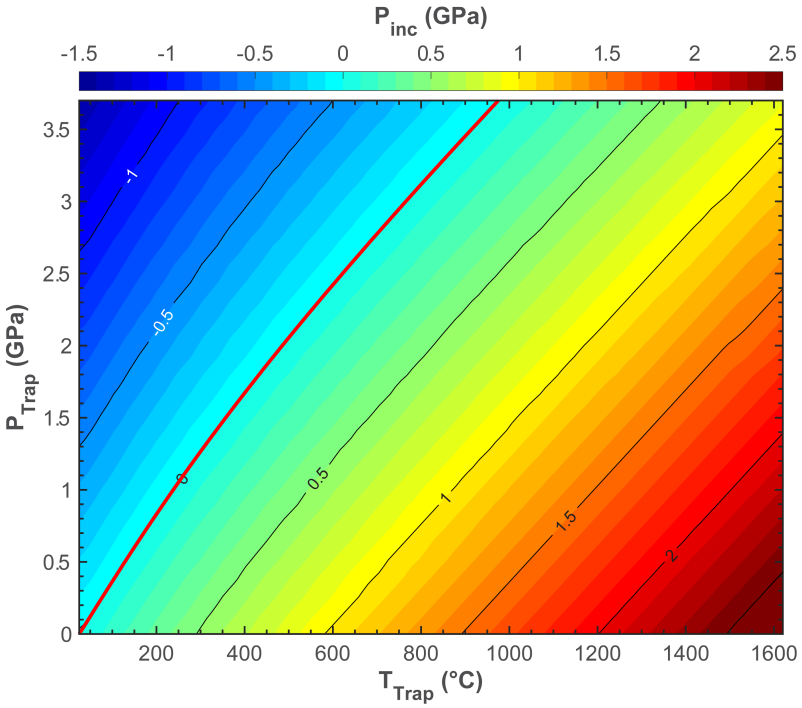

Figure 7.4: Diamond in grossular: residual pressure in the inclusion obtained from the relaxed stress ($P_{inc} = -(\sigma_{11} + \sigma_{22} + \sigma_{33})/3$) as a function of the entrapment conditions (P_{trap}, T_{trap}). The solid line is the isomeke passing through room conditions.

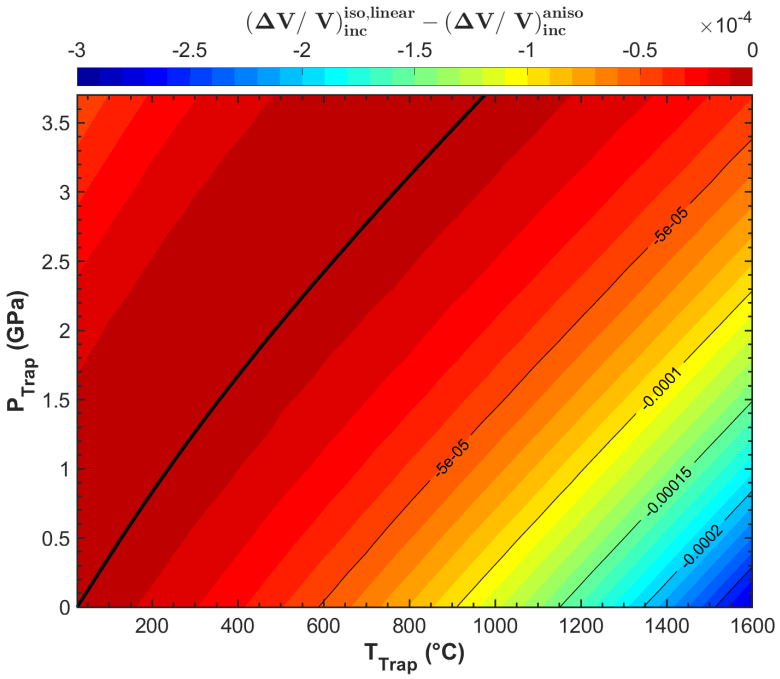

(a)

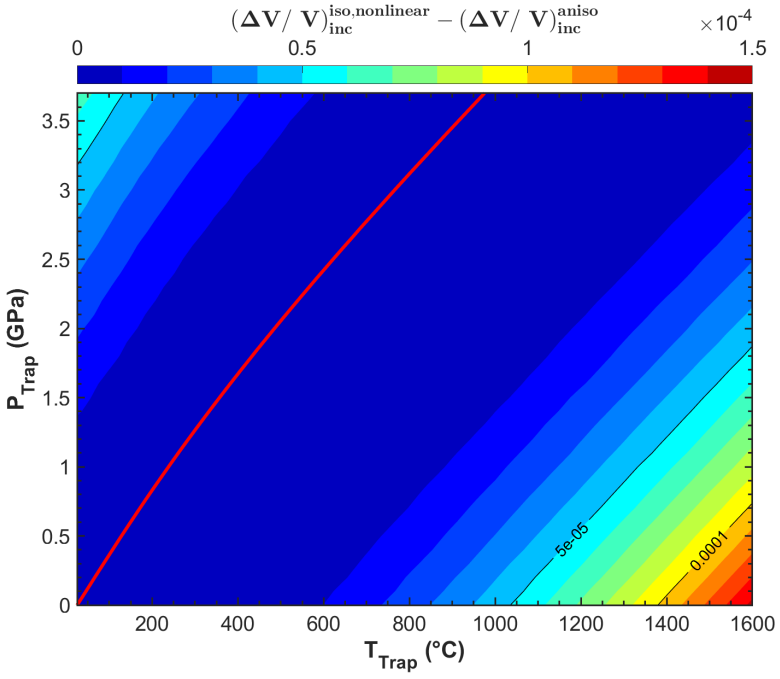

(b)

Figure 7.5: Diamond in grossular: discrepancy between the relaxed volume strain of the inclusion calculated with isotropic and anisotropic elasticity as a function of the entrapment conditions (P_{trap}, T_{trap}). In the isotropic model the relaxation is calculated with: (a) linear elasticity (i.e. the elastic properties are constant); (b) non-linear elasticity (i.e. the elastic properties are allowed to change). Solid line: zero-P_{inc} isomeke.

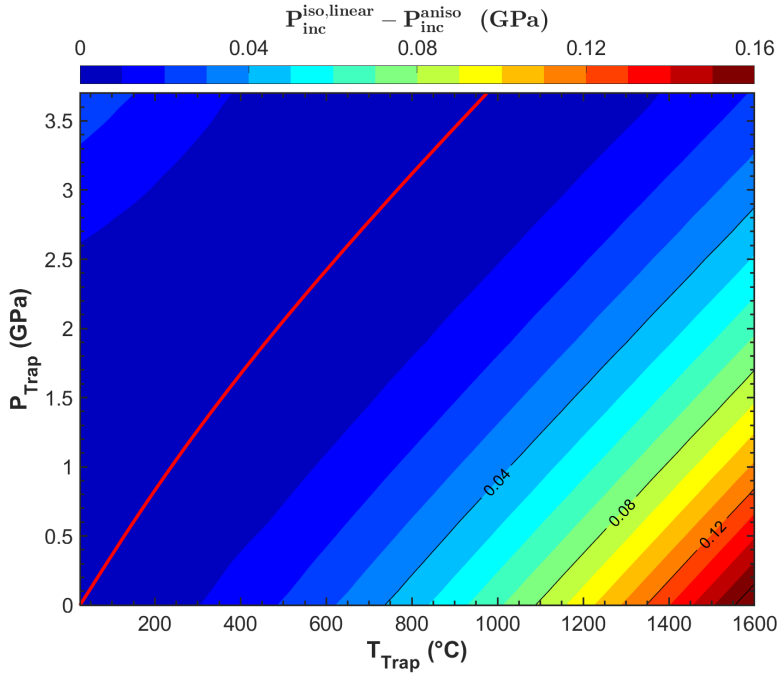

(a)

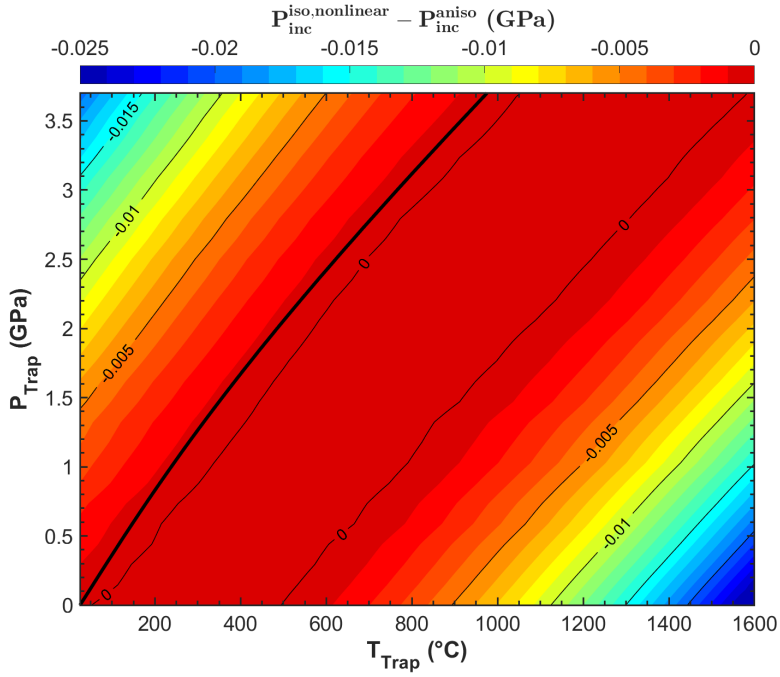

(b)

Figure 7.6: Diamond in grossular: discrepancy between the residual pressure in the inclusion calculated with isotropic (P_{inc}^{iso}) and anisotropic (P_{inc}^{aniso}) elasticity as a function of the entrapment conditions (P_{trap}, T_{trap}). In the isotropic model the relaxation is calculated with: (a) linear elasticity (i.e. the elastic properties are constant); (b) non-linear elasticity (i.e. the elastic properties are allowed to change). Solid line: zero-P_{inc} isomeke.

7.2 Non cubic inclusion in cubic host

7.2.1 Quartz in pyrope

The anisotropic relaxation tensor was calculated for a spherical quartz inclusion in pyrope with the elastic properties reported in Tables B.7 and B.5 with relative orientation $\boldsymbol{a}_{qtz}||\boldsymbol{a}_{pyr}$ and $\boldsymbol{c}_{qtz}||\boldsymbol{c}_{pyr}$:

$$R_{ij} = \begin{pmatrix} 0.74280 & 0.02442 & 0.02417 & -0.03041 & 0.00000 & 0.00000 \\ 0.02442 & 0.74280 & 0.02417 & 0.03041 & 0.00000 & 0.00000 \\ 0.01397 & 0.01397 & 0.69855 & 0.00000 & 0.00000 & 0.00000 \\ -0.06105 & 0.06105 & 0.00000 & 0.62979 & 0.00000 & 0.00000 \\ 0.00000 & 0.00000 & 0.00000 & 0.00000 & 0.62980 & -0.06099 \\ 0.00000 & 0.00000 & 0.00000 & 0.00000 & -0.06099 & 0.71763 \end{pmatrix}$$

To investigate how the symmetry of the host and of the inclusion affect the change in strain during the relaxation, we test several cases with different initial strain and stress states that range from isotropic to deviatoric. The results are reported in Table 7.2. When the initial unrelaxed strain is isotropic (Case 1) the relaxation of the quartz inclusion is larger along the c-axis. This follows from the fact that, the a, b and c crystallographic axes of the pyrope host are equally stiff, while c is the stiffest crystallographic axis of quartz that is therefore more stressed and relaxes more. The results in case 1 in Table 7.2 also show that the relaxation does not decrease the differential strain in the inclusion if the initial unrelaxed strain is isotropic. Case 3 shows that if the normal components $\sigma_{11}^{unrel} = \sigma_{22}^{unrel}$ are more compressive than σ_{33}^{unrel}, the relaxation along the c axis of the inclusion may be smaller than along a and b, even if c is the stiffest direction. Therefore, the relaxation in the inclusion depends on the overall balance between the stiffness of the inclusion along each direction and the magnitude of the component of the unrelaxed stress along that direction. Case 5 shows that one component of the normal stress (i.e. σ_{33}^{unrel} in case 5) may turn from extensional to compressive as a consequence of the relaxation if the other two components (i.e. $\sigma_{11}^{unrel} = \sigma_{22}^{unrel}$ in case 5) are sufficiently compressive.

Table 7.2: Relaxation calculated from a known unrelaxed strain state for quartz in pyrope with relative orientation $a_{qtz}||a_{pyr}$ and $c_{qtz}||c_{pyr}$. Stresses in GPa.

	Case 1			Case 2			Case 3			Case 4			Case 5		
	Unrelaxed state	Relaxed state	Change upon relax	Unrelaxed state	Relaxed state	Change upon relax	Unrelaxed state	Relaxed state	Change upon relax	Unrelaxed state	Relaxed state	Change upon relax	Unrelaxed state	Relaxed state	Change upon relax
ε_{11}	-0.00900	-0.00712	0.00188	-0.00850	-0.00676	0.00174	-0.01200	-0.00928	0.00272	-0.01200	-0.00911	0.00289	-0.01200	-0.00913	0.00287
ε_{22}	-0.00900	-0.00712	0.00188	-0.00850	-0.00676	0.00174	-0.01200	-0.00928	0.00272	-0.01200	-0.00911	0.00289	-0.01200	-0.00913	0.00287
ε_{33}	-0.00900	-0.00654	0.00246	-0.01000	-0.00722	0.00278	-0.00300	-0.00243	0.00057	0.00400	0.00246	-0.00154	0.00300	0.00176	-0.00124
$2\varepsilon_{23}$	0	0	0	0	0	0	0	0	0	0	0	0	0	0	0
$2\varepsilon_{13}$	0	0	0	0	0	0	0	0	0	0	0	0	0	0	0
$2\varepsilon_{12}$	0	0	0	0	0	0	0	0	0	0	0	0	0	0	0
Differential strain ($\varepsilon_{max} - \varepsilon_{min}$)	0.00000	-0.00058	—	0.00150	0.00046	—	-0.00900	-0.00685	—	-0.01600	-0.01157	—	-0.01500	-0.01089	—
σ_{11}	-0.944	-0.741	0.204	-0.909	-0.715	0.194	-1.157	-0.896	0.261	-1.078	-0.825	0.253	-1.089	-0.835	0.254
σ_{22}	-0.944	-0.741	0.204	-0.909	-0.715	0.194	-1.157	-0.896	0.261	-1.078	-0.825	0.253	-1.089	-0.835	0.254
σ_{33}	-1.161	-0.857	0.304	-1.256	-0.921	0.335	-0.590	-0.468	0.122	0.154	0.056	-0.099	0.048	-0.019	-0.067
σ_{23}	0	0	0	0	0	0	0	0	0	0	0	0	0	0	0
σ_{13}	0	0	0	0	0	0	0	0	0	0	0	0	0	0	0
σ_{12}	0	0	0	0	0	0	0	0	0	0	0	0	-1	0	0
Differential stress ($\sigma_{max} - \sigma_{min}$)	0.217	0.116	—	0.348	0.207	—	-0.567	-0.428	—	-1.232	-0.881	—	-1.137	-0.816	—

Relaxed strain, stress and pressure in the inclusion as a function of the entrapment conditions

The strain and the stress developed in the inclusion during the exhumation were investigated as a function of a wide range of entrapment conditions (P_{trap}, T_{trap}) following the procedure outlined in chapter 6.1. The EoS for quartz and pyrope used for the thermodynamic part of the anisotropic calculation and for the isotropic calculation are from (Angel et al., 2017a; Alvaro et al., 2019) and Milani et al. (2015), respectively. Since pyrope has cubic crystallographic symmetry, it follows from equation (4.2) that the strain imposed on quartz during the exhumation under an external lithostatic load, is isotropic if referred to the initial state at P_{trap}, T_{trap}. The unrelaxed strain on the quartz inclusion referred to a free quartz at room conditions can be found from equation (4.4) and in general is anisotropic (Fig. 7.7a).

The numerical precision on the calculation (see section 6.2 and equations 6.1 - 6.4) is $\delta(\varepsilon_i^{rel}) \approx 6 \cdot 10^{-6}$ on the components of the relaxed strain, $\delta(\sigma_i^{rel}) \approx 7 \cdot 10^{-4}$ GPa on the components of the relaxed stress, $\delta(P_{inc}) \approx 7 \cdot 10^{-4}$ GPa on the residual pressure, $\delta\left(\frac{\Delta V}{V}\right) \approx 1 \cdot 10^{-5}$ on the relaxed volume strain.

Differential strain and stress in the inclusion

Fig. 7.7 shows the differential strain $\varepsilon_3 - \varepsilon_1$ before and after the elastic relaxation. Since ε_3 is not necessarily the maximum strain in the inclusion, the difference $\varepsilon_3 - \varepsilon_1$ can be either positive or negative depending on the entrapment conditions. The strain in the inclusion is isotropic only for a limited range of entrapment P_{trap}, T_{trap} conditions (Fig. 7.7). As shown in Table 7.2, for an initial isotropic unrelaxed strain the final relaxed strain becomes slightly anisotropic due to the elastic anisotropy of quartz. As a consequence the lines of isotropic strain in Fig. 7.7a and b do not correspond. The line of isotropic strain divides the P-T space in two fields, one with $\varepsilon_3 - \varepsilon_1 > 0$ when the P_{trap} is increased or the T_{trap} decreased, and one with $\varepsilon_3 - \varepsilon_1 < 0$ when the P_{trap} is decreased or the T_{trap} increased. This is due to the c axis of quartz having a lower compressibility and thermal expansion compared to the a and b axes ($M_{c0} = 136.77$ GPa, $M'_{c0} = 29.56$, $\alpha_{c0} = 1.0212\ 10^{-5}$ K^{-1} vs. $M_{a0} = 102$ GPa, $M'_{a0} = 16.4$, $\alpha_{a0} = 1.3587\ 10^{-5}$ K^{-1}). As a consequence, for an entrapment at high P_{trap} and low T_{trap} (i.e above the line of final isotropic strain) the ratio c_{trap}/c_0 is larger than a_{trap}/a_0, and it follows from equation (4.4) that $\varepsilon_3 - \varepsilon_1 > 0$. For an entrapment at conditions below the line of final isotropic strain (i.e. at low P_{trap} and high T_{trap}), we find the opposite behaviour with $c_{trap}/c_0 < a_{trap}/a_0$ and therefore $\varepsilon_3 - \varepsilon_1 < 0$.

Since the inclusion is not cubic but trigonal, when the relaxed strain is isotropic the relaxed stress is not hydrostatic. For quartz, when the strain is compressive (i.e. negative components) and isotropic, the σ_3 component of the stress is more negative than $\sigma_1 = \sigma_2$ (because quartz c axis is stiffer than $a = b$ axes). As a consequence, the

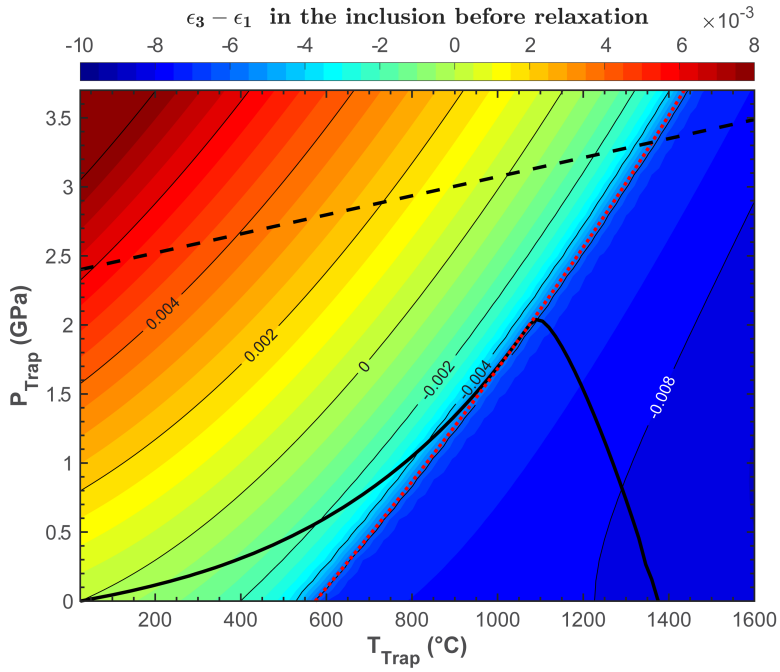

(a)

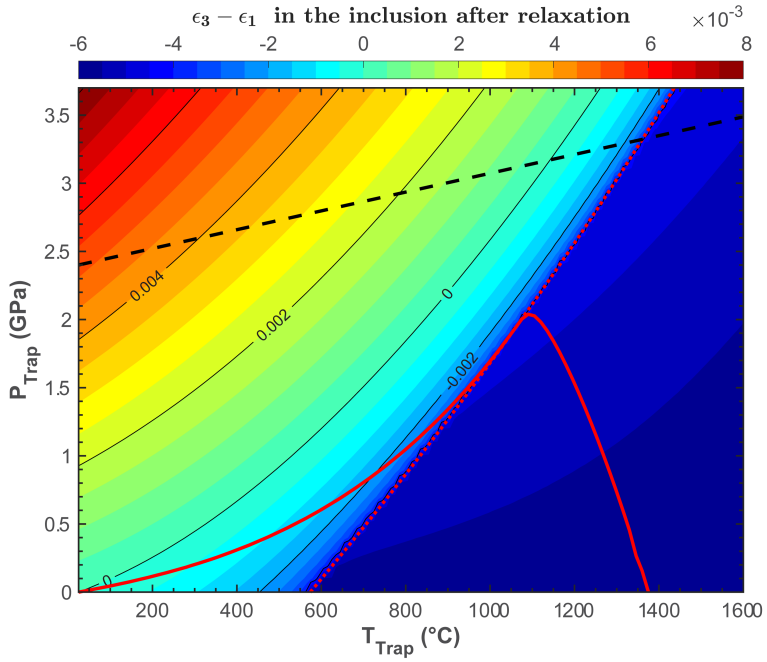

(b)

Figure 7.7: Quartz in pyrope: differential strain ($\varepsilon_3 - \varepsilon_1$) in the quartz inclusion before (a) and after (b) the elastic relaxation, as a function of the entrapment conditions (P_{trap}, T_{trap}). Dashed line: quartz-coesite phase transition (Bose and Ganguly, 1995); dotted line: $\alpha - \beta$ quartz phase transition (Angel et al., 2017a); solid line: zero-P_{inc} isomeke. The quartz-coesite phase transition is not included in the thermodynamic calculation, and all the results calculated for P_{trap}, T_{trap} conditions above the phase boundary do not represent the real behaviour.

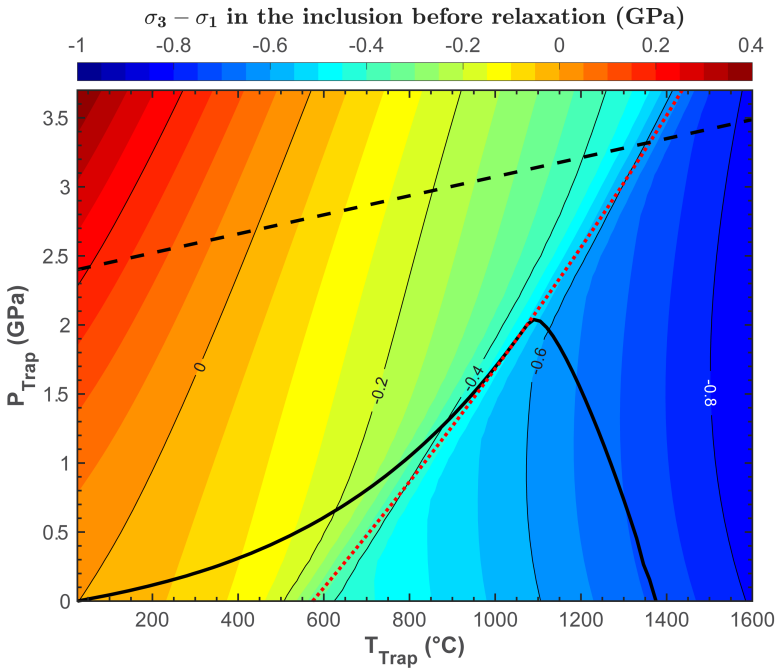

(a)

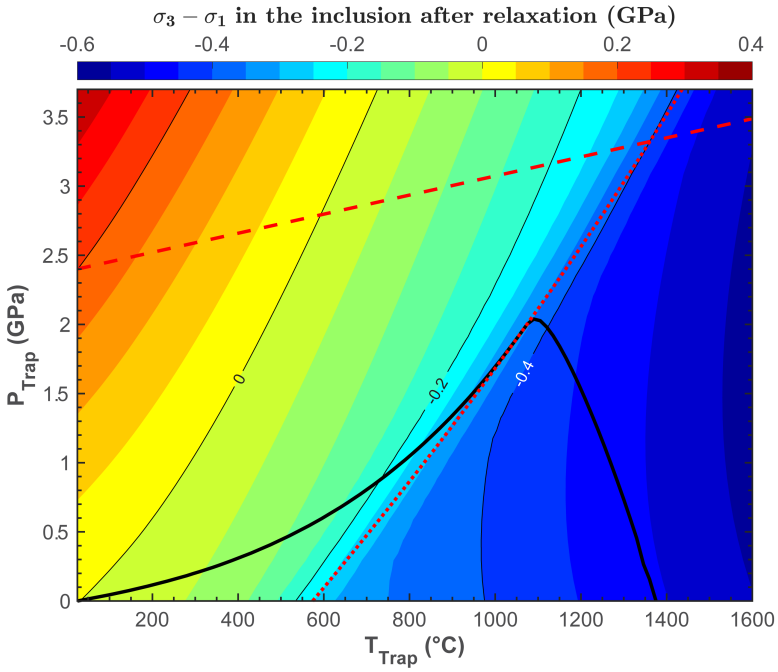

(b)

Figure 7.8: Quartz in pyrope: differential stress ($\sigma_3 - \sigma_1$) in the quartz inclusion before (a) and after (b) the elastic relaxation, as a function of the entrapment conditions (P_{trap}, T_{trap}). Dashed line: quartz-coesite phase transition (Bose and Ganguly, 1995); dotted line: $\alpha - \beta$ quartz phase transition (Angel et al., 2017a); solid line: zero-P_{inc} isomeke. The quartz-coesite phase transition is not included in the thermodynamic calculation, and all the results calculated for P_{trap}, T_{trap} conditions above the phase boundary do not represent the real behaviour.

$\sigma_3 - \sigma_1$ is negative. This is confirmed by comparing the position of bands of isotropic strain from Fig.7.7b to the value of $\sigma_3 - \sigma_1$ in the same area in Fig.7.8(b). On the other hand, when the compressive stress in quartz is isotropic the strain components $\varepsilon_1 = \varepsilon_2$ are more negative than ε_3, and $\varepsilon_3 - \varepsilon_1$ is positive. This is confirmed by comparing the position of the band of isotropic stress from Fig. 7.8b to the $\varepsilon_3 - \varepsilon_1$ in the corresponding region of Fig.7.7b. As for the strain, Fig. 7.8 shows that the band of isotropic stress divides the P-T space in two fields, one with $\sigma_3 - \sigma_1 > 0$ when the P_{trap} is increased or the T_{trap} decreased, and one with $\sigma_3 - \sigma_1 < 0$ when the $P_{trap}$is decreased or the T_{trap} increased, and, as shown above, this is a consequence of the c axis in quartz having a lower compressibility and thermal expansion compared to the a and b axes.

By comparing the strain (Fig. 7.7) and the stress (Fig. 7.8) before and after the elastic relaxation it can be seen that the maximum differential strain and differential stress are reduced after the elastic relaxation.

Residual pressure ($\mathbf{P_{inc}}$)

The residual pressure in the inclusion, obtained form the anisotropic calculation as $P_{inc}^{aniso} = -(\sigma_{11} + \sigma_{22} + \sigma_{33})/3$, is positive above the zero-P_{inc} isomeke and negative below as expected for a soft inclusion in a stiff host (Fig. 7.9). The line of $P_{inc} = 0$ GPa obtained from the anisotropic calculation overlaps perfectly with the zero-P_{inc} isomeke, that is based on isotropic elasticity, indicating a close agreement between the isotropic and the anisotropic calculations.

Discrepancy between the isotropic and the anisotropic volume strain

Fig. 7.10a shows the discrepancy between the volume strain in the inclusion calculated assuming linear isotropic elasticity ($(\Delta V/\ V)_{inc}^{iso,linear}$) and linear anisotropic elasticity ($(\Delta V/\ V)_{inc}^{aniso} = \varepsilon_{11} + \varepsilon_{22} + \varepsilon_{33}$) for the relaxation. At P_{trap}, T_{trap} conditions above the isomeke the volume strains are negative (i.e. compressive) and the discrepancy $(\Delta V/\ V)_{inc}^{iso,linear} - (\Delta V/\ V)_{inc}^{aniso}$ is negative meaning that the isotropic inclusion is more compressed than the anisotropic case. This implies that the anisotropic inclusion tends to relax more than the isotropic inclusion when both the calculations assume linear elasticity for the relaxation. The discrepancy between the isotropic and the anisotropic calculation are expected to be only slightly larger than the typical experimental uncertainties on the determination of the volume strain in natural inclusions ($\delta\left(\frac{\Delta V}{V}\right) \approx 3 \cdot 10^{-4}$ corresponding to about 0.01 GPa of residual pressure) for most of entrapment conditions. This suggests that for a quartz inclusion in pyrope the use of an elastically isotropic model for geobarometry leads to small errors in the estimation of the entrapment pressure.

The opposite behavior is found in Fig. 7.10b where the isotropic strain is calculated applying non-linear elasticity for the relaxation. At P_{trap}, T_{trap} conditions above the isomeke the volume strain are still negative (i.e. compressive) but the discrepancy

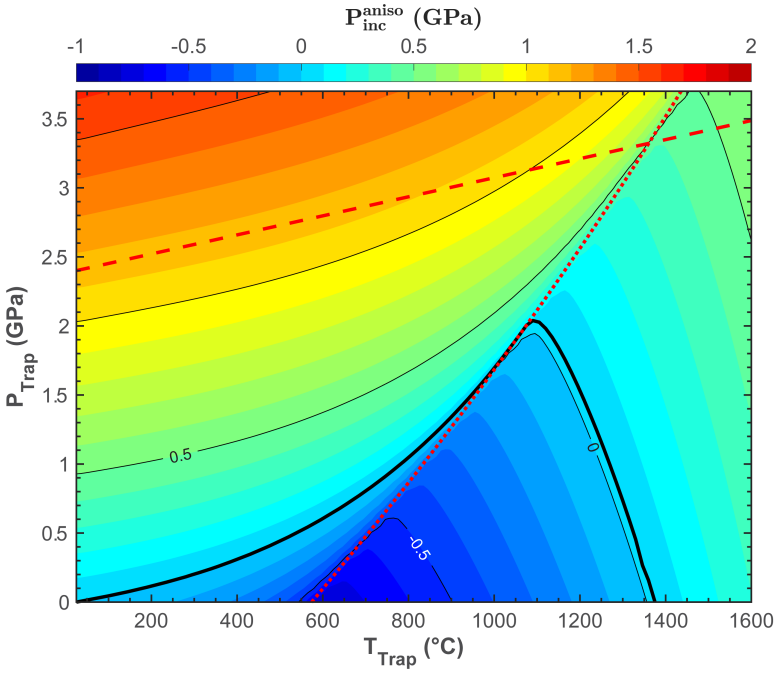

Figure 7.9: Quartz in pyrope: residual pressure in the inclusion obtained from the relaxed stress ($P_{inc} = -(\sigma_{11} + \sigma_{22} + \sigma_{33})/3$) as a function of the entrapment conditions (P_{trap}, T_{trap}). Dashed line: quartz-coesite phase transition (Bose and Ganguly, 1995); dotted line: $\alpha - \beta$ quartz phase transition (Angel et al., 2017a); solid line: zero-P_{inc} isomeke. The quartz-coesite phase transition is not included in the thermodynamic calculation, and all the results calculated for P_{trap}, T_{trap} conditions above the phase boundary do not represent the real behaviour.

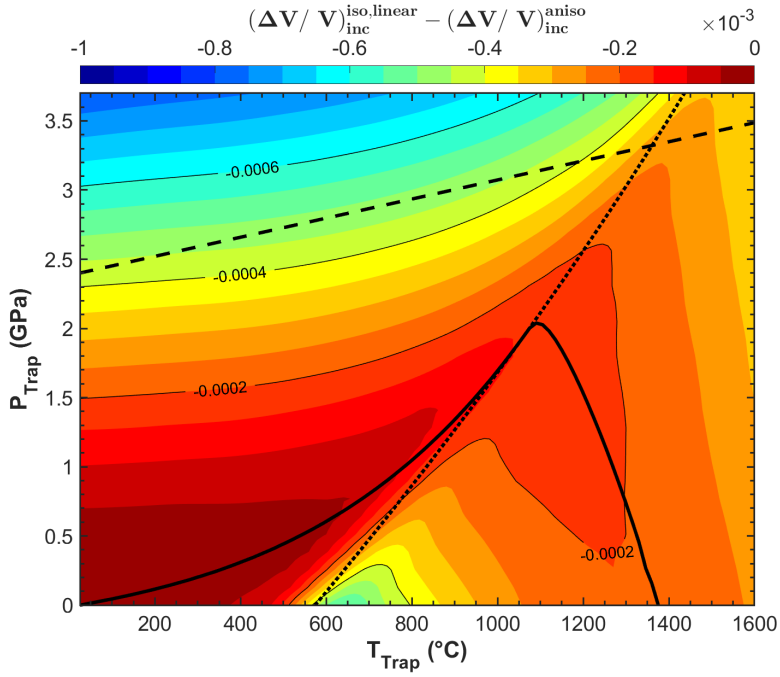

(a)

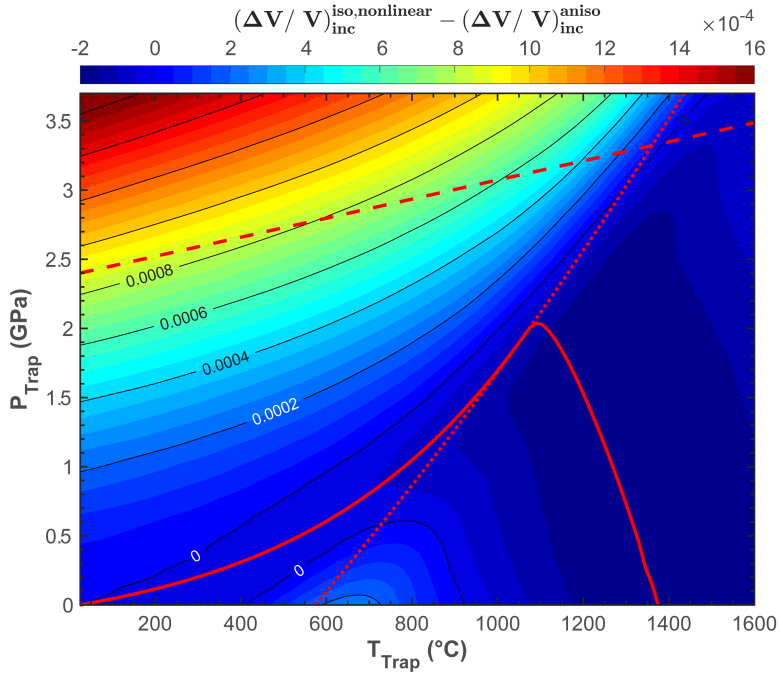

(b)

Figure 7.10: Quartz in pyrope: discrepancy between the relaxed volume strain of the inclusion calculated with isotropic and anisotropic elasticity as a function of the entrapment conditions (P_{trap}, T_{trap}). In the isotropic model the relaxation is calculated with: (a) linear elasticity (i.e. the elastic properties are constant); (b) non-linear elasticity (i.e. the elastic properties are allowed to change). Dashed line: quartz-coesite phase transition (Bose and Ganguly, 1995); dotted line: $\alpha - \beta$ quartz phase transition (Angel et al., 2017a); solid line: zero-P_{inc} isomeke. The quartz-coesite phase transition is not included in the thermodynamic calculation, and all the results calculated for P_{trap}, T_{trap} conditions above the phase boundary do not represent the real behaviour.

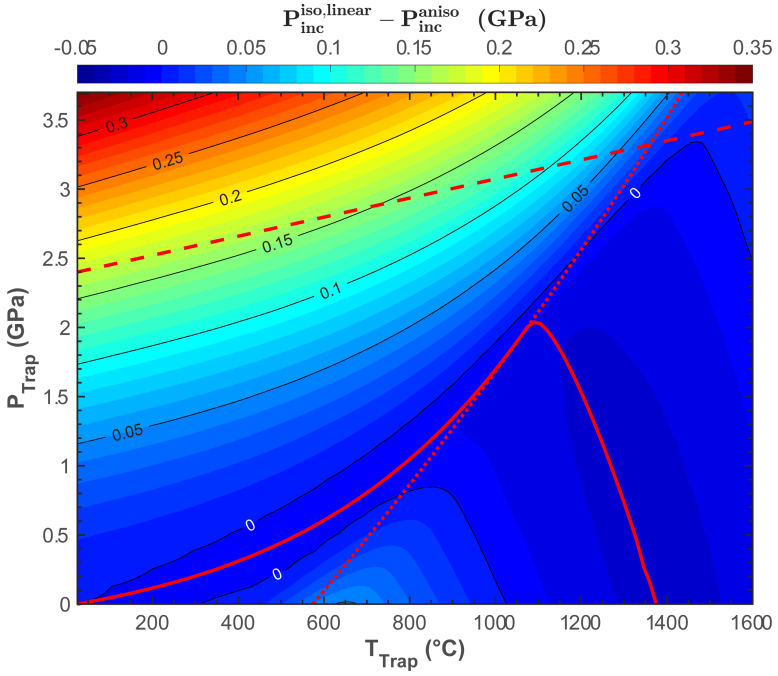

(a)

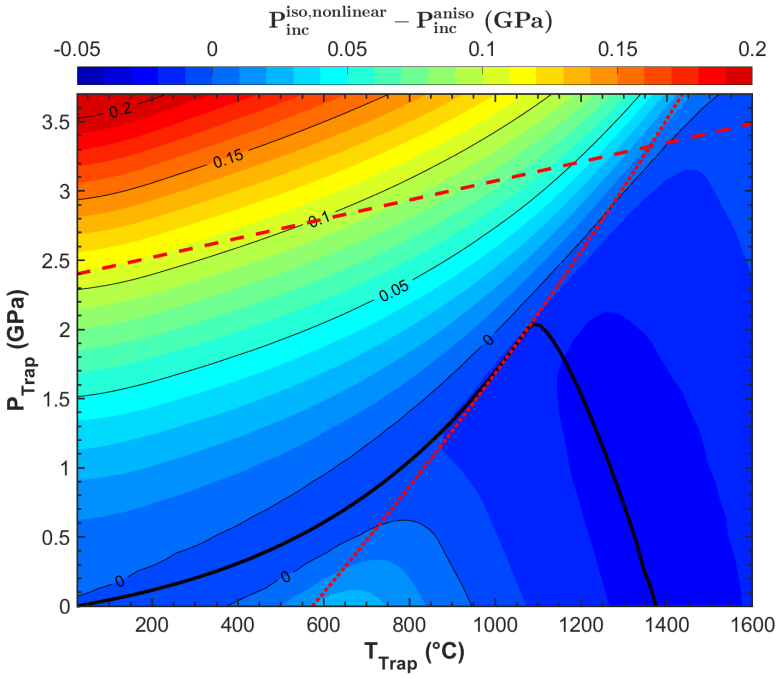

(b)

Figure 7.11: Quartz in pyrope: discrepancy between the residual pressure in the inclusion calculated with isotropic (P_{inc}^{iso}) and anisotropic (P_{inc}^{aniso}) elasticity as a function of the entrapment conditions (P_{trap}, T_{trap}). In the isotropic model the relaxation is calculated with: (a) linear elasticity (i.e. the elastic properties are constant); (b) non-linear elasticity (i.e. the elastic properties are allowed to change). Dashed line: quartz-coesite phase transition (Bose and Ganguly, 1995); dotted line: $\alpha-\beta$ quartz phase transition (Angel et al., 2017a); solid line: zero-P_{inc} isomeke. The quartz-coesite phase transition is not included in the thermodynamic calculation, and all the results calculated for P_{trap}, T_{trap} conditions above the phase boundary do not represent the real behaviour.

$(\Delta V/\ V)_{inc}^{iso,nonlinear} - (\Delta V/\ V)_{inc}^{aniso}$ is positive meaning that the isotropic inclusion is less compressed than the anisotropic case.

Discrepancy between the isotropic and the anisotropic P_{inc}

Fig. 7.11a shows the discrepancy between the relaxed pressure calculated assuming linear isotropic elasticity ($P_{inc}^{iso,linear}$) and linear anisotropic elasticity ($P_{inc}^{aniso} = -(\sigma_{11} + \sigma_{22} + \sigma_{33})/3$) for the relaxation. At P_{trap}, T_{trap} conditions above the isomeke the P_{inc} is positive and the discrepancy $P_{inc}^{iso,linear} - P_{inc}^{aniso}$ is positive meaning that the residual pressure of the isotropic calculation is higher than the pressure obtained form the anisotropic calculation. For a P_{inc} of 1 GPa the discrepancy is up to 0.15 GPa. This discrepancy is large compared to the relatively small discrepancy on the volume strain reported in Fig. 7.10a because of the bulk modulus of quartz used in isotropic solution that becomes rapidly stiffer with increasing P_{inc} (see example in Table 7.3).
Fig. 7.11b shows that the residual pressure calculated with non-linear isotropic elasticity is also higher then the anisotropic calculation at metamorphic conditions. This last result seems to disagree with what observed in Fig. 7.10b where the non-linear isotropic calculation gives a less compressed inclusion compared to the anisotropic calculation. This is shown with an example in Table 7.3 where the residual pressure and volume strain in the inclusion are reported for an entrapment at P_{trap}=2.5 GPa and T_{trap}=700 °C. This behavior is a consequence of the P-dependent isotropic elastic properties of the inclusion used to translate the volume strain into the P_{inc}^{iso} that are stiffer than the room-P anisotropic properties used to convert the relaxed strain into the relaxed stress, resulting in a $P_{inc}^{iso,nonlinear} > P_{inc}^{aniso}$.
These results show that, for a soft inclusion such as quartz, the discrepancy $P_{inc}^{iso} - P_{inc}^{aniso}$ is more affected by the assumption of constant elastic properties in the anisotropic relaxation rather than being a consequence of the anisotropic elasticity.

Table 7.3: Residual pressure and volume strain in the inclusion for an entrapment at P_{trap}=2.5 GPa and T_{trap}=700 °C. Pressures in GPa.

$(\Delta V/\ V)_{inc}^{aniso}$	$(\Delta V/\ V)_{inc}^{iso,linear}$	$(\Delta V/\ V)_{inc}^{iso,nonlinear}$
-0.0262	-0.0266	-0.0256
P_{inc}^{aniso}	$P_{inc}^{iso,linear}$	$P_{inc}^{iso,nonlinear}$
0.979	1.091	1.048
$(\Delta V/\ V)_{inc}^{iso,linear} - (\Delta V/\ V)_{inc}^{aniso}$		$(\Delta V/\ V)_{inc}^{iso,nonlinear} - (\Delta V/\ V)_{inc}^{aniso}$
-0.0004		0.0006
$P_{inc}^{iso,linear} - P_{inc}^{aniso}$		$P_{inc}^{iso,nonlinear} - P_{inc}^{aniso}$
0.112		0.069

7.2.2 Quartz in grossular

The anisotropic relaxation tensor was calculated for a spherical quartz inclusion in grossular garnet with the elastic properties reported in Tables B.7 and B.3 and with relative orientation $\boldsymbol{a}_{qtz}||\boldsymbol{a}_{grs}$, $\boldsymbol{c}_{qtz}||\boldsymbol{c}_{grs}$ (i.e. the host and the inclusion have the same orientation):

$$R_{ij} = \begin{pmatrix} 0.76332 & 0.02405 & 0.02385 & -0.02912 & 0.00000 & 0.00000 \\ 0.02405 & 0.76332 & 0.02385 & 0.02912 & 0.00000 & 0.00000 \\ 0.01398 & 0.01398 & 0.72146 & 0.00000 & 0.00000 & 0.00000 \\ -0.05904 & 0.05904 & 0.00000 & 0.65187 & 0.00000 & 0.00000 \\ 0.00000 & 0.00000 & 0.00000 & 0.00000 & 0.65192 & -0.05883 \\ 0.00000 & 0.00000 & 0.00000 & 0.00000 & -0.05883 & 0.73665 \end{pmatrix}$$

Relaxed strain, stress and pressure in the inclusion as a function of the entrapment conditions

The EoS for quartz and grossular used for the thermodynamic part of the anisotropic calculation and for the isotropic calculation are from Angel et al. (2017a) and Milani et al., 2017, respectively. As for quartz in pyrope, the unrelaxed strain on the quartz inclusion referred to a free quartz at room conditions can be found from equation (4.4) and in general is anisotropic. The relaxed strain in the inclusion is isotropic only for a limited range of entrapment P_{trap}, T_{trap} conditions (Fig. 7.12). Compared to the case of a pyrope host, the strain is slightly more deviatoric due to grossular being more anisotropic than pyrope (Universal anisotropic index A^U: 0.011 for grossular compared to 0.001 for pyrope).

The numerical precision on the calculations (see section 6.2 and equations 6.1 - 6.4) is

$\delta(\varepsilon_i^{rel}) \approx 6 \cdot 10^{-6}$ on the components of the relaxed strain, $\delta(\sigma_i^{rel}) \approx 7 \cdot 10^{-4}$ GPa on the components of the relaxed stress, $\delta(P_{inc}) \approx 7 \cdot 10^{-4}$ GPa on the residual pressure, $\delta\left(\frac{\Delta V}{V}\right) \approx 1 \cdot 10^{-5}$ on the relaxed volume strain.

Discrepancy between the isotropic and the anisotropic calculations The comparison of Fig. 7.10 and 7.13 shows that the discrepancy between the isotropic (linear and non-linear) and the anisotropic volume strain in the inclusion ($(\Delta V/\ V)_{inc}^{iso} - (\Delta V/\ V)_{inc}^{aniso}$) is slightly smaller in magnitude compared to the case of a pyrope host. The same is observed in Fig. 7.14 for the discrepancy in the residual pressure ($P_{inc}^{iso} - P_{inc}^{aniso}$). This is a consequence of grossular being slightly stiffer than pyrope (cf. Tables B.6 and B.4). These results suggest that for a quartz inclusion in grossular the use of an elastically isotropic model for geobarometry leads to small errors in the estimation of the entrapment pressure.

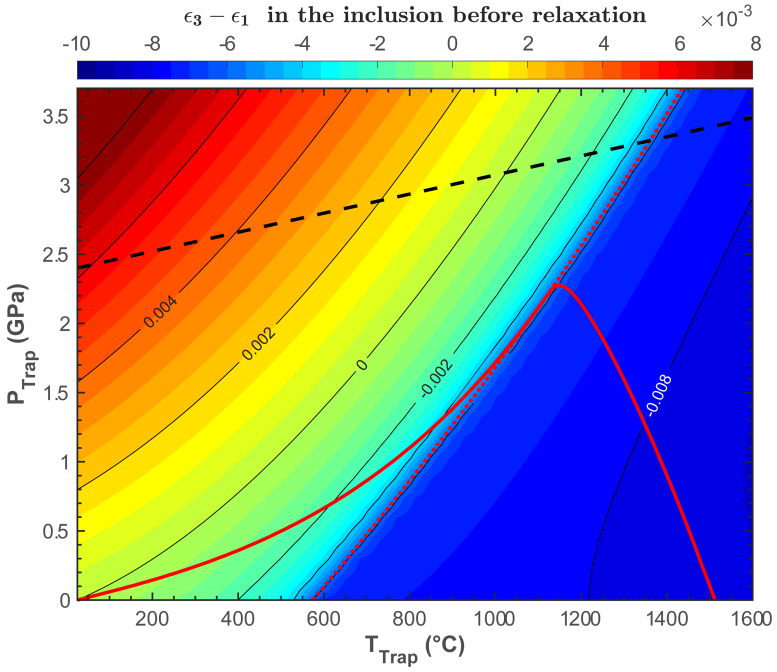

(a)

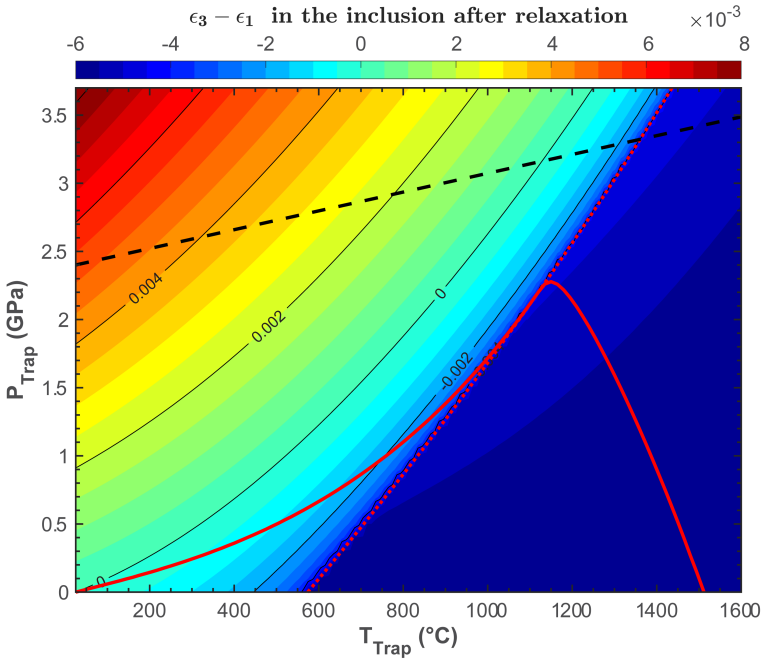

(b)

Figure 7.12: Quartz in grossular: differential strain ($\varepsilon_3 - \varepsilon_1$) in the quartz inclusion before (a) and after (b) the elastic relaxation, as a function of the entrapment conditions (P_{trap}, T_{trap}). Dashed line: quartz-coesite phase transition (Bose and Ganguly, 1995); dotted line: $\alpha - \beta$ quartz phase transition (Angel et al., 2017a); solid line: zero-P_{inc} isomeke. The quartz-coesite phase transition is not included in the thermodynamic calculation, and all the results calculated for P_{trap}, T_{trap} conditions above the phase boundary do not represent the real behaviour.

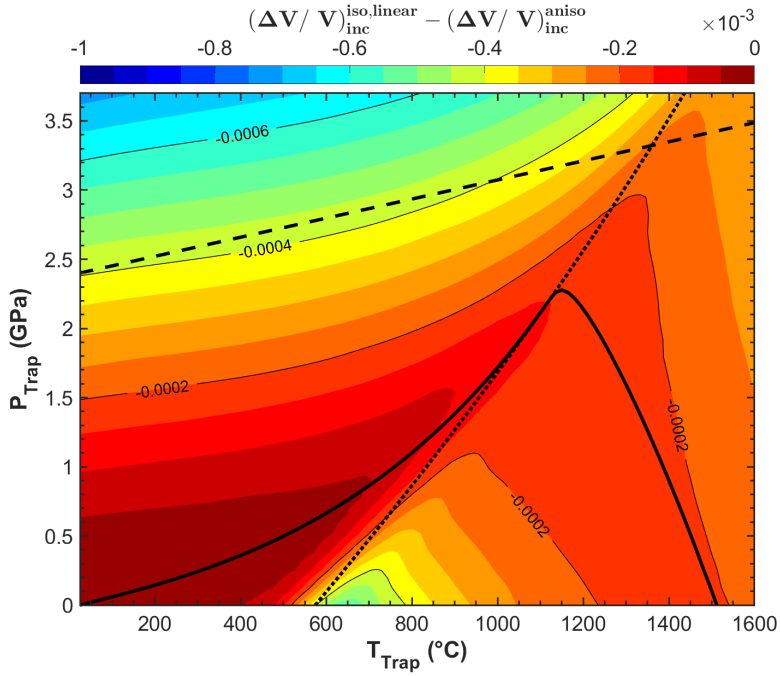

(a)

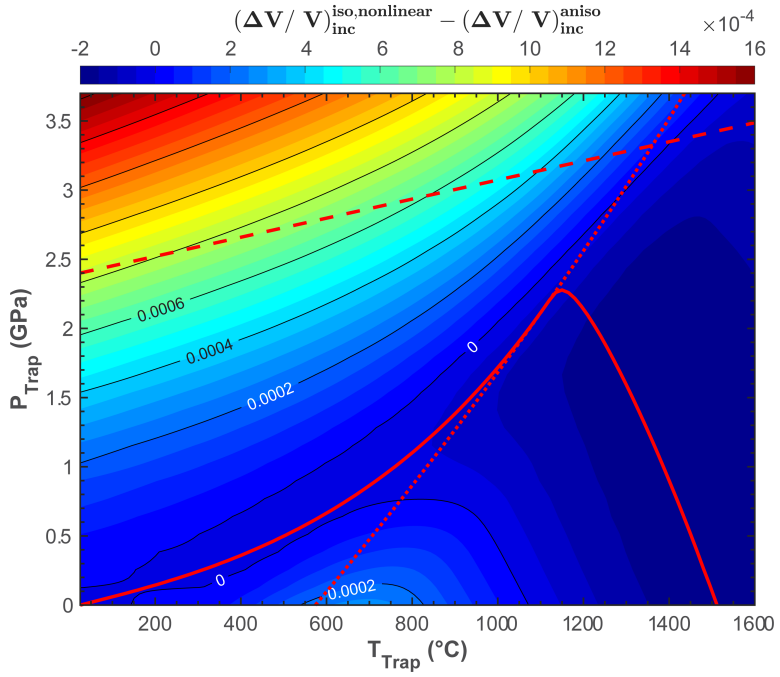

(b)

Figure 7.13: Quartz in grossular: discrepancy between the relaxed volume strain of the inclusion calculated with isotropic and anisotropic elasticity as a function of the entrapment conditions (P_{trap}, T_{trap}). In the isotropic model the relaxation is calculated with: (a) linear elasticity (i.e. the elastic properties are constant); (b) non-linear elasticity (i.e. the elastic properties are allowed to change). Dashed line: quartz-coesite phase transition (Bose and Ganguly, 1995); dotted line: $\alpha - \beta$ quartz phase transition (Angel et al., 2017a); solid line: zero-P_{inc} isomeke. The quartz-coesite phase transition is not included in the thermodynamic calculation, and all the results calculated for P_{trap}, T_{trap} conditions above the phase boundary do not represent the real behaviour.

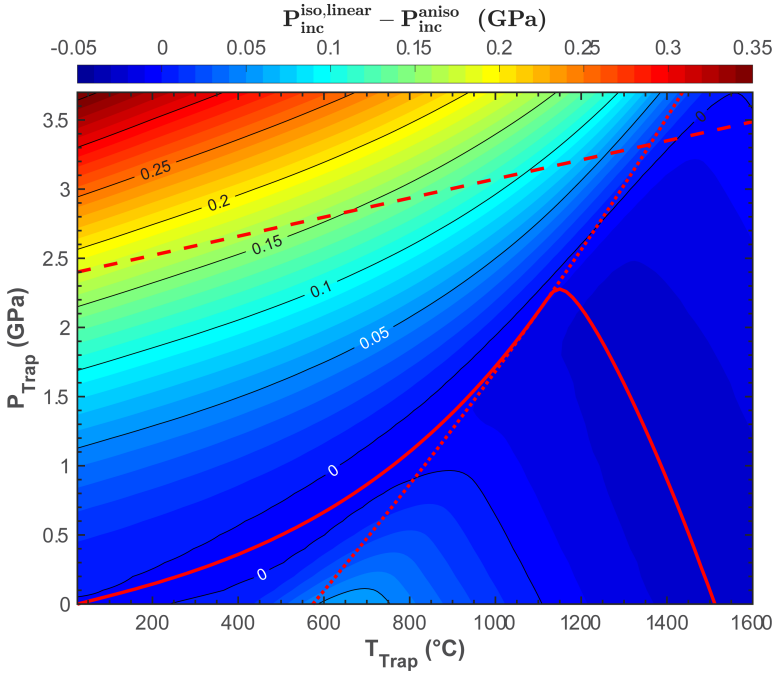

(a)

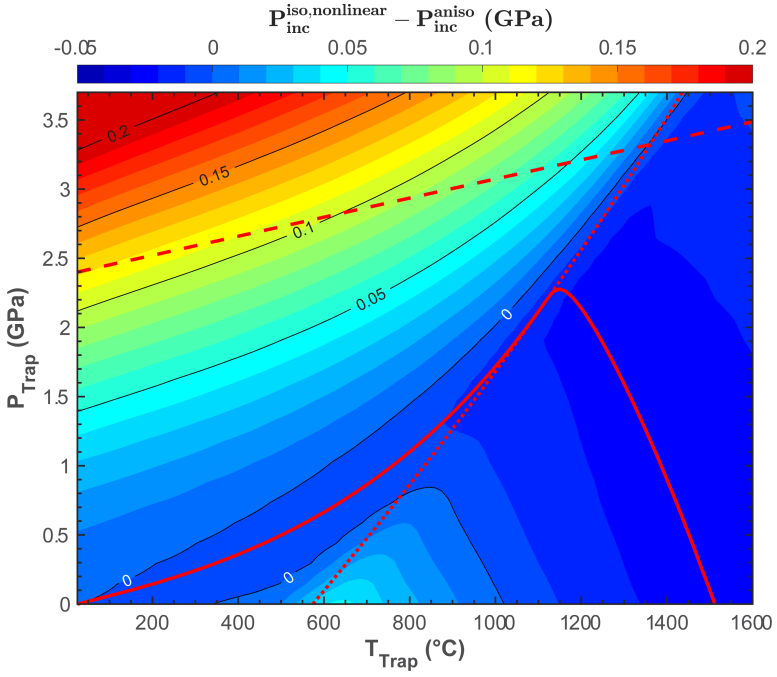

(b)

Figure 7.14: Quartz in grossular: discrepancy between the residual pressure in the inclusion calculated with isotropic (P_{inc}^{iso}) and anisotropic (P_{inc}^{aniso}) elasticity as a function of the entrapment conditions (P_{trap}, T_{trap}). In the isotropic model the relaxation is calculated with: (a) linear elasticity (i.e. the elastic properties are constant); (b) non-linear elasticity (i.e. the elastic properties are allowed to change). Dashed line: quartz-coesite phase transition (Bose and Ganguly, 1995); dotted line: $\alpha-\beta$ quartz phase transition (Angel et al., 2017a); solid line: zero-P_{inc} isomeke. The quartz-coesite phase transition is not included in the thermodynamic calculation, and all the results calculated for P_{trap}, T_{trap} conditions above the phase boundary do not represent the real behaviour.

7.2.3 Zircon in pyrope

The anisotropic relaxation tensor was calculated for a spherical zircon inclusion in pyrope with the elastic properties reported in Tables B.10 and B.5 with relative orientation $\boldsymbol{a}_{zrc}||\boldsymbol{a}_{pyr}$ and $\boldsymbol{c}_{zrc}||\boldsymbol{c}_{pyr}$:

$$R_{ij} = \begin{pmatrix} 0.38440 & 0.02445 & -0.01846 & 0.00000 & 0.00000 & 0.00000 \\ 0.02445 & 0.38440 & -0.01846 & 0.00000 & 0.00000 & 0.00000 \\ -0.03501 & -0.03501 & 0.35508 & 0.00000 & 0.00000 & 0.00000 \\ 0.00000 & 0.00000 & 0.00000 & 0.46567 & 0.00000 & 0.00000 \\ 0.00000 & 0.00000 & 0.00000 & 0.00000 & 0.46567 & 0.00000 \\ 0.00000 & 0.00000 & 0.00000 & 0.00000 & 0.00000 & 0.67120 \end{pmatrix}$$

Relaxed strain, stress and pressure in the inclusion as a function of the entrapment conditions

The strain and the stress developed in the inclusion during the exhumation were investigated as a function of a wide range of entrapment conditions (P_{trap}, T_{trap}) following the procedure outlined in chapter 6.1. The EoS for zircon and pyrope used for the thermodynamic part of the anisotropic calculation and for the isotropic calculation are from Zaffiro (personal communication) and Milani et al. (2015), respectively. Since pyrope has cubic crystallographic symmetry, it follows from equation (4.2) that the strain imposed on zircon during the exhumation under an external lithostatic load, is isotropic if referred to the initial state at P_{trap}, T_{trap}. The unrelaxed strain on the zircon inclusion referred to a free zircon at room conditions can be found from equation (4.4) and in general is anisotropic (Fig. 7.15a).

The numerical precision on the calculations (see section 6.2 and equations 6.1 - 6.4) is $\delta(\varepsilon_i^{rel}) \approx 4 \cdot 10^{-7}$ on the components of the relaxed strain, $\delta(\sigma_i^{rel}) \approx 3 \cdot 10^{-4}$ GPa on the components of the relaxed stress, $\delta(P_{inc}) \approx 3 \cdot 10^{-4}$ GPa on the residual pressure, $\delta\left(\frac{\Delta V}{V}\right) \approx 1 \cdot 10^{-6}$ on the relaxed volume strain.

Differential strain and stress in the inclusion

Fig. 7.15 shows the differential strain $\varepsilon_3 - \varepsilon_1$ before and after the elastic relaxation. The strain in the inclusion is isotropic only for an entrapment at room conditions (Fig. 7.15). For any other entrapment P_{trap}, T_{trap} the difference $\varepsilon_3 - \varepsilon_1$ is always positive. This is a consequence of the c axis in zircon having a lower compressibility ($M_{0,c} = 0.994 \cdot 10^{-3}$ GPa^{-1}, $M_{0,a} = 1.73 \cdot 10^{-3}$ GPa^{-1}) but larger thermal expansion ($\alpha_{0,c} = 0.4635 \cdot 10^{-5}$ K^{-1}, $\alpha_{0,a} = 0.2956 \cdot 10^{-5}$ K^{-1}) compared to the a and b axes.

Comparing Fig. 7.15b and 7.16b it can be seen that when the differential strain is low (i.e. for entrapment at P_{trap}, T_{trap} close to room conditions) also the differential

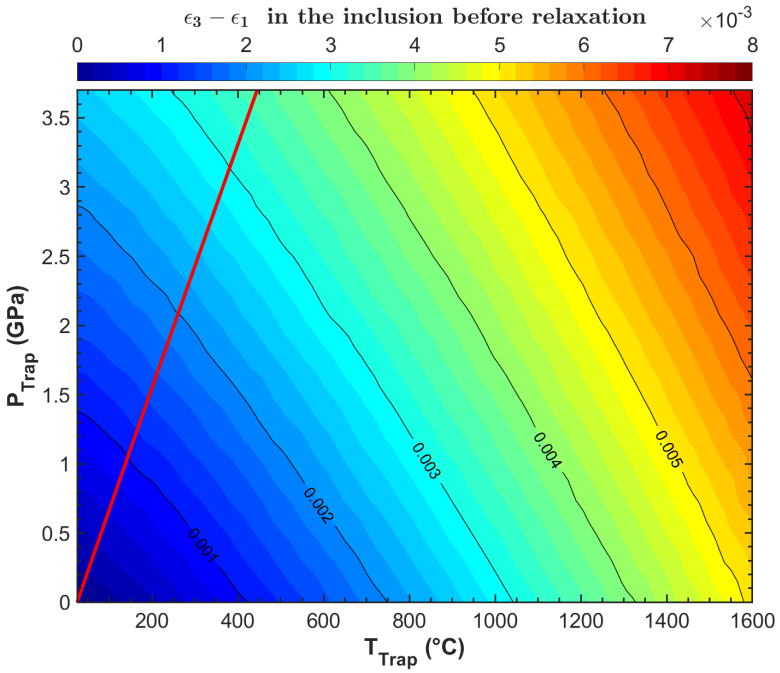

(a)

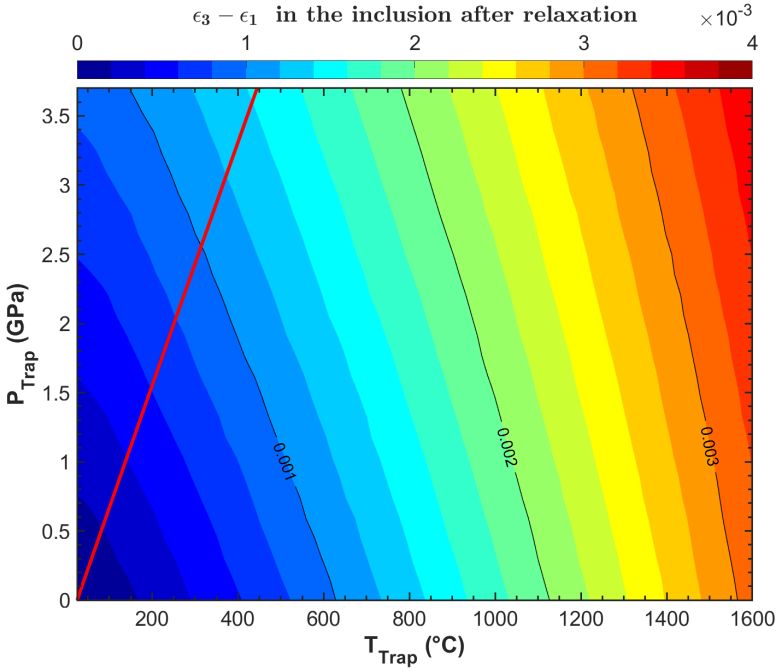

(b)

Figure 7.15: Zircon in pyrope: differential strain ($\varepsilon_3 - \varepsilon_1$) in the inclusion before (a) and after (b) the elastic relaxation, as a function of the entrapment conditions (P_{trap}, T_{trap}). Solid line: zero-P_{inc} isomeke.

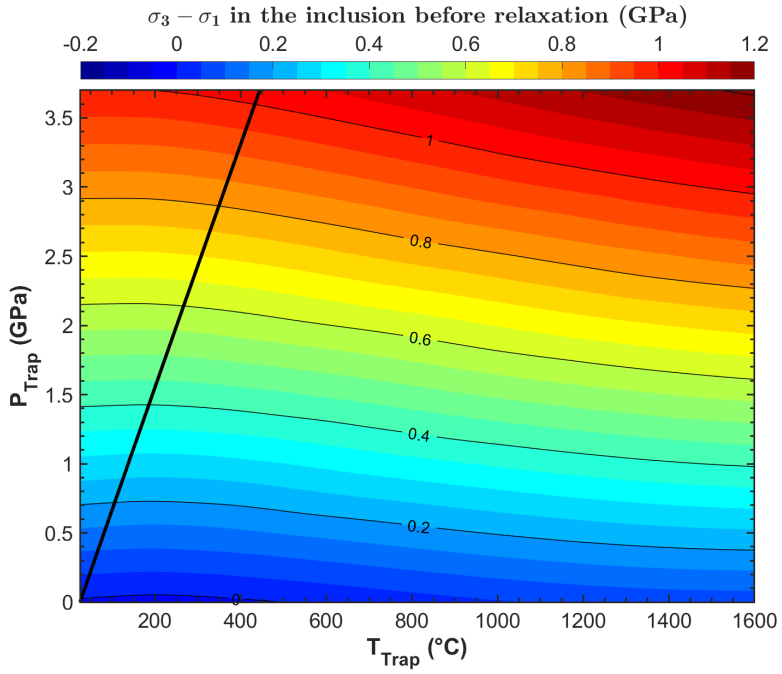

(a)

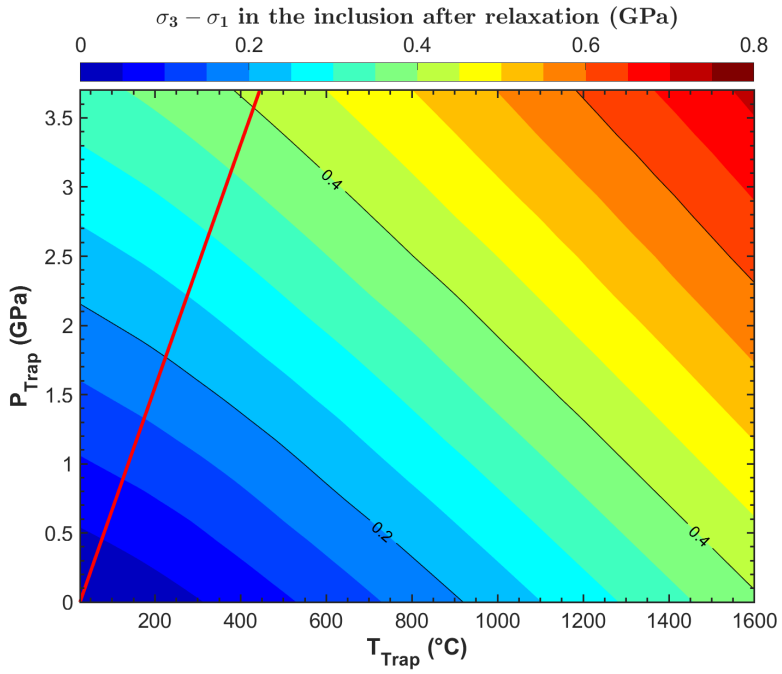

(b)

Figure 7.16: Zircon in pyrope: differential stress ($\sigma_3 - \sigma_1$) in the zircon inclusion before (a) and after (b) the elastic relaxation, as a function of the entrapment conditions (P_{trap}, T_{trap}). Solid line: zero-P_{inc} isomeke.

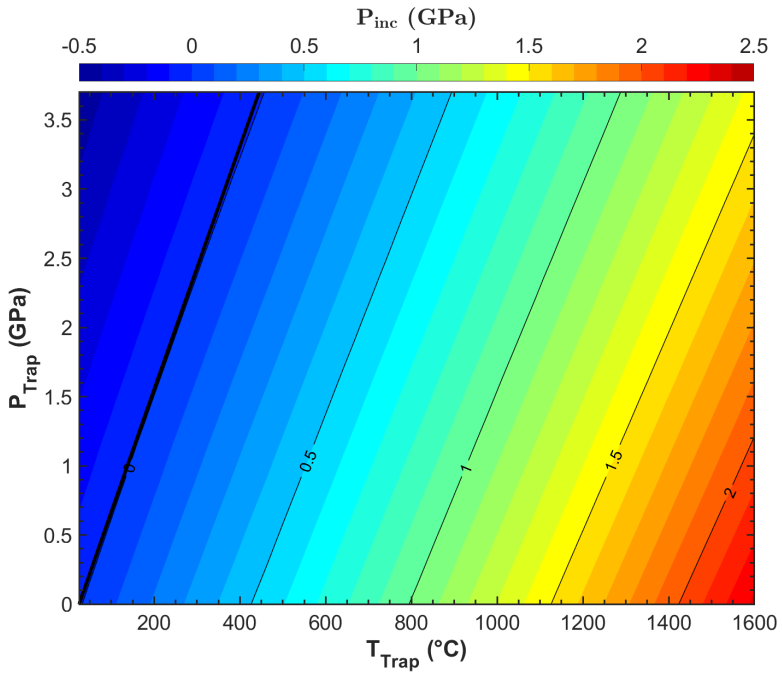

Figure 7.17: Zircon in pyrope: residual pressure in the inclusion obtained from the relaxed stress ($P_{inc} = -(\sigma_{11}+\sigma_{22}+\sigma_{33})/3$) as a function of the entrapment conditions (P_{trap}, T_{trap}). Solid line: zero-P_{inc} isomeke.

stress is low. Since the inclusion is not cubic but tetragonal, when the relaxed strain is isotropic the relaxed stress is not hydrostatic. Therefore, even if both the areas of small differential strain (Fig. 7.15b) and those of small differential stress (Fig. 7.15b) fall at low P_{trap}, T_{trap} conditions, they do not overlap perfectly. By comparing the strain (Fig. 7.15) and the stress (Fig. 7.16) before and after the elastic relaxation it can be seen that the maximum differential strain and differential stress are reduced after the elastic relaxation.

Residual pressure ($\mathbf{P_{inc}}$)

The residual pressure in the inclusion, obtained form the anisotropic calculation as $P_{inc}^{aniso} = -(\sigma_{11}+\sigma_{22}+\sigma_{33})/3$, is negative above the zero-P_{inc} isomeke and positive below as expected for a stiff inclusion in a soft host (Fig. 7.17). The line of $P_{inc} = 0$ GPa obtained from the anisotropic calculation overlaps perfectly with the zero-P_{inc} isomeke, that is based on isotropic elasticity, indicating a close agreement between the isotropic and the anisotropic calculations.

Discrepancy between the isotropic and the anisotropic volume strain

Fig. 7.18a shows the discrepancy between the volume strain in the inclusion calculated

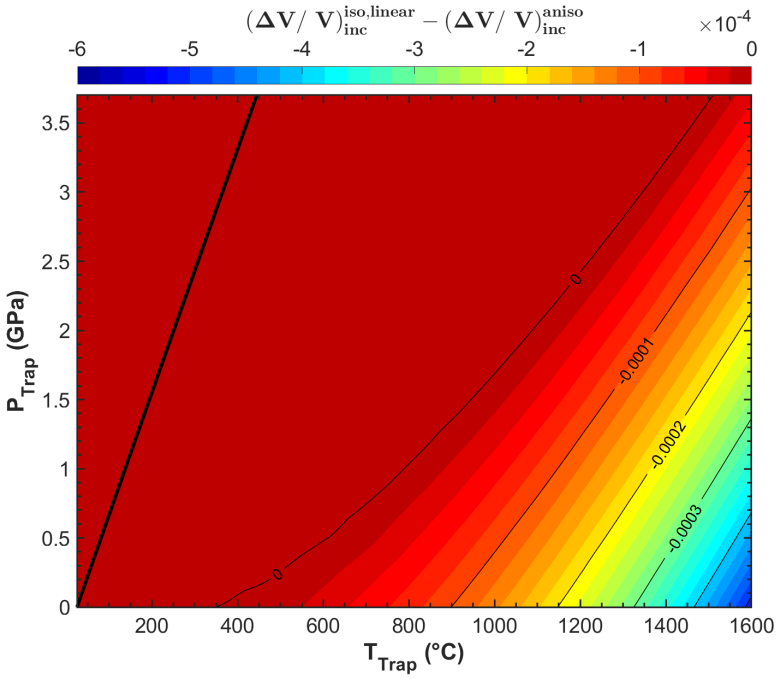

(a)

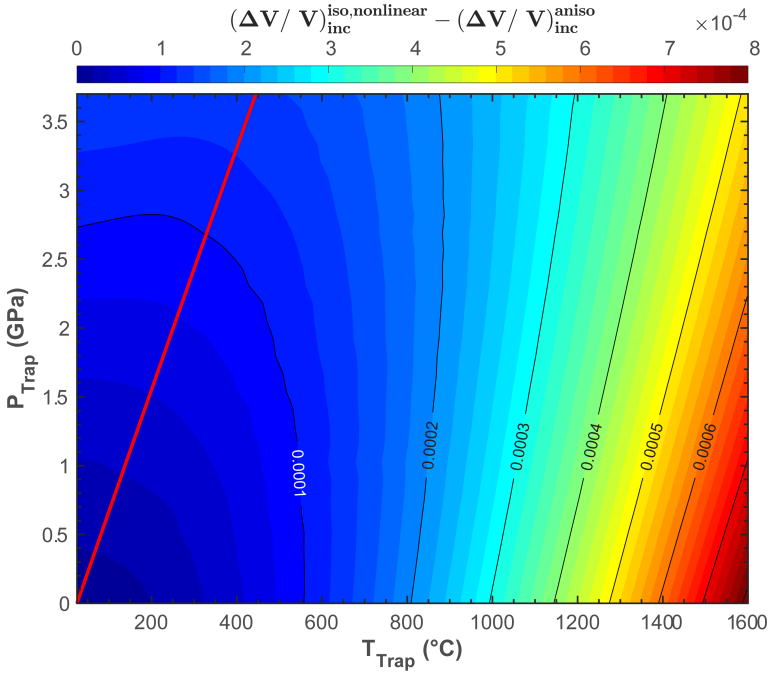

(b)

Figure 7.18: Zircon in pyrope: discrepancy between the relaxed volume strain of the inclusion calculated with isotropic and anisotropic elasticity as a function of the entrapment conditions (P_{trap}, T_{trap}). In the isotropic model the relaxation is calculated with: (a) linear elasticity (i.e. the elastic properties are constant); (b) non-linear elasticity (i.e. the elastic properties are allowed to change). Solid line: zero-P_{inc} isomeke.

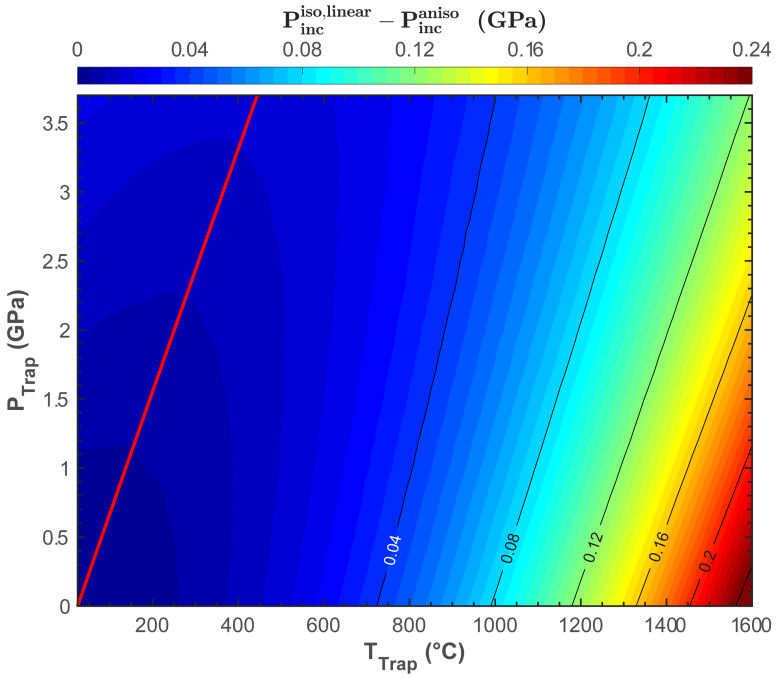

(a)

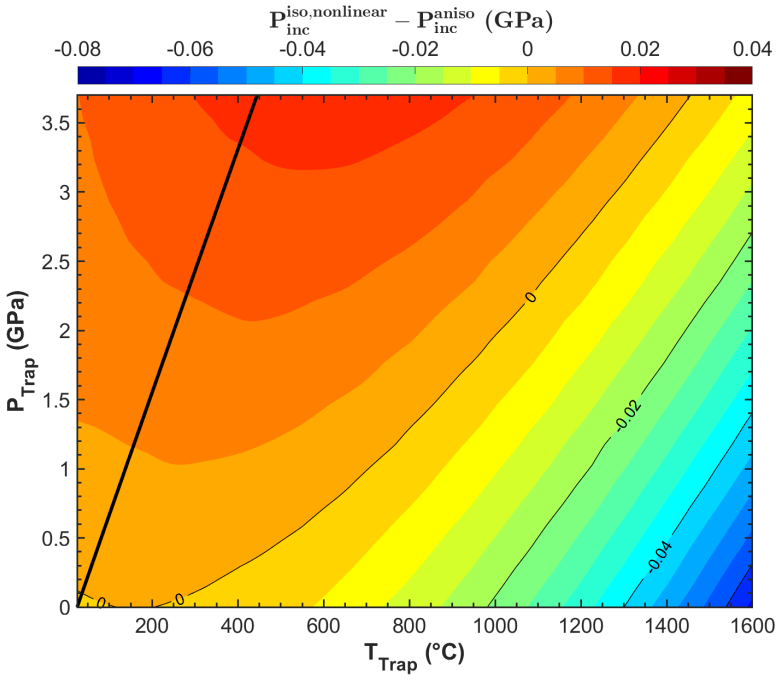

(b)

Figure 7.19: Zircon in pyrope: discrepancy between the residual pressure in the inclusion calculated with isotropic (P_{inc}^{iso}) and anisotropic (P_{inc}^{aniso}) elasticity as a function of the entrapment conditions (P_{trap}, T_{trap}). In the isotropic model the relaxation is calculated with: (a) linear elasticity (i.e. the elastic properties are constant); (b) non-linear elasticity (i.e. the elastic properties are allowed to change). Solid line: zero-P_{inc} isomeke.

assuming linear isotropic elasticity ($(\Delta V/\ V)_{inc}^{iso,linear}$) and linear anisotropic elasticity ($(\Delta V/\ V)_{inc}^{aniso} = \varepsilon_{11} + \varepsilon_{22} + \varepsilon_{33}$) for the relaxation. At P_{trap}, T_{trap} conditions below the isomeke the volume strains are negative (i.e. compressive) and the discrepancy $(\Delta V/\ V)_{inc}^{iso,linear} - (\Delta V/\ V)_{inc}^{aniso}$ is negative meaning that the isotropic inclusion is more compressed than the anisotropic case. This implies that the anisotropic inclusion tends to relax more than the isotropic inclusion when both the calculations assume linear elasticity for the relaxation. The discrepancy between the isotropic and the anisotropic calculation are expected to be smaller than the typical experimental uncertainties on the determination of the volume strain in natural inclusions ($\delta\left(\frac{\Delta V}{V}\right) \approx 3 \cdot 10^{-4}$) for most of entrapment conditions. This suggests that for a zircon inclusion in pyrope the use of an elastically isotropic model for geobarometry leads to small errors in the estimation of the entrapment pressure.
The opposite behavior is found in Fig. 7.18b where the isotropic strain is calculated applying non-linear elasticity for the relaxation. At P_{trap}, T_{trap} conditions above the isomeke the volume strain are still negative (i.e. compressive) but the discrepancy $(\Delta V/\ V)_{inc}^{iso,nonlinear} - (\Delta V/\ V)_{inc}^{aniso}$ is positive meaning that the isotropic inclusion is less compressed than the anisotropic case.

Discrepancy between the isotropic and the anisotropic $\mathbf{P_{inc}}$
Fig. 7.19a shows the discrepancy between the relaxed pressure calculated assuming linear isotropic elasticity ($P_{inc}^{iso,linear}$) and linear anisotropic elasticity ($P_{inc}^{aniso} = -(\sigma_{11} + \sigma_{22} + \sigma_{33})/3$) for the relaxation. At P_{trap}, T_{trap} conditions below the isomeke the P_{inc} is positive and the discrepancy $P_{inc}^{iso,linear} - P_{inc}^{aniso}$ is positive meaning that the residual pressure of the isotropic calculation is higher than the pressure obtained form the anisotropic calculation. As an example, for a P_{inc} less than 1 GPa the discrepancy is smaller than 0.05 GPa.
The opposite behaviour is observed in Fig. 7.19b where the residual pressure calculated with non-linear isotropic elasticity is lower than the anisotropic calculation at metamorphic conditions, in agreement with what observed in Fig. 7.18b where the non-linear isotropic calculation gives a less compressed inclusion compared to the anisotropic calculation. For a P_{inc} less than 1 GPa the discrepancy is smaller in magnitude than 0.015 GPa.

7.2.4 Zircon in grossular

The anisotropic relaxation tensor was calculated for a spherical zircon inclusion in grossular garnet with the elastic properties reported in Tables B.10 and B.3 and with relative orientation $\boldsymbol{a}_{Zrc} || \boldsymbol{a}_{grs}$, $\boldsymbol{c}_{Zrc} || \boldsymbol{c}_{grs}$ (i.e. the host and the inclusion have the same orientation):

$$R_{ij} = \begin{pmatrix} 0.41121 & 0.02614 & -0.01755 & 0.00000 & 0.00000 & 0.00000 \\ 0.02614 & 0.41121 & -0.01755 & 0.00000 & 0.00000 & 0.00000 \\ -0.03491 & -0.03491 & 0.38090 & 0.00000 & 0.00000 & 0.00000 \\ 0.00000 & 0.00000 & 0.00000 & 0.49003 & 0.00000 & 0.00000 \\ 0.00000 & 0.00000 & 0.00000 & 0.00000 & 0.49003 & 0.00000 \\ 0.00000 & 0.00000 & 0.00000 & 0.00000 & 0.00000 & 0.69237 \end{pmatrix}$$

Relaxed strain, stress and pressure in the inclusion as a function of the entrapment conditions

The EoS for zircon and grossular used for the thermodynamic part of the anisotropic calculation and for the isotropic calculation are from Angel et al. (2017a) and Milani et al. (2017), respectively. As for zircon in pyrope, the unrelaxed strain on the zircon inclusion referred to a free zircon at room conditions can be found from equation (4.4) and in general is anisotropic. The relaxed strain in the inclusion is isotropic only for a limited range of entrapment P_{trap}, T_{trap} conditions (Fig. 7.20).

Discrepancy between the isotropic and the anisotropic calculations

The comparison of Fig. 7.18 and 7.21 shows that the discrepancy between the isotropic (linear and non-linear) and the anisotropic volume strain in the inclusion ($(\Delta V/\ V)^{iso}_{inc} - (\Delta V/\ V)^{aniso}_{inc}$) is slightly smaller in magnitude compared to the case of a pyrope host. The same is observed in Fig. 7.22 for the discrepancy in the residual pressure ($P^{iso}_{inc} - P^{aniso}_{inc}$). This is a consequence of grossular being slightly stiffer than pyrope (cf. Tables B.6 and B.4). These results suggest that for a zircon inclusion in grossular the use of an elastically isotropic model for geobarometry leads to small errors in the estimation of the entrapment pressure.

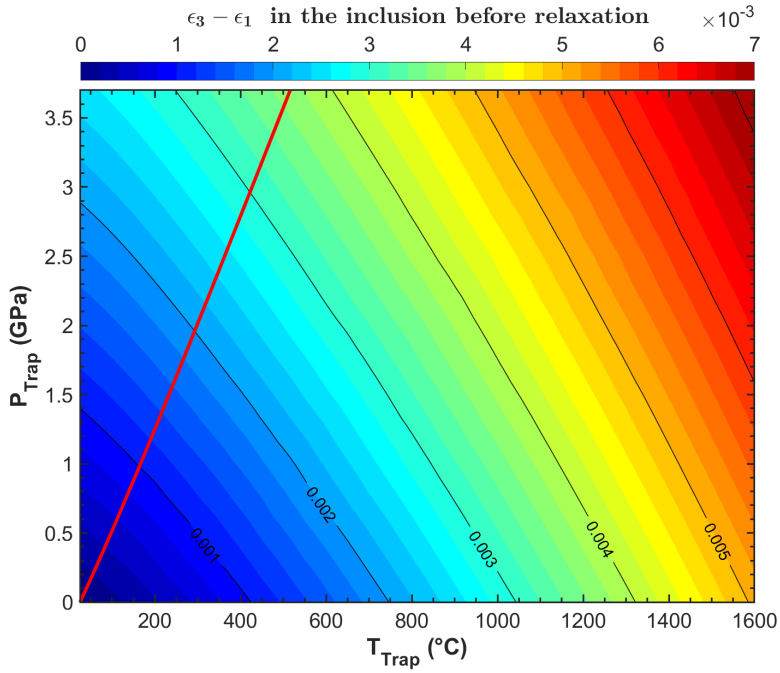

(a)

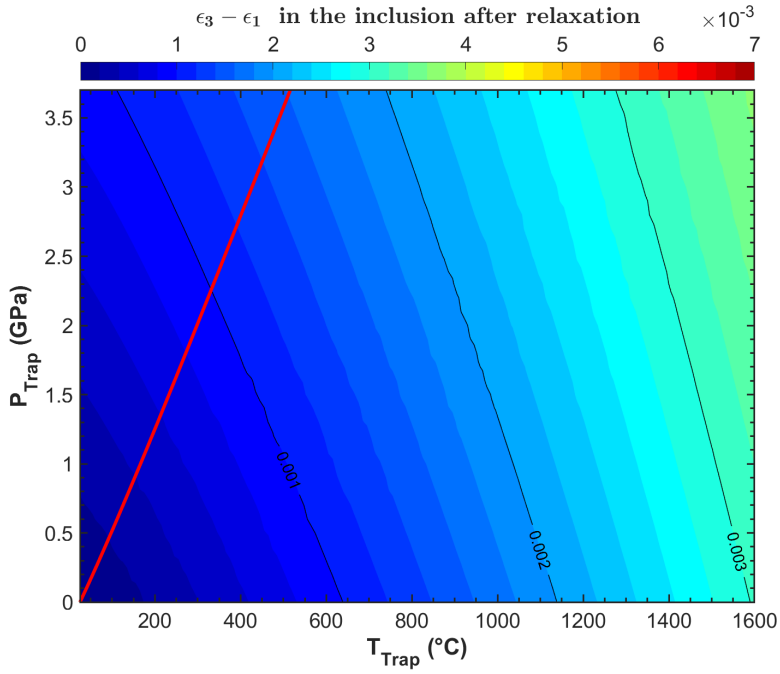

(b)

Figure 7.20: Zircon in grossular: differential strain ($\varepsilon_3 - \varepsilon_1$) in the zircon inclusion before (a) and after (b) the elastic relaxation, as a function of the entrapment conditions (P_{trap}, T_{trap}). Solid line: zero-P_{inc} isomeke.

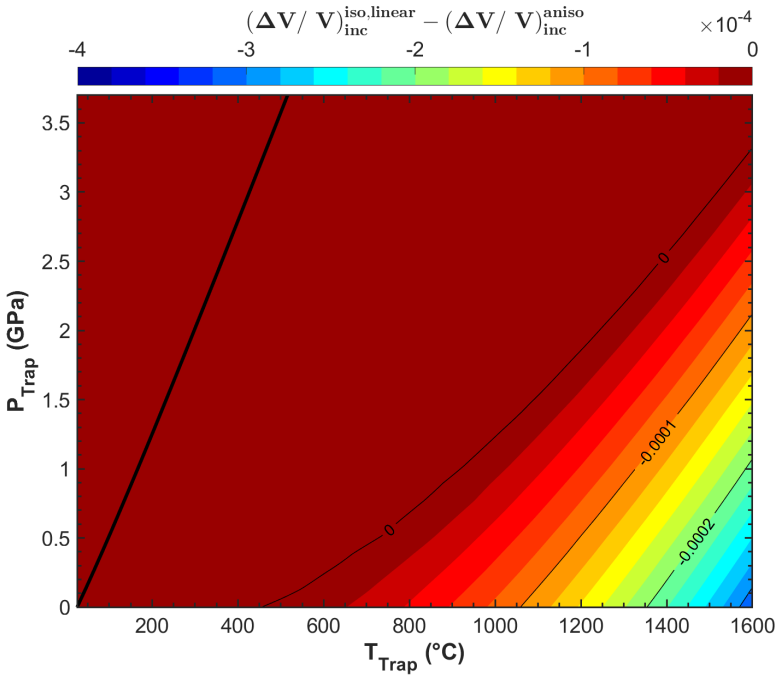

(a)

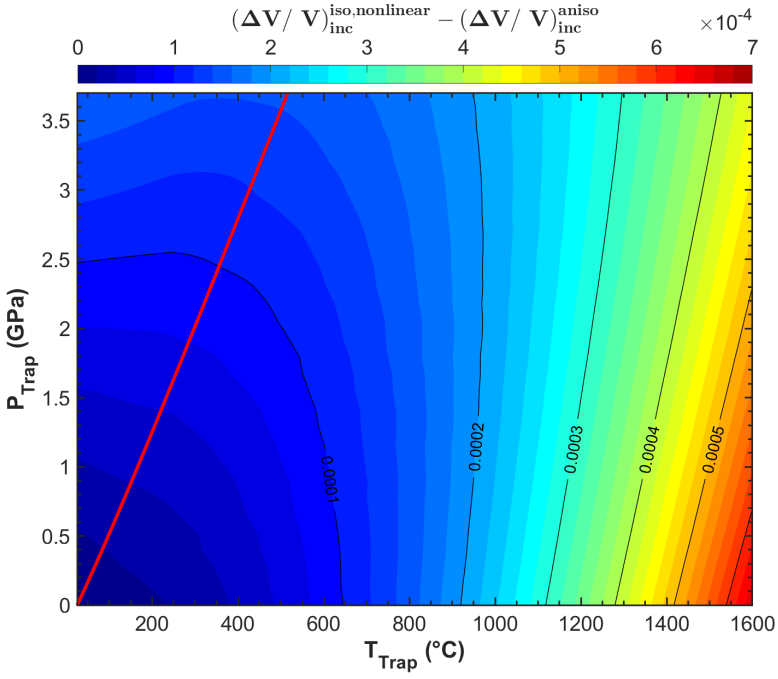

(b)

Figure 7.21: Zircon in grossular: discrepancy between the relaxed volume strain of the inclusion calculated with isotropic and anisotropic elasticity as a function of the entrapment conditions (P_{trap}, T_{trap}). In the isotropic model the relaxation is calculated with: (a) linear elasticity (i.e. the elastic properties are constant); (b) non-linear elasticity (i.e. the elastic properties are allowed to change). Solid line: zero-P_{inc} isomeke.

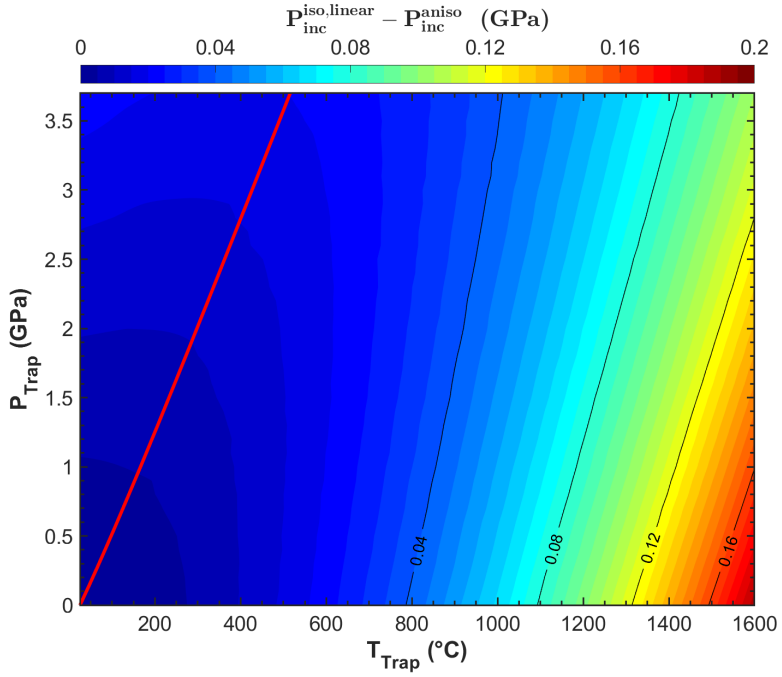

(a)

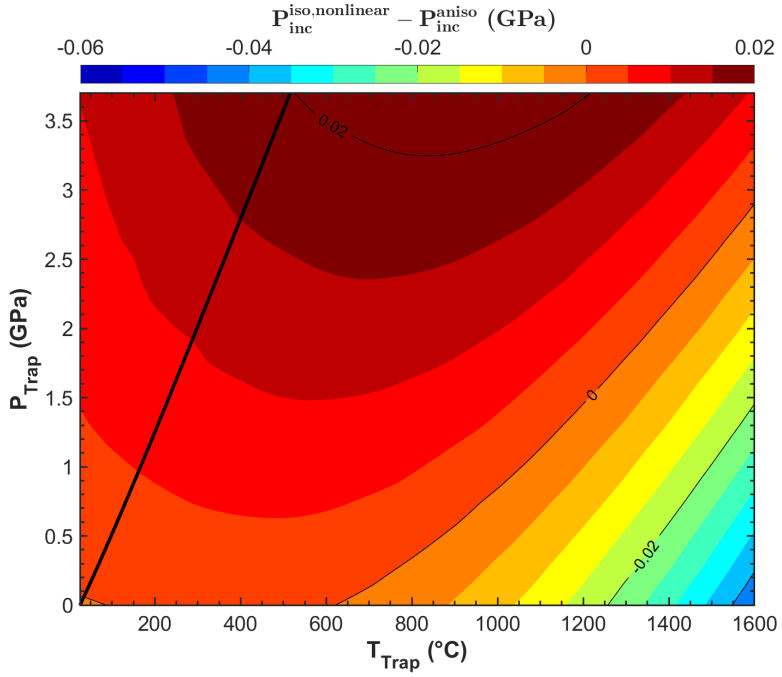

(b)

Figure 7.22: Zircon in grossular: discrepancy between the residual pressure in the inclusion calculated with isotropic (P_{inc}^{iso}) and anisotropic (P_{inc}^{aniso}) elasticity as a function of the entrapment conditions (P_{trap}, T_{trap}). In the isotropic model the relaxation is calculated with: (a) linear elasticity (i.e. the elastic properties are constant); (b) non-linear elasticity (i.e. the elastic properties are allowed to change). Solid line: zero-P_{inc} isomeke.

Chapter 8

Relative orientations between the host and the inclusion

The strain and the stress fields developed in an inclusion entrapped in an elastically isotropic host are not affected by the relative orientation between the two minerals. If the initial (P_{trap}, T_{trap} at entrapment) and the final (P_{room}, T_{room}) conditions are under external lithostatic stress, an isotropic host will always impose an isotropic strain field on the inclusion, and therefore the strain in the inclusion is not affected by its orientation within the host. An elastically isotropic host would allow the inclusion to relax equally in every direction and therefore in the inclusion the difference between the principal components of the relaxed strain is only a consequence of its elastic anisotropy, that is not affected by its orientation within the host. On the contrary, if both the host and the inclusion are elastically anisotropic the strain and the stress calculated in the inclusion are function of the relative crystallographic orientation between the two crystals. In the most general case both the thermodynamic calculation (section 4.1) and the relaxation (section 4.2.5) are affected by the orientation.

We will illustrate the effect of the relative orientation for garnet-inclusion systems. Since garnets are cubic minerals, the relative orientation between the host and the inclusion does not affect the thermodynamic calculations. If the initial (entrapment) and final (P_{room}, T_{room}) conditions are under external lithostatic stress, a cubic host will always impose an isotropic strain field on the inclusion (see equation (4.2) in section 4.1), and therefore the strain in the inclusion is not affected by its orientation within the host. However, the orientation becomes relevant when calculating the change in strain upon relaxation because the amount of relaxation in a given direction in the inclusion depends on the full state of stress/strain in the inclusion, the anisotropic elastic properties of the host and of the inclusion, including their variation with direction, and the relative orientation of their crystallographic axes. Therefore, the 36 components

of the relaxation tensor must be recalculated for each orientation, a procedure that can be extremely demanding from a computational point of view since it requires six FE analyses. We show that for garnet hosts, that are almost isotropic, the relative orientation of the inclusion introduces deviation in the residual strain and stress that are insignificant compared to the uncertainties on the experimental measurements. For each inclusion-garnet pair we investigate two representative orientations. For elastically anisotropic crystals the Young modulus (E), that represents the behavior of a material under simple tension, varies as a function of the direction in the crystal and its directional dependency can be calculated as (Nye, 1985):

$$E = \frac{1}{S'_{1111}} = \frac{1}{a_{1m}a_{1n}a_{1p}a_{1q}S_{mnpq}} \tag{8.1}$$

where a_{ij} is the transformation matrix, S_{mnpq} are the components of the compliance tensor of the mineral (where the compliance is the inverse of the stiffness tensor: $\mathbf{S} = \mathbf{C}^{-1}$) before the transformation and S'_{1111} is the component after the transformation.

An automatic procedure has been implemented in Matlab® to find the directions in a crystal associated with the maximum and the minimum values of the Young modulus. The algorithm then finds the two extreme conditions for the relaxation aligning the stiffest direction (i.e. where the Young modulus is highest) of the inclusion with the directions of lowest and highest Young moduli of the host. The anisotropic relaxation tensor is calculated for these two relative orientations. The full calculation that combines the thermodynamic calculation and the anisotropic relaxation is then performed to determine how the change in relative orientation affects the final strain in the inclusion, as a function of the entrapment conditions (P_{trap}, T_{trap}).

For the following examples we consider pyrope and grossular as garnets end-members. Pyrope is almost elastically isotropic with a Universal anisotropic index (Ranganathan and Ostoja-Starzewski, 2008) $A^U = 0.001$ while grossular is more anisotropic with $A^U = 0.011$

8.1 Diamond in pyrope and grossular

The Young modulus of pyrope is highest along the <100> directions ($E = 240$ GPa) and lowest along the <111> directions ($E = 236$ GPa). The Young modulus of grossular is highest along the <100> directions ($E = 276$ GPa) and lowest along the <111> directions ($E = 260$ GPa). For diamond the stiffest direction is the <111> ($E = 1163$ GPa) while the softest is the <100> ($E = 1052$ GPa)

Here we compare the strain and the stress calculated with the two relative orientations:

- Orientation 1: direction [111] of diamond aligned with the [111] of pyrope and grossular
- Orientation 2: direction [111] of diamond aligned with the [010] of pyrope and grossular

The anisotropic relaxation tensors were calculated for a spherical diamond inclusion in pyrope and grossular garnets with the elastic properties reported in Tables B.1, B.5 and B.3, for relative orientations 1 and 2. Results are reported in Table 8.1.

Table 8.1: Diamond in pyrope: relaxation tensor $\boldsymbol{R}$ *calculated with relative orientations 1 and 2 as described in the main text.*

Orientation 1

$$R_{ij} = \begin{pmatrix} 0.18856 & 0.01580 & 0.01580 & 0.00000 & 0.00000 & 0.00000 \\ 0.01580 & 0.18856 & 0.01580 & 0.00000 & 0.00000 & 0.00000 \\ 0.01580 & 0.01580 & 0.18857 & 0.00000 & 0.00000 & 0.00000 \\ 0.00000 & 0.00000 & 0.00000 & 0.14674 & 0.00000 & 0.00000 \\ 0.00000 & 0.00000 & 0.00000 & 0.00000 & 0.14674 & 0.00000 \\ 0.00000 & 0.00000 & 0.00000 & 0.00000 & 0.00000 & 0.14674 \end{pmatrix}$$

Orientation 2

$$R_{ij} = \begin{pmatrix} 0.18824 & 0.01592 & 0.01600 & 0.00003 & -0.00006 & 0.00003 \\ 0.01592 & 0.18833 & 0.01592 & -0.00006 & 0.00012 & -0.00006 \\ 0.01600 & 0.01592 & 0.18824 & 0.00003 & -0.00006 & 0.00003 \\ 0.00005 & -0.00010 & 0.00005 & 0.14694 & 0.00005 & 0.00021 \\ -0.00010 & 0.00020 & -0.00010 & 0.00005 & 0.14710 & 0.00005 \\ 0.00005 & -0.00010 & 0.00005 & 0.00021 & 0.00005 & 0.14694 \end{pmatrix}$$

The relaxed strain and the stress fields developed in the diamond inclusion with relative orientation 1 have already been discussed in sections 7.1.1 and 7.1.2. Since both the host and the inclusion are cubic the strain field in the inclusion remains isotropic for any relative orientation between the host and the inclusion. Fig. 8.1 shows that the volume strain (found as $(\Delta V/\ V) = \varepsilon_1 + \varepsilon_2 + \varepsilon_3$) is practically not affected by the relative orientation since the discrepancy is smaller than the typical uncertainties on the experimental determination of the strain components by X-ray diffraction or Raman spectroscopy ($\delta\left(\frac{\Delta V}{V}\right) \approx 3{\cdot}10^{-4}$). For P_{trap}, T_{trap} conditions below the zero-P_{inc} isomeke

Table 8.2: Diamond in grossular: relaxation tensor $\boldsymbol{R}$ *calculated with relative orientations 1 and 2 as described in the main text.*

Orientation 1

$$R_{ij} = \begin{pmatrix} 0.20639 & 0.01772 & 0.01772 & 0.00000 & 0.00000 & 0.00000 \\ 0.01772 & 0.20639 & 0.01772 & 0.00000 & 0.00000 & 0.00000 \\ 0.01772 & 0.01772 & 0.20639 & 0.00000 & 0.00000 & 0.00000 \\ 0.00000 & 0.00000 & 0.00000 & 0.15939 & 0.00000 & 0.00000 \\ 0.00000 & 0.00000 & 0.00000 & 0.00000 & 0.15939 & 0.00000 \\ 0.00000 & 0.00000 & 0.00000 & 0.00000 & 0.00000 & 0.15939 \end{pmatrix}$$

Orientation 2

$$R_{ij} = \begin{pmatrix} 0.20513 & 0.01818 & 0.01852 & 0.00012 & -0.00024 & 0.00012 \\ 0.01818 & 0.20548 & 0.01818 & -0.00024 & 0.00047 & -0.00024 \\ 0.01852 & 0.01818 & 0.20513 & 0.00012 & -0.00024 & 0.00012 \\ 0.00020 & -0.00039 & 0.00020 & 0.16020 & 0.00020 & 0.00081 \\ -0.00039 & 0.00078 & -0.00039 & 0.00020 & 0.16081 & 0.00020 \\ 0.00020 & -0.00039 & 0.00020 & 0.00081 & 0.00020 & 0.16020 \end{pmatrix}$$

the volume strain in the inclusion is negative because diamond is over-pressurized (see Fig. 7.1). At these conditions the change in volume strain is negative meaning that the inclusion with orientation 1 is less compressed, since with this orientation the stiffest direction of diamond points toward the softest direction of garnet allowing the inclusion to expand more. The comparison of Fig. 8.1 and 8.2 shows that for a grossular host the change in volume strain due to the relative orientation has a trend similar to the case of a pyrope host, but is lower in magnitude since grossular is stiffer than pyrope.

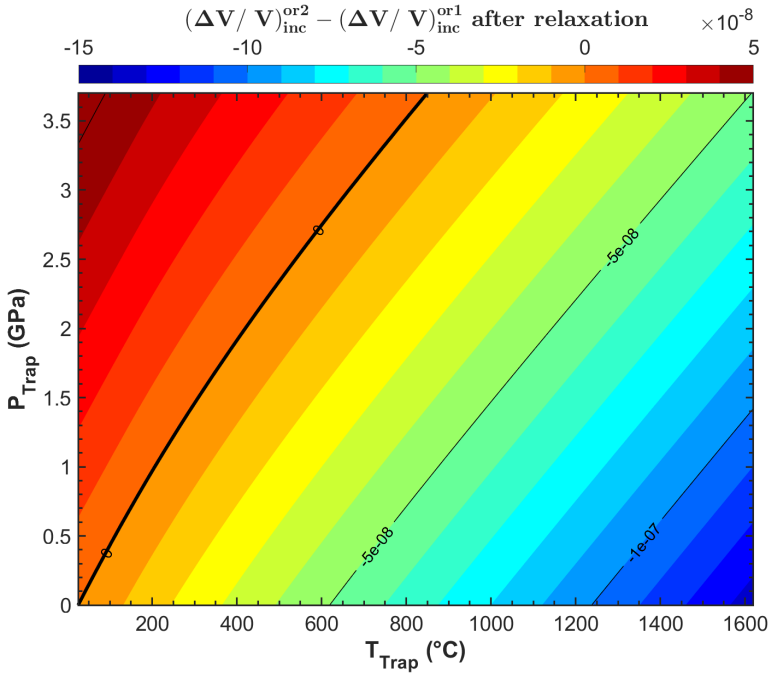

Figure 8.1: Diamond in pyrope: comparison between the volume strain in the inclusion ($(\Delta V/\ V) = \varepsilon_1 + \varepsilon_2 + \varepsilon_3$) calculated for relative orientations 1 and 2 as a function of the entrapment conditions (P_{trap}, T_{trap}). Solid line: zero-P_{inc} isomeke.

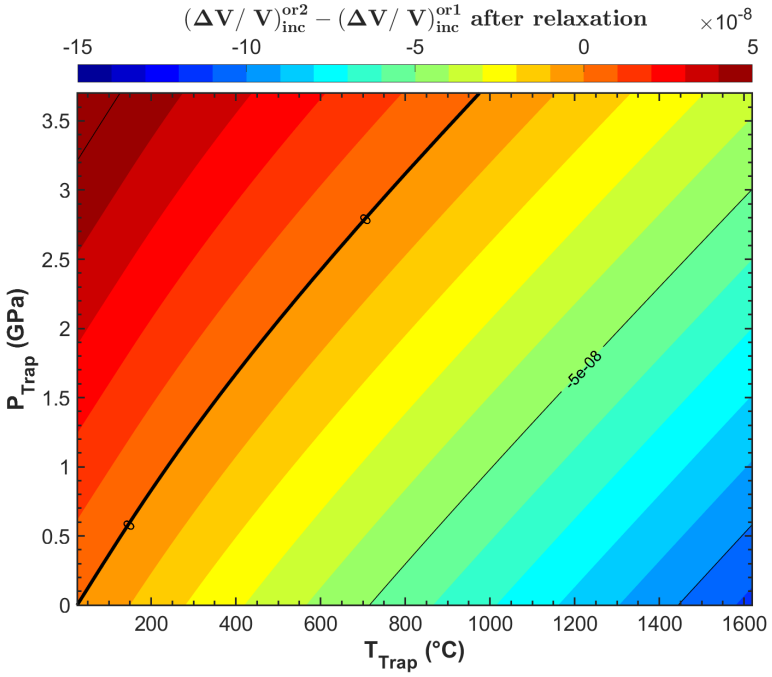

Figure 8.2: Diamond in grossular: comparison between the volume strain in the inclusion ($(\Delta V/\ V) = \varepsilon_1 + \varepsilon_2 + \varepsilon_3$) calculated for relative orientations 1 and 2 as a function of the entrapment conditions (P_{trap}, T_{trap}). Solid line: zero-P_{inc} isomeke.

8.2 Quartz in pyrope and grossular

The Young modulus of pyrope is highest along the <100> directions ($E = 240$ GPa) and lowest along the <111> directions ($E = 236$ GPa). The Young modulus of grossular is highest along the <100> directions ($E = 276$ GPa) and lowest along the <111> directions ($E = 260$ GPa). For quartz the stiffest crystallographic axis is the $\boldsymbol{c}$-axis ($E = 104$ GPa).

Here we compare the strain calculated with two relative orientations:

- Orientation 1: $\boldsymbol{c}$-axis of quartz aligned with the [001] of pyrope and grossular
- Orientation 2: $\boldsymbol{c}$-axis of quartz aligned with the [111] of pyrope and grossular

The anisotropic relaxation tensors were calculated for a spherical quartz inclusion in pyrope and grossular garnets with the elastic properties reported in Tables B.7, B.5, B.3 for relative orientations 1 and 2. Results are reported in Tables 8.3 and 8.4.

Table 8.3: Quartz in pyrope: relaxation tensor $\boldsymbol{R}$ calculated with relative orientations 1 and 2 as described in the main text.

Orientation 1

$$R_{ij} = \begin{pmatrix} 0.74280 & 0.02442 & 0.02417 & -0.03041 & 0.00000 & 0.00000 \\ 0.02442 & 0.74280 & 0.02417 & 0.03041 & 0.00000 & 0.00000 \\ 0.01397 & 0.01397 & 0.69855 & 0.00000 & 0.00000 & 0.00000 \\ -0.06105 & 0.06105 & 0.00000 & 0.62979 & 0.00000 & 0.00000 \\ 0.00000 & 0.00000 & 0.00000 & 0.00000 & 0.62980 & -0.06099 \\ 0.00000 & 0.00000 & 0.00000 & 0.00000 & -0.06099 & 0.71763 \end{pmatrix}$$

Orientation 2

$$R_{ij} = \begin{pmatrix} 0.74243 & 0.02456 & 0.02446 & -0.03049 & -0.00023 & -0.00005 \\ 0.02456 & 0.74243 & 0.02446 & 0.03049 & 0.00023 & 0.00005 \\ 0.01419 & 0.01419 & 0.69800 & 0.00000 & 0.00000 & 0.00000 \\ -0.06091 & 0.06091 & 0.00000 & 0.63037 & 0.00011 & 0.00032 \\ -0.00032 & 0.00032 & 0.00000 & -0.00011 & 0.63037 & -0.06091 \\ 0.00011 & -0.00011 & 0.00000 & 0.00047 & -0.06099 & 0.71788 \end{pmatrix}$$

The relaxed strain and the stress field developed in the quartz inclusion with relative

Table 8.4: Quartz in grossular: relaxation tensor $\boldsymbol{R}$ *calculated with relative orientations 1 and 2 as described in the main text.*

Orientation 1

$$R_{ij} = \begin{pmatrix} 0.76332 & 0.02405 & 0.02385 & -0.02912 & 0.00000 & 0.00000 \\ 0.02405 & 0.76332 & 0.02385 & 0.02912 & 0.00000 & 0.00000 \\ 0.01398 & 0.01398 & 0.72146 & 0.00000 & 0.00000 & 0.00000 \\ -0.05904 & 0.05904 & 0.00000 & 0.65187 & 0.00000 & 0.00000 \\ 0.00000 & 0.00000 & 0.00000 & 0.00000 & 0.65192 & -0.05883 \\ 0.00000 & 0.00000 & 0.00000 & 0.00000 & -0.05883 & 0.73665 \end{pmatrix}$$

Orientation 2

$$R_{ij} = \begin{pmatrix} 0.76203 & 0.02454 & 0.02487 & -0.02941 & -0.00083 & -0.00019 \\ 0.02454 & 0.76203 & 0.02487 & 0.02941 & 0.00083 & 0.00019 \\ 0.01475 & 0.01475 & 0.71953 & 0.00000 & 0.00000 & 0.00000 \\ -0.05856 & 0.05856 & 0.00000 & 0.65394 & 0.00037 & 0.00112 \\ -0.00112 & 0.00112 & 0.00000 & -0.00037 & 0.65395 & -0.05856 \\ 0.00037 & -0.00037 & 0.00000 & 0.00165 & -0.05882 & 0.73749 \end{pmatrix}$$

orientation 1 have already been discussed in sections 7.2.1 and 7.2.2 for pyrope and grossular hosts, respectively. Fig. 8.3 and 8.5 show the variation of the two independent components (ε_1 and ε_3) of the relaxed strain in the quartz inclusion changing the relative orientation. The variation is larger for the component ε_3 of the strain, since it is parallel to the $\boldsymbol{c}$-axis that is the stiffest direction in quartz. For both pyrope and grossular hosts the discrepancy is smaller than the typical uncertainties on the experimental determination of the strain components by X-ray diffraction or Raman spectroscopy ($\delta(\varepsilon_i^{rel}) \approx 1 \cdot 10^{-4}$), meaning that the relative orientation between the quartz inclusion and the host does not significantly affect the strain in the inclusion. The variation of the strain due to the orientation is slightly less for a pyrope host since it is elastically more isotropic than grossular. This is confirmed by the comparison of Fig. 8.4 and 8.6 which also show that in both the variation of the volume strain in the inclusion (found as $(\Delta V / V) = \varepsilon_1 + \varepsilon_2 + \varepsilon_3$) is much smaller than the typical experimental uncertainties ($\delta\left(\frac{\Delta V}{V}\right) \approx 3 \cdot 10^{-4}$).

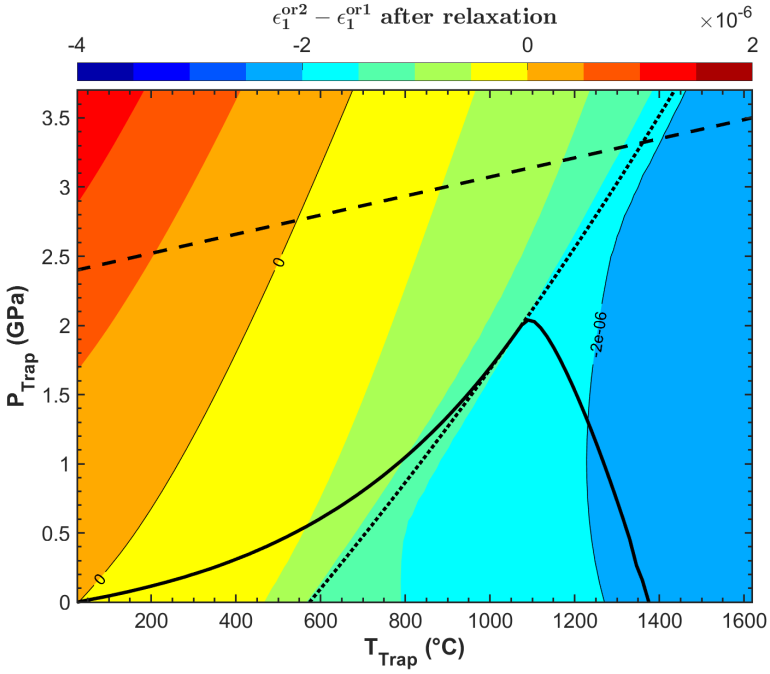

(a)

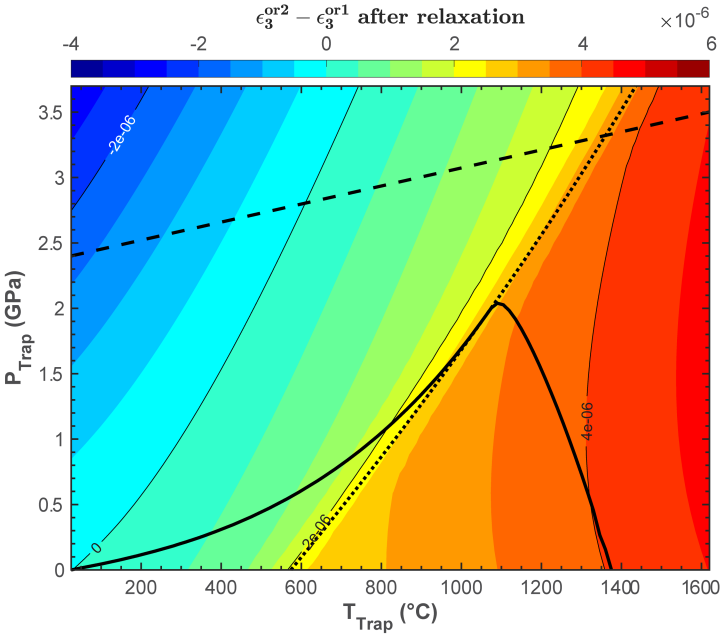

(b)

Figure 8.3: Quartz in pyrope: comparison between the components ε_1 (a) and ε_3 (b) of the relaxed strain of the inclusion calculated for relative orientations 1 and 2 as a function of the entrapment conditions (P_{trap}, T_{trap}). Dashed line: quartz-coesite phase transition (Bose and Ganguly, 1995); dotted line: $\alpha - \beta$ quartz phase transition (Angel et al., 2017a); solid line: zero-P_{inc} isomeke. The quartz-coesite phase transtion is not included in the thermodynamic calculation, and all the results calculated for P_{trap}, T_{trap} conditions above the phase boundary do not represent the real behaviour.

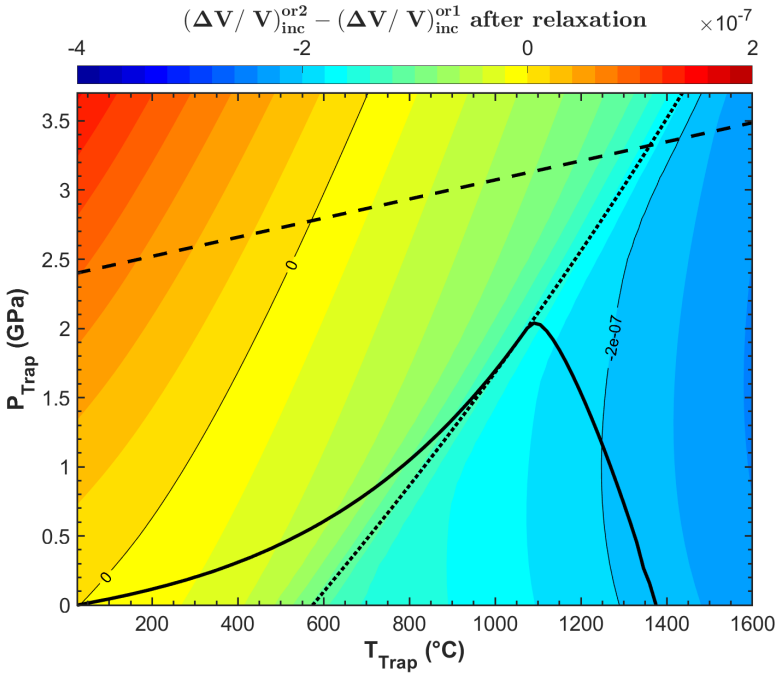

Figure 8.4: Quartz in pyrope: comparison between the volume strain in the inclusion ($(\Delta V/\ V) = \varepsilon_1 + \varepsilon_2 + \varepsilon_3$) calculated for relative orientations 1 and 2 as a function of the entrapment conditions (P_{trap}, T_{trap}). Dashed line: quartz-coesite phase transition (Bose and Ganguly, 1995); dotted line: $\alpha - \beta$ quartz phase transition (Angel et al., 2017a); solid line: zero-P_{inc} isomeke. The quartz-coesite phase transtion is not included in the thermodynamic calculation, and all the results calculated for P_{trap}, T_{trap} conditions above the phase boundary do not represent the real behaviour.

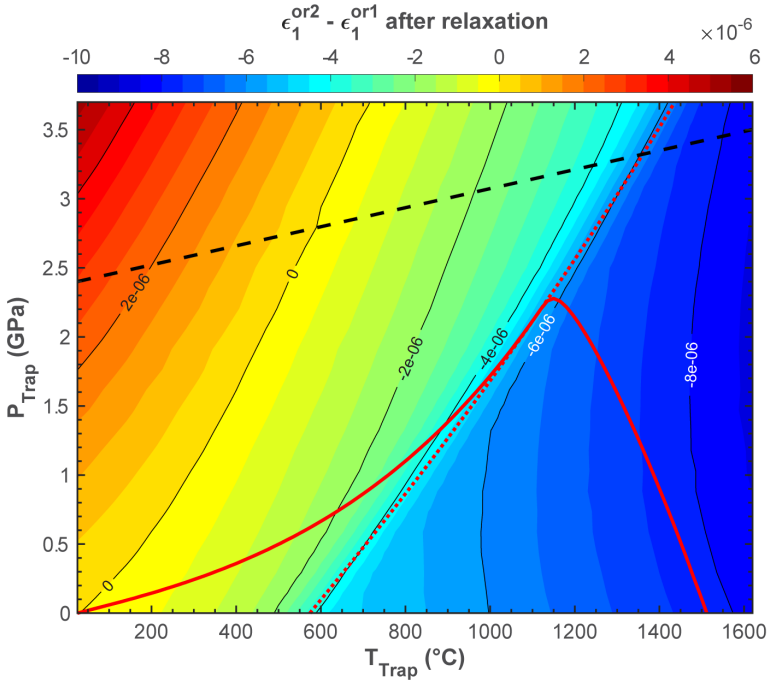

(a)

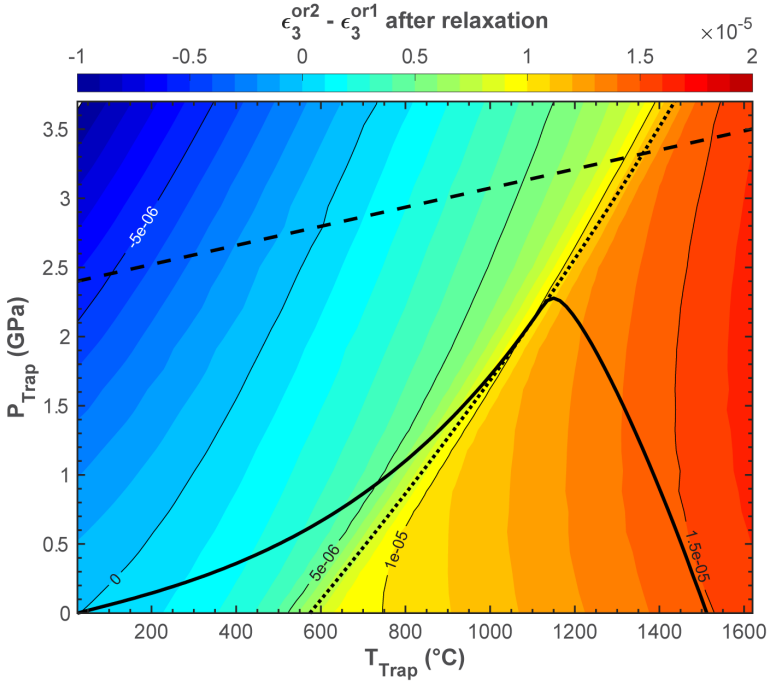

(b)

Figure 8.5: Quartz in grossular: comparison between the components ε_1 (a) and ε_3 (b) of the relaxed strain of the inclusion calculated for relative orientations 1 and 2 as a function of the entrapment conditions (P_{trap}, T_{trap}). Dashed line: quartz-coesite phase transition (Bose and Ganguly, 1995); dotted line: $\alpha - \beta$ quartz phase transition (Angel et al., 2017a); solid line: zero-P_{inc} isomeke. The quartz-coesite phase transtion is not included in the thermodynamic calculation, and all the results calculated for P_{trap}, T_{trap} conditions above the phase boundary do not represent the real behaviour.

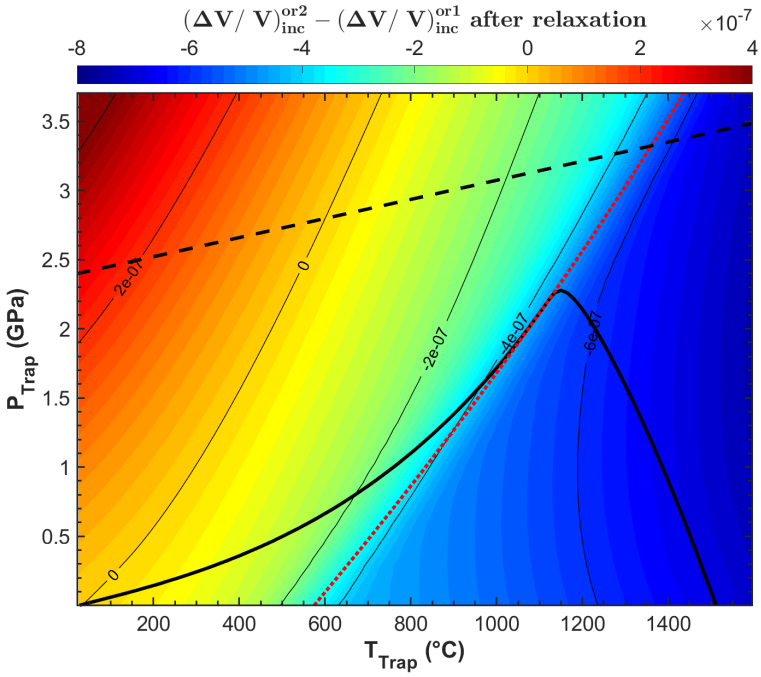

Figure 8.6: Quartz in grossular: comparison between the volume strain in the inclusion ($(\Delta V/\ V) = \varepsilon_1 + \varepsilon_2 + \varepsilon_3$) calculated for relative orientations 1 and 2 as a function of the entrapment conditions (P_{trap}, T_{trap}). Dashed line: quartz-coesite phase transition (Bose and Ganguly, 1995); dotted line: $\alpha - \beta$ quartz phase transition (Angel et al., 2017a); solid line: zero-P_{inc} isomeke. The quartz-coesite phase transtion is not included in the thermodynamic calculation, and all the results calculated for P_{trap}, T_{trap} conditions above the phase boundary do not represent the real behaviour.

8.3 Zircon in pyrope and grossular

The Young modulus of pyrope is highest along the <100> directions ($E = 240$ GPa) and lowest along the <111> directions ($E = 236$ GPa). The Young modulus of grossular is highest along the <100> directions ($E = 276$ GPa) and lowest along the <111> directions ($E = 260$ GPa). The $\boldsymbol{c}$-axis is the stiffest crystallographic direction in zircon ($E = 400$ GPa).

Here we compare the strain calculated with two relative orientations:

- Orientation 1: $\boldsymbol{c}$-axis of zircon aligned with the [001] of pyrope and grossular
- Orientation 2: $\boldsymbol{c}$-axis of zircon aligned with the [111] of pyrope and grossular

The anisotropic relaxation tensors were calculated for a spherical zircon inclusion in pyrope and grossular garnets with the elastic properties reported in Tables B.10, B.5, B.3 for relative orientations 1 and 2. Results are reported in Tables 8.5 and 8.6.

Table 8.5: Zircon in pyrope: relaxation tensor $\boldsymbol{R}$ calculated with relative orientations 1 and 2 as described in the main text.

Orientation 1

$$R_{ij} = \begin{pmatrix} 0.38440 & 0.02445 & -0.01846 & 0.00000 & 0.00000 & 0.00000 \\ 0.02445 & 0.38440 & -0.01846 & 0.00000 & 0.00000 & 0.00000 \\ -0.03501 & -0.03501 & 0.35508 & 0.00000 & 0.00000 & 0.00000 \\ 0.00000 & 0.00000 & 0.00000 & 0.46567 & 0.00000 & 0.00000 \\ 0.00000 & 0.00000 & 0.00000 & 0.00000 & 0.46567 & 0.00000 \\ 0.00000 & 0.00000 & 0.00000 & 0.00000 & 0.00000 & 0.67120 \end{pmatrix}$$

Orientation 2

$$R_{ij} = \begin{pmatrix} 0.38397 & 0.02459 & -0.01811 & 0.00000 & -0.00017 & 0.00000 \\ 0.02459 & 0.38397 & -0.01811 & 0.00000 & 0.00017 & 0.00000 \\ -0.03476 & -0.03476 & 0.35448 & 0.00000 & 0.00000 & 0.00000 \\ 0.00000 & 0.00000 & 0.00000 & 0.46629 & 0.00000 & 0.00027 \\ -0.00052 & 0.00052 & 0.00000 & 0.00000 & 0.46629 & 0.00000 \\ 0.00000 & 0.00000 & 0.00000 & 0.00062 & 0.00000 & 0.67147 \end{pmatrix}$$

The relaxed strain and the stress field developed in the zircon inclusion with relative

Table 8.6: Zircon in grossular: relaxation tensor $\boldsymbol{R}$ *calculated with relative orientations 1 and 2 as described in the main text.*

Orientation 1

$$R_{ij} = \begin{pmatrix} 0.41121 & 0.02614 & -0.01755 & 0.00000 & 0.00000 & 0.00000 \\ 0.02614 & 0.41121 & -0.01755 & 0.00000 & 0.00000 & 0.00000 \\ -0.03491 & -0.03491 & 0.38090 & 0.00000 & 0.00000 & 0.00000 \\ 0.00000 & 0.00000 & 0.00000 & 0.49003 & 0.00000 & 0.00000 \\ 0.00000 & 0.00000 & 0.00000 & 0.00000 & 0.49003 & 0.00000 \\ 0.00000 & 0.00000 & 0.00000 & 0.00000 & 0.00000 & 0.69237 \end{pmatrix}$$

Orientation 2

$$R_{ij} = \begin{pmatrix} 0.40961 & 0.02668 & -0.01627 & 0.00000 & -0.00062 & 0.00000 \\ 0.02668 & 0.40961 & -0.01627 & 0.00000 & 0.00062 & 0.00000 \\ -0.03399 & -0.03399 & 0.37865 & 0.00000 & 0.00000 & 0.00000 \\ 0.00000 & 0.00000 & 0.00000 & 0.49228 & 0.00000 & 0.00096 \\ -0.00194 & 0.00193 & 0.00000 & 0.00000 & 0.49229 & 0.00000 \\ 0.00000 & 0.00000 & 0.00000 & 0.00225 & 0.00000 & 0.69333 \end{pmatrix}$$

orientation 1 have already been discussed in sections 7.2.3 and 7.2.4 for pyrope and grossular hosts, respectively. Fig. 8.7 and 8.9 show the variation of the two independent components (ε_1 and ε_3) of the relaxed strain in the zircon inclusion changing the relative orientation. The variation is larger in magnitude and negative for the component ε_3 of the strain that is parallel to the $\boldsymbol{c}$-axis, i.e. the stiffest direction in zircon. The variation of the components $\varepsilon_1 = \varepsilon_2$ is smaller and positive. For both pyrope and grossular hosts the discrepancy is smaller than the typical uncertainties on the experimental determination of the strain components by X-ray diffraction or Raman spectroscopy ($\delta(\varepsilon_i^{rel}) \approx 1 \cdot 10^{-4}$), meaning that the relative orientation between the quartz inclusion and the host does not significantly affect the strain in the inclusion. The variation of the strain due to the orientation is less for a pyrope host since it is elastically more isotropic than grossular. This is confirmed by the comparison of Fig. 8.8 and 8.10 which also show that in both the variation of the volume strain in the inclusion (found as $(\Delta V/\, V) = \varepsilon_1 + \varepsilon_2 + \varepsilon_3$) is much smaller than the typical experimental uncertainties ($\delta\left(\frac{\Delta V}{V}\right) \approx 3 \cdot 10^{-4}$). In both cases (pyrope and grossular host) the variation of the volume strain is positive meaning that the inclusion with orientation

2 is less compressed, since with this orientation the stiffest direction of zircon points toward the softest direction of garnet allowing the inclusion to expand more.

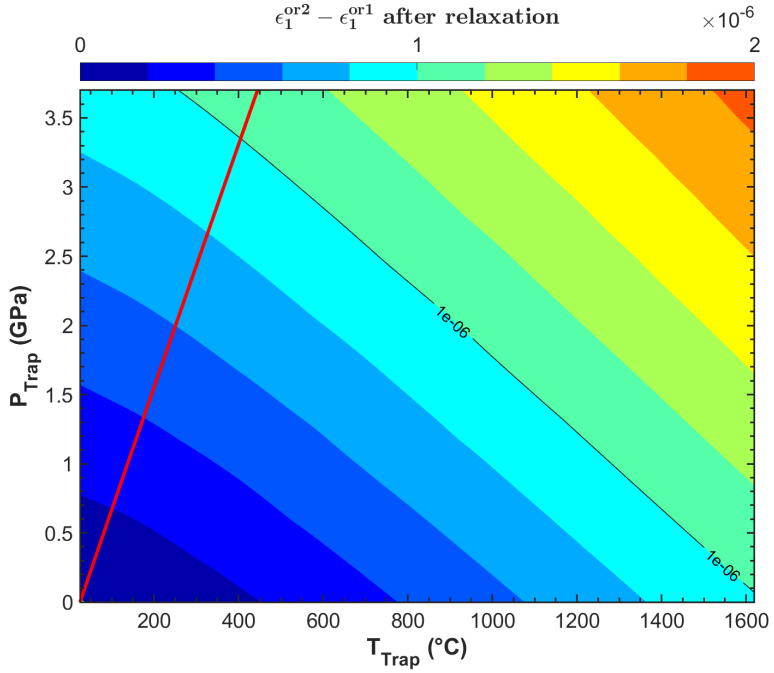

(a)

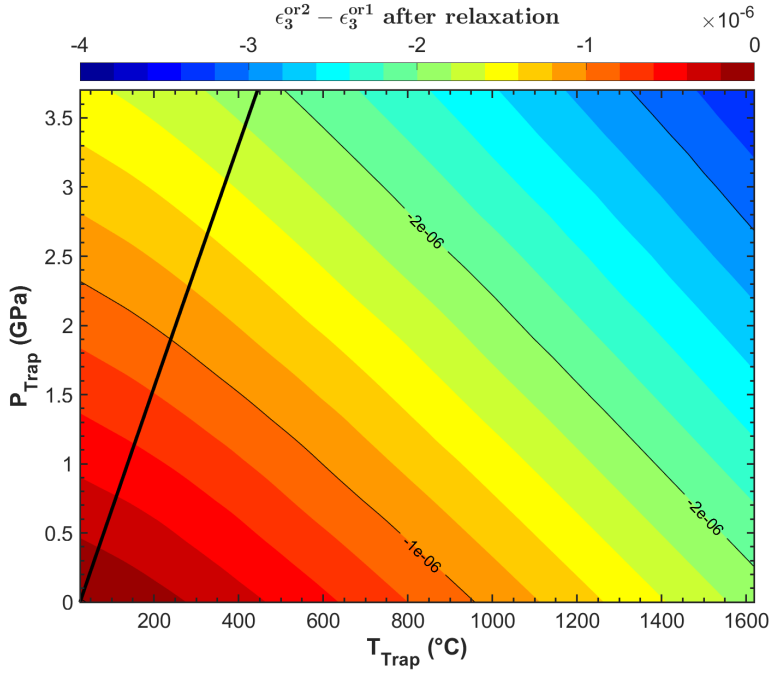

(b)

Figure 8.7: Zircon in pyrope: comparison between the components ε_1 (a) and ε_3 (b) of the relaxed strain of the inclusion calculated for relative orientations 1 and 2 as a function of the entrapment conditions (P_{trap}, T_{trap}). Solid line: zero-P_{inc} isomeke.

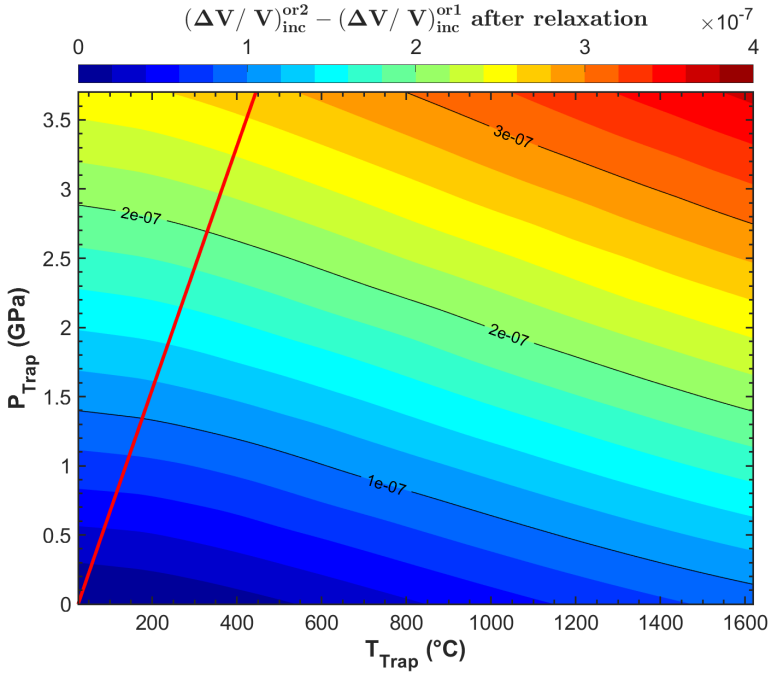

Figure 8.8: Zircon in pyrope: comparison between the volume strain in the inclusion ($(\Delta V/\ V) = \varepsilon_1 + \varepsilon_2 + \varepsilon_3$) calculated for relative orientations 1 and 2 as a function of the entrapment conditions (P_{trap}, T_{trap}). Solid line: zero-P_{inc} isomeke.

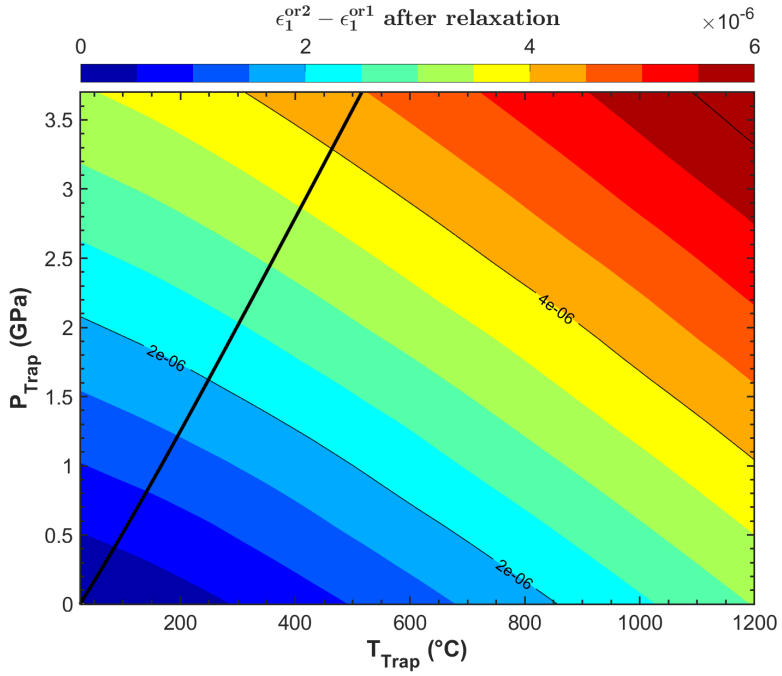

(a)

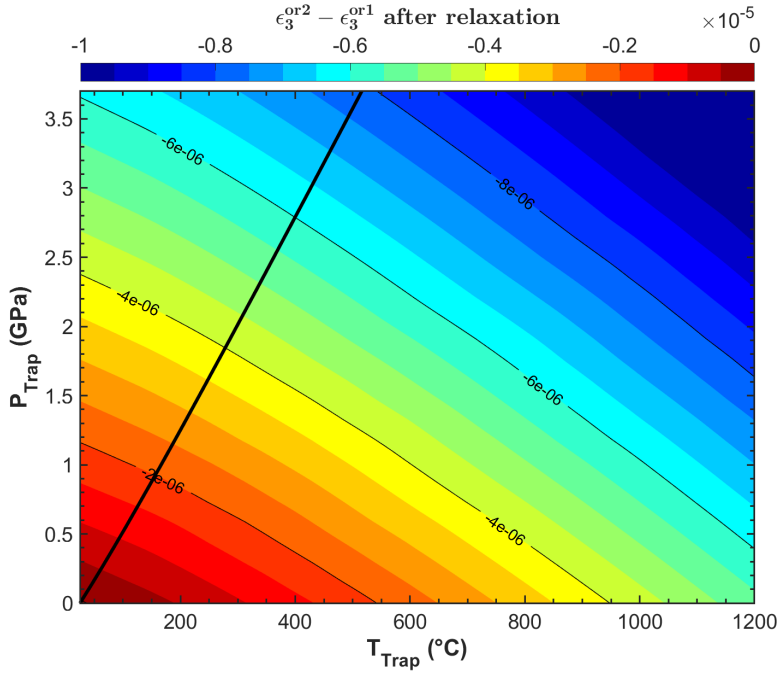

(b)

Figure 8.9: Zircon in grossular: comparison between the components ε_1 (a) and ε_3 (b) of the relaxed strain of the inclusion calculated for relative orientations 1 and 2 as a function of the entrapment conditions (P_{trap}, T_{trap}). Solid line: zero-P_{inc} isomeke.

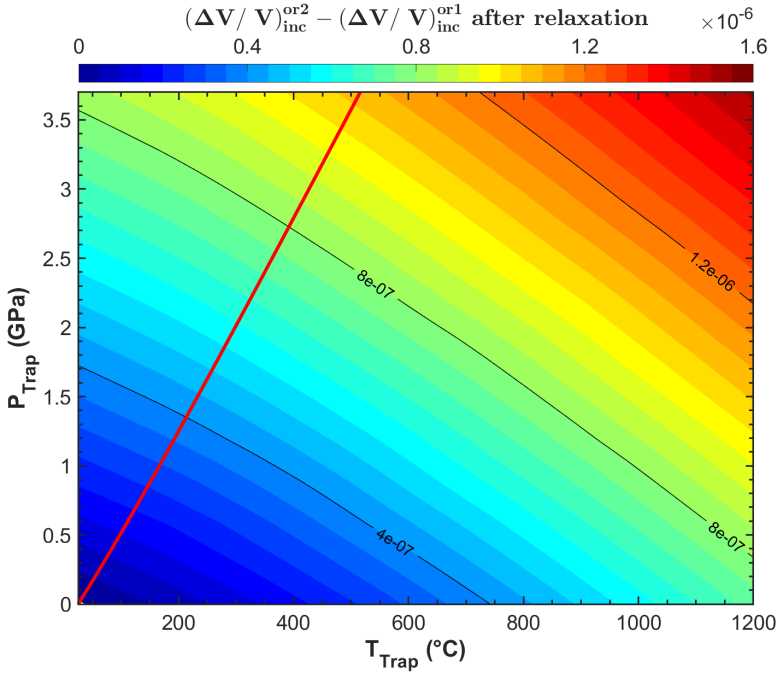

Figure 8.10: Zirconin grossular: comparison between the volume strain in the inclusion ($(\Delta V/\ V) = \varepsilon_1 + \varepsilon_2 + \varepsilon_3$) calculated for relative orientations 1 and 2 as a function of the entrapment conditions (P_{trap}, T_{trap}). Solid line: zero-P_{inc} isomeke.

Conclusions

Even if more recent models for elastic geobarometry (Angel et al., 2017b) incorporate non-linear elasticity, still they make several assumptions such as the simplified geometry of the system (the inclusion is spherical and isolated at the center of an effectively infinite host) and the use of isotropic elastic properties for both the host and the inclusion. These conditions mean that during the exhumation the stress in the inclusion is homogeneous and hydrostatic allowing for a simple analytical solution of the problem (Goodier, 1933; Eshelby, 1957; Zhang, 1998). However, none of these conditions apply in natural systems: no mineral is perfectly elastically isotropic and inclusions are often close to grain boundaries or other inclusions, and they might be not spherical.

In general, the effects of these deviations from the "ideal" case can be evaluated only through numerical calculations. With the Finite Element Method (FEM) I first investigated, keeping the assumption of isotropic elasticity, how the non-ideal geometry affects the residual pressure P_{inc} in the inclusion during the exhumation of the rock from entrapment conditions to the Earth's surface. With this approach a geometrical factor (Γ) can be introduced, defined as the normalized deviation of the actual inclusion pressure from that expected for an ideal isolated spherical inclusion, for the same decompression (Fig. 1.1). The quantification of Γ provides, as a first approximation, guidelines as to which geometries of host-inclusion systems lead to deviations in the final P_{inc} smaller than the typical experimental uncertainties in inclusion pressures obtained from conventional experimental measurements, and can therefore be safely used for geobarometry without any correction. On the other hand, when the deviation due to the geometry is not small, the Γ factor can be used to correct the residual pressure measured experimentally accounting for the geometric effects. The corrected P_{inc} can then be used with available isotropic geobarometric methods to calculate entrapment conditions. Regardless of the relative stiffness of host and inclusion, for a big inclusion in a small host and for an inclusion close to the external surface of the host, the residual pressure is reduced relative to the ideal case ($\Gamma < 0$, Fig. 1.2). For isotropic elasticity, our FEM results show that 'isolated' means that the inclusion must be at least 3 radii from external surfaces or other inclusions, for the geometric effects on P_{inc} to be below 1 %. Under these conditions the shape effects then dominate the geometric correc-

tions to the measured P_{inc}. For soft inclusions in a stiff host (e.g., quartz in garnet) non-spherical inclusions ($\Gamma < 0$), will exhibit a lower pressure than spherical inclusions (Fig. 1.3). The opposite is found for stiff inclusions in soft hosts for which $\Gamma > 0$. Pressures from inclusions for which the geometrical effects on the residual pressure are less than 5% will provide reliable estimates of P_{inc}, and hence P_{trap}, without the need for correction. For soft inclusions in stiff hosts, such as quartz in garnet, this means the following:

1. The radius of the inclusion must be smaller than one-half of that of the host.
2. The distance from the external surface is larger than one-half the radius of the inclusion.
3. The inclusion aspect ratio is lower than 1:3:3, with few sharp edges and corners.

These guidelines do not apply to inclusions stiffer than the host (e.g., diamond in garnet, zircon in garnet) that usually require larger corrections.

When the shape of the inclusion is not ellipsoidal, or it is not isolated within an infinite host but is close to the external surface of the host or to other inclusions, the stress and the strain fields in the inclusion are not homogeneous (Fig. 1.6). Also, the residual "pressure" (defined as the negative of the mean normal stress $P = -(\sigma_{11}+\sigma_{22}+\sigma_{33})/3$) is not constant within the inclusion (Fig. 1.2 and 1.5), and, as a consequence, the geometrical factor may change in value from point to point within the inclusion. In these cases Γ was calculated as a local factor arbitrarily referred to the geometrical center of the inclusion. The correction factor Γ must be defined keeping in mind the experimental measurement that needs to be interpreted and corrected. Γ as a local factor is especially appropriate for experimental measurement obtained from Raman spectroscopy. With this technique point measurements are obtained, and, if the crystal is sufficiently large compared to the section of the laser beam, it can be used to effectively track the variation of the strain field within an inclusion (e.g. Fig. 3.2 and A.4). On the other hand, X-ray diffraction gives the average state of strain of the inclusion since the information on its deformation is averaged over all the unit-cells in the crystal, and the interpretation of such results requires Γ to be defined as a bulk factor averaged over the entire volume of the sample. Moreover, since the geometrical factor incorporates the effects of several deviations from the ideal geometry (shape,size and position of the inclusion), for more accurate results it should be evaluated on a case-by-case basis with finite element method (FEM) analysis carried out on realistic digital models of the system. This approach was applied to a sub-lithospheric diamond containing two ferropericlase inclusions. A FE model was created based on the CAD model of the diamond obtained from X-ray micro-tomography, preserving the shape of the inclusions and their reciprocal position and orientation. The X-ray diffraction

measurements give a lower P_{inc} for the platy inclusion compared to that more rounded (Fig. 2.2 and Table 2.1), consistent with the prediction of the FE analysis that assumes that both the inclusions were entrapped under the same external conditions. For each inclusion the average Γ factor, integrated over their entire volume, was obtained and then applied to correct the measured P_{inc}. The entrapment pressures calculated with isotropic elasticity after the correction are 13.4(1.4) and 12.8(1.6) GPa at a temperature T_{trap} = 1790(30) K (Fig. 2.4) placing the formation of this diamond at least at the lower part of the upper mantle.

Experimental measurements performed with Raman spectroscopy on zircon and coesite inclusions in pyrope from the ultrahigh-pressure (UHP) Alpine Dora Maira Massif showed that Raman shift is homogeneous only in rounded inclusions while it is non-homogeneous in faceted ones (Fig. 3.2 A and B), in agreement with the results from FEM calculations. Therefore, multiple Raman spectra collected on faceted inclusions should not be averaged if their differences are larger than the instrumental peak precision. Instead, to avoid the effects of grain shape on Raman peak positions, only Raman spectra measured at the center of the inclusions should be used because there the stress perturbation given by corners and edges is less and we can apply the local geometrical correction. The effect of the proximity of the inclusion to the external surface of the host is particularly crucial for high-pressure metamorphic rocks that are investigated on thick (thickness 100 μm) or thin (thickness 30 μm) sections cut from the rock specimen, possibly leading to large errors in the back-calculation of the entrapment conditions. To quantify this effect, Raman spectra were collected on a zircon inclusion initially entrapped at the center of the rock thick section and after performing several steps of polishing to expose the inclusion towards the external surface of the host. The residual pressure was obtained from the Raman shifts using a hydrostatic calibration. The Raman shifts measured on the inclusion, and as a consequence its residual pressure, decrease as the inclusion gets closer to the external surface (e.g. Fig. 3.3A). Results show that only inclusions whose centers are distant more than 4 radii (Fig. 3.3 B) from the surface of the host should be used for the back calculation of the entrapment pressure. Even when an inclusion is exposed at the surface of the host grain, it can still exhibit a variation in the peak position with respect to a free crystal, and thus residual strains and stresses. Therefore, partially entrapped grains should never be used as a strain free standard against which to measure the Raman shifts of unexposed inclusions. The residual pressures obtained from the Raman spectra were compared with the results of a set of FEM models that closely reproduce the shape of the inclusion and its proximity to the external surface, and that also account for the elastic anisotropy of the inclusion and its crystallographic orientation within the section. The trends of "pressure" release estimated from experimental measurements agree with those calculated from numerical simulations (Fig. 3.3B), but the experimental data suggest a greater amount of stress release. For example, at a normalized distance

of 1 (inclusion just in contact with the external surface), the calculated stress release is approximately 50%, whereas that obtained from experimental data is about 70% (Fig. 3.3B). There are at least two contributions to this discrepancy: (i) for non-cubic inclusions (such as zircon) direct conversion of Raman shifts into pressures using a hydrostatic calibration is incorrect; (ii) when the inclusion is close to the surface, strain gradients may be relaxed through plasticity or micro-fractures that are not considered in our purely elastic numerical models. However, both experiments and calculations show that the elastic anisotropy coupled with the crystallographic and the morphological orientation of the inclusion with respect to the external surface have a large influence on the strain release during polishing.

Elastic geobarometry can be extended to include elastic anisotropy, and to this aim the calculation of the final residual strain developed in the inclusion after exhumation must be split into two steps: thermodynamic calculation and relaxation. The thermodynamic step considers the final strain in the inclusion as imposed only by the deformation of the cavity (i.e. the host) during the exhumation, without considering any mechanical coupling between the host and the inclusion. The calculation is based on non-linear elasticity and requires the knowledge of the volume and axial Equations of State (EoS) of both the host and of inclusion to describe how their crystallographic axes change in length with changing pressure and temperature. If the host and the inclusion are different minerals, after the exhumation to room conditions the host and the inclusion are not in mechanical equilibrium, and the discontinuity in traction at the interface between the host and the inclusion forces the elastic relaxation of the system until the mechanical equilibrium is restored. The calculation of the change in strain upon anisotropic relaxation requires the knowledge of the unrelaxed strain state, the full elastic properties of the host and the inclusion, including their variation with direction, and the relative orientation of their crystallographic axes. This problem is related to the Eshelby's equivalent inclusion problem and can be solved analytically for a few cases with specific crystallographic symmetries (e.g. transversely isotropic symmetry), but not for host minerals typical of high-pressure metamorphic rocks (e.g. garnets, zircon). The strain and stress in the inclusion after the relaxation can be found numerically with FE analyses, without any restriction given by the elastic anisotropic properties of the host and of the inclusion and their reciprocal orientation. However, this approach is extremely time consuming and would greatly restrict the routine applicability of elastic geobarometry since a new analysis is needed for any specific initial unrelaxed strain state, requiring hours of computational time. This can be avoided assuming that the elastic properties of both the host and the inclusion stay constant during the relaxation. Under this assumption, I demonstrated that a linear mapping represented by a fourth order non-symmetric tensor (the relaxation tensor $\mathbf{R}$) exists that transforms the unrelaxed strain into the relaxed strain (section 4.2.2). The 36 independent components of $\mathbf{R}$ can be found with a set of only six FE analyses.

A semi-automatic procedure was developed in Matlab®, in which the user can select the elastic properties for the host and the inclusion and set their relative orientation. For each of the six analyses, Abaqus® is called as FEM solver, and the outputs are automatically processed to obtain the components of the relaxation tensor. Once the relaxation tensor is calculated for a specific reciprocal orientation of the host and the inclusion it can be applied to relax any unrelaxed strain state for that system, without the need of new FE analyses. With this approach the final residual strain and stress in the inclusion can be predicted after exhumation from any entrapment condition. Our results show that on a first approximation, the amount of relaxation along a specific direction in the inclusion is a consequence of the combined stiffness of the host and of the inclusion along that direction. If the inclusion and the host both have cubic symmetry the relaxation is equal along each of the crystallographic axes of the inclusion (e.g. Table 7.1). If the inclusion has a symmetry lower than cubic and the host is cubic, the largest relaxation is along the stiffest direction of the inclusion (e.g. Table 7.2). However, more strained directions tend to relax more. Therefore, the amount of the elastic relaxation depends on the overall balance between the stiffnesses of the host and of inclusion and the magnitude of the component of the unrelaxed strain along each direction. The former is the contrast of the elastic properties at room T and low stresses, the latter is the result of the contrast in thermal expansion and compressibilities from entrapment to room conditions.

I have shown the application of these calculations to several cases typical of UHP metamorphic rocks, using garnet as hosts. The geometry is kept simple with a spherical inclusion at the center of an "infinite" host. I developed an algorithm in Matlab® to generate a grid of equally-spaced points of entrapment within a desired range of P_{trap}, T_{trap} and the exhumation of the host-inclusion system from each of these points to room conditions is simulated combining the thermodynamic and the relaxation steps. The calculations provide the relaxed strain in the inclusion, from which the relaxed stress and all the other related quantities (e.g. volume strain, residual pressure ecc.) are obtained. Results show that the deviatoric strain and stress obtained from the thermodynamic calculation are reduced by the elastic relaxation. For example, for quartz in pyrope there is a large difference between the unrelaxed and the relaxed strain states (Fig. 7.7). This demonstrates that the contribution given by the anisotropic relaxation is relevant and must be included in the calculation. Calculations confirm the expected result that when both the host and the inclusion have cubic crystallographic symmetry the residual strain and stress in the inclusion are always isotropic. If at least one of the host or the inclusion has a crystallographic symmetry less than cubic, the relaxed strain and stress in the inclusion are generally anisotropic. They are expected to be isotropic only for extremely limited range of entrapment conditions P_{trap}, T_{trap} (e.g. for quartz in pyrope see Fig. 7.7 and 7.8). This is in agreement with the

experimental measurements performed with Raman spectroscopy on a natural quartz inclusion in eclogitic garnet from Mir kimberlite that showed that the residual strain is anisotropic at its central point (see appendix A). The volume in the inclusion obtained from the residual strain in the inclusion ($\Delta V/V = \varepsilon_{11} + \varepsilon_{22} + \varepsilon_{33}$) can be compared to the $(\Delta V/V)^{iso}_{inc}$ calculated for the same exhumation with geobarometric models that assume isotropic elastic properties for the host and the inclusion. The comparison shows that when both the host and the inclusion have cubic crystallographic symmetry the discrepancy is small, and generally well within the experimental uncertainties on the determination of $(\Delta V/V)_{inc}$ in natural inclusions. For a diamond inclusion in pyrope the discrepancy on volume strain is less than $3 \cdot 10^{-4}$ for any entrapment condition up to 3.5 GPa and 1600°C (Fig. 7.2). This suggests that for a cubic inclusion in a cubic host, the use of an elastically isotropic model for geobarometry leads to a reliable estimation of the entrapment pressure. This is particularly relevant when the experimental measurement is performed with Raman spectroscopy, that for cubic minerals only gives the volume strain (Angel et al., 2018), and therefore only allows the application of isotropic geobarometry. The discrepancy between the isotropic and the anisotropic $(\Delta V/V)_{inc}$ increases when the symmetry of the inclusion is lower than cubic (e.g. quartz). Taking quartz in pyrope as an example, for an entrapment within the quartz stability field the discrepancy is up to $8 \cdot 10^{-4}$, larger than the typical experimental uncertainties on the determination of the volume strain ($\approx 3 \cdot 10^{-4}$). Therefore, in this case using the measured residual volume strain in an elastically isotropic model could lead to incorrect estimates of the entrapment pressure. The discrepancy in general becomes smaller for stiffer hosts, since they can better constrain the inclusion and limit the amount of elastic relaxation (cf. for example Fig. 7.10 and 7.13 with pyrope and grossular as hosts, respectively).

In general, the stress and the strain developed in the inclusion change with different mutual crystallographic orientations between the host and the inclusion, and in real samples a new calculation would be required for each orientation. When the host is cubic, in principle only the relaxation step is affected. However, when the host is a garnet, a typical host in high-pressure metamorphic rocks, the orientation does not affect the strain in the inclusion. This has been demonstrated for inclusions with a wide range of stiffness and anisotropy (diamond, quartz and zircon) in garnet (see Fig. 8.1 - 8.10). Calculations on a single orientation are therefore enough to constrain the behavior of garnet-inclusion systems.

The approach outlined so far that includes the anisotropic elasticity of minerals can be also used to back calculate the entrapment conditions if the residual strain in the inclusion is measured with X-ray diffraction or Raman spectroscopy. Its application to real samples, both natural and synthetic, is currently under testing.

Future challenges

The solution for anisotropic geobarometry presented in this thesis is restricted to systems with ideal geometry (the inclusion is spherical and infinitesimally small compared to the host). In principle, the relaxation tensor can be calculated also for non-spherical inclusions, or, more in general, for non-ideal geometries applying the procedure outlined in this thesis using FEM models that reproduce the real geometry of the system. However, whenever the geometrical symmetry is less than the crystallographic symmetry of the inclusion, the relaxation is associated with a break of the crystallographic symmetry of the inclusion. This adds complexity to the problem, because the numerical calculation is based on elastic properties that are associated with the initial crystallographic symmetry and cannot account for the break in symmetry. However, small symmetry breaking can still be described starting from the high symmetry phase since the new components of the elastic tensor C_{ij} will be initially equal to zero and the others equal to the corresponding components of the high symmetry phase tensor. For example, after a small deformation that reduces the symmetry from cubic to orthorhombic is still true that $C_{11} \approx C_{22} \approx C_{33}$, $C_{44} \approx C_{55} \approx C_{66}$ and $C_{12} \approx C_{13} \approx C_{23}$. When the degree of symmetry breaking is large, a conceptually different approach has to be found. In simple cases, the new elastic constants can be found with ab-initio methods, such as Density Functional Theory (DFT), that can explicitly calculate the second derivative of the energy with respect to the applied strain (Perger et al., 2009).

Moreover, the formulation of the relaxation tensor $\mathbf{R}$ requires that the elastic properties of the host and of the inclusion stay constant with pressure. This is a good approximation only for stiff minerals (e.g diamond, garnets), and for other minerals if the change in stress due to the relaxation is not larger than 1 GPa. A more accurate solution of the problem would require the knowledge of how the elastic constants (C_{ij}) of the two minerals changes with pressure and stress. In principle this can be implemented in FEM models, but the pressure dependency of the the elastic constants need first to be determined experimentally, and at the moment it is known only for few minerals typical of high-pressure rocks (e.g. quartz, Wang et al., 2015), while the stress dependency can only be evaluated theoretically through DFT calculations.

The solution presented here is purely elastic. While this is usually considered a good approximation at low T regimes and for strong minerals such as garnet (Karato et al., 1995), recent studies pointed out that high-pressure metamorphic rocks may have experienced thermal regimes high enough to induce viscous relaxation (Zhong et al., 2018). The models presented are however limited to the isotropic case, and the extension to include anisotropic viscoelasticity would require an extensive reformulation of the problem (e.g Nguyen et al., 2007).

In this thesis several examples were presented in which the computational results were

compared to experimental measurements. Calculations were able to reproduce, at least qualitatively, the pressure release measured on a pressurized inclusion that is close to the external surface of its host. They were also successful in predicting which shapes of the inclusion lead to higher or lower residual pressure after the exhumation. However, to evaluate the shortcomings of our models a higher statistical significance is required. To this aim systematic experiments have been performed in piston-cylinder apparatus to reproduce the entire exhumation process from known entrapment conditions (up to $P_{trap} = 3$ GPa and $T_{trap} = 800$ °C) to room conditions ("Assessing the reliability of elastic geobarometry methods"). It will provide us a unique controlled environment to test if our models are able to predict, with sufficient precision compared to experimental uncertainties, the change in stress in the inclusion during the exhumation of the rock.

References for part II and conclusions

Alvaro, M., Mazzucchelli, M., Angel, R. J., Scambelluri, M., Korsakov, A. V., Murri, M., Campomenosi, N., Marone, F., Morana, M., and Geddo, Z. (2019). "The search for non-lithostatic stresses in the lower crust". In: *in prep.*

Angel, R. J., Jackson, J. M., Reichmann, H. J., and Speziale, S. (2009). "Elasticity measurements on minerals: a review". In: *Eur J Mineral* 21.3, pp. 525–550.

Angel, R. J., Mazzucchelli, M. L., Alvaro, M., Nimis, P., and Nestola, F. (2014). "Geobarometry from host-inclusion systems: The role of elastic relaxation". In: *American Mineralogist* 99.10, pp. 2146–2149.

Angel, R. J., Alvaro, M, Nestola, F., and Mazzucchelli, M. L. (2015a). "Diamond thermoelastic properties and implications for determining the pressure of formation of diamond–inclusion systems". In: *Russ Geol Geophys* 56, pp. 225–234.

Angel, R. J., Nimis, P, Mazzucchelli, M. L., Alvaro, M, and Nestola, F. (2015b). "How large are departures from lithostatic pressure? Constraints from host–inclusion elasticity". In: *Journal of Metamorphic Geology* 33.8, pp. 801–813.

Angel, R. J., Alvaro, M., Miletich, R., and Nestola, F. (2017a). "A simple and generalised P–T–V EoS for continuous phase transitions, implemented in EosFit and applied to quartz". In: *Contributions to Mineralogy and Petrology* 172.5, p. 29.

Angel, R. J., Mazzucchelli, M. L., Alvaro, M., and Nestola, F. (2017b). "EosFit-Pinc: A simple GUI for host-inclusion elastic thermobarometry". In: *American Mineralogist* 102.9, pp. 1957–1960.

Angel, R. J., Murri, M., Mihailova, B., and Alvaro, M. (2018). "Stress , strain and Raman shifts". In: *Zeitschrift für Kristallographie-Crystalline Materials.*

Anzolini, C., Angel, R., Merlini, M., Derzsi, M., Tokár, K., Milani, S., Krebs, M., Brenker, F., and Harris, J. (2016). "Depth of formation of CaSiO3-walstromite included in super-deep diamonds". In: *Lithos* 265, pp. 138–147.

Ashley, K. T., Steele-MacInnis, M., Bodnar, R. J., and Darling, R. S. (2016). "Quartz-in-garnet inclusion barometry under fire: Reducing uncertainty from model estimates". In: *Geology* 44.9, pp. 699–702.

Bonazzi, M., Tumiati, S., Thomas, J., Angel, R., and Alvaro, M. "Assessing the reliability of elastic geobarometry methods". In: *in prep* ().

Bose, K. and Ganguly, J. (1995). "Quartz-coesite transition revisited: reversed experimental determination at 500-1200°C and retrieved thermochemical properties". In: *American Mineralogist* 80.3-4, pp. 231–238.

Enami, M., Nishiyama, T., and Mouri, T. (2007). "Laser Raman microspectrometry of metamorphic quartz : A simple method for comparison of metamorphic pressures". In: 92.2001, pp. 1303–1315.

Eshelby, J. (1957). "The determination of the elastic field of an ellipsoidal inclusion, and related problems". In: *Proceedings of the Royal Society of London A: Mathematical, Physical and Engineering Sciences*. Vol. 241. The Royal Society, pp. 376–396.

Gillet, P, Ingrin, J, and Chopin, C (1984). "Coesite in subducted continental crust: P T history deduced from an elastic model". In: *Earth and Planetary Science Letters* 70.2, pp. 426–436.

Goodier, J. N. (1933). "Concentration of stress around spherical and cylindrical inclusions and flaws". In: *J. appl. Mech* 55.7, pp. 39–44.

Guiraud, M. and Powell, R. (2006). "P–V–T relationships and mineral equilibria in inclusions in minerals". In: *Earth and Planetary Science Letters* 244.3-4, pp. 683–694.

Isaak, D. G., Anderson, O. L., and Oda, H (1992). "High-temperature thermal expansion and elasticity of calcium-rich garnets". In: *Physics and Chemistry of Minerals* 19.2, pp. 106–120.

Karato, S.-I., Wang, Z., Liu, B., and Fujino, K. (1995). "Plastic deformation of garnets: systematics and implications for the rheology of the mantle transition zone". In: *Earth and Planetary Science Letters* 130.1-4, pp. 13–30.

Korsakov, A. V., Perraki, M., Zhukov, V. P., De Gussem, K., Vandenabeele, P., and Tomilenko, A. A. (2009). "Is quartz a potential indicator of ultrahigh-pressure metamorphism? Laser Raman spectroscopy of quartz inclusions in ultrahigh-pressure garnets". In: *European Journal of Mineralogy* 21.6, pp. 1313–1323.

Lakshtanov, D. L., Sinogeikin, S. V., and Bass, J. D. (2007). "High-temperature phase transitions and elasticity of silica polymorphs". In: *Physics and Chemistry of Minerals* 34.1, pp. 11–22.

Martelat, J. E., Malamoud, K., Cordier, P., Randrianasolo, B., Schulmann, K., and Lardeaux, J. M. (2012). "Garnet crystal plasticity in the continental crust, new example from south Madagascar". In: *Journal of Metamorphic Geology* 30.4, pp. 435–452.

Milani, S., Angel, R., Scandolo, L., Mazzucchelli, M., Ballaran, T., Klemme, S., Domeneghetti, M., Miletich, R., Scheidl, K., Derzsi, M., Tokár, K., Prencipe, M., Alvaro, M., and Nestola, F. (2017). "Thermo-elastic behavior of grossular garnet at high pressures and temperatures". In: *American Mineralogist* 102.4, pp. 851–859.

Milani, S., Nestola, F., Alvaro, M., Pasqual, D., Mazzucchelli, M. L., Domeneghetti, M. C., and Geiger, C. A. (2015). "Diamond–garnet geobarometry: The role of garnet compressibility and expansivity". In: *Lithos* 227.0, pp. 140–147.

Muir, J. M. and Brodholt, J. P. (2016). "Ferrous iron partitioning in the lower mantle". In: *Physics of the Earth and Planetary Interiors* 257, pp. 12–17.

Nguyen, T., Jones, R., and Boyce, B. (2007). "Modeling the anisotropic finite-deformation viscoelastic behavior of soft fiber-reinforced composites". In: *International Journal of Solids and Structures* 44.25-26, pp. 8366–8389.

Nye, J. F. (1985). *Physical properties of crystals: their representation by tensors and matrices*.

Özkan, H., Cartz, L., and Jamieson, J. C. (1974). "Elastic constants of nonmetamict zirconium silicate". In: *Journal of Applied Physics* 45.2, pp. 556–562.

Parnell, W. J. (2016). "The Eshelby, Hill, Moment and Concentration Tensors for Ellipsoidal Inhomogeneities in the Newtonian Potential Problem and Linear Elastostatics". In: *Journal of Elasticity* 125.2, pp. 231–294. arXiv: 1507.07165.

Perger, W., Criswell, J., Civalleri, B., and Dovesi, R. (2009). "Ab-initio calculation of elastic constants of crystalline systems with the CRYSTAL code". In: *Computer Physics Communications* 180.10, pp. 1753–1759.

Ranganathan, S. I. and Ostoja-Starzewski, M. (2008). "Universal elastic anisotropy index". In: *Physical Review Letters* 101.5, pp. 3–6.

Rosenfeld, J. L. and Chase, A. B. (1961). "Pressure and temperature of crystallization from elastic effects around solid inclusions in minerals?" In: *American Journal of Science* 259.7, pp. 519–541.

Sinogeikin, S. V. and Bass, J. D. (2002). "Elasticity of pyrope and majorite-pyrope solid solutions to high temperatures". In: *Earth and Planetary Science Letters* 203.1, pp. 549–555.

Spear, F. S., Thomas, J. B., and Hallett, B. W. (2014). "Overstepping the garnet isograd: a comparison of QuiG barometry and thermodynamic modeling". In: *Contributions to Mineralogy and Petrology* 168.3, pp. 1–15.

Tajčmanová, L, Podladchikov, Y, Powell, R, Moulas, E, Vrijmoed, J. C., and Connolly, J. A. D. (2014). "Grain-scale pressure variations and chemical equilibrium in high-grade metamorphic rocks". In: *Journal of Metamorphic Geology* 32.2, pp. 195–207.

Thomas, J. B. and Spear, F. S. (2018). "Experimental study of quartz inclusions in garnet at pressures up to 3.0 GPa: evaluating validity of the quartz-in-garnet inclusion elastic thermobarometer". In: *Contributions to Mineralogy and Petrology* 173, pp. 1–14.

Van der Molen, I and Van Roermund, H. L. M. (1986). "The pressure path of solid inclusions in minerals: the retention of coesite inclusions during uplift". In: *Lithos* 19.3, pp. 317–324.

Voegelé, V., Ando, J. I., Cordier, P., and Liebermann, R. C. (1998). "Plastic deformation of silicate garnets. I. High-pressure experiments". In: *Physics of the Earth and Planetary Interiors* 108.4, pp. 305–318.

Wang, J., Mao, Z., Jiang, F., and Duffy, T. S. (2015). "Elasticity of single-crystal quartz to 10 GPa". In: *Physics and Chemistry of Minerals* 42.3, pp. 203–212.

Weinberger, C., Cai, W., and Barnett, D. (2005). *Lecture Notes–Elasticity of Microscopic Structures*, p. 118.

Zhang, Y. (1998). "Mechanical and phase equilibria in inclusion-host systems". In: *Earth and Planetary Science Letters* 157.3-4, pp. 209–222.

Zhong, X., Moulas, E., and Tajčmanová, L. (2018). "Tiny timekeepers witnessing high-rate exhumation processes". In: *Scientific Reports* 8.1, pp. 1–9.

Zouboulis, E., Grimsditch, M., Ramdas, a., and Rodriguez, S. (1998). "Temperature dependence of the elastic moduli of diamond: A Brillouin-scattering study". In: *Physical Review B* 57.5, pp. 2889–2896.

Acknowledgments

Foremost, I would express my gratitude to my advisor Prof. M. Chiara Domeneghetti, who introduced me to mineralogy and crystallography, for the encouragement and the support along the road. I would like to thank Dr. Ross J. Angel who taught me the rigor in scientific research and the importance of explaining things effectively. A special thanks goes to Prof. Matteo Alvaro for conceiving such a great project. With his enthusiasm he guided me through my first steps in academia. He has taught me a lot, from science to problem solving attitudes. But above all he always trusted me, something that cannot be overlooked. By the way, he also funded me for several years...

I wish to thank Prof. Pamela Burnley for introducing me to Finite Element Modeling, for helping me at the beginning of my project, and for and giving an opportunity to become part of her team as an intern for some months.

I am also pleased to say thank you to Prof. Alessandro Reali and Dr. Simone Morganti, who have always had the patience to listen and understand the problems of a geologist struggling with the mechanics of solids...and those problems can really be a lot. Their suggestions were very much appreciated both in the theory and in the practice. Thanks to Prof. Marco Scambelluri that remembered me to not forget the real geology while I was conceiving my models, and to Prof. Marcello Campione for his suggestions on how to improve my thesis. A thanks goes to Dr. Antonio Langone for coordinating the review process of my thesis and to Chiara Trabella who with his efforts helped me a lot with the administrative tasks during these years and made sure that I did not miss any deadline, despite my attitude in forgetting things.

I wish also to thank Prof. Vittorio Tazzoli because even short conversations with him create the opportunity to think about science and philosophy for several days.

Thanks to Nicola Campomenosi, Mattia Bonazzi, Dr. Mattia Gilio, Prof. Boriana

Mihailova, Marta Morana, Mara Murri, Dr. Marco Piazzi, Prof. Mauro Prencipe, Dr. Claudia Stangarone, Hugo Van Schrojenstein Lantman and Gabriele Zaffiro because our project is really a team work and I learned something from each of them.

Finally, my gratitude goes to my parents, that supported me from the beginning, to my brother, who is always ready for a joke, and to Greta who believed in me during tough times.

This project has received fundings from:

The European Research Council (ERC) under the European Union's Horizon 2020 research and innovation program (grant agreements 714936 to Matteo Alvaro and 307322 to Fabrizio Nestola)

The Italian Ministry for University and Research under the MIUR-SIR grant "MILE DEEp" (RBSI140351) to Matteo Alvaro

The computational resources were provided by:

The United States National Nuclear Security Administration under the Stewardship Science Academic Alliances program through DOE Cooperative Agreement DE-NA0001982 to Pamela Burnley

The department of Civil Engineering and Architecture, University of Pavia, Italy

Appendices

Appendix A

Raman elastic geobarometry for anisotropic mineral inclusions

This chapter was published as an article in *American Mineralogist* with the title:

Raman elastic geobarometry for anisotropic mineral inclusions

Authors: M. Murri[1], M.L. Mazzucchelli[1], N. Campomenosi[2], A. V. Korsakov[3], M. Prencipe[4], B.D. Mihailova[5], M. Scambelluri[2], R.J. Angel[1], and M. Alvaro[2]

A.1 Abstract

Elastic geobarometry for host-inclusion systems can provide new constraints to assess the pressure and temperature conditions attained during metamorphism. Current experimental approaches and theory are developed only for crystals immersed in a hydrostatic stress field whereas inclusions experience deviatoric stress. We have developed a method to determine the strains in quartz inclusions from Raman spectroscopy using the concept of the phonon-mode Grüneisen tensor. We used ab initio Hartree-

[1]Department of Earth and Environmental Sciences, University of Pavia, Via A. Ferrata, 1 I-27100 Pavia, Italy; [2]Department of Earth Science, Environment & Life, University of Genoa, Corso Europa 26, 16132 Genoa, Italy; [3]V S Sobolev Institute of Geology and Mineralogy SB RAS, Novosibirsk, Russia; [4]Earth Sciences Department, University of Torino, Via Valperga Caluso 35 Italy; [5]Department of Earth Sciences, University of Hamburg, Grindelallee 48, D-20146 Hamburg, Germany.

Fock/Density Functional Theory to calculate the wavenumbers of the Raman-active modes as a function of different strain conditions. Least-squares fits of the phonon-wavenumber shifts against strains have been used to obtain the components of the mode Grüneisen tensor of quartz (γ_1^m and γ_3^m) that can be used to calculate the strains in inclusions directly from the measured Raman shifts. The concept is demonstrated with the example of a natural quartz inclusion in eclogitic garnet from Mir kimberlite and has been validated against direct X-ray diffraction measurement of the strains in the same inclusion.

A.2 Introduction

Mineral inclusions entrapped in ultra-high-pressure metamorphic rocks can provide fundamental information about geological processes such as subduction and continental collision. When a host-inclusion pair is exhumed from depth to the Earth's surface non-lithostatic stresses are developed in the inclusion because of the contrast in their elastic properties (Angel et al. 2015 and references therein). The inclusion is under compressive stress if it is more compressible than the host. If correctly interpreted, these stresses on the inclusion allow the stress conditions at entrapment to be estimated. However, the theory for elastic geobarometry for host-inclusion pairs is only developed for crystals immersed in a hydrostatic stress field. This is valid for an isotropic and spherical inclusion entrapped in an isotropic host as it is subject to isotropic strains imposed by the host and will therefore exhibit isotropic stresses; that means the inclusion will be under hydrostatic pressure. However, if inclusions of elastically anisotropic minerals such as quartz or coesite, are entrapped in a cubic host such as garnet the same isotropic strain imposed by the garnet will result in anisotropic (i.e. deviatoric) stresses in the inclusion (see Fig. A.1). Thus, the stress state of the inclusion will be different from the hydrostatic case, and it cannot be characterized by a single "pressure" value (Anzolini et al. 2018). Further, the shifts of Raman mode frequencies under deviatoric stress are unknown in general. The limited experimental evidence (e.g.Briggs & Ramdas 1977) is that the Raman modes change differently from those measured under hydrostatic pressure. Therefore, the key question remains that posed by Korsakov et al. (2010), can shifts of Raman modes measured in hydrostatic experiments be used to interpret the Raman shifts from an inclusion under non-hydrostatic stress? And what errors does this introduce into estimates of inclusion stress and entrapment conditions? Since it is challenging to perform experiments under controlled deviatoric stress conditions, we have performed ab initio HF/DFT (Hartree-Fock/Density Functional Theory) calculations to determine how the Raman modes of quartz change under both hydrostatic pressure and deviatoric stress conditions. We show how the HF/DFT simulations can be used to determine the strains (and by inference the stresses) within a crystal inclusion via mode Grüneisen tensors and measurement of its Raman shifts.

A.3 Grüneisen tensor and strains

It is well known that when stresses are applied to a crystal, for example by changing the pressure, the phonon wavenumbers are shifted. This is most easily seen in the change in Raman peak positions measured under hydrostatic pressure. The shifts of certain modes of materials (e.g. the 464 cm^{-1} mode of quartz) have frequently been used as secondary pressure standards. However, there is a common misconception that the observed wavenumber shifts of the Raman-active modes are directly related to the magnitude of the applied pressure or stress. If that were true, then Raman modes would not show a change in wavenumber when the temperature of a free crystal is changed at ambient pressure. Instead, Raman modes generally exhibit a decrease in wavenumber as temperature is increased. As Fig. A.2 shows, the shift of the 464 cm^{-1} mode of quartz with both pressure and temperature shows the same dependence upon volume. These observations point to the correct interpretation that the shift $\Delta\omega$ of the wavenumber ω of a vibrational mode is primarily due to the strains of the crystal induced by the applied temperature or pressure. Thus, the Raman peak position of a crystal under a strain $\boldsymbol{\varepsilon}$ (i.e. the full strain tensor) is determined by the second-rank symmetric tensor: the mode Grüneisen tensor $\boldsymbol{\gamma}^m$ (Ziman 1960, Key 1967, Cantrell 1980) characteristic of each phonon mode m, which can be written in Voigt (1910) notation as:

$$-\frac{\Delta\omega}{\omega} = \gamma_1^m\varepsilon_1 + \gamma_2^m\varepsilon_2 + \gamma_3^m\varepsilon_3 + \gamma_4^m\varepsilon_4 + \gamma_5^m\varepsilon_5 + \gamma_6^m\varepsilon_6 \tag{A.1}$$

This equation means that the changes in the Raman peak positions in general depend on all the components of the strain tensor (see supplementary materials), not just on the relative change in the volume (i.e. $\varepsilon_1 + \varepsilon_2 + \varepsilon_3$). Because the mode Grüneisen tensor is a symmetric second-rank property tensor, it is subject to the same symmetry constraints on its component values as other second-rank property tensors, such as the thermal expansion and compressibility tensors. For the trigonal symmetry of quartz $\gamma_1^m = \gamma_2^m \neq \gamma_3^m$, and $\gamma_4^m = \gamma_5^m = \gamma_6^m = 0$. Garnet is almost elastically isotropic (Sinogeikin and Bass 2002) so the strain imposed by the garnet host does not break the symmetry of the quartz inclusion. Therefore, we are interested specifically in the cases when $\varepsilon_1 = \varepsilon_2$, for which the shift in the phonon wavenumbers should be given by:

$$-\frac{\Delta\omega}{\omega} = 2\gamma_1^m\varepsilon_1 + \gamma_3^m\varepsilon_3 \tag{A.2}$$

To determine the values of γ_1^m and γ_3^m independently of one another it is not sufficient to measure the Raman shifts under hydrostatic pressure, because only a single series of

values of ε_1 and ε_3 are measured. We therefore use HF/DFT simulations to calculate the Raman modes at different imposed strains on the crystal to determine its structure and properties at those strains.

A.4 Raman shifts and strains from *ab initio* calculations

Ab initio HF/DFT simulations have been performed by means of CRYSTAL 14 code (Dovesi et al. 2014) employing the hybrid Hamiltonian WC1LYP (Wu and Cohen 2006) which has been demonstrated to be particularly suitable for the accurate reproduction of the elastic and vibrational properties (Prencipe et al. 2014; Zicovich-Wilson et al. 2004). Further computational details are reported in the supplementary materials.

We will only discuss in detail the Raman-active modes near 464 cm^{-1} (non-degenerate A_1 mode) and 696 cm^{-1} (doubly degenerate E mode) because they give peaks in the Raman spectra that are easily-resolved from the peaks of the host garnets. Note that all E modes in quartz are polar, and therefore have longitudinal optical (LO) and transverse optical (TO) components that generate two separate Raman peaks, whose intensity ratio varies depending on the scattering geometry. Because of the polarization mixing (Loudon 1964), the wavenumber of the LO component depends on the angle between the triad axis of quartz and the phonon-propagation direction that in the case of backscattering geometry coincides with the direction of the laser beam. For the E mode of interest in this study, the LO-TO splitting is rather small. At ambient conditions $\omega_{ETO} = 696$ cm^{-1}, while the maximum $\omega_{ETO} \sim 697.5$ cm^{-1} and it corresponds to the case when the c axis is perpendicular to the laser beam. The two components are thus very close to each other and in specific experimental geometries may generate peaks of similar intensity. To avoid possible contribution from the LO component that may lead to a subtle artificial shift of the corresponding Raman peak towards higher wavenumbers, one should either rotate the sample about the direction of the laser beam to verify that the peak position does not change, or find the orientation at which the wavenumber of the Raman peak is lowest (which should be when the c axis is perpendicular to the polarization of the incident light).

Fig. A.3a, b are contour maps that display the HF/DFT wavenumber shifts of the A_1 mode near 464 cm^{-1} and ETO mode near 696 cm^{-1} as a function of the two independent strain components. For small strains (close to the origin) the iso-shift lines are parallel to one another and equally spaced, confirming that the values of γ_1^m and γ_3^m are constants over these strain ranges. The contour lines for the two modes have different slopes (e.g Fig. A.3a,b and c) indicating that the values of their Grüneisen components are different. Further, Fig. A.3a shows that the iso-shift lines are not parallel to

isochors which are represented by lines of equal volume strain ($\varepsilon_V = 2\varepsilon_1 + \varepsilon_3$). If the wavenumber shifts are plotted against the stress components σ_1 and σ_3 (see Fig. A.8 in supplementary material) then the iso-shift lines are not parallel to isobars (lines of constant pressure $(2\sigma_1 + \sigma_3)/3 = -P$. Therefore, in general, Raman shifts do not measure either volume or pressures; for uniaxial crystals like quartz they indicate the principal normal strain components ε_1 and ε_3. The Grüneisen tensor components for all modes were then determined by fitting equation (A.2) by least-squares to the wavenumber shifts at different strain states simulated by HF/DFT calculations. For the 464 mode, the maximum misfit was 1.76 cm^{-1} (see supplementary materials for residual plots and full details). HF/DFT calculations are performed under static stress at absolute-zero temperature. Inclusions are measured at room temperature. In order to use the mode Grüneisen tensors to determine strains in inclusions, one has to also demonstrate that their values are independent of P and T. This is equivalent to the solid behaving according to the quasi-harmonic approximation (QHA). We achieve this by calculating the strains of a free quartz crystal relative to room conditions from the known unit-cell parameter variation of quartz (Angel et al. 2017a) with P and T. We then compare the wavenumber shifts from room-condition values using the Grüneisen components (γ_1^m and γ_3^m) for the two modes at 464 cm^{-1} and 696 cm^{-1} (i.e. 0.60 and 1.19; 0.50 and 0.36) determined by HF/DFT and equation 2 with experimental data. The line in Fig. A.2 shows that for the mode near 464 cm^{-1} the experimentally-measured wavenumber shifts under high pressure at room T and those up to ∼400°C at room P are reproduced by the Grüneisen components determined by HF/DFT. At higher temperatures the predicted shifts differ from the experimental data because of pre-transition effects associated with the $\alpha - \beta$ quartz transition that cannot be accounted using QHA. Further, the fundamental soft mode near 206 cm^{-1}, which is heavily involved in the temperature $\alpha-$ to $\beta-$quartz phase transition (Scott, 1968), clearly violates the QHA, and HF/DFT simulations cannot be used to determine the mode Grüneisen components. In order to use this band to determine strains in inclusions, the variation of its position with strain must be determined experimentally.

A.5 Validation from Raman scattering and X-ray diffraction

To validate this approach, we performed micro-Raman spectroscopy and X-ray diffraction measurements on quartz inclusion in garnet from a diamond-grade eclogite xenolith (TM90-1) from the Mir kimberlite pipe (Yakutiya). We selected this example as it has the highest Raman shifts reported for quartz inclusions in garnet (Korsakov et al. 2009; Zhukov and Korsakov 2015). Parallel polarized Raman spectra were collected in backscattering geometry with a Horiba Jobin-Yvon T64000 triple-monochromator spec-

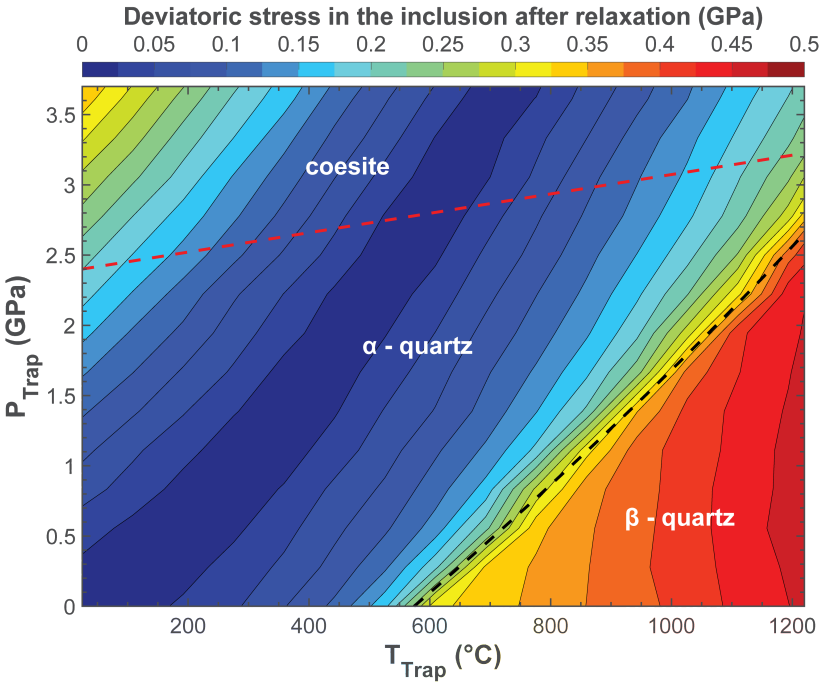

Figure A.1: Deviatoric stress $|\sigma_3 - \sigma_1|$ in a quartz inclusion in a pyrope garnet (where σ_1 and σ_3 are parallel to the a and c axes in quartz, respectively) at room conditions as a function of P (GPa) and T (°C) of entrapment. The EoS of quartz and pyrope are from Angel et al. (2017) and Milani et al. (2015). The anisotropic relaxation was calculated using the elastic tensors for quartz and pyrope (Lakshtanov et al. 2007; Sinogeikin and Bass 2002). Red dashed line: α-quartz to coesite phase boundary; black dashed line: α to β quartz phase boundary. From Murri et al. (2018).

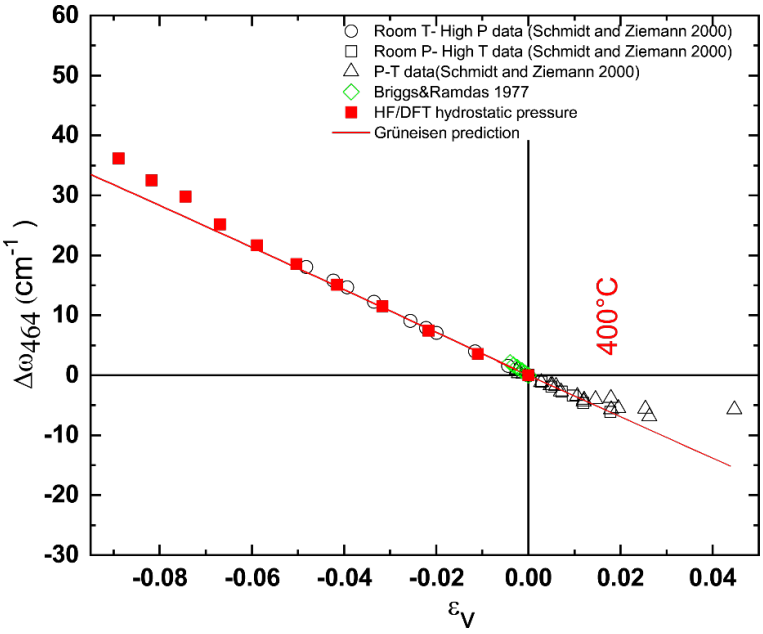

Figure A.2: The wavenumber shift ($\Delta\omega$) of the 464 cm^{-1} mode of a free quartz crystal measured under different P, T and stress conditions form a single trend with volume strain ε_V. The deviation at positive strains is caused by the transition from α to β quartz that occurs at 573 °C. The deviation becomes relevant from 400 °C, at $\varepsilon_V = 0.02$. Away from the transition, the experimental data are reproduced by both the HF/DFT simulations under hydrostatic pressure [red filled squares], and the prediction from the mode Grüneisen parameters (line). From Murri et al. (2018).

trometer (spectral resolution of ∼2 cm–1, instrumental accuracy in peak positions of ∼0.35 cm–1 and 2 μm spot size) following the same protocol reported in Campomenosi et al. (2018). Fig. A.4 shows that the shift of the 464 cm^{-1} Raman line changes significantly across the crystal as a consequence of edge and corner effects (Campomenosi et al. 2018 and Mazzucchelli et al. 2018), and is lowest at the center of the inclusion. We determined the unit-cell parameters of the inclusion by single crystal X-ray diffraction measurements using the 8-position centering method (SINGLE, Angel and Finger, 2011) using a newly developed Huber 4-circle Eulerian cradle diffractometer equipped with point detector and microfocus source (120 μm spot size). The difference between the unit cell parameters of the inclusion a = 4.86669(44) Å, c = 5.35408(14) Å and those of a free crystal measured on the same instrument (a = 4.91160(7) Å, c = 5.40325(9) Å) shows that the inclusion is under strains $\varepsilon_1 = -0.00914(9)$, $\varepsilon_3 = -0.00910(26)$, and $\varepsilon_V = -0.02714(30)$. Relative to room conditions the quartz inclusion is currently under isotropic strain within the experimental uncertainties. From these strains and the Grüneisen-tensor components for the mode near 464 cm^{-1} (i.e. $\gamma_1^{464} = 0.60$ and $\gamma_3^{464} = 1.19$), we calculate an expected wavenumber shift of 10.12 cm^{-1}. This is between the minimum and maximum shifts actually measured on the inclusion (Fig. A.4) because the unit-cell parameters measured by X-ray diffraction are an average over the entire volume of the inclusion. Conversely, if we take the shifts of the Raman modes near 464 and 696 cm^{-1} measured at the center of the inclusion and the calculated mode Grüneisen components we predict the following strains: $\epsilon_1 = -0.0093(5)$ and $\epsilon_3 = -0.0070(5)$. In this case the total strain that is lower than that measured by X-ray diffraction, again because this method provides an average over the inclusion.

A.6 Implications

We have demonstrated by a combination of HF/DFT simulations and comparison to experimental Raman data that quartz has some Raman-active modes whose wavenumbers are only a function of strain (for small strains) and are not directly dependent on P and T. The HF/DFT simulations show also that in general the shift of a Raman line does not indicate either the volume change (or volume strain) or the mean normal stress but is a more complex function of the linear strains (Fig. A.3). The linear strains of a quartz inclusion can be determined from the wavenumber shifts of at least two Raman peaks by using the mode Grüneisen components determined by HF/DFT. Conversely, a wavenumber shift for a specific Raman-active mode can be determined from the linear strains measured by X-ray diffraction and by using the mode Grüneisen components determined by HF/DFT. We proved that strains and Raman shifts vary significantly across an inclusion (Fig. A.4) as a result of the influence of shape combined with elastic anisotropy (Mazzucchelli et al. 2018, Campomenosi et al. 2018), and should never be averaged. The Raman shifts measured in the center of inclusions

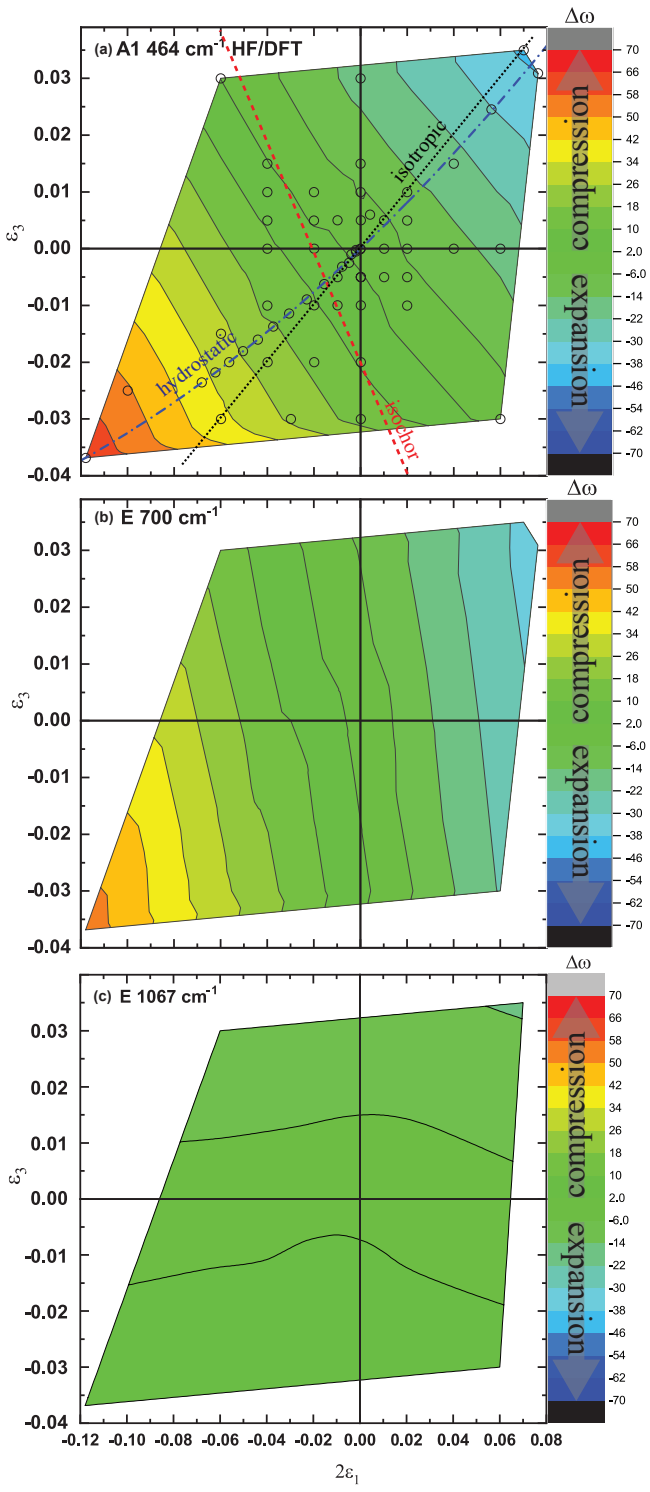

Figure A.3: (a,b,c) Wavenumber shifts $\Delta\omega$ (cm^{-1}) of quartz calculated by HF/DFT as a function of the two independent strain components ($\varepsilon_1 = \varepsilon_2 \neq \varepsilon_3$). The reference value at zero strain is the ab initio datum at 0 K and 0 GPa (static pressure). The symbols indicate strains at which HF/DFT simulations were performed. The colored bands are the iso-shift lines (lines with the same frequency shift for a specific Raman mode). The iso-shift lines are approximately parallel to one another and equally spaced. The iso-shift lines are not parallel to isochors defined by constant volume strain $\varepsilon_V = 2\varepsilon_1 + \varepsilon_3$. From Murri et al. (2018).

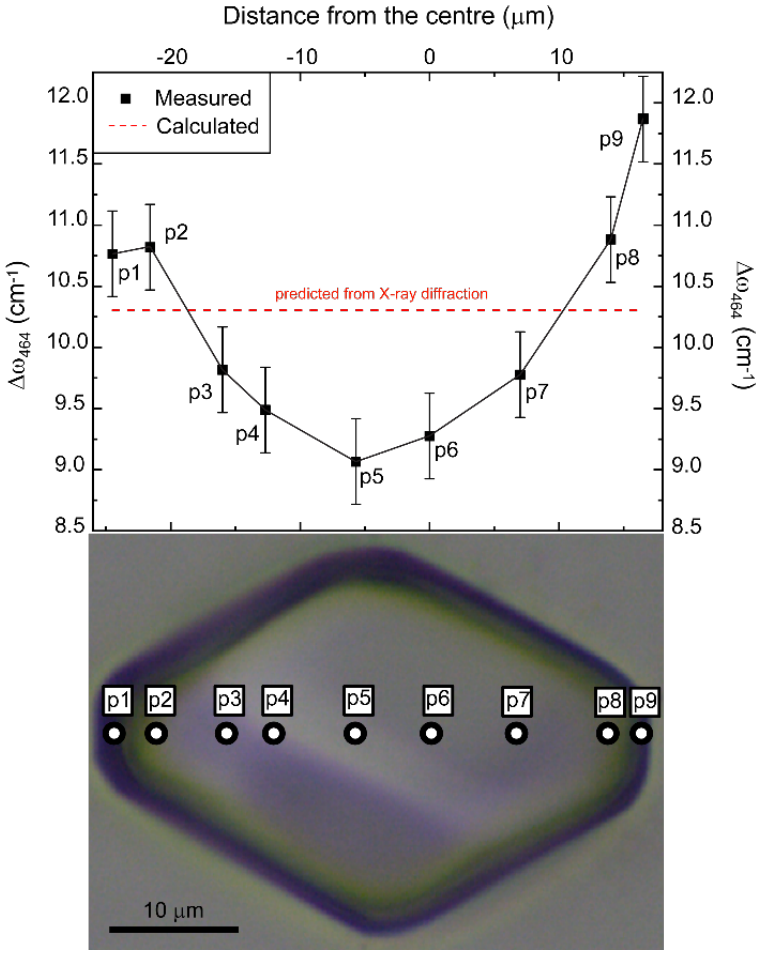

Figure A.4: Wavenumber shifts of the 464 cm^{-1} and 696 cm^{-1} modes measured in a traverse across a quartz inclusion in pyrope from the eclogite xenolith TM90-1 (Korsakov et al.2009). The phonon wavenumber shifts calculated from the strains determined by X-ray diffraction and the mode Grüneisen tensor are in good agreement with the average of the measured shifts. From Murri et al. (2018).

are least affected by the presence of edges and should be the only ones used to infer, after shape corrections (Mazzucchelli et al. 2018), the entrapment conditions. On the other hand, X-ray diffraction measurements give strain components that are averaged over the entire volume of the investigated crystal. For the example discussed, the interpretation of wavenumber shift of the mode near 464 cm^{-1} measured at the center of the quartz inclusion with the hydrostatic calculation (Schmidt and Ziemann 2000) leads to only a small error in the estimation of the mean normal stress (i.e. pressure) of ca. 0.03 GPa. This would lead to an error in the calculated entrapment pressure of 0.06 GPa. However, this is not always the case. When the deviatoric stress (Fig. A.1) in the inclusion is higher, the error is larger. For example, a quartz inclusion in garnet reset at 1.5 GPa and 1100°C during exhumation will have a wavenumber shift of the Raman mode near 464 cm^{-1} that would yield an entrapment pressure of 0.6 GPa too low when the hydrostatic calibration is used. In anisotropic hosts the discrepancy from the hydrostatic calibration also depends on the relative orientation of the host and inclusion. For example, for quartz in zircon the error in the calculated entrapment pressure can vary from 0.2 to 0.6 GPa for the same entrapment condition (i.e. 0.3 GPa and 800°C) depending on orientation.

A.7 Supplementary materials

A.7.1 Voigt notation

The band position under a strain $\boldsymbol{\varepsilon}$ is determined by the second-rank symmetric mode Grüneisen tensor $\boldsymbol{\gamma}^m$ (Ziman, 1960; Key, 1967; Cantrell, 1980) for each Raman mode:

$$\frac{-\partial\omega}{\omega} = \boldsymbol{\gamma}^m : \boldsymbol{\varepsilon} \tag{A.3}$$

The ":" in equation (A.3) is a double-scalar product between the two tensors. Because both tensors are second-rank and symmetric this can be written out in full in Voigt (1910) notation as:

$$\frac{-\partial\omega}{\omega} = \gamma_1^m\varepsilon_1 + \gamma_2^m\varepsilon_2 + \gamma_3^m\varepsilon_3 + \gamma_4^m\varepsilon_4 + \gamma_5^m\varepsilon_5 + \gamma_6^m\varepsilon_6 \tag{A.4}$$

Note that under the Voigt convention here for strains, the values of the shear strains ε_4,ε_5,ε_6 are one-half of the values of the corresponding tensor components ε_{23},ε_{13},ε_{12}. Instead, γ_4^m,γ_5^m and γ_6^m are equal of the values of the corresponding tensor components γ_{23}, γ_{13},γ_{12}. This equation means that the changes in the Raman peak positions in general depend on all of the strains in three dimensions experienced by the crystal, not just the volume. In principle, the values of the six components, γ_i^m with $i = 1$ to 6,

of a mode Grüneisen tensor may change with pressure and temperature, and with the magnitude of the strains. And, as we will show for quartz, the values of γ_i^m are different for different modes. The mode will be indicated by the superscript m, in various forms. Because the mode Grüneisen tensor is a symmetric second-rank property tensor, it is subject to the same symmetry constraints on its component values as other second-rank property tensors, such as the thermal expansion and compressibility tensors. This is required to make the frequency shift given by equations (A.3) and (A.4) invariant under coordinate transformations. Thus, in all crystals with orthorhombic symmetry or higher, $\gamma_4^m = \gamma_5^m = \gamma_6^m = 0$. For uniaxial crystals in the standard setting $\gamma_1^m = \gamma_2^m$, and for cubic crystals and isotropic materials $\gamma_1^m = \gamma_2^m = \gamma_3^m$. Therefore, for the trigonal symmetry of quartz $\gamma_1^m = \gamma_2^m$. For the specific case of quartz inclusions in an isotropic host, such as garnet, the strain imposed by the garnet does not break the symmetry of the quartz crystal. Therefore, we are interested specifically in the cases when $\varepsilon_1 = \varepsilon_2$, for which the shift in the wave numbers of modes should be given by:

$$\frac{-\partial\omega}{\omega} = 2\gamma_1^m\varepsilon_1 + \gamma_3^m\varepsilon_3 \tag{A.5}$$

A.7.2 Computational details

The hybrid Hamiltonian WC1LYP is based on the generalized gradient approximation (GGA) exchange functional WC (Wu and Cohen 2006), mixed with 16% of the exact non-local Hartree–Fock exchange to correct for the self-interaction error (the interaction of an electron with itself), which is typical of both pure DFT local density (LDA) and generalized gradient approximation functionals. The Hamiltonian also includes the LYP correlation functional (Lee et al. 1988). The grid for the evaluation of the DFT exchange–correlation functionals was chosen by the keyword XLGRID of the CRYSTAL14 user manual (Dovesi et al. 2014) and corresponds to a total of 37547 points in the unit cell. A measure of the numerical accuracy provided by such a grid is the evaluation of the total number of electrons in the unit cell, by the numerical integration of the electron density over the cell volume. For quartz we obtained 90.00003 electrons out of 90 for the reference volume at 0 K and 0 GPa static pressure. The localised contracted atomic basis sets used were Si 86-311G** (Pascale et al. 2005) and 8-411G(2d) (Valenzano et al. 2006) for Si and O, respectively, which were successfully employed to calculate ab initio structures and properties of silicates (e.g. Stangarone et al. 2017). Within the CRYSTAL code the accuracy in evaluating the Coulomb and Hartree-Fock exchange series is controlled by the keyword TOLINTEG, for which we set the five parameters to 8 (T1, T2, T3 and T4) and 18 (T5) (Dovesi et al. 2014). The diagonalization of the Hamiltonian matrix was performed at 7 independent k vectors in the reciprocal space (Monkhorst net; Monkhorst and Pack 1976) by setting to 3

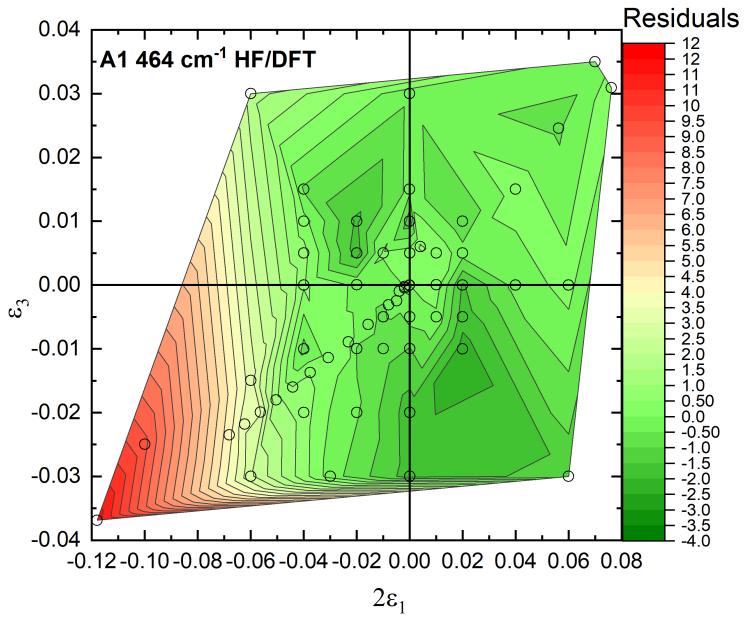

Figure A.5: Residual plot from the fitting procedure for the Raman line near 464 cm^{-1}. From Murri et al. (2018).

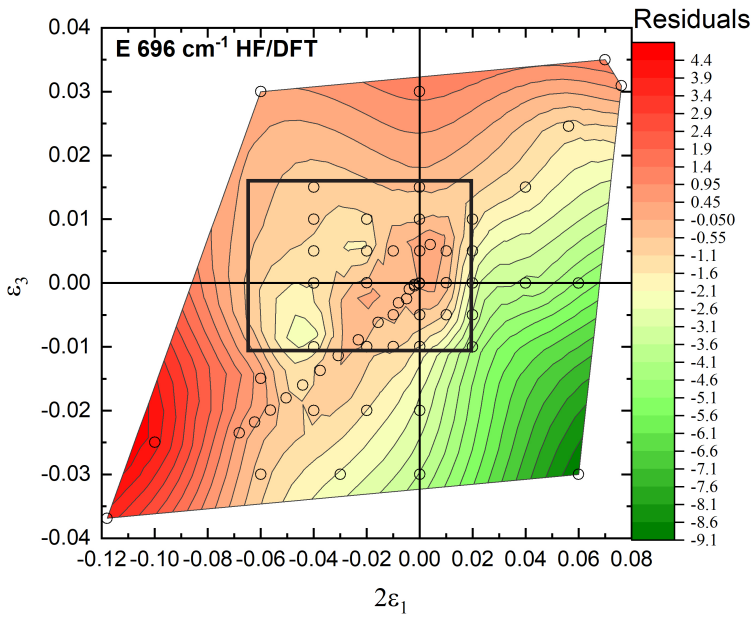

Figure A.6: Residual plot from the fitting procedure for the Raman line near 696 cm^{-1}. From Murri et al. (2018).

the shrinking factor IS (Dovesi et al. 2014). Cell parameters and fractional coordinates were optimized by analytical gradient methods, as implemented in CRYSTAL14 (Civalleri et al. 2001; Dovesi et al. 2014). Geometry optimization was considered converged when each component of the gradient (TOLDEG parameter in CRYSTAL14) was smaller than 0.00003 hartree/bohr and displacements (TOLDEX) were smaller than 0.00012 bohr with respect to the previous step. Lattice parameters and fractional coordinates were optimized at the WC1LYP level (static values: no zero point and thermal effects included), at the static pressures from 0 to 10 GPa (with step of 0.5 GPa from 0 to 5 GPa and then a simulation at 10 GPa). For the non-hydrostatic simulations, the cell parameters were fixed at the chosen strain conditions and only the fractional coordinates were optimized with the keyword ATOMONLY (Civalleri et al. 2001; Dovesi et al. 2014). Vibrational wavenumbers of all of the normal modes were calculated at the Γ point within the limit of the harmonic approximation, by diagonalizing a mass-weighted Hessian matrix, whose elements are the second derivatives of the full potential of the crystal with respect to the mass-weighted atomic displacements (Pascale et al. 2004).

A.7.3 Residual plots from the fitting procedure

The Grüneisen tensor components for all modes were then determined by fitting equation (A.2) by least-squares to the wavenumber shifts at different strain states simulated by HF/DFT calculations. The maximum misfits (i.e. $\Delta\omega_{obs} - \Delta\omega_{calc}$) are -1.76 cm^{-1} and -3.41 cm^{-1} and for the 464 and 696 cm^{-1} bands, respectively, considering only the values in the black box because is where we could assume this surface to be planar (area of small strains). Outside from this box the misfit increases and therefore we did not include the other values in the fitting.

A.7.4 Raman spectroscopy details

Raman spectra were excited by the 514.532 nm line of a Coherent 90C Fred Ar+ laser. The laser power on the sample surface was approximately 14 mW, while the laser spot on the sample surface was approximately 2 micrometers. Spectra were collected for 15 s averaging over 3 accumulations. These conditions were proven not to cause overheating of the sample. The spectrometer was calibrated to the silicon Raman peak at 520.5 cm^{-1}. The spectral resolution was 2 cm^{-1}, while the precision in measuring the peak positions was 0.35 cm^{-1}. In the case of the quartz inclusion i6, the angle between the c axis of the quartz inclusion and the polarization of the incident light was 30°. For the inclusion a series of spot measurements were carried out along the two crystallographic axes. The OriginLab-Pro 2018 software package was used for data fitting and evaluation. The collected spectra were baseline corrected for the continuum luminescence background when necessary, temperature-reduced to account for the Bose-Einstein occupation factor (Kuzmany, 2009) and normalized to the acquisition time. Peak positions, full-widths at half maximum (FWHMs), and integrated intensities were determined from fits with pseudo-Voigt functions [PV = (1 – q)·Lorentz + q·Gauss, q is the weight coefficient]. The criterion for the maximum number of fitted peaks was $\Delta I < I/2$, where I and ΔI are the calculated magnitude and uncertainty of each peak intensity, respectively.

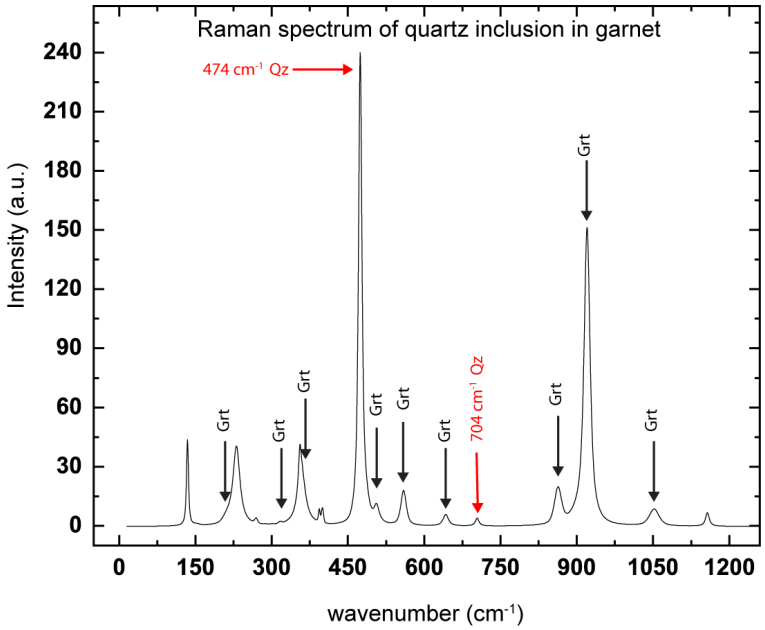

Figure A.7: Raman spectrum of the quartz inclusion (i6) in the garnet host measured at the center of the inclusion. The two selected peaks of quartz are those at 474 and 704 cm^{-1} (highlighted in red). The peaks are shifted towards higher wavenumbers since the inclusion is strained. For un unstrained quartz they appear at 464 and 696 cm^{-1}. The non-labelled peaks are those of quartz. From Murri et al. (2018).

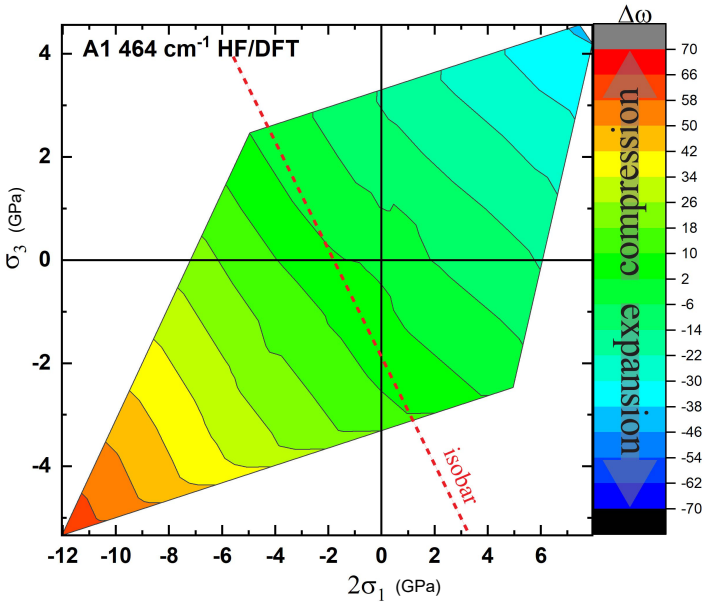

Figure A.8: The iso-shift lines are not parallel to isobars, which are lines of equal pressure $(2\sigma_1 + \sigma_3)/3 = -P$ *(GPa), meaning that, in general, Raman shifts do not measure either pressure or stresses. From Murri et al. (2018).*

A.8 Acknowledgments

This project received funding from the European Research Council under the European Union's Horizon 2020 research and innovation program grant agreements 714936 and from the MIUR-SIR (Ministry of Education, University and Research–Scientific Independence of Young Researchers, Italy) grant MILE DEEp (Mineral Inclusion Elasticity for a New Deep Subduction Geobarometer; RBSI140351) to Matteo Alvaro. Andrey V. Korsakov was supported by the Russian Federation state assignment project No. 0330-2016-0006.

A.9 References

Angel, R.J., and Finger, L.W. (2011). SINGLE: a program to control single-crystal diffractometers. Journal of Applied Crystallography, 44(1), 247-251.

Angel, R.J., Nimis, P., Mazzucchelli, M.L., Alvaro, M., and Nestola, F. (2015). How large are departures from lithostatic pressure? Constraints from host–inclusion elasticity. Journal of Metamorphic Geology, 33(8), 801-813.

Angel, R.J., Alvaro, M., Miletich, R., and Nestola, F. (2017). A simple and generalised P–T–V EoS for continuous phase transitions, implemented in EosFit and applied to quartz. Contributions to Mineralogy and Petrology, 172(5), 29.

Anzolini, C., Prencipe, M., Alvaro, M., Romano, C., Vona, A., Lorenzon, S., Smith, E.M., Brenker F.E., and Nestola, F. (2018). Depth of formation of super-deep diamonds: Raman barometry of CaSiO3-walstromite inclusions. American Mineralogist, 103(1), 69-74.

Briggs, R.J., and Ramdas, A.K. (1977). Piezospectroscopy of the Raman spectrum of α-quartz. Physical Review B, 16(8), 3815.

Campomenosi N., Mazzucchelli M.L., Mihailova B.D., Scambelluri M., Angel R.J, Nestola F., Reali A, and Alvaro M. (2018) Raman elastic geobarometry revisited: insights from zircon and coesite inclusions in pyrope from the ultra-high pressure alpine Dora Maira Massif. Geology, under review.

Cantrell Jr, J.H. (1980). Generalized Grüneisen tensor from solid nonlinearity parameters. Physical review B, 21(10), 4191.

Civalleri, B., D'Arco, P., Orlando, R., Saunders, V., and Dovesi, R. (2001) Hartree–Fock geometry optimisation of periodic systems with the CRYSTAL code. Chemical Physics Letters, 348, 131–138.

Dovesi, R., Orlando, R., Erba, A., Zicovich-Wilson, C.M., Civalleri, B., Casassa,

S., Maschio, L., Ferrabone, M., De La Pierre, M., D'Arco, P. and Noël, Y. (2014). CRYSTAL14: A program for the ab initio investigation of crystalline solids. International Journal of Quantum Chemistry, 114(19), 1287-1317.

Key, S.W. (1967). Grüneisen tensor for anisotropic materials. Journal of Applied Physics, 38(7), 2923-2928.

Korsakov, A.V., Perraki, M., Zhukov, V.P., De Gussem, K., Vandenabeele, P., and Tomilenko, A.A. (2009). Is quartz a potential indicator of ultrahigh-pressure metamorphism? Laser Raman spectroscopy of quartz inclusions in ultrahigh-pressure garnets. European Journal of Mineralogy, 21(6), 1313-1323.

Korsakov, A.V., Zhukov, V.P., and Vandenabeele, P. (2010). Raman-based geobarometry of ultrahigh-pressure metamorphic rocks: applications, problems, and perspectives. Analytical and bioanalytical chemistry, 397(7), 2739-2752.

Kuzmany, H., 2009, Solid state spectroscopy, an introduction, second edition, cap-9 (185-200): 185-200 p., doi: 10.1007/978-3-642-01479-6.

Lakshtanov, D.L., Sinogeikin, S.V., and Bass, J.D. (2007). High-temperature phase transitions and elasticity of silica polymorphs. Physics and Chemistry of Minerals, 34(1), 11-22.

Lee, C., Yang, W., and Parr, R.G. (1988) Development of the Colle-Salvetti correlation-energy formula into a functional of the electron density. Physical review B, 37, 785.

Loudon, R. (1964). The Raman effect in crystals. Advances in Physics, 13(52), 423-482.

Mazzucchelli, M.L., Burnley, P., Angel, R.J., Morganti, S., Domeneghetti, M.C., Nestola, F., and Alvaro, M. (2018). Elastic geothermobarometry: Corrections for the geometry of the host-inclusion system. Geology, 46(3), 231-234.

Milani, S., Nestola, F., Alvaro, M., Pasqual, D., Mazzucchelli, M.L., Domeneghetti, M.C., and Geiger, C.A. (2015). Diamond–garnet geobarometry: The role of garnet compressibility and expansivity. Lithos, 227, 140-147.

Monkhorst, H.J., and Pack, J.D. (1976) Special points for Brillouin-zone integrations. Physical Review B, 13, 5188.

Murri, M., Mazzucchelli, M.L., Campomenosi, N., Korsakov, A. V., Prencipe, M., Mihailova, B.D., Scambelluri, M., Angel, R.J., and Alvaro, M. (2018) Raman Elastic Geobarometry For Anisotropic Mineral Inclusions. American Mineralogist, 103, 1869–1872.

Pascale, F., Zicovich-Wilson, C.M., Lopez Gejo, F., Civalleri, B., Orlando, R., and Dovesi, R. (2004) The calculation of the vibrational frequencies of crystalline compounds and its implementation in the CRYSTAL code. Journal of Computational Chemistry, 25, 888–897.

Pascale, F., Zicovich-Wilson, C. M., Orlando, R., Roetti, C., Ugliengo, P., and Dovesi, R. (2005). Vibration frequencies of Mg3Al2Si3O12 pyrope. An ab initio study with the CRYSTAL code. The Journal of Physical Chemistry B, 109(13), 6146-6152.

Prencipe, M., Maschio, L., Kirtman, B., Salustro, S., Erba, A., and Dovesi, R. (2014). Raman spectrum of NaAlSi2O6 jadeite. A quantum mechanical simulation. Journal of Raman Spectroscopy, 45(8), 703-709.

Schmidt, C., and Ziemann, M.A. (2000). In-situ Raman spectroscopy of quartz: A pressure sensor for hydrothermal diamond-anvil cell experiments at elevated temperatures. American Mineralogist, 85(11-12), 1725-1734.

Scott, J.F. (1968) Evidence of coupling between one- and two-phonon excitations in quartz. Physical Review Letters, 21(13) 907-910.

Sinogeikin, S.V., and Bass, J.D. (2002). Elasticity of majorite and a majorite-pyrope solid solution to high pressure: Implications for the transition zone. Geophysical Research Letters, 29(2).

Stangarone, C., Böttger, U., Bersani, D., Tribaudino, M., and Prencipe, M. (2017). Ab initio simulations and experimental Raman spectra of Mg2SiO4 forsterite to simulate Mars surface environmental conditions. Journal of Raman Spectroscopy, 48(11), 1528-1535.

Valenzano, L., Torres, F. J., Doll, K., Pascale, F., Zicovich-Wilson, C. M., and Dovesi, R. (2006). Ab initio study of the vibrational spectrum and related properties of crystalline compounds; the case of CaCO3 calcite. Zeitschrift für Physikalische Chemie, 220(7/2006), 893-912.

Voigt W. Lehrbuch der Kristallphysik (B. G. Teubner. Berlin. 1910). p.754.

Wu, Z., and Cohen, R.E. (2006) More accurate generalized gradient approximation for solids. Physical Review B, 73, 235116.

Zhukov, V.P., and Korsakov, A.V. (2015). Evolution of host-inclusion systems: a visco-elastic model. Journal of Metamorphic Geology, 33(8), 815-828.

Zicovich-Wilson, C.M., Pascale, F., Roetti, C., Saunders, V.R., Orlando, R., and Dovesi, R. (2004). Calculation of the vibration frequencies of α-quartz: The

effect of Hamiltonian and basis set. Journal of Computational Chemistry, 25(15), 1873-1881.

Ziman, J.M. (1960). Electrons and phonons: the theory of transport phenomena in solids. Oxford University Press. p.469

Appendix B

Elastic properties

This appendix reports the anisotropic elastic properties and the isotropic averages of the minerals used in the calculations reported in this thesis. The anisotropic elastic properties are described by the 4^{th}-order stiffness tensor (C_{ijkl}, with components in GPa), here are reported as the components C_{ij} of the corresponding matrix in Voigt notation. The isotropic averages are described through the bulk (K) and the shear (G) moduli at room conditions as obtained from their P-V-T equation of state (EoS). The elastic constants and the EoS usually are not determined experimentally on the same crystal and with the same experimental settings. Moreover, the experimental determination of the EoS is an isothermal measurement while that of the elastic constants is adiabatic (Angel et al., 2009). This leads to the consequence that the isothermal Reuss bulk modulus determined at room conditions ($K_{TR,0}$) from the EoS does not coincide exactly with the adiabatic Reuss bulk modulus that can be calculated from the elastic tensor as $K_{SR,0} = (S_{11} + S_{22} + S_{33} + 2 \cdot (S_{12} + S_{13} + S_{23}))$, where $S_{ij} = C_{ij}^{-1}$ are the components of the compliance matrix (in GPa^{-1}).

The calculations performed in this thesis combine thermodynamic calculations based on the EoS and mechanical calculations performed with FE that require the elastic constants C_{ij} of the minerals involved (see section 4.1). To keep the consistency among the different steps of the calculations, the C_{ij} of the minerals were rescaled to obtain a new elastic tensor that gives a $K_{R,0}$ equal to that obtained from the EoS. To this aim, all the C_{ij} were multiplied by a scalar value (close to 1) that was adjusted until the agreement in the value of $K_{TR,0}$ was reached. This approach guarantees that the anisotropy of the mineral is not changed by the rescaling.

B.1 Diamond

The elastic properties of diamond were measured by Zouboulis et al. (1998) with Brillouin scattering in the temperature range 300–1600 K. The room P,T adiabatic elastic constants were rescaled by the same small factor (0.9985) to obtain a new elastic tensor that gives a $K_{TR,0}$= 444.0 GPa (Table B.2), to be consistent with the non-linear EoS reported by Angel et al., 2015a. The close-to-isothermal elastic constants (Cij) obtained with this procedure were then used in FE analysis (Table B.1). The anisotropy of diamond was not modified with respect to the original experimental stiffness tensor, as evaluated through the universal anisotropic index (Ranganathan and Ostoja-Starzewski, 2008) A^U=0.0438.

Table B.1: Elastic constants (C_{ij}, GPa) of diamond. Modified from Zouboulis et al. (1998) as described in the text.

C_{11}	C_{12}	C_{44}
1078.4	126.8	575.7

Table B.2: Isotropic elastic bulk properties (GPa) of diamond.

$K_{TR,0}$	$K_{TV,0}$	$G_{TR,0}$	$G_{TV,0}$
444.0	444.0	531.1	535.8

B.2 Grossular

The elastic properties of a natural 97%-pure grossular single crystal were measured by Isaak et al. (1992) with rectangular parallelepiped resonance (RPR) method, from room temperature to 1350 K. The room P,T adiabatic elastic constants were rescaled by a small factor (0.993465) to obtain a new elastic tensor that gives a $K_{TR,0}$= 166.57 GPa (Table B.4), consistent with the non-linear EoS reported by Milani et al., 2017. The elastic constants (Cij) obtained with this procedure were then used in FE analysis (Table B.3). The anisotropy of grossular was not modified with respect to the original experimental stiffness tensor, as evaluated through the universal anisotropic index (Ranganathan and Ostoja-Starzewski, 2008) A^U=0.01124.

Table B.3: Elastic constants (C_{ij}, GPa) of grossular. Modified from Isaak et al. (1992) as described in the text.

C_{11}	C_{12}	C_{44}
316.72	91.50	102.23

Table B.4: Isotropic elastic bulk properties (GPa) of grossular.

$K_{TR,0}$	$K_{TV,0}$	$G_{TR,0}$	$G_{TV,0}$
166.57	166.57	106.14	106.38

B.3 Pyrope

The elastic properties of a pure synthetic pyrope were measured by Sinogeikin and Bass (2002) with Brillouin scattering. They determined the variation of the adiabatic elastic constants from room temperature up to 1073 K. The room P,T adiabatic elastic constants were modified (Table B.5) to obtain a $K_{TR,0}$= 163.7 GPa (as in Milani et al., 2015) and a $G_{TR,0}$= 94 GPa (Table B.6), to be consistent with the non-linear EoS implemented in Eosfit. The anisotropy of pyrope was not modified with respect to the original experimental stiffness tensor, and the universal anisotropic index (Ranganathan and Ostoja-Starzewski, 2008) A^U=0.0009 means that pyrope is practically isotropic.

Table B.5: Elastic constants (C_{ij}, GPa) of anisotropic pyrope. Modified from Sinogeikin and Bass (2002) as described in the text

C_{11}	C_{12}	C_{44}
291.1	100	93

Table B.6: Isotropic elastic bulk properties (GPa) of pyrope.

$K_{TR,0}$	$K_{TV,0}$	$G_{TR,0}$	$G_{TV,0}$
163.7	163.7	94.0	94.0

B.4 Quartz

The adiabatic elastic constants (C_{ij}) of a natural quartz were determined by Lakshtanov et al. (2007). The room P,T adiabatic elastic constants were multiplied by a small correction factor to obtain a bulk modulus equal to to the isothermal value $K_{TR,0}$=37.15 GPa of the $P-T-V$ EoS reported in Angel et al., 2017a. This small correction can be considered an appropriate approximation to convert the original constants from adiabatic into isothermal (Table B.7). Moreover it allows the use of the anisotropic relaxation obtained from FE calculations in the modeling of the entrapment conditions performed with the non-linear EoS.

Table B.7: Elastic constants (C_{ij}, GPa) of quartz. Modified from Lakshtanov et al. (2007) as described in the text.

C_{11}	C_{33}	C_{44}	C_{66}	C_{12}	C_{13}	C_{14}
86.9	106.4	59.5	40.1	6.7	11.3	13.5

Table B.8: Isotropic elastic bulk properties (GPa) of quartz.

K_{0TR}	K_{0TV}	G_{0TR}	G_{0TV}
37.2	37.6	44.0	48.5

Table B.9: Isotropic elastic bulk properties (GPa) of quartz.

K_{0TR}	K_{0TV}	G_{0TR}	G_{0TV}
37.2	37.6	44.0	48.5

B.5 Zircon

The elastic properties of nonmetamict natural and synthetic crystals of zircon were measured by Özkan et al., 1974 using the pulse superposition and the phase comparison method. The adiabatic elastic constants measured at room conditions on the two samples were averaged and are reported in Table B.10. Since the Reuss bulk modulus agrees with the isothermal Reuss bulk modulus reported in the EoS by Zaffiro (personal communication), we did not rescale the experimental C_{ij}. The anisotropy of zircon is evaluated through its universal anisotropic index (Ranganathan and Ostoja-Starzewski, 2008) A^U=1.115.

Table B.10: Elastic constants (C_{ij}, GPa) of zircon from Özkan et al. (1974).

C_{11}	C_{33}	C_{44}	C_{66}	C_{12}	C_{13}
423.7	490.0	113.6	48.5	70.3	149.5

Table B.11: Isotropic elastic bulk properties (GPa) of zircon.

K_{0TR}	K_{0TV}	G_{0TR}	G_{0TV}
225.3	230.7	98.2	119.7

Appendix C

Conventions for stress and strain

Throughout the text and in the development of the Matlab® code to automate the FE analysis that are solved with Dassault Systemes Abaqus®, the Voigt convention has been used to convert from tensors to vectors/matrices. The Voigt convention used for stresses is:

$$\begin{bmatrix} \sigma_{11} \\ \sigma_{22} \\ \sigma_{33} \\ \sigma_{23} \\ \sigma_{13} \\ \sigma_{12} \end{bmatrix} = \begin{bmatrix} \sigma_1 \\ \sigma_2 \\ \sigma_3 \\ \sigma_4 \\ \sigma_5 \\ \sigma_6 \end{bmatrix} \tag{C.1}$$

The Voigt convention used for strains is:

$$\begin{bmatrix} \varepsilon_{11} \\ \varepsilon_{22} \\ \varepsilon_{33} \\ \varepsilon_{32} + \varepsilon_{23} \\ \varepsilon_{31} + \varepsilon_{13} \\ \varepsilon_{21} + \varepsilon_{12} \end{bmatrix} = \begin{bmatrix} \varepsilon_1 \\ \varepsilon_2 \\ \varepsilon_3 \\ \varepsilon_4 \\ \varepsilon_5 \\ \varepsilon_6 \end{bmatrix} \tag{C.2}$$

The convention used for stress and strain components in Abaqus® is different from the Voigt convention specified above. Whenever the stress or the strain components are specified in Abaqus® they are listed in the following order (see section 1.2.2-7 "Conventions", Abaqus® Analysis User's Manual- Vol. I - Abaqus 6.12). The convention for stresses in Abaqus® is:

$$\begin{bmatrix} \sigma_{11} \\ \sigma_{22} \\ \sigma_{33} \\ \sigma_{12} \\ \sigma_{13} \\ \sigma_{23} \end{bmatrix} = \begin{bmatrix} \sigma_1 \\ \sigma_2 \\ \sigma_3 \\ \sigma_4 \\ \sigma_5 \\ \sigma_6 \end{bmatrix} \tag{C.3}$$

The convention for strains in Abaqus® is:

$$\begin{bmatrix} \varepsilon_{11} \\ \varepsilon_{22} \\ \varepsilon_{33} \\ \varepsilon_{12} + \varepsilon_{21} \\ \varepsilon_{13} + \varepsilon_{31} \\ \varepsilon_{23} + \varepsilon_{32} \end{bmatrix} = \begin{bmatrix} \varepsilon_{11} \\ \varepsilon_{22} \\ \varepsilon_{33} \\ \gamma_{12} \\ \gamma_{13} \\ \gamma_{23} \end{bmatrix} = \begin{bmatrix} \varepsilon_1 \\ \varepsilon_2 \\ \varepsilon_3 \\ \varepsilon_4 \\ \varepsilon_5 \\ \varepsilon_6 \end{bmatrix} \tag{C.4}$$

As a consequence, in Abaqus also the matrix notation for the tensor of the elastic properties (i.e. the stiffness tensor that is usually defined as C_{ijkl} but in Abaqus is defined as D_{ijkl}) does not correspond to the usual Voigt convention, but is defined as follows:

$$\begin{bmatrix} \sigma_{11} \\ \sigma_{22} \\ \sigma_{33} \\ \sigma_{12} \\ \sigma_{13} \\ \sigma_{23} \end{bmatrix} = \begin{bmatrix} D_{1111} & D_{1122} & D_{1133} & D_{1112} & D_{1113} & D_{1123} \\ & D_{2222} & D_{2233} & D_{2212} & D_{2213} & D_{2223} \\ & & D_{3333} & D_{3312} & D_{3313} & D_{3323} \\ & symm. & & D_{1212} & D_{1213} & D_{1223} \\ & & & & D_{1313} & D_{1323} \\ & & & & & D_{2323} \end{bmatrix} \begin{bmatrix} \varepsilon_{11} \\ \varepsilon_{22} \\ \varepsilon_{33} \\ \gamma_{12} \\ \gamma_{13} \\ \gamma_{23} \end{bmatrix} \tag{C.5}$$

The difference between the Voigt and the Abaqus convention can be noted taking for example the component D_{1213} of the stiffness tensor. Written as a matrix it would be the component C_{65} using the Voigt convention, while it becomes the component D_{45} in the Abaqus convention.

Understanding the Abaqus notation becomes extremely important when interpreting the shear components of the strain in the Abaqus output. The results can be viewed as contour map or exported as XY data along a specified path and saved in a text file with .rpt extension. In both cases the components of the stress and of the strain are reported with the following notation:

$$\begin{bmatrix} S_{11} \\ S_{22} \\ S_{33} \\ S_{12} \\ S_{13} \\ S_{23} \end{bmatrix} = \begin{bmatrix} \sigma_{11} \\ \sigma_{22} \\ \sigma_{33} \\ \sigma_{12} \\ \sigma_{13} \\ \sigma_{23} \end{bmatrix} \tag{C.6}$$

$$\begin{bmatrix} E_{11} \\ E_{22} \\ E_{33} \\ E_{12} \\ E_{13} \\ E_{23} \end{bmatrix} = \begin{bmatrix} \varepsilon_{11} \\ \varepsilon_{22} \\ \varepsilon_{33} \\ \varepsilon_{12} + \varepsilon_{21} \\ \varepsilon_{13} + \varepsilon_{31} \\ \varepsilon_{23} + \varepsilon_{32} \end{bmatrix} \tag{C.7}$$

I developed a program, written in Matlab®, to automatize the pre-processing and the post-processing of FE analysis that are solved with Abaqus. This program allows the user to set the elastic properties and the crystallographic orientation of the host and of the inclusion, the pre-strain or the pre-stress in the inclusion, and the external pressure acting on the host. When the simulation is run with a pre-stress or pre-strain in the inclusion, the program always asks the user the tensor components of the strain or the stress. For example, when the component e12 of the strain is asked it refers to the component ε_{12} of the strain tensor and not to the component $E_{12} = \varepsilon_{12} + \varepsilon_{21}$ of the Abaqus convention. The code then takes care of all the conversions to Abaqus conventions while writing the input file for the FE analysis. When this program is used to process the results after a simulation, it makes the back transformation from the Abaqus convention (that is assumed in the .rpt files produce by Abaqus) to the Voigt convention or directly to the tensor components. But the user should be careful when interpreting the results of the contour plot directly in Abaqus, or when reading the data directly from the output file with .rpt extension, since those data are written with the Abaqus convention (equations C.6 and C.7).